

FLEXIBLE ANTENNA DESIGN FOR 5G APPLICATIONS

A THESIS SUBMITTED TO AUCKLAND UNIVERSITY OF TECHNOLOGY
IN FULFILMENT OF THE REQUIREMENTS FOR THE DEGREE OF
DOCTOR OF PHILOSOPHY

By

Erfeng Li

School of Engineering, Computer and Mathematical Sciences

October 2021

Attestation of Authorship

I hereby declare that this submission is my own work and that, to the best of my knowledge and belief, it contains no material previously published or written by another person nor material which to a substantial extent has been accepted for the qualification of any other degree or diploma of a university or other institution of higher learning.

Signature of candidate

Acknowledgements

First of all, I would like to express my greatest thanks to my primary supervisor **Dr. Jack Xuejun Li** Associate Professor, School of Engineering, Computer Science and Mathematical Science, Auckland University of Technology, New Zealand, for offering me the opportunity to conduct this doctoral research work and providing his technical inspirations and insights, constructive guidance, critical reviews, valuable feedback, and heartwarming encouragement. My sincere appreciation also goes to my secondary supervisor Associate Professor **Dr. Boon-Chong Seet** for his critical and valuable support and advice.

Secondly, many thanks to my family who has been accompanying and supporting me through these years spiritually and financially. I also would like to acknowledge the loveful support from my dearest friends: Dr. Google Leigh, Anthony Russell, MCGL Chris, Four Musketeers (Phil, Philippe, and Onn), Ash, Sisi An, Xiaoyou Lin, David Zheng, Doncha John, and Jadeheart Gregory, who have made my life in New Zealand cheerful and meaningful.

Erfeng Li

October 2021

Abstract

Recent advancements in the fifth generation (5G) technology and internet of things (IoT) along with the development of printed electronics (PE) have inspired flexible antenna designs, which features low-profile and low-cost. They open the door to extend wireless communication to support wearable applications on conformal curvature surfaces in the context of wireless personal area networks (WPANs). Most of current existing antenna design focus on traditional materials and fabrication methods, yielding rigid metallic structures, which makes them not suitable for the applications with flexible and conformal surfaces, let alone the WPAN applications. Therefore, this thesis focuses on antenna designs with the promising flexible structure, which can be fabricated with proper methods and materials and applied to curvature surfaces.

Firstly, a comprehensive literature review, including ink-printed antennas and their fabrication techniques is presented. Next, three low-profile planar antennas are proposed with flexible dielectric substrates, which are suitable for fabrication using modern printing technologies. These antennas include a microstrip slot antenna operating at 5.8 GHz, a triband microstrip patch antenna with multiple slots operating at 5.8 GHz, 6.2 GHz, and 8.4 GHz, and a wideband dipole array antenna whose operating frequency covers 24.5 GHz and 28 GHz in industrial, scientific and medical (ISM) band. These above antennas demonstrate promising measured and simulated performance, acceptable tolerance in the conformal tests, and positive specific absorption rate (SAR)

when interacting with human body part. Furthermore, a metasurface based S-shaped split ring resonator (SRR) linear-to-circular (LTC) polarization converter is presented to enhance the gain and bandwidth of planar patch and slot antennas. Its performance in curvature situation is evaluated as well.

These antenna designs proposed in this thesis provide a deeper insight into flexible low-profile planar antenna design for curvature surfaces and add to the rapidly expanding field of WPAN applications. In addition, they have important practical implications for fabrication using printing technologies. Moreover, the results and findings in this thesis contribute to existing knowledge of interaction between antennas and human body.

Contents

Attestation of Authorship	ii
Acknowledgements	iii
Abstract	iv
Contents	vi
List of Tables	ix
List of Tables	ix
List of Figures	x
List of Figures	x
Glossary and Notations	xiv
1 Introduction	1
1.1 Background	1
1.2 Motivation	3
1.3 Objectives	4
1.4 Original Contribution	5
1.5 Publications	6
1.5.1 Journal Papers	6
1.5.2 Conference Papers	7
1.5.3 Contributions in other Related Works	8
1.6 Outline of the Thesis	8
2 Literature Review	10
2.1 Antennas Characteristics	10
2.1.1 Antenna Parameters	10
2.1.2 Antenna Simulation	24
2.1.3 Antenna Measurements	27
2.2 Microstrip Patch Antenna	29

2.2.1	Fundamental Characteristics	30
2.2.2	Feeding Methods	31
2.2.3	Analysis Methods	32
2.3	Ink-Printed Flexible Antennas	37
2.3.1	Conductive Inks	39
2.3.2	Characterisation for Conductive Ink	41
2.3.3	Conductive Ink-Printed Antennas	44
2.4	Printing Techniques	53
2.4.1	Inkjet Printing	55
2.4.2	Screen Printing	62
2.4.3	Gravure Printing	68
2.4.4	Flexographic Printing	70
2.5	Antennas and Metamaterials	76
2.5.1	Metamaterials	77
2.5.2	Metamaterial Functions	82
2.5.3	Metasurfaces	83
2.6	Chapter Summary	85
3	Silver Ink-Printed Flexible Wideband Dipole Array Antenna	86
3.1	Background	86
3.2	Dipole Array Antenna Design	88
3.3	Enhancement with Yagi-Uda Directors	91
3.4	Flexible Polyester Fabric Substrate	95
3.5	Metalon HPS-021LV Silver Nanoparticle Ink	95
3.6	Antenna Fabrication	97
3.7	Measurement Results and Discussion	100
3.8	Conformal Tests	108
3.9	Chapter Summary	114
4	A Flexible Slot Antenna for Conformal and Wearable Applications	115
4.1	Slot Antennas	115
4.1.1	Common Slot Antenna Designs	116
4.1.2	Microstrip Slot Antennas	120
4.2	Slot Antenna Design for Conformal Applications	122
4.2.1	A Slot Antenna with Parallel Slits Loading	122
4.2.2	Triband Slot Patch Antenna for Conformal and Wearable Ap- plications	138
4.2.3	Remarks	168
4.3	Chapter Summary	169
5	Metasurface in Antenna Design as Polarization Converter	170
5.1	Metasurface Design Algorithm	171
5.1.1	System Level Design	171
5.1.2	Particle Level Design	172

5.1.3	Mask Generation	181
5.2	Metasurface Waves Analysis	181
5.3	Metasurface Based S-Shaped Split Ring Resonator for Linear-to-Circular Polarization Conversion	189
5.3.1	Structure Design and Parametric Study	191
5.3.2	Simulation Results and Discussion	202
5.3.3	Conformal Test with Wavy Curvature Surface	205
5.3.4	Remarks	208
5.4	Chapter Summary	208
6	Conclusion and Recommendations for Future Work	209
6.1	Conclusion	209
6.2	Recommendations for Future Work	210
	References	212

List of Tables

2.1	Comparison of conductive inks used in antenna designs.	54
2.2	Comparison between Inkjet Printed Antennas	61
2.3	Comparison between Screen Printed Antennas	67
2.4	Results of printed lines for RFID antennas	73
3.1	Dimensional Parameters of Proposed Antenna (Unit: mm)	90
3.2	Physical Properties of HPS-021LV Silver Ink.	95
3.3	Comparison of Designs in the Literature	108
3.4	Antenna Parameters for Bending Tests	113
4.1	Safe distance under skin for different scenarios	138
4.2	Antenna Parameters for Conformal Tests	159

List of Figures

1.1	First wireless telephone conversation via photophone in 1880.	2
1.2	5G for internet of things.	2
2.1	Coordinate system for antennas.	12
2.2	Illustration of beamwidth and directivity.	16
2.3	Illustration of antenna efficiency components.	18
2.4	Illustration of antenna polarization.	21
2.5	Elliptical Polarization.	22
2.6	Cases of simulations with ANSYS HFSS.	25
2.7	Adaptive refinement and automatic mesh in ANSYS HFSS.	26
2.8	FEM solution example in ANSYS HFSS.	27
2.9	Diagram of gain transfer method setup.	29
2.10	Microstrip patch antenna.	30
2.11	Equivalent circuits for common feeding methods.	31
2.12	Electric field lines of fringing effect.	33
2.13	Effective dielectric constant.	34
2.14	Silver ink printed Sierpinski fractal antenna.	45
2.15	Return loss of the silver ink printed Sierpinski fractal antenna.	45
2.16	Silver screen printed RFID antenna on wood	47
2.17	Grains in wood veneer surface.	47
2.18	Geometry of antenna (a) top view (b) cross-section view.	48
2.19	Multilayer patch antenna (a) first layer of the silver printer on Kapton sheet (b) final antenna.	48
2.20	Aperture coupled patch antenna with carbon nanotube meshed ground plane.	50
2.21	Different space between meshed carbon nanotube threads.	50
2.22	Simulation results with different spaces between CNT threads.	51
2.23	Carbon nanotube monopole antenna design.	52
2.24	Influence on VSWR from cylinder radius change.	52
2.25	Illustration of continuous inkjet printing principle.	56
2.26	Illustration of drop-on-demand inkjet printing principle.	57
2.27	Popular drop on demand inkjet printers.	57
2.28	Antennas fabricated with inkjet printing technique.	59
2.29	Illustration of screen printing progress.	63

2.30	Automatic screen printers.	63
2.31	Antennas fabricated with screen printing technique.	66
2.32	Illustration of gravure printing.	68
2.33	Gravure cell under microscopy.	69
2.34	Illustration of flexographic printing mechanism.	70
2.35	Flexographic printed RFID for biomedical applications.	72
2.36	Gravure printed RFID antenna.	74
2.37	Monopole antenna printed by flexographic printing.	75
2.38	Results of monopole antenna by flexographic printing and screen printing.	75
2.39	Metamaterials.	77
2.40	Right-handed and left-handed triplet vectors.	79
2.41	Entire span of possible material properties in ϵ - μ domain.	81
2.42	Comparison of metasurfaces with metamaterials: (a) Cloaking. (b) Superlens. (c) Conformal metasurface.	84
3.1	(a) Proposed antenna design and (b) its dimensional parameters.	89
3.2	Parametric study for directors.	91
3.3	Effects of directors on total directivity D_0 at $\phi = 0^\circ$ at 24.5 GHz.	93
3.4	Effects of directors on total directivity D_0 at $\phi = 0^\circ$ at 28 GHz.	93
3.5	Effects of directors on antenna gain.	94
3.6	Curing temperature and duration for HPS-021LV silver ink.	96
3.7	Process of making a silk screen stencil.	98
3.8	Cross-section image of silver ink print trace under SEM.	98
3.9	Printed ink trace surface under SEM.	99
3.10	Copper laser-cut antenna (a) and silver-ink printed antenna (b).	100
3.11	The measurement of antenna under test in anechoic chamber.	101
3.12	Reference horn antenna in the anechoic chamber.	101
3.13	The forward gains and efficiency of silver-ink printed and copper laser-cutting antennas.	102
3.14	The return loss of silver-ink printed and copper laser-cut antennas.	103
3.15	Illustration of air gap analysis.	103
3.16	Effect of air gap size on return loss.	104
3.17	Effect of substrate thickness on return loss.	105
3.18	Radiation patterns of silver-ink printed antenna: (a) 24.5 GHz E-plane, (b) 24.5 GHz H-plane, (c) 28 GHz E-plane and (d) 28 GHz H-plane (Co: Co-polarization; X: Cross-polarization; M: Measured; S: Simulated).	106
3.19	Radiation patterns of of copper laser-cutting antenna: (a) 24.5 GHz E-plane, (b) 24.5 GHz H-plane, (c) 28 GHz E-plane and (d) 28 GHz H-plane (Co: Co-polarization; X: Cross-polarization; M: Measured; S: Simulated).	107
3.20	Conformal bending tests for the dipole array antenna in HFSS.	109
3.21	Approximation of bending angle.	110
3.22	Antenna return loss for bending tests.	111
3.23	Antenna performance for bending tests.	111

3.24	E-plane and H-plane for bending tests.	112
4.1	Structure of the slotted spherical antenna (a) entire view, (b) half-profile view.	117
4.2	Illustration of the SIW slot antenna.	117
4.3	Band-gap slot antenna with 2×2 slot array.	118
4.4	Basic structure of a microstrip slot antenna.	120
4.5	Feeding techniques to reduce antenna input impedances.	120
4.6	Equivalent circuit and network model of microstrip slot antenna.	121
4.7	Parametric study of the size of the slit.	125
4.8	Slit slot antenna layout and dimensions.	125
4.9	Front and back side of fabricated antenna.	126
4.10	Simulated and measured results of the antenna.	126
4.11	Principle planes radiation patterns at 5.8 GHz.	127
4.12	Antenna wrapped onto a cylinder for conformal surface test.	128
4.13	Antenna return loss and input impedance with different bending tests.	128
4.14	Radiation patterns for different bending tests.	129
4.15	Antenna Peak Gain for different bending tests	130
4.16	Antenna front to back ratio for different bending tests	131
4.17	Simulation with human left hand model in HFSS.	132
4.18	Antenna return loss with human body model.	132
4.19	E-plane radiation patterns with different distances from human body model.	134
4.20	H-plane radiation patterns with different distances from human body model.	134
4.21	Antenna front to back ratio with human hand model.	135
4.22	Antenna peak gain with human hand model.	135
4.23	SAR plot on 2D cross-section planes for 20 mm distance.	136
4.24	Average SAR along the line across hand model	137
4.25	Adding first joint part on the top of ring slot.	140
4.26	Parametric study of joint1 length L_{joint1}	141
4.27	Parametric study of joint1 position Y_{joint1}	142
4.28	Parameter sensitivity of Y_{joint1} and L_{joint1}	143
4.29	Adding second joint part at the bottom right of ring slot.	144
4.30	Parametric study of joint2 length L_{joint2}	144
4.31	Parametric study of joint2 position X_{joint2}	145
4.32	Parameter sensitivity of X_{joint2} and L_{joint2}	146
4.33	Triband slot antenna structure layout.	146
4.34	Return loss and gain of proposed antenna	147
4.35	Antenna performance at three bands	149
4.36	Conformal test with antenna wrapped onto a cylinder	150
4.37	Antenna return loss for bending tests	150
4.38	Electric field 3D polar plot for cylinder radius of 20 mm.	151
4.39	Electric field 3D polar plot for cylinder radius of 50 mm.	152

4.40	Electric field 3D polar plot for cylinder radius of 80 mm.	153
4.40	E-plane and H-plane for conformal tests	155
4.41	Surface current distribution at 5.8 GHz for cylinder radius of 50 mm .	155
4.42	Surface current distribution at 6.2 GHz for cylinder radius of 50 mm .	156
4.43	Surface current distribution at 8.4 GHz for cylinder radius of 50 mm .	157
4.44	Antenna peak gain for bending tests	158
4.45	Antenna radiation efficiency for bending tests	158
4.46	Triband antenna with hand model in HFSS.	160
4.47	E-field 3D plot for $d_{ant} = 0$ mm	161
4.48	SAR plot on XoZ -plane when $d_{ant} = 0$ mm	162
4.49	SAR plot on YoZ -plane when $d_{ant} = 0$ mm	163
4.50	SAR plot on XoZ -plane when $d_{ant} = 40$ mm	164
4.51	SAR plot on YoZ -plane when $d_{ant} = 40$ mm	165
4.52	Reference line inside hand model to calculate SAR.	166
4.53	Average SAR vs. d_{ref} along the reference line.	166
4.54	Average SAR vs. d_{ref} along the reference line.	167
5.1	Metamaterial design procedure diagram.	172
5.2	SRR unit cell example and its equivalent circuit spatial model.	174
5.3	Boundary conditions for (a) two adjacent materials and (b) a third thin slab material between two different materials.	182
5.4	Illustration of two types of metasurface waves: (a) $k_x < k_0$, (b) $k_x > k_0$	187
5.5	Antenna layout and simulation setup.	194
5.6	Effect of g_1 on R_{yy}	195
5.7	Effect of g_1 on R_{xy}	196
5.8	Effects of g_1 on phase difference $\Delta\phi$	196
5.9	Effects of g_1 on ellipticity e	197
5.10	Effects of g_1 on axial ratio.	197
5.11	Effects of g_1 on conversion efficiency η	198
5.12	Effects of g_1 on polarization conversion rate.	198
5.13	Effect of W_s on R_{yy}	199
5.14	Effect of W_s on R_{xy}	200
5.15	Effects of W_s on phase difference $\Delta\phi$ and ellipticity e	201
5.16	Effects of W_s on axial ratio.	201
5.17	Effects of W_s on conversion efficiency η and PCR.	202
5.18	Performance of proposed LTC polarization converter.	203
5.19	Axial ratio and efficiency.	203
5.20	Simulation of the patch antenna and proposed LTC converter.	204
5.21	Return loss bandwidth of the patch antenna with LTC converter.	204
5.22	Over view of the curvature surface of the proposed LTC converter.	205
5.23	Effects of A_{bend} on R_{yy}	206
5.24	Effects of A_{bend} on R_{xy}	206
5.25	Effects of A_{bend} on phase difference $\Delta\phi$	207
5.26	Effects of A_{bend} on ellipticity e and AR.	207

Glossary and Notations

Glossary

3D	Three dimensional
3GGP	The 3rd Generation Partnership Project
5G	the fifth generation
AR	Axial ratio
AUT	Antenna under test
balun	Unbalance-to-balance
BW	Backward-wave
%BW	Percentage bandwidth
CCW	Counterclockwise
CEM	Computational electromagnetics
CIJ	Continuous inkjet
CNT	Carbon nanotube
Co-pol	Co-polarization
CP	Circularly polarized
CPS	Coplanar stripline
CPW	Coplanar waveguide
CSRR	Complimentary SRR
CVD	Chemical vapor deposition

CW	Clockwise
dB	Decibels
DGS	Defect ground structure
DMF	dimethyl formamide
DMSO	Dimethyl sulfoxide
DNG	Double Negative Material
DOD	Drop on demand
DWCNT	Double-wall carbon nanotube
EHF	Extremely High Frequency
ELC	Electric field coupled resonator
EM	Electromagnetic
ENZ	ε -near zero
FEM	Finite element methods
FIT	Finite integration technique
FNBW	First-Null Beamwidth
FR1	5G low-band (sub-6 GHz)
FR2	5G high-band (24-86 GHz)
FSS	Frequency Selective Surface
GPS	Global positioning system
HFSS	High Frequency Structural Simulator
HPBW	Half Power Bandwidth
IC	Integrated circuit
IMI	Insulator-metal-insulator
IMT	International Mobile Telecommunications
IoT	Internet of Things
ISM	Industrial, scientific and medical

ITS	Intelligent transportation system
ITU	Internation Telecommunication Union
ITU	International Telecommunication Union
LHCP	Left-handed circular polarization
LHM	Left-handed Material
LMDS	Local multipoint distribution service
LMDS	Local multipoint distribution service
LOS	Line-of-Sight
LP	Linearly polarized
LPDA	Log-periodic dipole array
LTC	Linear-to-circular
MIMO	Multiple-input multiple output
mmWave	Millimeter Wave
MTC	Machine-type communication
NFC	Near-field communication
NIM	Negative-refractive Index Material
NPV	Negative phase velocity
PCB	Printed Circuit Board
PCR	Polarization conversion rate
PDMS	Polydimethylsiloxone
PE	Printed electronics
PET	Polyethylene terephthalate
PVP	Polyvinylpyrrolidone
RCS	Radar corss-section
RFID	Radio-frequency identification
RHCP	Right-handed circular polarization

RHM	Right-handed Material
RLBW	Return-loss bandwidth
SAR	Specific absorption rate
SEM	Scanning electron microscope
SHF	Super High Frequency
SIW	Substrate integrated waveguide
SMA	Sub-Miniature Version A
S-parameter	Scattering parameter
SPP	Surface plasmon polariton
sr	Steradian
SRR	Split ring resonator
SSR	Split Ring Resonator
SWCNT	Single-wall carbon nanotube
TE	Transverse electric
TM	Transverse magnetic
TPU	Thermoplastic polyurethane
UHF	Ultra-high frequency
UV	Ultraviolet
UWB	Ultra wideband
VNA	Vector network analyser
VSWR	Voltage standing wave ratio
WLAN	Wireless local area network
WPAN	Wireless personal area network
X-pol	Cross-polarization

Notation

A	area of a sphere
A_{bend}	amplitude of the bending sinusoidal curve
α	attenuation constant
α	bending angle
\vec{B}	magnetic flux density vector
β	phase constant
d	distance between transmit and receive antennas
D	largest dimension of an antenna
D	directivity of an antenna
\vec{D}	electric flux density vector
d	unit cell dimension
D_0	maximum directivity of an antenna
d_{ant}	distance between antenna and hand model
δ	surface depth of skin effect
$\Delta\phi$	phase difference
ΔL	extended microstrip patch length
d_l	director length coefficient
D_{max}	maximum directivity of an antenna
$\Delta\phi$	phase difference
d_{ref}	distance on the reference line
d_s	director space coefficient
E	electric field
\mathcal{E}	instantaneous electric-field intensity
e	eccentricity
e_0	total antenna efficiency

$\bar{\epsilon}$	dispersive permittivity
e_c	conduction efficiency
e_{cd}	conduction and dielectric efficiency
e_d	dielectric efficiency
E_{end}	voltage at the end of propagation
ϵ	electric permittivity
ϵ_0	free space electric permittivity
E_ϕ	far-zone electric-field ϕ component
ϵ_m	modified permittivity
ϵ_r	relative permittivity
ϵ_{reff}	effective dielectric constant
e_r	reflection efficiency
E_r	electric field of reflected wave
E_{start}	voltage at the end of propagation
η	intrinsic impedance of medium
η	wave impedance
η	conversion efficiency
E_θ	far-zone electric-field θ component
\mathcal{E}_x	x component of instantaneous electric-field
E_x	x component of electric field
e_x	unit direction vector on x -axis
E_{x0}	maximum magnitude of x component of electric-field
$\exp(j\omega t)$	time-harmonic convention
\mathcal{E}_y	y component of instantaneous electric-field
E_y	y component of electric field
e_y	unit direction vector on y -axis

E_{y0}	maximum magnitude of y component of electric-field
f	frequency
F	fitting parameter
f_0	resonant frequency
f_{0e}	electric resonant frequency
f_{0u}	magnetic resonant frequency
F_e	electric resonant intensity
f_{min}	minimum frequency
f_r	resonant frequency
F_u	magnetic resonant intensity
G_0	maximum gain
G_{0abs}	maximum absolute gain
$G_{0forward}$	maximum gain in forward direction
g_1	gap between "S" and "C" resonators
G_{abs}	absolute gain
Γ	reflection coefficient
G	antenna gain
γ	complex propagation constant
γ	damping factor
γ_e	electric damping factor
γ_u	magnetic damping factor
G_{dBi}	gain expressed in decibels
G_{max}	maximum gain
G_ϕ	ϕ component of gain
G_r	radiation conductance
$G_{r,dB}$	received gain in dB

G_θ	θ component of gain
H	magnetic field
\mathcal{H}	instantaneous magnetic-field intensity
\vec{J}_s	surface current density
k	wave vector
L	microstrip patch length
λ	wavelength of electromagnetic wave
λ_{eff}	effective wavelength
λ_g	guided wavelength of electromagnetic wave in waveguide
L_{eff}	effective length of microstrip patch
L_{joint1}	length of joint1
L_{joint2}	length of joint 2
L_{slit}	slit length
μ	magnetic permeability
μ_0	free space magnetic permeability
$\bar{\mu}$	dispersive permeability
μ_{eff}	effective permeability
μ_m	modified permeability
μ_r	relative permeability
n	refractive index
\hat{n}	unit vector normal to a surface
∇	curl of a vector
Ω	solid angle
Ω_A	beam solid angle
ω	angular frequency
ω_{pl}	plasmon frequency

\mathcal{P}	instantaneous total power
P	perimeter of the cross-section area
p	periodicity
P_{avg}	average radiated power
P_{end}	power at the end of propagation
ϕ	azimuth angle
ϕ_x	x component phase
ϕ_{xy}	phase of y -to- x conversion
ϕ_y	y component phase
ϕ_{yy}	phase of y -to- y conversion
P_{in}	total input power
P_{lc}	conductor loss
$P_{L,dB}$	path loss in dB
P_{rad}	radiated power
P_r	received power level
P_{start}	power at the start of propagation
P_t	transmit power level
r	distance in spacial coordinates
R	field distance
r	reflection coefficient
R_{dc}	direct current resistance
ρ	resistivity
R_{rf}	effective radio frequency resistance
R_S	surface resistance
R_{xy}	reflection coefficient of y -to- x conversion
R_{yy}	reflection coefficient of y -to- y conversion

S_0	unit cell area
$S_{21,dB}$	S_{21} in dB
S	cross-section area of a conductor
σ	conductivity
σ	spacing factor of dipole array
t or h	substrate thickness
τ	scale factor of dipole array
t	transmission coefficient
θ	elevation angle
U	radiation intensity
U_0	radiation intensity of an isotropic source
U_{max}	maximum radiation intensity
U_ϕ	ϕ component of radiation intensity
U_θ	θ component of radiation intensity
v_0	speed of light in free space
V	unit cell volume
\mathcal{W}	instantaneous Poynting vector
W	microstrip patch width
W_{avg}	average radiated power density
W_{rad}	radiated power density
W_{slit}	slit width
X_{joint2}	location of joint2 on x -axis
Y	admittance
Y_e	electric admittance
Y_{joint1}	location of joint1 on y -axis
Z_0	transmission line characteristic impedance

Z_0	characteristic impedance of microstrip line
Z	load impedance
Z_{in}	antenna input impedance
Z_m	magnetic impedance

Chapter 1

Introduction

1.1 Background

Wireless communication has been playing an important role in the daily life of humankind ever since the first wireless telephone conversation occurred in 1880 with the photophone invented by Alexander Graham Bell and Charles Sumner Tainter [1] as represented in Figure 1.1. From the wireless telegraphy using electrostatic and electromagnetic (EM) induction in the late 19th century [2] to wireless revolution in the 1990s [3, 4], wireless system has evolved rapidly. After the first to the fourth generation wireless communication technology, the fifth generation (5G) technology has entered its worldwide deployment phase when the 3rd Generation Partnership Project (3GPP) specified the Release 15 to Release 17 version of specification.

5G technology was proposed to provide incomparable and ubiquitous connectivity [5, 6]. With the high speed and data rate brought by 5G technology, the connection between different entities can be further enhanced through Internet of Things (IoT) [7–9]. Consequently, the massive machine-type communication (MTC) has emerged in our lives, such as e-health services [10–13], smart city/town/home [14–16], industry



Figure 1.1: First wireless telephone conversation via photophone in 1880 [1].

4.0 [17, 18], and intelligent transportation system (ITS) [19–22].

As a key component in wireless communication systems, an antenna plays an irreplaceable role and is literally ubiquitous in our life, especially for commercial applications, such as smart mobile devices, radio-frequency identification (RFID) tags, wireless routers, and satellites. There are miscellaneous types of antennas for various applications, such as whip antenna, aperture antenna, wire antenna, loop antenna, horn antenna, and microstrip antenna [23, 24], etc. Correspondingly, there are different antenna

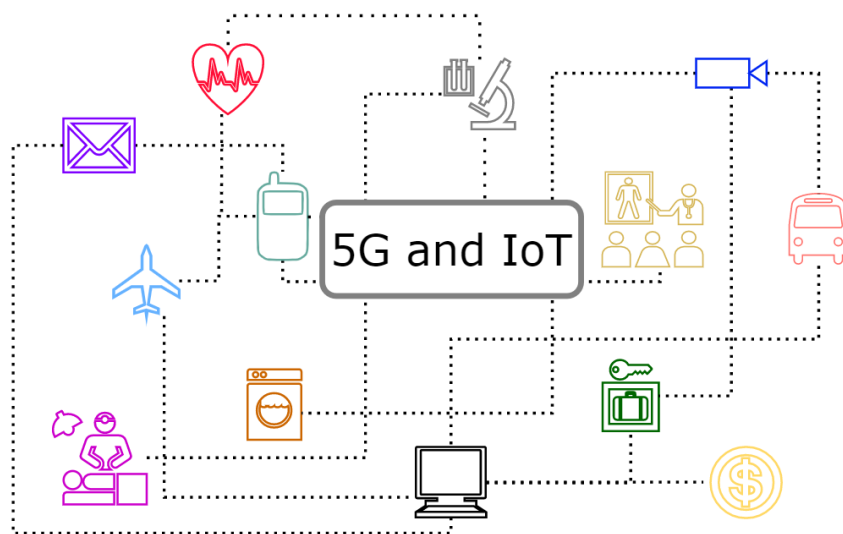


Figure 1.2: 5G for internet of things.

fabrication methods based on the antenna structure. For those three dimensional (3D) antennas, the metallic radiating part can be made by a combination of metal wire, rod, and patch; whereas the planar antennas are normally fabricated by printed circuit board (PCB) technique [25].

1.2 Motivation

With the rapid development of 5G and IoT technology, the demand for compact and flexible antennas has been phenomenally increasing, especially for wireless body area networks (WBANs), such as health monitoring and medical sensing. However, despite recent advances in the antenna design techniques and their fabrication methods, most antenna designs are still limited to conventional rigid dielectric and conductive materials. This creates a bottleneck for the possible flourish of wearable applications using wireless communications [26, 27]. A flexible and low-profile antenna is able to be integrated with complex and conformal devices for various application circumstances. The flexibility of the antenna will create more opportunities for a complex system design without structural compromises. On the other hand, the low-profile feature simplifies design and fabrication. To design a low-profile and flexible antenna, innovative materials and techniques are required to fabricate antennas that can withstand flexible circumstances with promising performance. Furthermore, the effect of the human body and other factors should be considered for potential applications of WBANs.

Through careful literature review [28–46], the author found that most antenna designs consists of rigid metallic structures and there have been few antenna designs with flexible structure for conformal circumstances [28, 45–52], despite their lack of low-profile and low cost features [47–49]. Furthermore, the interaction and performance with human body are not discussed for potential wearable applications. Therefore, the

author is motivated to investigate and study antenna designs with flexible structures and explore their performances under conformal situations and interactions with human body.

1.3 Objectives

The objective of this thesis is to propose low-profile planar antenna designs with flexible structures, which are suitable in conformal surfaces and wearable applications. The specific goals include antenna design, parametric studies of antenna geometries, conformal tests, and evaluation of integration with human body. The details of these goals are listed below:

1. To propose low-profile antennas types that are suitable for planar structure. Planar structures are chosen for the antenna design to adapt the flexible structure. In addition, based on the operating frequencies, the antennas may have different orders of overall dimensions. All these requirements should be considered for applications and fabrications.
2. To identify proper materials and fabrication techniques. Compared with conventional antenna design and fabricating techniques, the recently emerged printing electronics (PE) and conductive inks have drawn great attentions, where electronic components are ink-printed and a bendable or stretchable substrate can be applied, such as paper, plastic, and textile. Proper conductive ink and printing technique are to be selected.
3. To simulate flexible or curvature surface situation to evaluation the proposed antennas. Curvature surfaces are needed to embed the proposed antennas so that their tolerance under these circumstances can be evaluated.

4. To investigate the interactions with human body for potential wearable applications. To qualify as part of a wearable device, the proposed antennas should not only have high tolerance to flexible surface, but also meet the criteria for human health, such as the amount of the radiated energy absorbed by the human body.

1.4 Original Contribution

The main contribution of this thesis includes:

- **A silver Ink-Printed Flexible Wideband Dipole Array Antenna**

This proposed low-profile planar antenna is reported in Chapter 3 and corresponds to all the four objectives. It is comprised of dipole arrays and Yagi-Uda directors and operates from 23 GHz to 30 GHz, including industrial scientific and medical (ISM) bands (24.5 GHz and 28 GHz). The antenna is fabricated on flexible textile substrate by screen printing with silver nano-particle based conductive ink. The printed antenna demonstrates good performance compared with the identical copper reference antenna. The simulations under conformal surfaces also confirm its application in this area.

- **A slot antenna with Parallel Slit Loading for 5G Conformal and Wearable Applications**

This design is presented in Chapter 4 and corresponds to objective 1, 3, and 4. It consists of a low-profile and low-cost slot antenna with parallel slit loading for enhancement. The slot antenna operates at 5.8 GHz and has a compact size of 20×30 mm² on a flexible PCB for conformal surfaces and wearable applications. The bending tests and simulation with human body suggest that the proposed design has strong tolerance against conformal circumstances and potential application for wearable devices on human body.

- **A triband Slot Patch Antenna for Conformal and Wearable Applications**

This antenna is reported in Chapter 4 and covers objective 1, 3, and 4. It has a low-profile planar patch structure with multiple slots to achieve three operating frequency bands at 5.8 GHz, 6.2 GHz and 8.4 GHz, respectively. The proposed flexible PCB substrate enables the antenna to be applied on curvature surfaces. Supplementary simulations under conformal situations and close contact with human body confirm that the proposed antenna can tolerate a certain level of bending effect without having severe discrepancy.

- **A metasurface Based S-Shaped Split Ring Resonator for Linear-to-Circular Polarization Conversion**

This proposed polarization converter is stated in Chapter 5 and corresponds to objective 1 and 3. It is based on metasurface with split ring resonators, which can convert linearly polarized signal into circularly polarized one to broaden the return-loss bandwidth and antenna gain. This low-profile single layer structure can countervail the disadvantages of the planar patch and slot antennas.

1.5 Publications

Publications of the author are listed in chronological order as below [53–59]:

1.5.1 Journal Papers

1. E. Li, X. J. Li, and B.-C. Seet, “A triband slot patch antenna for conformal and wearable applications”, *Electronics*, 2021, 10, 3155. <https://doi.org/10.3390/electronics10243155>.
2. E. Li, X. J. Li, and B.-C. Seet, “A Metasurface Based Linear-to-Circular Polarization Converter with S-Shaped Split Ring Resonator Structure for Flexible

1.5 PUBLICATIONS

Applications”, *International Journal on Communications Antenna and Propagation (IRECAP)* (under review), Jun 2022.

3. E. Li, X. J. Li, B.-C. Seet, and X. Lin, “Ink-printed flexible wideband dipole array antenna for 5G applications,” *Physical Communication*, vol. 43, p. 101193, 2020.

1.5.2 Conference Papers

1. E. Li, X. J. Li, and B.-C. Seet, “A 5.8 GHz slot antenna with parallel slit loading for 5G conformal and wearable applications”, in proceedings of *Workshop on Microwave Theory and Techniques in Wireless Communications (MTTW'21)*, Riga, 2021. (Best Paper Award)
2. E. Li, X. J. Li, and B.-C. Seet, “Metasurface design based on S-shaped split ring resonator for Linear-to-Circular polarization conversion”, in proceedings of *2021 Fourth International Conference on Electrical, Computer and Communication Technologies (ICECCT)*, Erode, 2021.
3. E. Li, X. J. Li and Q. Zhao, "A design of ink-printable triband slot microstrip patch antenna for 5G applications," *2020 4th Australian Microwave Symposium (AMS)*, 2020, pp. 1-2, doi: 10.1109/AMS48904.2020.9059378.
4. E. Li, X. J. Li, B. Seet and X. Lin, "Flexible ink-printable wideband log-periodic dipole array antenna for 5G applications," *2018 IEEE Asia-Pacific Conference on Antennas and Propagation (APCAP)*, 2018, pp. 206-207, doi: 10.1109/APCAP.2018.8538041.
5. B. E. Li, X. Lin, X. J. Li and A. Aneja, "Design of ink-printed RFID tags for electronic article surveillance systems," *2017 Mediterranean Microwave Symposium (MMS)*, 2017, pp. 1-4, doi: 10.1109/MMS.2017.8497077.

1.5.3 Contributions in other Related Works

1. E. Li, X. Lin, B. Seet, F. Joseph and J. Neville, "Low profile and low cost textile smart mat for step pressure sensing and position mapping," *2019 IEEE International Instrumentation and Measurement Technology Conference (I2MTC)*, 2019, pp. 1-5, doi: 10.1109/I2MTC.2019.8826892.
2. A. Aneja, X. J. Li and B. E. Li, "Design of continuously tunable low noise amplifier for multiband radio," *2017 Mediterranean Microwave Symposium (MMS)*, 2017, pp. 1-4, doi: 10.1109/MMS.2017.8497156.
3. X. Lin, B. Seet, F. Joseph and E. Li, "Flexible fractal electromagnetic bandgap for millimeter-wave wearable antennas," in *IEEE Antennas and Wireless Propagation Letters*, vol. 17, no. 7, pp. 1281-1285, July 2018, doi: 10.1109/LAWP.2018.2842109.

1.6 Outline of the Thesis

The rest of this thesis is organised as follows:

Chapter 2 starts with antenna characteristics, then revisits the microstrip patch antenna property and analysis methods. After that, a comprehensive review on miscellaneous types of conductive ink is given, ranging from silver nano-particle based ink to graphene based ink. Then, different types of available printing techniques used for antenna fabrication are reviewed. Moreover, metamaterials and metasurface are mentioned for the planar antenna enhancement design.

Chapter 3 presents a silver ink-printed flexible dipole array antenna for wideband 5G applications. The proposed antenna consists of a dipole array, and Yagi-Uda directors

as directivity enhancement. After finalising the antenna geometries through parametric studies, the antenna is fabricated with silver nanoparticle based conductive ink and screen printing technique on a flexible polyester textile substrate. A laser-cut copper foil reference antenna is also fabricated as comparison. Both simulated and measured results are provided together with analysis and discussion. In addition, conformal simulations are also presented.

Chapter 4 demonstrates two flexible slot antenna designs. The first one is a microstrip slot antenna with parallel slits loading that operates at 5.8 GHz; the second design is a microstrip patch antenna with multiple slots to achieve three operating frequency bands at 5.8 GHz, 6.2 GHz, and 8.4 GHz. Both antennas are designed on flexible PCB substrate to adapt curvature and conformal applications. Simulations where the antennas are bent along a tunable curvature are presented as well as the influences from close contact with human body.

Chapter 5 provides a low-profile metasurface polarization converter, which can be used together with planar antennas like patch antennas and slot antennas to broaden their return-loss bandwidth and enhance gain by converting the original linear polarization into circular polarization. This converter is designed on a flexible PCB and is evaluated under conformal circumstance as well.

Chapter 6 concludes this thesis and provides recommendations for future work.

Chapter 2

Literature Review

This chapter presents literature and theories about the topics covered in this thesis. There are totally five sections in this chapter: Section 2.1 reviews important antenna parameters and critical points in antenna simulation and measurement; Section 2.2 revisits microstrip patch antennas, which feature the main antenna type in this thesis; Next, in Section 2.3, a comprehensive review on conductive inks and antennas fabricated with them is given; Section 2.4 discusses the major printing techniques suitable for printing antennas; In Section 2.5, metamaterials and metasurfaces are discussed for the attempts of applying them in flexible antenna designs.

2.1 Antennas Characteristics

2.1.1 Antenna Parameters

Ever since the International Telecommunication Union (ITU) International Mobile Telecommunication (IMT)-2020 and 3GPP Release 15, the 5G Wireless System has become a global phenomenal topic in both research and industries, which has drawn great attention [60]. As a new kind of network, 5G is designed to connect everyone

2.1 ANTENNAS CHARACTERISTICS

and everything together virtually, including devices, machines, and database. As an essential and important part of a wireless system, antennas design has become one of the key procedures for 5G communication system, especially in the area of IoT, medical image scanning, and wearable devices. As the application circumstance are becoming more and more complex, special requirements for antenna design are also increasing, such as flexible antenna design for curvature surface and conformal situations.

Antennas are transmission portals of wireless communication systems, which can be used as both transmitters and receivers. Antennas need to match a set of certain standards according to the system requirements. Antenna parameters describe the characteristics and performance of an antenna. To evaluate an antenna, various parameters need to be considered for both theoretical and practical measurements. In the following section, definition of the following parameter will be given: (a). Radiation pattern, (b). Radiation power density, (c). Radiation intensity, (d). Beamwidth, (e). Directivity, (f). Antenna efficiency, (g). Antenna gain, (h). Polarization, (i). Antenna radiation efficiency [23, 24, 61].

2.1.1.1 Radiation Pattern

The radiation pattern of an antenna describes how energy is radiated as a function of a space coordinates (r, θ, ϕ) as shown in Figure 2.1(a), and often illustrated by a graphical representation [61]. Generally, the space surrounding an antenna is divided into three regions: reactive near-field region at distance $R \leq 0.62\sqrt{D^3/\lambda}$, radiating near-field (Fresnel) region at distance $0.62\sqrt{D^3/\lambda} \leq R < 2D^2/\lambda$, far-field (Fraunhofer) regions at distance $R \geq 2D^2/\lambda$, where λ is the wavelength and D is the largest dimension of the antenna. Typically, the radiation pattern of an antenna refers to its far-field radiation pattern.

2.1 ANTENNAS CHARACTERISTICS

Radiation patterns are generally plotted on a logarithmic scale in decibels (dB) determined as

$$dB = 10 \log_{10} \left(\frac{P_{\text{end}}}{P_{\text{start}}} \right) = 20 \log_{10} \left(\frac{|E_{\text{end}}|}{|E_{\text{start}}|} \right). \quad (2.1)$$

The half-power (-3 dB) points (HPBW) are important in radiation patterns. Typically, in an antenna radiation pattern, *major*, *side* and *back lobes* are shown in Figure 2.1(b).

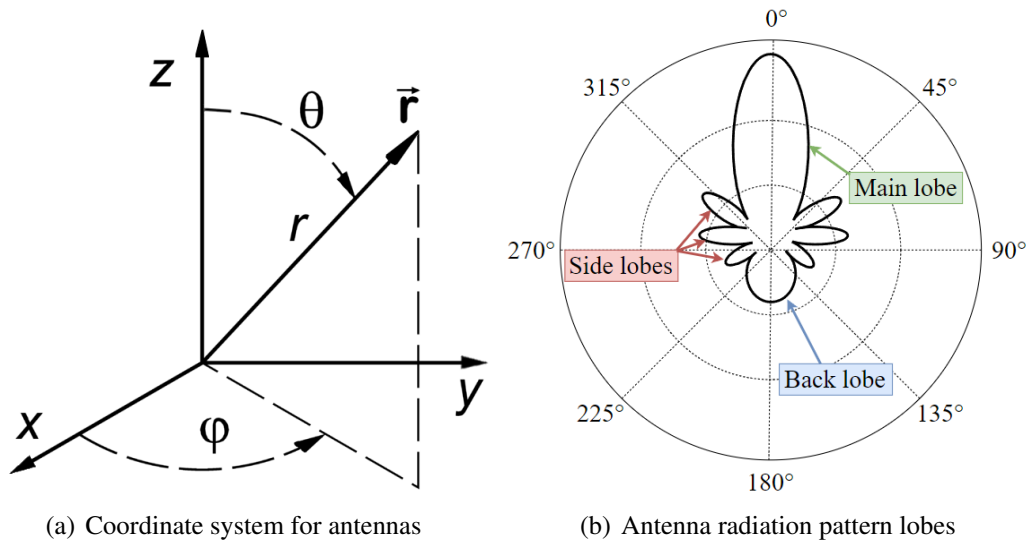


Figure 2.1: Coordinate system for antennas.

Based on the radiation directions of antennas, their radiation patterns can be categorised as *isotropic*, *directional*, and *omnidirectional* patterns [61]. Ideally, an isotropic radiator has an isotropic radiation pattern, as it has radiation in all directions hypothetically without any loss. Isotropic radiator is usually used as a reference in terms of the radiation and directive properties of practical antennas. If an antenna has much more effective radiation in some certain directions than in others, it is denoted as a directional antenna. Omnidirectional pattern is one special directional pattern, where it has nondirectional pattern in in a given plane and a directional pattern in any orthogonal plane.

2.1.1.2 Radiation Power Density

In a polar coordinate system, a solid angle Ω , is defined as a measure of the amount of the field of view from some particular point that a given object covers [61]. The unit of solid angle is steradian (sr). The infinitesimal area dA and the element of solid angle $d\Omega$ are expressed as

$$\begin{cases} dA = r^2 \sin \theta d\theta d\phi, \\ d\Omega = \frac{dA}{r^2} = \sin \theta d\theta d\phi. \end{cases} \quad (2.2)$$

The quantity to describe the power related to EM wave is the instantaneous Poynting vector denoted as

$$\mathcal{W} = \mathcal{E} \times \mathcal{H}, \quad (2.3)$$

where \mathcal{W} is instantaneous Poynting vector (W/m^2), \mathcal{E} is instantaneous electric-field intensity (V/m), and \mathcal{H} is instantaneous magnetic-field intensity (A/m). The script letters and roman letters are applied to denote instantaneous fields and their complex counterparts, respectively. Given the power density vector \mathcal{W} , the total power crossing a closed surface can be determined by the integral equation (2.4)

$$\mathcal{P} = \oiint_S \mathcal{W} \cdot ds = \oiint_S \mathcal{W} \cdot \hat{\mathbf{n}} da, \quad (2.4)$$

where \mathcal{P} is instantaneous total power (W), $\hat{\mathbf{n}}$ is unit vector normal to the surface, and da is infinitesimal area of the closed surface (m^2). The average power radiated power from an antenna can be given as

$$\begin{aligned} P_{\text{rad}} = P_{\text{avg}} &= \oiint_S \mathbf{W}_{\text{rad}} \cdot ds = \oiint_S \mathbf{W}_{\text{avg}} \cdot \hat{\mathbf{n}} da \\ &= \frac{1}{2} \oiint_S \text{Re}(\mathbf{E} \times \mathbf{H}^*) \cdot ds, \end{aligned} \quad (2.5)$$

2.1 ANTENNAS CHARACTERISTICS

where the real part of $(\mathbf{E} \times \mathbf{H}^*) / 2$ represents the average (real) power density, as for the imaginary part not shown yet, it represents the reactive (stored) power density associated with the EM fields.

2.1.1.3 Radiation Intensity

Radiation intensity U of an antenna is a commonly used far-field antenna parameter and defined as the power radiated from the antenna per unit solid angle [61], whose mathematical expression is given

$$U = r^2 W_{\text{rad}}. \quad (2.6)$$

Explained in another way, the radiation intensity is also associated with the far-zone electric field components (E_θ , E_ϕ , and E_r) of an antenna (refer to Figure 2.1(b), given by

$$\begin{aligned} U(\theta, \phi) &= \frac{r^2}{2\eta} |\mathbf{E}(r, \theta, \phi)|^2 \simeq \frac{r^2}{2\eta} [|E_\theta(r, \theta, \phi)|^2 + |E_\phi(r, \theta, \phi)|^2] \\ &\simeq \frac{1}{2\eta} [|E_\theta^\circ(\theta, \phi)|^2 + |E_\phi^\circ(\theta, \phi)|^2], \end{aligned} \quad (2.7)$$

where $\mathbf{E}(r, \theta, \phi) = \mathbf{E}^\circ(\theta, \phi) \frac{e^{-jkr}}{r}$, is far-field electric field intensity of the antenna; E_θ and E_ϕ are the antenna far-field electric field components; η is intrinsic impedance of the medium. Here it is assumed that the radial electric-field component E_r is small enough in the far zone, hence, the radiation intensity can be measured by antenna power pattern derived earlier. Integrating the radiation intensity over the entire solid angle 4π , we can obtain the total power as

$$P_{\text{rad}} = \oiint_{\Omega} U d\Omega = \int_0^{2\pi} \int_0^\pi U \sin \theta d\theta d\phi. \quad (2.8)$$

For an isotropic source U is independent of both θ and ϕ , as was the case for W_{rad} ,

2.1 ANTENNAS CHARACTERISTICS

therefore, P_{rad} of the isotropic source can be written as

$$P_{rad} = \oint_{\Omega} U_0 d\Omega = U_0 \oint_{\Omega} d\Omega = 4\pi U_0, \quad (2.9)$$

and the radiation intensity of the isotropic source can be expressed as

$$U_0 = \frac{P_{rad}}{4\pi}. \quad (2.10)$$

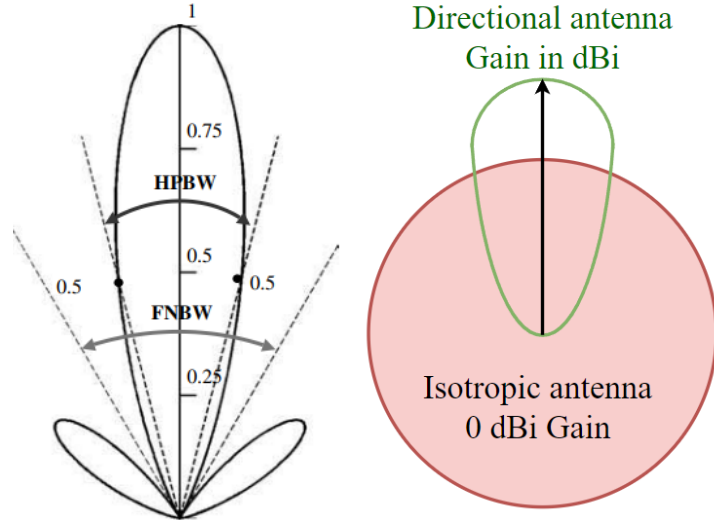
2.1.1.4 Beamwidth

Beamwidth is defined as the angular separation (in degrees) between two points with the same value and located on opposite sides of the pattern maximum [61]. Depending on different evaluation scenarios, various beamwidth can be obtained. One is Half-Power Beamwidth (HPBW), which is defined as "the angle between the two half-radiation-intensity directions of the maximum beam in a plane". Another important beamwidth is the First-Null Beamwidth (FNBW), which is regarded as an angular separation between the first nulls of the pattern. In practice, the general term beamwidth refers to HPBW. As illustrated in Figure 2.2(a), the HPBW and FNBW of the antenna pattern are 28.65° and 60° , respectively. The beamwidth of an antenna is used to balance its side lobe level.

2.1.1.5 Directivity

Directivity measures the fraction of radiation intensity in a given direction to that of averaged overall directions. Directivity describes how concentrated the radiation is emitted in a single direction [61]. Figure 2.2(b) shows an isotropic antenna and a directional antenna are located at the same reference point with the same total power radiated. The directivity D of the directional antenna can be interpreted as the ratio of its maximum power intensity U radiated along z-axis to the isotropic source radiated

2.1 ANTENNAS CHARACTERISTICS



(a) Illustration of HPBW and FNBW (b) Directivity of isotropic source

Figure 2.2: Illustration of beamwidth and directivity.

power intensity U_0 ,

$$D = \frac{U}{U_0} = \frac{4\pi U}{P_{\text{rad}}}, \quad (2.11)$$

where the average radiation intensity is equal to the total radiated power divided by 4π .

Thus, the direction of maximum radiation intensity, i.e. maximum directivity D_{max} can be expressed as

$$D_{\text{max}} = D_0 = \frac{U|_{\text{max}}}{U_0} = \frac{U_{\text{max}}}{U_0} = \frac{4\pi U_{\text{max}}}{P_{\text{rad}}}, \quad (2.12)$$

where D is directivity (dimensionless), D_0 is maximum directivity (dimensionless), U is radiation intensity (W/sr), U_{max} is maximum radiation intensity (W/sr), U_0 is radiation intensity of isotropic source (W/sr), P_{rad} is total radiated power (W).

Consequently, the directivity of the isotropic source is unity, because it radiates power equally in all directions. For all other sources, the maximum directivity is always greater than unity ($D_{\text{max}} > 1$). The value of directivity could be zero, if there is no power

2.1 ANTENNAS CHARACTERISTICS

radiated. Overall, the range of directivity values is $0 \leq D \leq D_{\max}$.

By substituting (2.8) into (2.12), D_{\max} can be expressed as

$$\begin{aligned} D_{\max} &= 4\pi \frac{U(\theta, \phi)|_{\max}}{\int_0^{2\pi} \int_0^\pi U(\theta, \phi) \sin \theta \, d\theta \, d\phi} \\ &= \frac{4\pi}{\left[\int_0^{2\pi} \int_0^\pi U(\theta, \phi) \sin \theta \, d\theta \, d\phi \right] / U(\theta, \phi)|_{\max}} = \frac{4\pi}{\Omega_A}, \end{aligned} \quad (2.13)$$

where the Ω_A is the beam solid angle, and it is given by

$$\Omega_A = \int_0^{2\pi} \int_0^\pi U_n(\theta, \phi) \sin \theta \, d\theta \, d\phi, \quad (2.14)$$

$$U_n(\theta, \phi) = \frac{U(\theta, \phi)}{U(\theta, \phi)|_{\max}}, \quad (2.15)$$

where $U_n(\theta, \phi)$ is the normalized term of radiation intensity. The definition of beam solid angle Ω_A can be given as the solid angle through which all the power of the antenna would flow if the radiation intensity is a constant value equal to U_{\max} for all angles within Ω_A .

2.1.1.6 Antenna Efficiency

As illustrated in Figure 2.3, the total antenna efficiency e_0 can be given as

$$e_0 = e_r e_c e_d, \quad (2.16)$$

where e_r is the reflection (mismatch) efficiency, e_c is the conduction efficiency, e_d is the dielectric efficiency. e_r can be measured and calculated as

$$e_r = 1 - |\Gamma|^2, \quad (2.17)$$

2.1 ANTENNAS CHARACTERISTICS

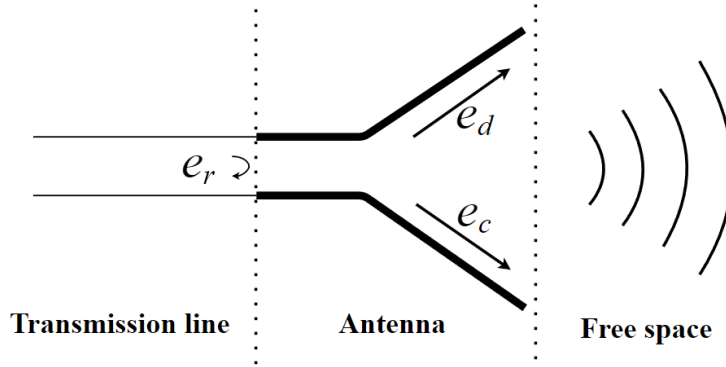


Figure 2.3: Illustration of antenna efficiency components.

$$\Gamma = (Z_{in} - Z_0) / (Z_{in} + Z_0), \quad (2.18)$$

where Z_{in} is the antenna input impedance and Z_0 is the characteristic impedance of the transmission line. Unlike e_r , e_c and e_d are difficult to measure or calculate, they can only be determined through experiments. Therefore, they are normally combined as one term, i.e. $e_{cd} = e_c e_d =$ antenna radiation efficiency [61]. In this case, antenna efficiency can be rewritten as

$$e_0 = e_r e_{cd} = e_{cd} (1 - |\Gamma|^2). \quad (2.19)$$

2.1.1.7 Antenna Gain

Antenna gain G is related to both antenna directivity and antenna efficiency, and defined as the ratio of its radiation intensity U in a given direction to the average radiation intensity of the antenna if it has perfect efficiency and radiates total input power P_{in} isotropically [61]. Therefore, G is given by

$$G(\theta, \phi) = \frac{U(\theta, \phi)}{P_{in} / 4\pi}. \quad (2.20)$$

2.1 ANTENNAS CHARACTERISTICS

The antenna gain is often expressed as relative gain, in which the antenna is compared to a reference antenna with the same input power. The direction of maximum radiation is taken for gain measurement. Knowing that $P_{\text{rad}} = e_{cd}P_{\text{in}}$, the equation (2.20) can be rewritten as

$$G(\theta, \phi) = e_{cd} \left[4\pi \frac{U(\theta, \phi)}{P_{\text{rad}}} \right] = e_{cd}D(\theta, \phi). \quad (2.21)$$

Similar to the antenna directivity,

$$G_0 = G(\theta, \phi)|_{\text{max}} = e_{cd}D(\theta, \phi)|_{\text{max}} = e_{cd}D_0. \quad (2.22)$$

The absolute antenna gain G_{abs} is given by

$$\begin{aligned} G_{\text{abs}}(\theta, \phi) &= e_r G(\theta, \phi) = (1 - |\Gamma|^2) G(\theta, \phi) \\ &= e_r e_{cd} D(\theta, \phi) = e_o D(\theta, \phi). \end{aligned} \quad (2.23)$$

Antenna gain is normally expressed in decibels (dB) as

$$G_{\text{dBi}} = 10 \cdot \log_{10}(G). \quad (2.24)$$

2.1.1.8 Bandwidth

The bandwidth of an antenna can be defined as a range of frequencies within which the performance and characteristics of the antenna are considered as acceptable. The frequency in the middle is defined as the centre frequency of the antenna. There are broadband and narrowband antennas. For a broadband antenna, the bandwidth is defined by the ratio of the upper frequency to the lower frequency. However, the bandwidth of a narrowband antenna is defined as the ratio of the frequency difference to the centre frequency as a percentage.

2.1 ANTENNAS CHARACTERISTICS

Among the antenna characteristics, only radiation pattern and impedance demonstrate a distinctive variation associated with frequencies. Therefore, there are pattern bandwidth and impedance bandwidth to distinguish the variation. Generally, antenna gain, side-lobe level, beamwidth, and polarization are associated with pattern bandwidth; input impedance and radiation efficiency are associated with impedance bandwidth.

2.1.1.9 Polarization

Polarization of an antenna refers to the polarization of the radiating waves in the direction of maximum gain. Different portions of the antenna pattern may have different polarization, however, it may not be considered as it is not important part of the antenna [61].

Similarly, polarization of a radiated EM wave describes the time-varying direction and the relative magnitude of the electric-field vector. The polarization figure is recorded by tracing the extremity of the vector as a function of time, and normally from a fixed location and along the direction of propagation. This can be visualised by imagining standing directly behind an antenna and looking in the direction it radiates EM waves to, and recording all the locations the electric-field vectors have passed.

Based on the shape of "observed" pattern, polarization can be classified as *linear*, *circular*, or *elliptical* as illustrated in Figure 2.4:

- *Linear polarization*, where the vector of the electric field at a given point in space is always directed along a straight line as a function of time. Three common cases are illustrated, vertical polarization, horizontal polarization and slant polarization, respectively. For vertical and horizontal polarization, the electric field vector lies on the vertical plane and horizontal plane, respectively, whereas the slant polarization, it has a 45° with the axis.

2.1 ANTENNAS CHARACTERISTICS

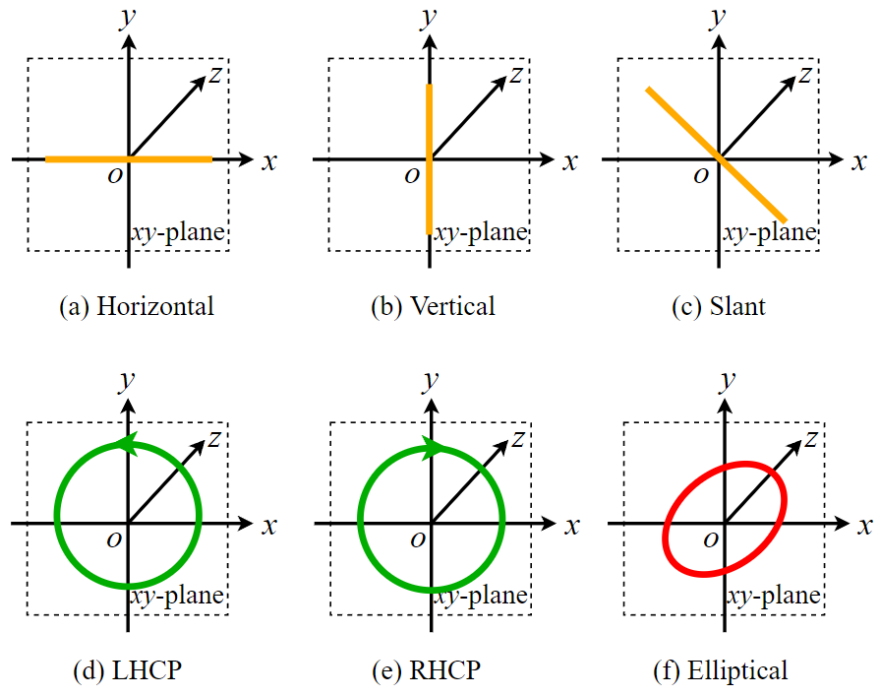


Figure 2.4: Illustration of antenna polarization.

- *Circular polarization*, where the vector of the electric field at a given point in space is rotating in a circular path as a function of time, either clockwise (CW), indicating right-hand circular polarization (RHCP), or counterclockwise (CCW), indicating left-hand circular polarization (LHCP).
- *Elliptical polarization*, refers to the scenario where the electric-field vector at a given point in space has an elliptical trace as a function of time. Similarly, elliptical polarization also has right-hand and left-hand patterns.

Geometrically, a straight line and circle both are special cases of ellipse. As illustrated in Figure 2.5, for a general ellipse, its eccentricity e , meaning the deviation of the ellipse from circularity, is defined by $e = \sqrt{1 - \left(\frac{OB}{OA}\right)^2}$, where OB and OA are the axes of the ellipse. When $OB = OA$, $e = 0$, it is a circle; when $OB = 0$, $e = 1$, it is a line. Moreover, for an elliptical polarization, the ratio of OA to OB is denoted as the axial ratio (AR), given by

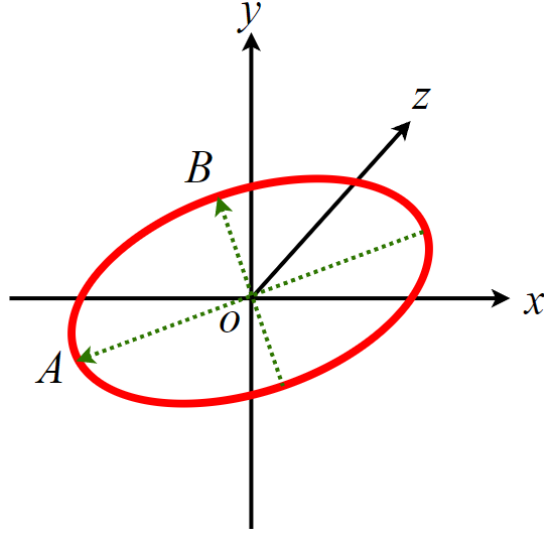


Figure 2.5: Elliptical Polarization.

$$\text{AR} = \frac{OA}{OB}, \quad 1 \leq \text{AR} \leq \infty. \quad (2.25)$$

To express the polarizations in mathematical forms, we need to introduce the instantaneous field of a plane wave, which travels along the $-z$ axis, given by

$$\mathcal{E}(z; t) = \hat{\mathbf{a}}_x \mathcal{E}_x(z; t) + \hat{\mathbf{a}}_y \mathcal{E}_y(z; t), \quad (2.26)$$

and the corresponding instantaneous components can be expressed in terms of their complex counterparts as

$$\begin{aligned} \mathcal{E}_x(z; t) &= \text{Re} [E_x^- e^{j(\omega t + kz)}] = \text{Re} [E_{x0} e^{j(\omega t + kz + \phi_x)}] \\ &= E_{x0} \cos(\omega t + kz + \phi_x), \end{aligned} \quad (2.27)$$

$$\begin{aligned} \mathcal{E}_y(z; t) &= \text{Re} [E_y^- e^{j(\omega t + kz)}] = \text{Re} [E_{y0} e^{j(\omega t + kz + \phi_y)}] \\ &= E_{y0} \cos(\omega t + kz + \phi_y), \end{aligned} \quad (2.28)$$

2.1 ANTENNAS CHARACTERISTICS

where E_{x0} and E_{y0} are the maximum magnitudes of the x and y components, respectively.

The polarization is determined by both the time-phase difference, $\Delta\phi = \phi_y - \phi_x$, and magnitudes, $|\mathcal{E}_x|$ and $|\mathcal{E}_y|$, of the two components. For linear polarization, $\Delta\phi = \phi_y - \phi_x = n\pi$, where $n = 0, 1, 2, 3, \dots$. As for circular polarization, it happens only when the magnitudes of the two components are equal and the time-phase difference is in the form of $\pm(1/2 + 2n)\pi$, which can be expressed as

$$|\mathcal{E}_x| = |\mathcal{E}_y| \Rightarrow E_{x0} = E_{y0}, \quad (2.29)$$

$$\Delta\phi = \phi_y - \phi_x = \begin{cases} +\left(\frac{1}{2} + 2n\right)\pi, n = 0, 1, 2, \dots \text{ for CW,} \\ -\left(\frac{1}{2} + 2n\right)\pi, n = 0, 1, 2, \dots \text{ for CCW.} \end{cases} \quad (2.30)$$

Elliptical polarization can be achieved in two circumstances. First, when the time-phase difference between the two components is odd multiples of $\pi/2$ and their magnitudes are not the same, given by

$$|\mathcal{E}_x| \neq |\mathcal{E}_y| \Rightarrow E_{x0} \neq E_{y0}, \quad (2.31)$$

$$\text{when } \Delta\phi = \phi_y - \phi_x = \begin{cases} +\left(\frac{1}{2} + 2n\right)\pi & \text{for CW,} \\ -\left(\frac{1}{2} + 2n\right)\pi & \text{for CCW,} \end{cases} \quad (2.32)$$

and second, when the time-phase difference is not equal to multiples of $\pi/2$ despite of their magnitudes, given by

$$\Delta\phi = \phi_y - \phi_x \neq \pm\frac{n}{2}\pi = \begin{cases} > 0 & \text{for CW,} \\ < 0 & \text{for CCW.} \end{cases} \quad (2.33)$$

2.1.1.10 Input Impedance

Input impedance of an antenna is defined as the impedance presented by the antenna at its terminals or the ratio of the voltage to current at its terminals. The expression of antenna input impedance is given by

$$Z_A = R_A + jX_A \quad (2.34)$$

where Z_A is the antenna impedance at terminals, R_A is the antenna resistance at terminals, and X_A is the antenna reactance at terminals, respectively. Generally, the antenna resistance has two parts, given by

$$R_A = R_r + R_L \quad (2.35)$$

where R_r is the radiation resistance of the antenna, and R_L is the resistance loss of the antenna.

2.1.2 Antenna Simulation

To achieve the goal of virtual designs and evaluation between designs and final manufactured products, electromagnetic simulation tools are pivotal and indispensable. Ansys High Frequency Structural Simulator (HFSS) as shown in Figure 2.6 is a compelling commercialised software widely used in antenna design, which stands out from a wide variety of high frequency, full-wave, electromagnetic softwares because it applies numerous advanced solver techniques to simulate the antenna and the ambient objects in the entire system.

HFSS possesses a key feature, which is automatic adaptive mesh refinement. This technique can generate a precise solution according to the physical geometries and electromagnetics of the design. With this key feature, it is time-efficient in determining and

2.1 ANTENNAS CHARACTERISTICS

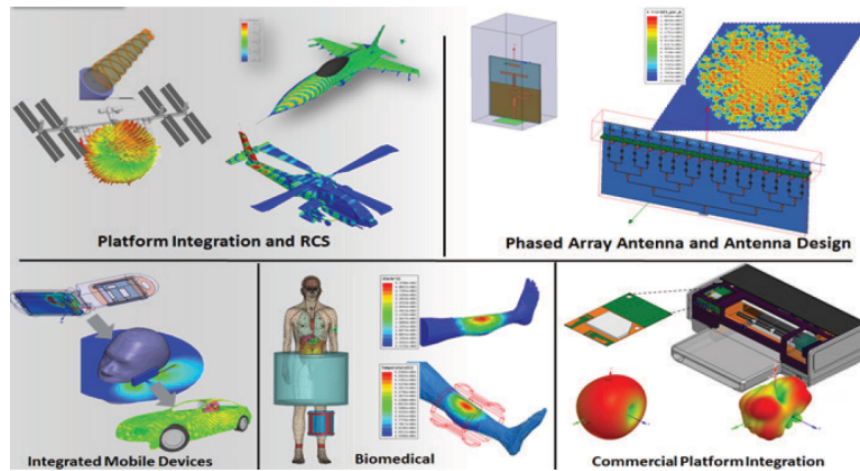


Figure 2.6: Cases of simulations with ANSYS HFSS [62].

composing the best mesh and leaves the focus on antenna design itself. The automatic adaptive meshing technique enables HFSS define and create the mesh by physics but not the other way around, at the same time guarantees the accuracy. The automation and guaranteed accuracy makes HFSS compelling among all other electromagnetics simulators.

As illustrated in Figure 2.7, the meshing algorithm adaptively refines the mesh throughout the geometry; and then, mesh elements are added iteratively in the areas where it needs finer mesh due to the localised electromagnetic field behaviours. The example process in Figure 2.7 is for a patch antenna operating at 11.5 GHz. Generally, an initial mesh is produced and is assigned to solve the fields. Then a localised error estimate is determined based on the previous solution for each tetrahedron element. Only those ones with relatively higher errors are refined to smaller and finer ones for higher precision of the localised behaviour of the fields. With the refined mesh, HFSS produces another set of adaptive solution, meanwhile, errors are recomputed as well. This process will iterate until HFSS convergence parameter $\text{Max}(|\Delta S|)$, where $|\Delta S|$ is the calculated scattering parameter difference between the current and previous adaptive mesh attempts) meets a predefined standard, which indicates the solution achieves a

2.1 ANTENNAS CHARACTERISTICS

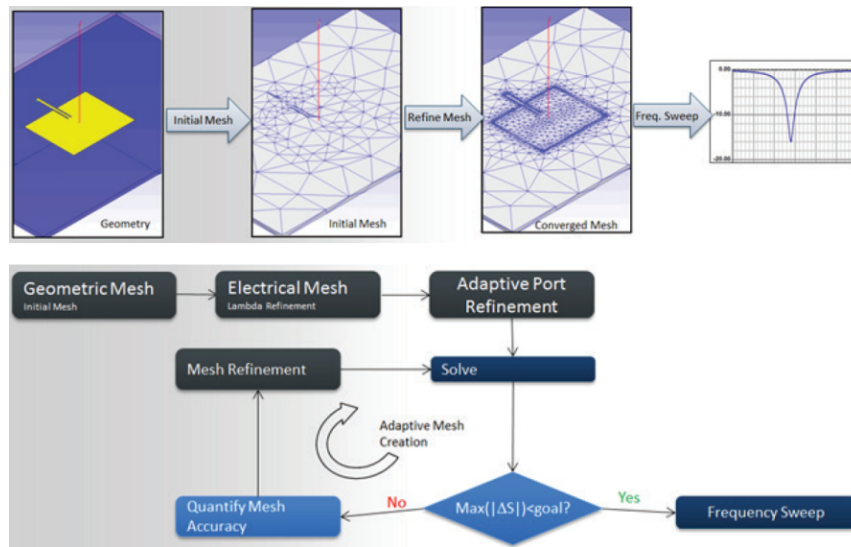


Figure 2.7: Adaptive refinement and automatic mesh in ANSYS HFSS [62].

certain accuracy. For higher accuracy, it can be achieved by lowering the convergence criteria and thus HFSS will further refine the mesh.

HFSS utilises the following simulation methods for different design model to be solved: Finite Element Methods (FEM, in HFSS), Integral Equations (enabled with HFSS-IE), Physical Optics (enabled with HFSS-IE), and FEM Transient (enabled with HFSS-TR). FEM is the main method used for antenna design cases. In this thesis, FEM simulation method is employed for the antenna designs.

The FEM is highly suited for 2D or 3D arbitrarily-shaped geometries. Every 3D model is divided into numerous tetrahedral elements, which are conformal to all the surfaces in the geometry. The reason to apply tetrahedral elements is because of their high stretchability, which enables them to fit every fine corner of any given unstructured and non-uniform mesh.

The finite element formulation employs several comprehensive mathematical techniques to fulfil Maxwell's equations in the whole model. FEM can solve different models by generating a volume based mesh for the complex materials and geometries. As

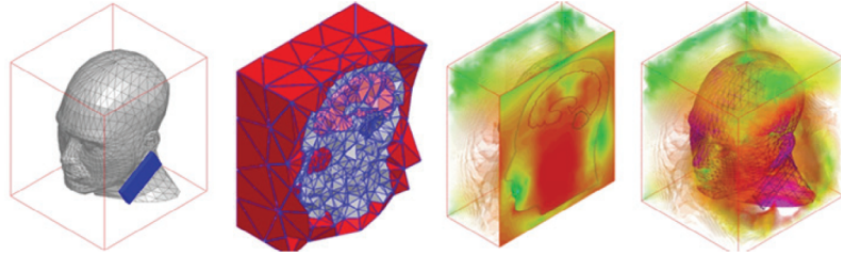


Figure 2.8: FEM solution example in ANSYS HFSS [62].

illustrated in Figure 2.8, explicit solutions are given throughout the entire volume, including the human head model and the environment the antenna is placed, not just the antenna itself. The example in the figure demonstrates the realistic specific absorption rate (SAR) measurements in the system of a smartphone antenna and the human head phantom model in the vicinity. By using the advanced HFSS FEM solver and HFSS Optimetrics, the placement of the smartphone antenna can be determined efficiently.

2.1.3 Antenna Measurements

After computer simulations, an antenna design is usually fabricated and then measured to compare the practical performance. For both commercial and laboratory measuring methods, it requires a measurement sweep over both Azimuth and Elevation, which are usually controlled and synchronised through a computer. Vector network analyser (VNA) with two or more ports is usually used in the measurement.

The fundamental theory of antenna measurement is based on Friis formula [63]:

$$P_r = \left(\frac{\lambda}{4\pi d} \right)^2 G_t G_r P_t, \quad (2.36)$$

where P_r is received power level, P_t is transmit power level, λ is transmit wave length, G_t is gain of the transmit antenna, G_r is gain of the receive antenna, and d is separation distance between antennas.

2.1 ANTENNAS CHARACTERISTICS

For the convenience of practical measurement and reading from VNA, Friis formula in terms of $S_{21}^2 = P_r/P_t$ and dB is given as:

$$S_{21,dB} = P_{L,dB} + G_{t,dB} + G_{r,dB}, \quad (2.37)$$

where $P_{L,dB}$ denotes the path loss:

$$P_{L,dB} = 20 \log \left(\frac{\lambda}{4\pi d} \right). \quad (2.38)$$

By making $\lambda = d$, we can derive a useful constant as follows:

$$P_{L,dB}(\lambda = d) = 20 \log \left(\frac{1}{4\pi} \right) = -21.98dB, \quad (2.39)$$

so that path loss can be expressed as

$$P_{L,dB} = -21.98 + 20 \log \left(\frac{\lambda}{d} \right). \quad (2.40)$$

Three common relationships can be concluded based on this:

1. Minimum path loss between any two antennas is -22 dB;
2. Every increase of 2 in the distance factor will lead path loss increase of 6 dB;
3. Every increase of 10 in the distance factor will lead path loss increase of 10 dB.

In practical antenna measurements, the gain transfer method is the most widely used technique. Once the path loss between the AUT and a reference antenna is given, measurements can be achieved via comparison between the two antennas. In this method, assumptions are made based on far field conditions for most antenna designs, except those electrically large ones. In this thesis, only far-field simulation and measurement

2.2 MICROSTRIP PATCH ANTENNA

are considered, and no near-field application is applied due to the transmission range of the proposed antennas are out of the near-field range.

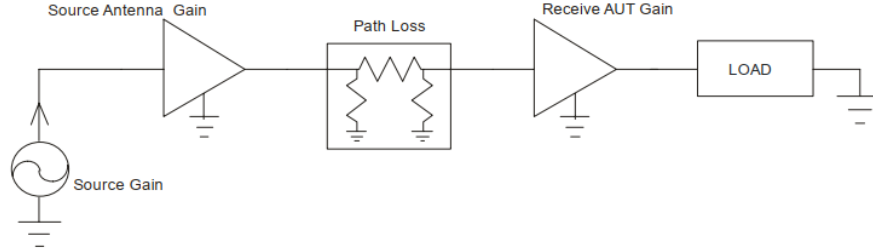


Figure 2.9: Diagram of gain transfer method setup [64].

Figure 2.9 shows a schematic diagram of the gain transfer method measurement, where source antenna gain and path loss are known and only AUT gain is to be determined. Rearranging equation (2.37), it yields

$$G_{r,dB} = S_{21,dB} - P_{L,dB} - G_{t,dB}, \quad (2.41)$$

where both $G_{t,dB}$ and $P_{L,dB}$ are already known.

2.2 Microstrip Patch Antenna

Low-profile antennas are in great demand in high-performance areas, such as aircraft, aerospace craft [65] and medical applications. The antenna design for these applications are constrained by the antenna size, cost, performance, ease of fabrication and installation [66, 67]. As a simple and inexpensive low-profile antennas, microstrip antennas can be applied to many cases, where it needs to be mounted onto rigid or flexible surfaces with present popular printing technology [40, 68–72]. With different patch shape and specific substrate material, microstrip antennas also show great versatility regarding operating frequency, radiation pattern and polarization [73, 74].

2.2.1 Fundamental Characteristics

The microstrip antenna usually features a patch-shaped structure as shown in Figure 2.10, which consists of four parts, i.e. the patch on the very top, ground plane at very bottom, substrate (under patch) or superstrate (above patch), and the feeding part [75]. Essentially, microstrip antenna is a single-element resonant antenna. Given the desired operating frequency, we can calculate and simulate the other key parameters and characteristics like radiation pattern and input impedance [73, 76]. Due to the skin effect, the patch thickness t must be thin enough but thicker than the skin depth λ_0 , i.e., $t \ll \lambda_0$ (λ_0 is the free space wavelength). It is usually a shaped metal strip mounted on one side of a thin dielectric substrate/superstrate. The ground plane is usually a much larger piece of the same metal on the other side of the substrate [66, 74]. Many shapes of patches are designed and the most popular shape is the rectangular and circular patch. For a rectangular patch, the length L is usually $\lambda_0/3 < L < \lambda_0/2$ [77].

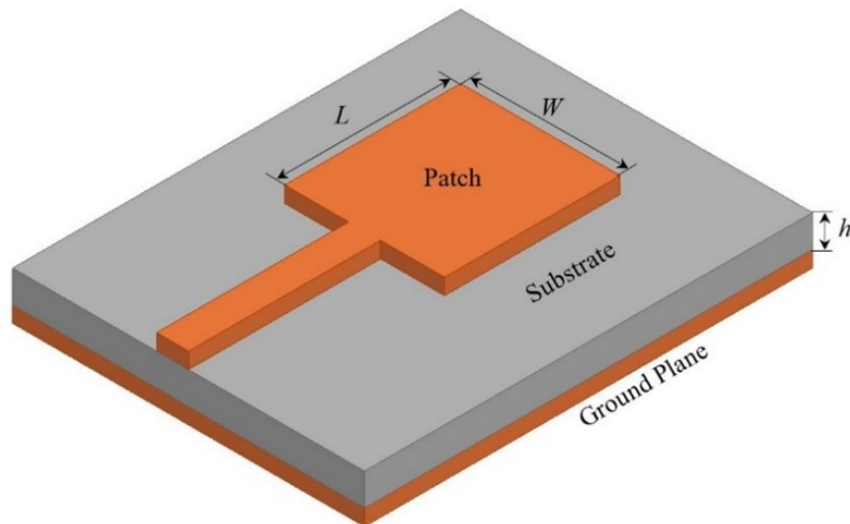


Figure 2.10: Microstrip patch antenna [23, 24].

Depending on different application scenarios, various substrates can be selected to design and fabricate microstrip antennas, which normally have a dielectric constant

2.2 MICROSTRIP PATCH ANTENNA

ϵ_r from 2.2 to 12 [76]. The dielectric with smaller dielectric constants and large thickness can guarantee better efficiency, wider bandwidth and loosely bound fields, at the expense of a larger patch size [73]. On the other hand, thinner dielectric with high dielectric constants are usually suitable for microwave or even millimetre wave (mmWave) application as tightly bound fields are required to enhance radiation and decoupling, and yield a smaller patch size [67].

2.2.2 Feeding Methods

Four popular methods to feed microstrip antennas are microstrip line, coaxial probe, aperture coupling, and proximity coupling [66]. The equivalent circuits to analyse the feeding structure are given in Figure 2.11. In the equivalent circuits, the resistor and the inductor represent the electrical resistance and inductance of the connected conductor, respectively, while the capacitor represents the equivalent capacitance of the disconnected conductors separated by dielectrics (substrate or air). For example, the capacitor in Figure 2.11(a) represents the capacitance across the substrate, and the capacitors in Figure 2.11(c) represent the capacitance across the substrate (capacitor on the left) and the capacitance across the air in the aperture (capacitor on the right).

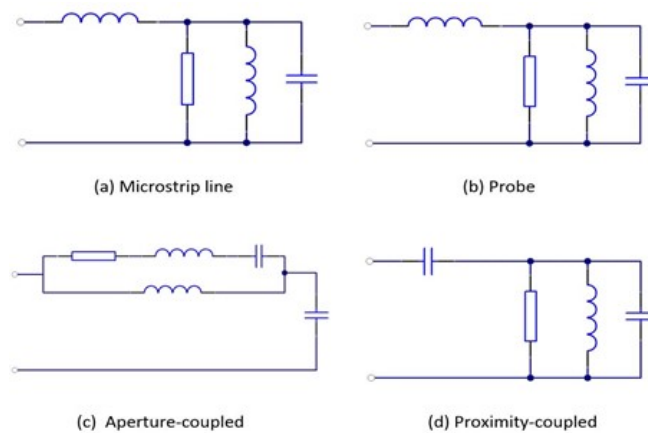


Figure 2.11: Equivalent circuits for common feeding methods [23, 24].

2.2 MICROSTRIP PATCH ANTENNA

The microstrip feed line is actually a much smaller conducting strip, compared to the patch. This method is popular because it is easy to fabricate, match and model. However, the bandwidth of the design greatly depends on the substrate thickness, as there are more surface waves and spurious feed radiation with a thicker substrate [67].

In a coaxial-line feed structure, the inner and outer conductor of the coax are connected to the patch and ground plane, respectively [74]. Besides the easy fabrication and matching, the coaxial probe feed also has low spurious radiation, compared to the microstrip feed line. However, its bandwidth is narrower and it is much more difficult to model [66].

The inherent asymmetrical structure in both the microstrip feed line and coaxial probe feed can produce cross-polarised radiation [67, 73]. To avoid this, two non-contacting feeding methods are commonly used, i.e., aperture-coupled feed and proximity-coupled feed. The aperture coupling method is the most difficult to fabricate, and its bandwidth is also very narrow. However, it is easier to model and has less spurious radiation. The aperture coupling structure normally has two substrates on both sides of the ground plane. The designed patch is on the top of the upper substrate while a microstrip line feed is on the bottom of the lower substrate. The ground plane has a slot, through which, the energy is coupled from microstrip line to the patch [66]. In this structure, the feeding part and radiating element can be optimised individually and independently, which guarantees the flexibility in design. Typically, the upper substrate is thick and has low dielectric constant while the lower one has high dielectric constant [67].

2.2.3 Analysis Methods

There are different ways to analyse microstrip antennas and the most popular ones are the transmission-line, cavity, and full wave method [73, 76]. Transmission-line model is the easiest one but it is lack of accuracy; the cavity model is more accurate but it is

2.2 MICROSTRIP PATCH ANTENNA

complex and hard to operate as well. In general, with proper application, the full-wave model is more accurate and versatile [74]. The transmission-line method is discussed in the following part, using rectangular patch as an example.

Transmission-line model is easy to analyse but it also yields inevitable discrepancy because some approximation and assumptions are made. Basically, the transmission-line model represent the microstrip antenna by two slots, which are separated by a transmission line with low-impedance. In the transmission-line model analysis, the following procedure and assumptions are made.

2.2.3.1 Fringing Effects

The fields undergo fringing at the edges of the patch, which has finite length and width. Taking the fringing along the length as an example, it is associated with the length of the patch L and the thickness of the substrate h . For the fringing of the principal E-plane (xy -plane), it is associated with both the ratio of the L to h (L/h) and the dielectric constant of the substrate ϵ_r . It is noticeable as the resonant frequency of the antenna differs with the fringing effects, although for a microstrip antenna, its length is much larger than its thickness, i.e. $L/h \gg 1$.

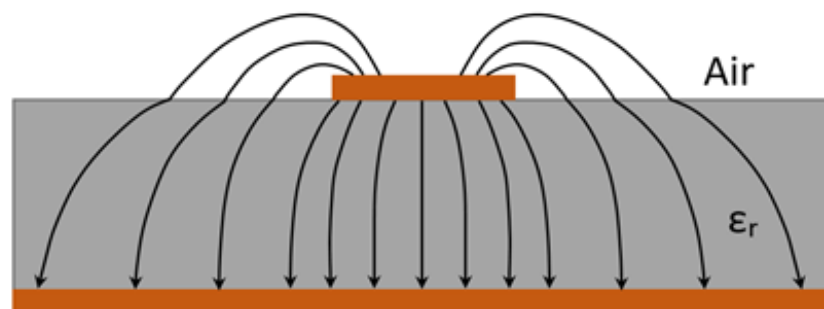


Figure 2.12: Electric field lines of fringing effect [23].

Normally, the electric field lines in a parallel plate capacitor start from one plate

2.2 MICROSTRIP PATCH ANTENNA

(positive) and end at the other plate (negative). The electric field lines are paralleled due to the same size of the plates. They are also homogeneous because they only go through one medium between the plates. However, in a microstrip line, the electric field lines are typically non-paralleled because the microstrip is much narrower than the ground plate; they are also nonhomogeneous because part of the electric field lines go through the air and the dielectric substrate as shown in Figure 2.12. It can be seen, on one hand, a small fraction of electric field lines are in the air. On the other hand, a relatively larger portion of the electric field lines go through the substrate and undergo fringing, which makes them look wider electrically than its physical dimensions. To elucidate the fringed electric field lines and the wave propagation in them, an effective dielectric constant ϵ_{eff} is introduced.

2.2.3.2 Effective dielectric constant

The equivalent structure to illustrate the effective dielectric constant is shown in Figure 2.13, where the centre conductor of the microstrip line is embedded into one uniform dielectric substrate. The dielectric constant of this dielectric material is the effective dielectric constant so that the electric field lines in Figure 2.13 possess identical electrical and propagation features as the ones in Figure 2.12.

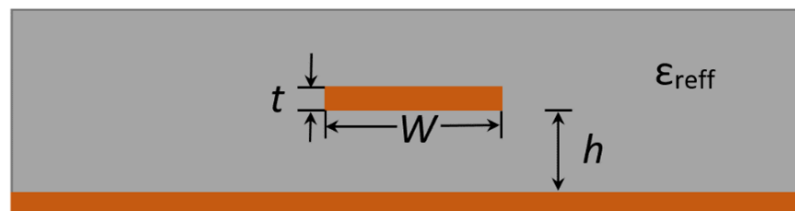


Figure 2.13: Effective dielectric constant [23].

The effective dielectric constant ϵ_{eff} is also a function of frequency f . The effective

2.2 MICROSTRIP PATCH ANTENNA

dielectric constant is basically constant at low frequencies; with an increasing frequency, more and more electric field lines concentrate in the substrate and less in the air, therefore, making the microstrip line more like the homogeneous structure in Figure 2.13. At the same time, the effective dielectric constant starts monotonically increasing and approaching the value of the dielectric constant of the substrate ϵ_r . The static values, also known as the initial values of the effective dielectric constant at low frequencies, are given by [61]

$$\epsilon_{reff} = \frac{\epsilon_r + 1}{2} + \frac{\epsilon_r - 1}{2} \left[1 + 12 \frac{h}{W} \right]^{-\frac{1}{2}}. \quad (2.42)$$

2.2.3.3 Effective length

Due to the fringing effect, the electrical dimensions of the microstrip antenna are greater than its physical ones. For example, the length of the microstrip antenna has been extended by a distance L on both ends. A practical approximate evaluation for this extended length L is given by [61]

$$\frac{\Delta L}{h} = 0.412 \frac{(\epsilon_{reff} + 0.3) \left(\frac{W}{h} + 0.264 \right)}{(\epsilon_{reff} - 0.258) \left(\frac{W}{h} + 0.8 \right)}. \quad (2.43)$$

Therefore, the effective length of the microstrip antenna becomes:

$$L_{eff} = L + 2\Delta L. \quad (2.44)$$

The resonant frequency f_r of the microstrip antenna is given by

$$f_r = \frac{1}{2L\sqrt{\epsilon_r}\sqrt{\mu_0\epsilon_0}} = \frac{v_0}{2L\sqrt{\epsilon_r}}, \quad (2.45)$$

2.2 MICROSTRIP PATCH ANTENNA

where v_0 is the speed of light in free space. If taking the fringing effect into account, equation (2.45) should be modified as

$$\begin{aligned} f_{rc} &= \frac{1}{2L_{eff}\sqrt{\epsilon_{reff}}\sqrt{\mu_0\epsilon_0}} = \frac{1}{2(L + 2\Delta L)\sqrt{\epsilon_{reff}}\sqrt{\mu_0\epsilon_0}} \\ &= q \frac{1}{2L\sqrt{\epsilon_r}\sqrt{\mu_0\epsilon_0}} = q \frac{v_0}{2L\sqrt{\epsilon_r}}, \end{aligned} \quad (2.46)$$

where q is defined as

$$q = \frac{f_{rc}}{f_r}. \quad (2.47)$$

As mentioned above, the most commonly used and easiest method to analyse microstrip antennas is transmission line method. In this method, the assumption is made that the patch itself is equivalent to part of a transmission line. Therefore, an equivalent transmission line model is represented, which consists of the microstrip patch antenna plus two slots, and they are separated by a low-impedance transmission line of length L . We can get approximately accurate results from the above assumption, which is good enough to proceed microstrip antenna design. Furthermore, it is assumed that the effect of the thickness of the conductor t can be neglected, as it is negligible comparing with that of the substrate h , i.e. $h \gg t$. Therefore, the empirical formulas with only line dimensions as variables (W , L , h , and ϵ_r) can be applied. Thus, the characteristic impedance of the target microstrip line can be expressed as [61]:

$$Z_0 = \begin{cases} \frac{60}{\sqrt{\epsilon_{reff}}} \ln \left[\frac{8h}{W} + \frac{W}{4h} \right], & \text{when } \frac{W}{h} \leq 1; \\ \frac{120\pi}{\sqrt{\epsilon_{reff}} \left(1.393 + \frac{W}{h} \right) + \frac{2}{3} \ln \left(\frac{W}{h} + 1.444 \right)}, & \text{when } \frac{W}{h} > 1, \end{cases} \quad (2.48)$$

where the width of the microstrip line can be further expressed [61]:

$$W = \frac{1}{2f_r\sqrt{\mu_0\varepsilon_0}}\sqrt{\frac{2}{\varepsilon_r + 1}} = \frac{v_0}{2f_r}\sqrt{\frac{2}{\varepsilon_r + 1}}. \quad (2.49)$$

To conclude, the key dimensions of the microstrip patch antenna will be carefully considered when designing and fabricating the antennas. The errors caused by printing quality should be measured and compared between different cases. The measurement of patch antenna physical size will also be challenged, especially the thickness (in micrometre level).

2.3 Ink-Printed Flexible Antennas

As a device to radiate or receive electromagnetic waves, an antenna is normally in metallic structure, despite the fact that its shapes vary from wire, rod, lens, to patch. An antenna is also known as a transitional device between free-space and a guiding device, where it is always attached to an electronic circuit to transport electromagnetic energy. Ever since the rapid development of semiconductors based integrated circuits (ICs) and wireless communication technology in the past decades, antenna design techniques have undergone through significant revolutions, especially in antenna size and integration methods. Electronic devices are getting smaller and smaller, so is the required size of the corresponding antenna. For example, the physical size of the antenna for upper band 5G (above 28 GHz) cellular communication systems will be in the order of millimetres. For each integration with other IC components, patch (or planar) antennas are the most popular type in transceivers, especially in PCB implementation.

Based on PCB fabrication, a large variety of antenna designs have emerged in the recent decades for different radio frontends like mobile devices, cellular base station, wireless network sensors and medical sensors. These antennas usually consist of metallic radiators (normally copper) and rigid dielectric substrates. .

2.3 INK-PRINTED FLEXIBLE ANTENNAS

The rigid substrates in traditional PCB restrain their applications in flexible and conformal circumstances [28, 51, 78]. Several studies [79–82] have found that flexible PCB can be applied in some conformal cases. In [79], researchers investigated the bending effects of meandered microstrip lines on a flexible PCB with a sharp bending angle from 0° to 30° . With different flexible PCB substrates, the insertion loss coefficient showed various distortions. This indicates that the bending effect could vary from different dielectric materials due to the difference between their dielectric constants. In [80], an electronic cube wireless sensor was reported. The cubic sensor was fabricated with PCB and formatted as a cube to cover a larger 3D detection range. A stack-up structure with several materials was also applied in the PCB design. The bending was implemented by cutting some part of the rigid substrates to create bending axes. This has provided a method for achieving the sharp bending effect with the PCB, but irreversible damage to the PCB is involved, which is also not durable.

The rise of printed electronics (PE) has opened the door to flexible antennas. PE is created using printing technology. PE has combined electronic science and conventional printing techniques to manufacture electronic devices and systems. Unlike conventional printing technology, PE can print electronic components on different substrates, like paper, plastic film etc. Compared with the traditional PCBs, PE has two distinctive features: *additive fabrication process of printing layer by layer to fabricate a device; the relative independence of the functionality of a device to the printing substrate*. PE also have advantages of rapid prototyping, low-cost fabrication, large scale production, and flexible printing substrates [28, 50–52, 78, 83–87]. With the above advantages, PE with conductive inks has been applied to antenna fabrication, including single antennas [88–95] and antenna arrays [96–100]. Despite the advantages mentioned above, there is a potential challenge for conductive ink printed antennas, namely the low electric conductivity compared to traditional metal. This is caused by the fabrication of the

conductive inks. The conductive inks are usually formulated with volatile and dielectric solvent. After sintering, there are nonconductive particles remaining in the printed traces, resulting in a relatively lower conductivity. Therefore, a conduction loss exists in the antenna system, which decreases the overall radiation efficiency and antenna gain [23, 25, 101].

2.3.1 Conductive Inks

Conventional printing is a process of making a replication of information, such as images, graphics, text and so forth. As for printed electronics, its replication process is to produce electronic devices, like antennas, rather than representing visual information. Therefore, there lies a key difference between printed electronics and conventional visual information printing, i.e., the printable ink, which normally functions as conductors, semiconductors, and dielectrics [25, 101, 102].

Conductive ink is the essential and critical part for fabricating antennas in printed electronics. Conductive ink can be divided into two main categories, namely organic conductive ink and inorganic conductive ink. It follows that whether the conductive elements in the ink are organic or inorganic [25].

Generally, organic conductive ink contains organic compounds as electron carrier (conductor). The history of conductive organic compound can be traced back to 1954 when pyrene and bromine were found to form charge transfer complexes (a charge-transfer complex or electron-donor-acceptor complex is an association of two or more molecules, in which a fraction of electronic charge is transferred between the molecular entities.) [103], and then the relatively recent discovery are single crystal of sexithiophene in 1996 [104]. Conductive polymer materials are a major part of conductive organic material and can be further divided into two subcategories based on their structure and conductive mechanism, namely structural type and composite

2.3 INK-PRINTED FLEXIBLE ANTENNAS

type. Structural type organic materials are typically prepared by chemical synthesis or electrochemical methods. Conversely, composite type ones are prepared by adding conductive fillers (metal or carbon powder) into the polymer. Conductive ink is one common typical example of composite [25].

Inorganic electronic materials have been dominating microelectronics in the last decades. Many inorganic electronic materials have been widely applied in logic circuitry, lighting, sensors, solar cells and so forth, because of their outstanding performance, chemical stability and environmental sustainability. Given the accumulated knowledge and technologies about these inorganic electronic materials we already have, it is reasonable and wise to utilise inorganic materials for printed electronics as well. Especially the conductor part for printing ink [25].

Conductor is essential in conventional electronic structure and devices, as well as printed electronics. The printable conducting formulation in the early stage is basically conductive paste, which is a mixture of metal or carbon particles and resin. However, extreme low conductivity and high sintering temperature are big drawbacks of these pastes, failing them to fulfill the high standard of modern electronics design.

The recent rapid development in nanomaterials, it brings better conductive ink, namely nanoparticle conductive ink. The common types are silver nanoparticle ink, nanowires and copper nanoparticles. Instead of mixing with resin like conventional conductive paste, nanoparticle conductive inks are made of conductive nanoparticles, volatile solvents and surfactant (also known as surface-active agent). Consequently, the printed film thickness is smaller than that of conventional paste. The conductivity is much closer to their bulk conductivity compared with conventional paste. The sintering temperature for post processing is below 200°C [88, 91, 93, 102, 105–107].

Conductive inks with metallic nanoparticles are available nowadays. Taking the example

2.3 INK-PRINTED FLEXIBLE ANTENNAS

of Ag nanoparticle conductive ink as an example, there two most prominent synthesis methods for production, namely the Lee-Meisel method [108] and the Creighton method [109], respectively. For nanoparticles, size distribution is one important structural aspect to evaluate both of their physical and chemical properties. For Lee-Meisel method, it prepares Ag nanoparticles by utilising the reduction of silver nitrate (AgNO_3) by sodium citrate [108, 110]. Conversely, Creighton method applies sodium borohydride (NaBH_4) as a stronger reducing agent to achieve narrower size distribution in Ag nanoparticles. On top of the aforementioned methods, some other modified methods have also been explored for nanoparticle solution synthesis, differing from solvents, capping agents, and reactive reagents etc.

Apart from metallic nanoparticle conductive inks, carbon nanotube and graphene are also commonly studied and applied for printed electronics. Ever since its discovery in 1990s, considerable research has been conducted for carbon nanotubes, but it is still difficult to overcome some major issues to achieve large-scale use for electronics industry. One of the major hurdles is that it is hard to produce high quantity of carbon nanotubes with high level of desirable characteristics. Nevertheless, substantial and continuous improvement and refinement have been made over the past years on its synthesis, purification, dispersion, printing composite etc. Similarly, after graphene was discovered in 2004 [111, 112], the story goes pretty much the same way as carbon nanotube [25].

2.3.2 Characterisation for Conductive Ink

Unlike solid metal materials, conductive inks used in printing electronics have various characteristics, depending on the type of conductive particles, the type of the solvent, and solidification of the particles after sintering. Therefore, it is an important step to characterise the materials before applying it in an RF design.

2.3 INK-PRINTED FLEXIBLE ANTENNAS

In RF structure design, ideally, both conductive and dielectric materials are supposed to be lossless so that all the EM energy should be transferred to destination system. In such system, all EM energy are distributed on the outside of conductors without any attenuation when propagating within dielectrics. However, every conductive material has a finite conductivity, and dielectrics have attenuating properties, which lead to the attenuation and energy loss during transmission.

The energy dissipated by conductors are due to the finite conductivity, which is the reciprocal of the resistivity ρ . It is known that the conductor loss P_{lc} of a conductive wire can be modelled by integrating the current flow over the conductor's cross-sectional area S [113]:

$$P_{lc} = \frac{R_s}{2} \int_s |\vec{J}_s|^2 ds, \quad (2.50)$$

where R_s is the surface resistance of the conductor and \vec{J}_s is the surface current density.

On the other hand, the skin effect appears and becomes more significant with increasing operating frequency, thus enlarging the effective RF resistance R_{rf} and causing additional energy loss. The relationship among R_s , R_{dc} , R_{rf} , surface depth δ (due to skin effect) and angular frequency ω for a uniform cylindrical metal structure (e.g. conductive wire) is given below [113]:

$$R_{dc} = \rho \frac{L}{S} = \frac{L}{\sigma S}, \quad (2.51)$$

$$\delta = \sqrt{\frac{2}{\mu_0 \omega \sigma}}, \quad (2.52)$$

$$R_s = \frac{1}{\sigma \delta} \sqrt{\frac{\omega \mu_0}{2\sigma}}, \quad (2.53)$$

$$R_{rf} = \frac{L}{\sigma P \delta} = \frac{L}{P} R_s, \quad (2.54)$$

where μ_0 is the vacuum permeability, L is the length of conductor with uniformly distributed current flow, S is the cross-sectional area and P is the perimeter of the cross section. By comparing equations (2.51) and (2.54), we could infer that the product $P\delta$ is the equivalent cross-sectional area of the conductor at microwave and mmWave frequencies, which is much thinner than its physical radius due to the skin effect. Therefore, the total power loss in the conductor could be derived from (2.50) to (2.54).

Wave propagation in dielectrics is normally characterised as the complex propagation constant $\gamma = \alpha + j\beta$, where α is the attenuation constant and β is the phase constant. Another parameter used is the complex permittivity ε , the real part $\varepsilon' = \varepsilon_0 \varepsilon_r$ with ε_r defined as the real relative permittivity (a.k.a. dielectric constant, although it is not a constant for materials under different conditions) and ε_0 defined as the permittivity in free space. The energy loss within the dielectric material is related to its loss tangent $\tan \delta = \frac{\varepsilon''}{\varepsilon'}$. The relationship between γ and ε for a lossy dielectric material is:

$$\gamma = j\omega\sqrt{\mu\varepsilon}. \quad (2.55)$$

It should be noted that the power dissipated within dielectrics P_{lc} is restricted by the distribution of EM fields. Thus, from the viewpoint of circuit theory, RF systems deploying different structures have different formulas for calculating this loss. However, it could be generally described by equation (2.56) for a transmission line with 1 meter length [52, 113, 114]:

$$P_{ld} = \frac{\omega\varepsilon''}{2} \int_S \vec{E} \cdot \vec{E}^* ds, \quad (2.56)$$

where \vec{E} is the electric field and S is the cross-sectional surface of the field distribution

area.

Unlike uniform conductors, the behaviour of high-frequency printed conductive inks is highly determined by the conductive particle type of conductive ink and the microstructure of the solidified ink. Furthermore, intrinsic properties of conductive ink also affect the performance of high-frequency conductive inks. Therefore, new approaches are required to characterise the electrical behaviour of conductive ink at higher frequencies. It was stated in [115] that the inkjet printed films have different electrical properties and quality factor with SU-8 polymer-based and thin PVPh-based dielectric inks, respectively. Also, great changes were captured in the cases of different conductive ink thickness (achieved by different print times).

2.3.3 Conductive Ink-Printed Antennas

In this section, miscellaneous antenna designs fabricated with different types of conductive inks are reviewed and comparison about the ink properties and fabrication conditions is given as well.

2.3.3.1 Antennas Printed with Silver Particle Based Ink

In [102], Elmobarak et al. proposed a silver ink printed Sierpinski fractal antenna on a paper substrate for multiband applications as shown in Figure 2.14. The printing technique employed for this design was inkjet printing. The antenna operates at two bands, i.e., 1.5-2.7 GHz and 5.1-11 GHz bands. A coplanar waveguide (CPW) feed and Sierpinski fractal structure were adopted in the design. The measured return loss basically matched the simulated one except the resonant frequency band at near 2 GHz as shown in Figure 2.15.

The antenna was printed with conductive silver nanoparticles ink from AgIc Co. (Japan) and post-processed by chemical sintering technique. Chemical sintering technique is

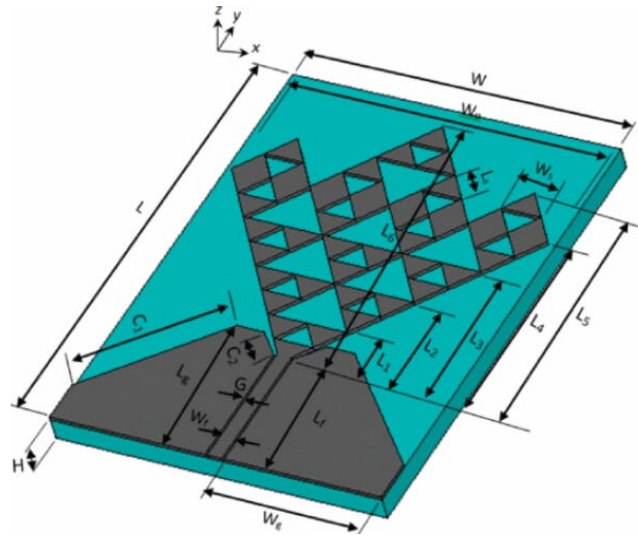


Figure 2.14: Silver ink printed Sierpinski fractal antenna [102] Copyright © 2017 IEEE.

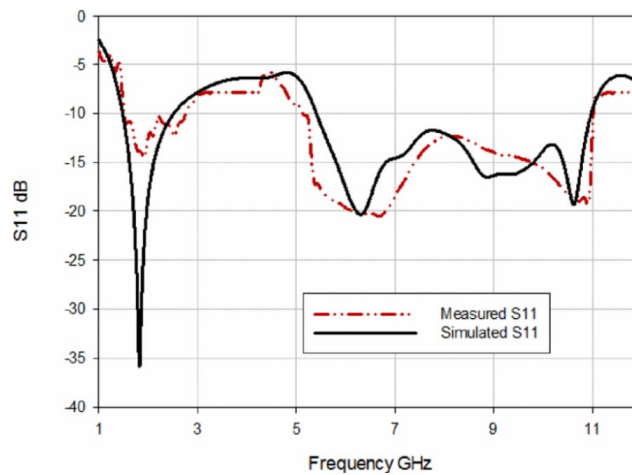


Figure 2.15: Return loss of the silver ink printed Sierpinski fractal antenna [102] Copyright © 2017 IEEE.

introduced for paper or plastic substrates to avoid possible damage caused by thermal sintering. The theory behind chemical sintering is to dissolve silver nanoparticles into a solvent of polymer latex and halide emulsion. The required the nanoparticle size is less than $0.1 \mu\text{m}$. The high conductivity is supposed to be achieved after the chemical solution is dried. Due to the micro-structure of paper substrate, it needs a resin coating to guarantee the absorption of the silver ink, as well as avoid smearing. The coating

2.3 INK-PRINTED FLEXIBLE ANTENNAS

layer also helps with chemical sintering process. The printed silver ink trace resulted in a sheet resistance of $0.12 \Omega/\text{sq}$ after two layer printings. This indicates a low resistance of the antenna, which results in low conduction loss and correspondingly high radiation efficiency.

The printing device used for this design was a desktop inkjet printer MFC J430W from Brother Co., with special ink cartridges are needed for silver ink [102]. However, the silver ink can easily block the printing nozzle, which is rather difficult to clean. Additionally, the process to produce multiple passes to enhance conductivity requires accurate alignment between the printing substrate and printing nozzle, especially when the pattern size is small. A tiny misalignment could cause severe performance degradation.

A silver ink printed ultra-high frequency (UHF) RFID on wood structure was proposed in [106] for automated identification system in wood industry as shown in Figure 2.16. The UHF RFID antenna was a rectangular patch antenna operating at 866 MHz and 915 MHz and was printed with screen printing technique on wood veneer. Nanoparticle silver ink Harima NPS-JL was chosen for the design. Due to the porosity and high roughness of the wood veneer surface, antenna has to be printed along the grain of the veneer so that the disconnection between ink metallisation will be minimised. The printed traces along the grain of the veneer are shown in Figure 2.17. However, different type of wood may demonstrate various porous surface, which differs the absorption of conductive ink and may significantly affect the conductivity of printed traces.

After exposed at a high-energy and efficient photonic flashlight at 3000 V voltage for a single pulse time of $4000 \mu\text{s}$, the silver ink was sintered and demonstrated 2.2Ω resistance for the overall patch of $14.3 \times 8.125 \text{ mm}^2$. The achieved resistance is acceptable for a low frequency (MHz level) application, but the resistance will increase greatly for higher frequency (GHz level) application and corresponding skin effect will increase accordingly. Performance evaluation of the RFID antenna were conducted by

2.3 INK-PRINTED FLEXIBLE ANTENNAS

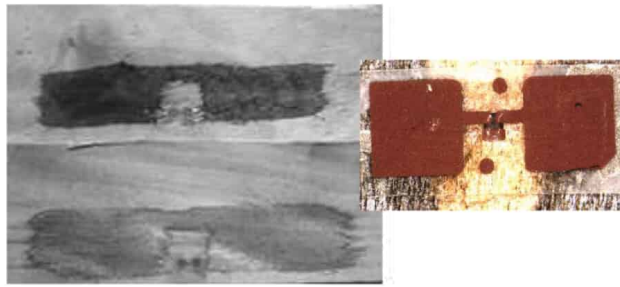


Figure 2.16: Silver screen printed RFID antenna on wood [106] *Copyright © 2015 IEEE.*



Figure 2.17: Grains in wood veneer surface [106] *Copyright © 2015 IEEE.*

measuring the maximum reading distance at some certain angle, approximately 4-5 meters over the operating frequency range. Radiation patterns of E-plane and H-plane were also measured to confirm the antenna performance.

In [116], Kirschenmann et al. reported an silver inkjet printed multilayer patch antenna, operating at 5 GHz. The antenna has two conductive silver layers and one polyimide adhesive layer. Both conductive part and dielectric part of the antenna were printed as illustrated in Figure 2.18. As shown in Figure 2.19, this design used very complex fabrication process, which included printing two silver patch layers with Dimatix inkjet printer and four passes for each layer, printing feed line on a 100- μm Kapton sheet, combining the above three layers by applying polyimide adhesive layer twice, and binding the entire structure onto RO4003C laminate substrate with another polyimide layer. Curing process was applied for each silver ink and polyimide layer. The whole

2.3 INK-PRINTED FLEXIBLE ANTENNAS

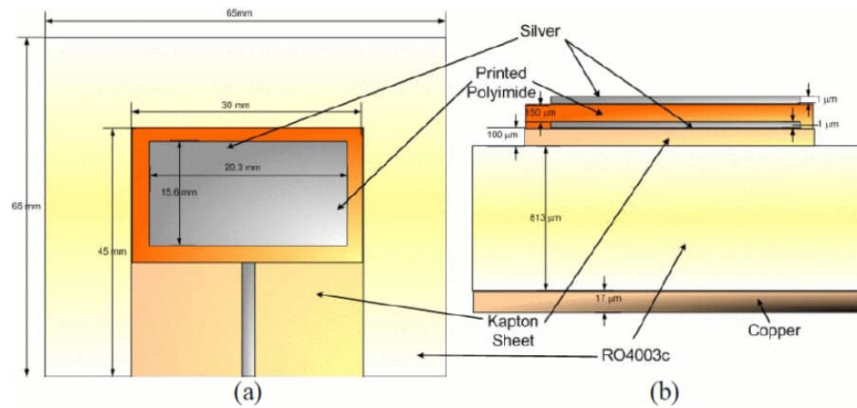


Figure 2.18: Geometry of antenna (a) top view (b) cross-section view [116] *Copyright © 2007 IEEE.*

progress was rather complicated and time-consuming, not suitable for rapid and mass production. The printing device used for the design was Dimatix DMP-2830 inkjet printer, which is a rather high-end and expensive device, and only suitable for small volume fabrication. The polyimide layer also added parasitic capacitance into the design and affected the resonant frequency.

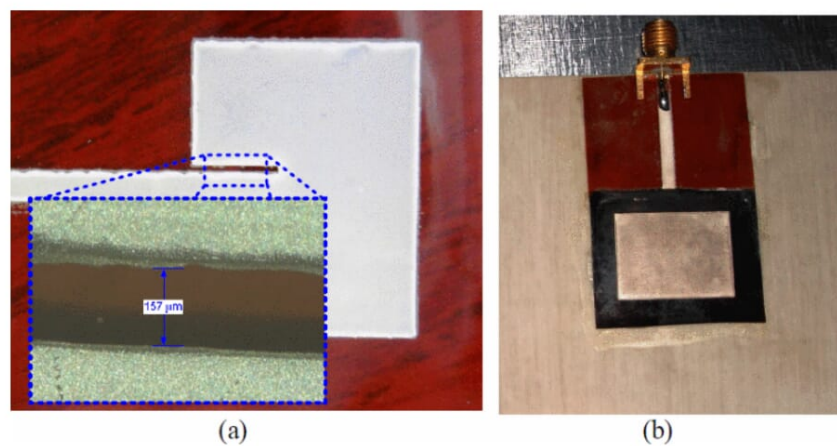


Figure 2.19: Multilayer patch antenna (a) first layer of the silver printer on Kapton sheet (b) final antenna [116] *Copyright © 2007 IEEE.*

2.3.3.2 Antennas Printed with Carbon Nanotube Based Conductive Ink

Carbon nanotubes (CNTs) have emerged with both attractive physical and chemical characteristics, and they are extremely light-weight, durable and conductive. Keller et al. explored a patch antenna design using carbon nanotube thread mesh structure in [117], where carbon nanotube bundles were applied instead of single-wall carbon nanotubes (SWCNTs) to enhance their radiation efficiency at microwave frequencies. The antenna design consists of an X-band aperture-coupled microstrip-fed patch antenna with a ground plane constructed with carbon nanotube threads. Figure 2.21 shows the patch antenna, which has a size of $8.89 \times 10.16 \text{ mm}^2$ and is fed by a $50\text{-}\Omega$ microstrip line. An illustration was given in Figure 2.20. Two dielectric materials, RT/Duroid 3010 and 5870, were chosen for feed line layer and patch layer, respectively. The mesh of the patch was fabricated with carbon nanotube threads by combining parallel multi-wall nanotubes with chemical vapor deposition (CVD) on a silicon (Si) wafer. The nanotubes have an average length of $300\text{-}500 \text{ }\mu\text{m}$ and are bonded together by Van Der Waals forces. Ultimately, the thread can reach $20\text{-}25 \text{ }\mu\text{m}$ in diameter. Post-processing is to apply dimethyl sulfoxide (DMSO) to the carbon nanotube threads, which can draw the adjacent threads closer and tighter via the force caused by the evaporation of the DMSO solvent, so that the thread conductivity and tensile strength were enhanced.

The effects of the thread spacing was studied via various simulations, with a set of adjusted values from $\lambda/60$ to $\lambda/15$, as shown in Figure 2.21. Results of return loss and E-plane radiation patterns showed that with different spacing between carbon nanotube threads, there would be resonant frequency shift (Figure 2.22(a)) and radiation pattern gain deviations (Figure 2.22(b)). The marginal frequency shift varies from 0.5% to 6.5% and the realised gain at corresponding resonant frequencies also differs from 4 dBi to 10 dBi, as well as the radiation efficiency from 26.1% to 92.3%. All the above results are based on the space difference between CNT threads only, without accounting

2.3 INK-PRINTED FLEXIBLE ANTENNAS

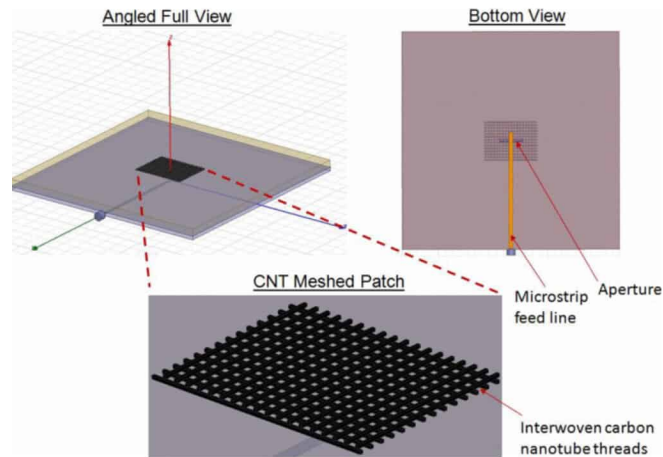


Figure 2.20: Aperture coupled patch antenna with carbon nanotube meshed ground plane [117] *Copyright* © 2013 *IEEE*.

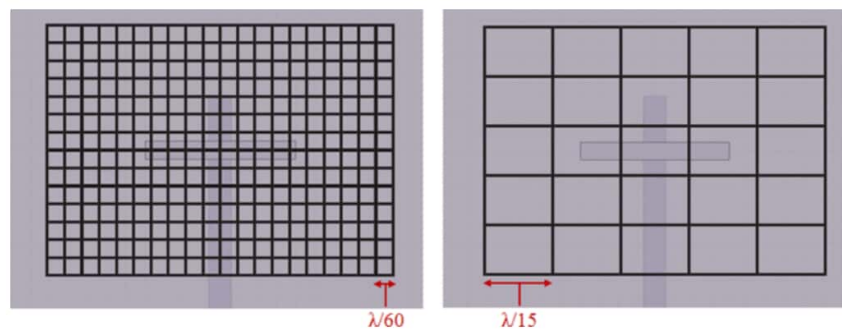


Figure 2.21: Different space between meshed carbon nanotube threads [117] *Copyright* © 2013 *IEEE*.

for potential defects of each CNT wall and quantum capacitance and kinetic inductance in nanoscale, which both would be resisting electron movement, causing reactance and resistance increase. Simulation results showed that antenna fabrication with meshed carbon nanotubes is feasible, with proper tuning in the carbon nanotube threads size and mesh spaces. In addition, the nanotube defects and nanoscale quantum influences should be considered.

A theoretical study about carbon nanotube based conformal antenna design for inkjet printing was conducted by Cheng et al. in [118]. A dual-band monopole antenna was

2.3 INK-PRINTED FLEXIBLE ANTENNAS

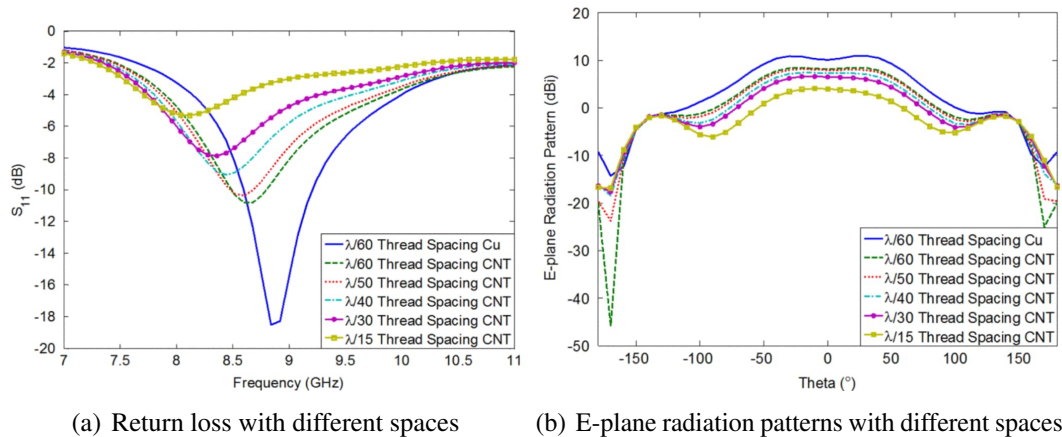


Figure 2.22: Simulation results with different spaces between CNT threads [117]
Copyright © 2013 IEEE.

simulated in CST Microwave Studio with predicted CNTs' conductivity of 30,000 S/m for conductors and a paper substrate with a dielectric constant of 3.1 and a thickness of 254 μm . The monopole patch antenna has a circular ring with a tongue patch and was fed by a 50- Ω CPW as shown in Figure 2.23.

The antenna was also placed on a cylindrical surface for conformal application, where three values of the cylinder radius were simulated, 130 mm, 225 mm, and 320 mm, respectively. And the voltage standing wave ratios (VSWRs) at 2.45 GHz and 5.8 GHz were compared to demonstrate the effects from the cylindrical surface. However, the cylinder radius has negligible effect on the resonant frequency as indicated in Figure 2.24.

There are still limitations in this study, albeit the results showed promising performance of the proposed carbon nanotube antenna for conformal applications. Firstly, the simulation only considered the conductivity of carbon nanotubes. In practice, due to the complexity of the nanolevel structure of the nanotubes, it may have different influences on the electrical properties and radiation performance. Secondly, the absorption of carbon nanotube ink by the paper was not considered. The printed film thickness should

2.3 INK-PRINTED FLEXIBLE ANTENNAS

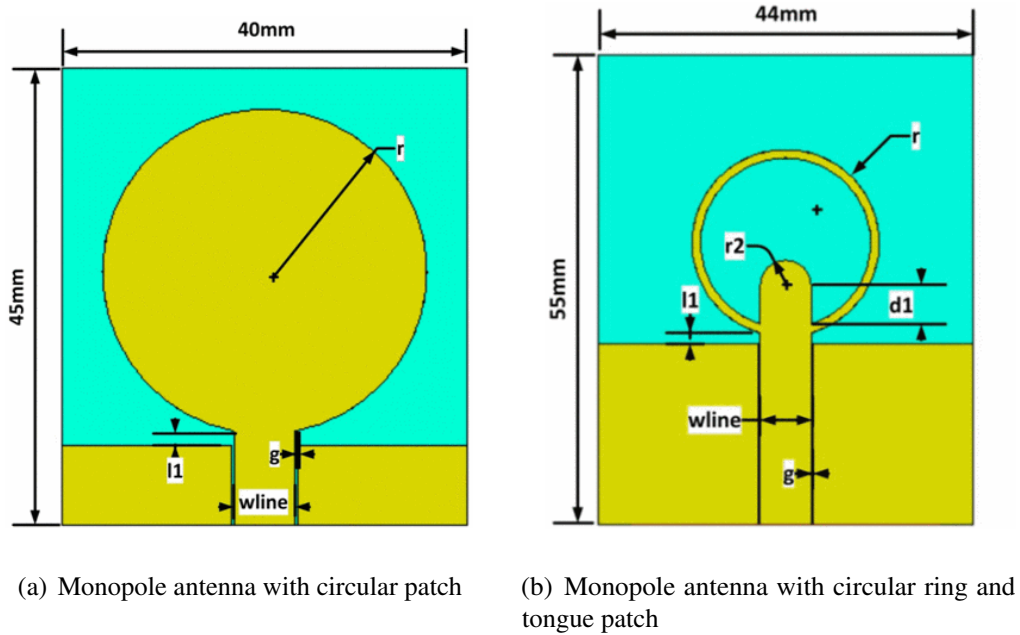


Figure 2.23: Carbon nanotube monopole antenna design [118] Copyright © 2017 IEEE.

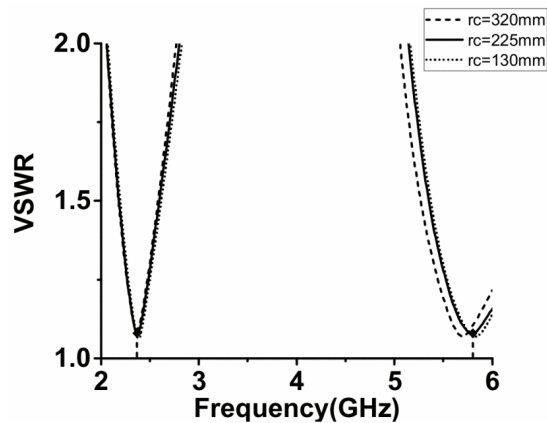


Figure 2.24: Influence on VSWR from cylinder radius change [118] Copyright © 2017 IEEE.

also be taken into account.

To summarise, the aforementioned antenna designs printed with conductive inks are listed in Table 2.1 for comparison. One can conclude that: first, most of those inks are for inkjet printing with relatively low viscosity; second, most of the inks can obtain their designated conductivity with naturally drying at room temperature and reach

optimal result if further sintering is applied; third, there are special sintering methods like chemical sintering and high voltage pulsed light sintering.

2.4 Printing Techniques

Printing is a process to make a replication of some pre-designed information, with different types of techniques. Generally, printing techniques can be divided into two categories, based on the employment of a template. A template is a device that contains the pre-designed pattern for printing, and the area of the pattern allows the ink to pass through but not the rest area. First, without a template, there is only one method available, i.e., *jet printing*. Second, if a template is applied, it is called *replicate printing*. There are four major types of printing techniques: *screen printing*, *gravure printing*, *letterpress printing*, and *offset printing*. All these aforementioned printing techniques require different types of inks, of which the characteristics vary in carrier particles, viscosity, sintering temperature etc. For instance, the inkjet printing ink normally has low viscosity due to the mechanics of inkjet printer, whereas for screen printing, the viscosity of the ink is normally higher to form a stable pattern.

Printing resolution is another key property that will distinguish one printing method from the others. With high printing resolution, it is possible to produce devices with extra small size and high integration density. Currently, most of the available printing techniques have resolution up to micrometer range, between 50 and 100 μm . Some high-end printing techniques with novel concepts developed recently can push the printing resolution to a level of less than 10 μm and even approaching 1 μm . Some printing techniques have adopted flexible printing substrates so that it is possible to realise roll-to-roll rapid printing process for mass production.

Replicate printing techniques rely on a template that carries the desired patterns. The

Table 2.1: Comparison of conductive inks used in antenna designs.

Ref.	Particle	Solvent	Printer	Sintering	Condition	Conductivity	Layers
[102]	Ag	polymer latex and halide emulsion	inkjet	chemical sintering	25°C	0.12 Ω /sq	2
[106]	Cu	water	screen printing	high voltage pulsed light	3000V, 4000 μ s	3.8 Ω over 14.3 \times 8.1 mm ²	1
[116]	Ag	poly ALT	inkjet	naturally drying	25°C	N.A.	2
[118]	CNT	N.A.	inkjet	naturally drying	25°C	3 \times 10 ⁴ S/m	1
[119]	CNT	N.A.	inkjet	sintering	140°C	50 Ω of entire antenna	25
[120]	graphene & Ag	alcoholic solvent	inkjet	naturally drying	25°C	N.A.	1
[121]	graphene	Cyrene solvent	inkjet	naturally drying	25°C	4.1 \times 10 ⁵ S/m	1

2.4 PRINTING TECHNIQUES

printing process is replicating the patterns from the template to a target substrate. The template is generally crafted through physical carving or chemical etching. Consequently, once it is made, it is impossible to make any changes, but it is suitable for the situation where a large number of printings with the same designed pattern are needed.

With distinguished features of their templates, replicate printing can be divided into three major subgroups, namely screen printing, gravure printing, and flexographic printing. All of them are capable of direct replicating desired patterns to substrates.

2.4.1 Inkjet Printing

Unlike other printing methods, inkjet printing does not require a template but a digital pattern stored and controlled by computer. The ink nozzle of the printer follows the digital pattern to precisely jet out ink droplets on a predefined path. Currently, there are two major types of inkjet printing principles, namely continuous inkjet (CIJ) and drop on demand (DOD) inkjet, respectively [88, 89, 116].

As indicated in its name, CIJ printer produces and ejects ink droplets continuously [122]. As shown in Figure 2.25, the ink droplets are charged during the printing process and precisely controlled by an electrostatic or magnetic field. At the location of an image pixel, the droplets will be let pass through the electrostatic field onto receptor substrate, whereas at the non-printing area, droplets are deflected and then retrieved by an ink catcher for next cycle. The predominant advantages of CIJ are very high velocity of ink droplets and high drop ejection frequency, which enable high printing speed and fairly long distance between print head and printing substrate. Additionally, the continuous printing process makes the nozzle and jet always in use, so that ink with volatile solvent can be applied to allow fast drying, hence avoid nozzle clogging [122].

Generally, for a DOD printer, the ink droplets are ejected only when a voltage/data

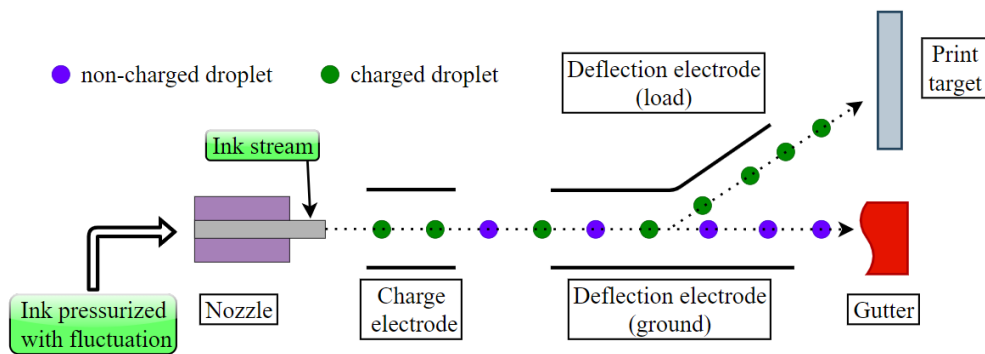


Figure 2.25: Illustration of continuous inkjet printing principle [123] (reproduced).

pulse is detected. No deflection or retrieving is needed, therefore, the inkjet head has a much simpler structure compared with the one of CIJ printer. The printing principle is illustrated in Figure 2.26. There are basically two main methods to produce DOD inkjet, namely thermal DOD and piezoelectric DOD, respectively [25, 124, 125]. In the thermal inkjet process, the printing head consists of a number of miniature chambers, inside which a heating element is installed. When a small electric current goes through the heating element, it causes a rapid vaporization of the ink in the chamber and forms a bubble with high pressure. Then the bubble propels the ink droplet out of the nozzle. On the other hand, for piezoelectric DOD inkjet, piezos, which are electrically polarized ceramic devices, are applied in the inkjet head [25]. Normally, a piezoelectric material is placed in the ink chamber behind each nozzle. The piezoelectric material bends or change shape when a voltage is applied across it. The bending or shape change causes a pressure to propel a ink droplet out from the nozzle [124].

To prepare inkjet printing, there is no need for a master plate for replication. Instead, it requires a digital printing pattern stored in computer. Generally, the manufacturer provides corresponding software to compose and edit digital images for desired standards. Monochrome bitmap format is the common type for these printers to recognize.

2.4 PRINTING TECHNIQUES

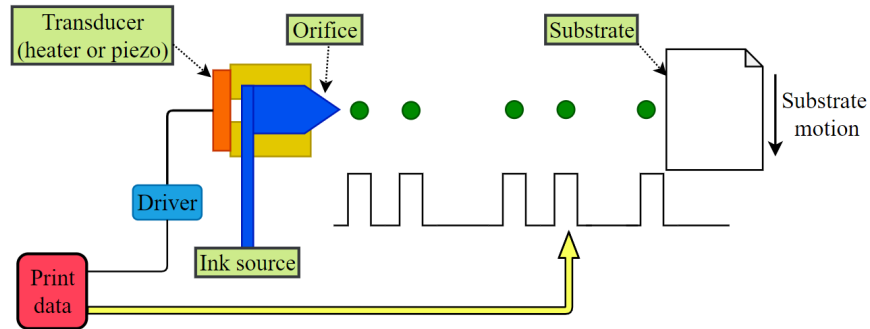
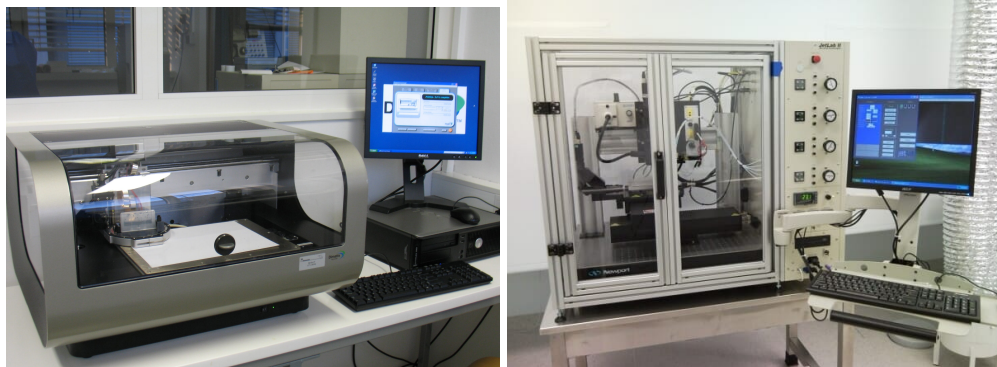


Figure 2.26: Illustration of drop-on-demand inkjet printing principle [125] (reproduced).

Black and white pixels on the printing pattern will be interpreted into a string of electrical pulses to trigger the transducers (either thermal or piezoelectric) to control ink propelling. The printer will prompt ink droplets where it is indicated by black pixels, while the white pixels represents blank area [91, 124, 125].



(a) Fujifilm Dimatix DMP-2831 printer

(b) Jetlab II printer

Figure 2.27: Popular drop on demand inkjet printers [124, 126].

For inkjet printers, the printing heads are the most important part, where critical aspects and challenges lie. Generally, there are two major design philosophies for printing heads: fixed head and disposable head. The fixed head is normally built in the printer and needs not be removed or replaced when ink runs out. Thus, the cost of replacement and calibration is minimised [25, 91, 92]. However, once the fixed head is damaged, it might be difficult and expensive to replace it, only if replacement is possible. Given

2.4 PRINTING TECHNIQUES

the above, fixed heads are normally available on industrial high-end models for mass production and large plotters [92].

Alternatively, disposable head philosophy utilises a printing head integrated with a replaceable ink cartridge. The printing head will be replaced together with the cartridge once the ink runs out. The replacement of disposable head will increase the cost of consumable as well as the difficulty in manufacturing printing heads with high precision and relatively low cost [25, 89, 91]. However, this openness makes the clogging issue less concerned because replacing a new head will solve the problem fast and easily.

First, the nozzle size determines the ink volume propelled of each single pump, therefore, it also influences the printing resolution. Second, it is also where clogging always happens, which causes great efforts and cost to clean and maintain. Thus, to achieve very fine printing resolution, it requires a precise coordination between (1) nozzle size, which controls the size and number of the ink droplets released by the printer nozzle; (2) ink viscosity, which affect the speed of the ink droplet passing through the nozzle and how strong the ink droplet can attach to the substrate; (3) ink volatility, which determines how fast the ink solvent evaporates [124, 125].

Finally, unlike the fact that screen printing is suitable for rapid and mass production, inkjet printing has been regarded as one of the most promising methods for laboratory research in printed electronics, even possible to replace conventional photo-lithography, due to its outstanding features, such as high resolution, low fabrication cost, and fast fabrication process [25, 88, 93].

Currently, in printed electronics, piezoelectric DOD inkjet printers are the most popular ones, and as shown in Figure 2.27 are Fujifilm Dimatix DMP-2831 (left) and Jetlab II (right), respectively. In [28], a compact inkjet-printed mmWave antenna on flexible polyethylene terephthalate (PET) substrate was presented, whose operating frequency

2.4 PRINTING TECHNIQUES

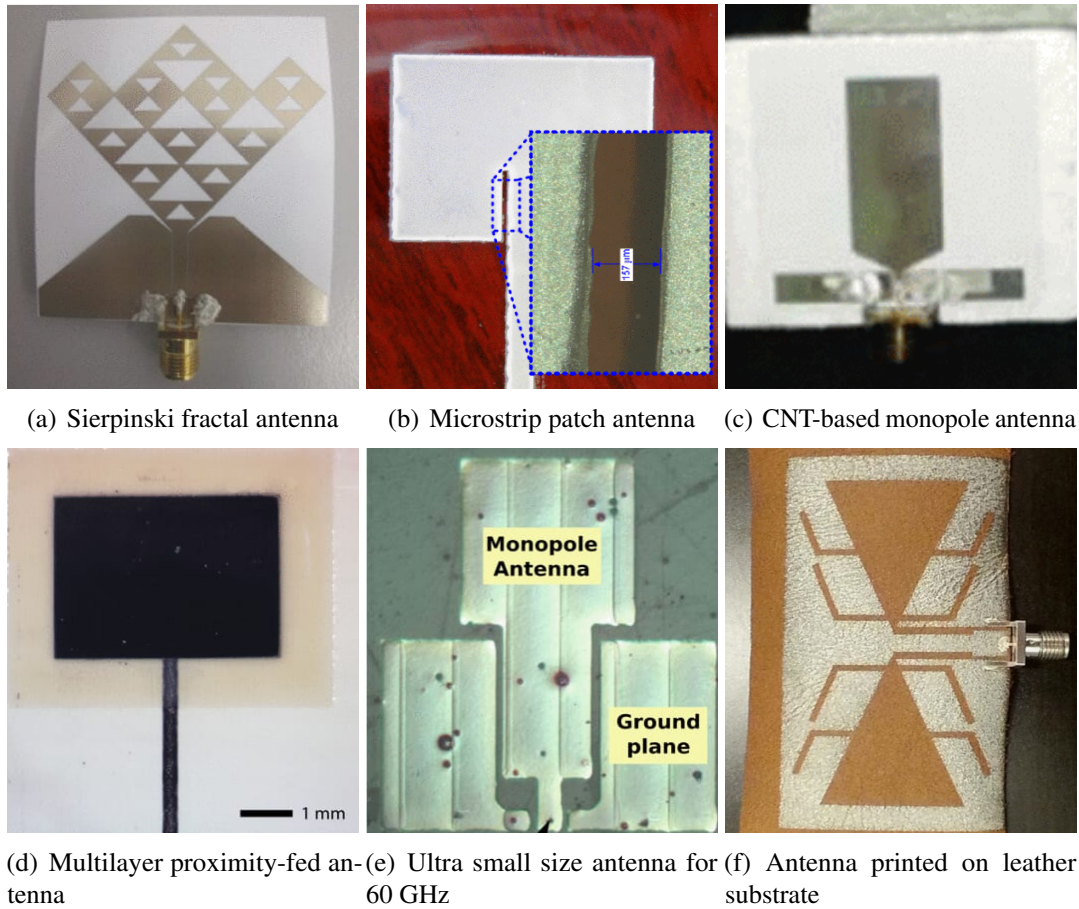


Figure 2.28: Antennas fabricated with inkjet printing technique [88–90, 102, 116, 118] Copyright © 2007-2013 IEEE.

can be switched between 28 and 38 GHz by controlling the switches integrated in the slots of the antenna. In [127], the physical and electrical characteristics of a RFID HF antenna are studied and two different cases of screen printing and inkjet printing are compared. It concludes that multiple inkjet-printed layers must be done to achieve low value of resistance and desired radiation performance.

By applying a digital pattern, inkjet printing uses replaceable printing heads, whose movement is controlled by computer programme. Thus, the resolution of inkjet printing can be high and inkjet printing has become one of the most popular techniques used for laboratory research. However, due to the sheet-to-sheet substrate feeding mechanism for

2.4 PRINTING TECHNIQUES

most of the inkjet printers, the printing speed is limited and not suitable for massively rapid production.

In [102], the authors proposed a silver ink printed Sierpinski fractal antenna with a paper substrate as shown in Figure 2.28(a). A commercial desktop inkjet printer MFCJ430W from Brother Co. was employed and chemical sintering technique was chosen for post-processing. The antenna in [116] was printed with FUJIFILM Dimatix DMP-2830 inkjet printer on Kapton film, which can be seen in Figure 2.28(b) and both sintering and coating procedure were applied for the printed silver laminates. Figure 2.28(c) presents that an CNT-based inkjet printed antenna was reviewed in [118]. Furthermore, in Figure 2.28(d), a multi-layer inkjet printed proximity-fed antenna was reported in [88] for millimetre-wave application. The printer was the commercial Dimatix model with a piezo drop-on-demand mechanism and UV sintering processing was applied after printing. Another antenna design for 60 GHz ISM applications was proposed in [89] with ultra fine resolution printed film on PET substrate with the DMP-2800 inkjet printer as illustrated in Figure 2.28(e). Lastly, in [90] an intriguing antenna was inkjet printed on a leather substrate for a dual band application, 1.7 GHz and 2.9 GHz respectively. The printed antenna is presented in Figure 2.28(f).

Further details of these aforementioned inkjet printed antennas are listed in Table 2.2 for comparison, which includes substrate material, printing resolution, post sintering, substrate coating, printing film conductivity, and printers types.

From Table 2.2, we can see that inkjet printing can achieve printing accuracy in terms of micrometers. If advanced printer model, like Dimatix is applied, its drop-on-demand feature can yield an accuracy of 40 μm in printing trace as a result of both the printer mechanism and ink properties. For most of inkjet printed traces, a proper sintering is needed and the duration is less than 30 minutes. In [90], the sintering process lasted 6 hours to achieve the best conductivity. Moreover, the overall conductivity of the inkjet

Table 2.2: Comparison between Inkjet Printed Antennas

Ref.	Substrate	Resolution	Sintering	Coating	Conductivity	Printer	Extra Comments
[102]	thick paper	0.3 mm	chemical sintering based ink, no further curing	resin coated	0.12 Ω /sq for 2 passes	MFC J430W from Brother Co.	fast chemical sintering without post curing
[116]	Kapton film	157 μ m	internal sintering in printer	No	3×10^7 S/m	FUJIFILM Dimatix DMP-2830	connected with other different printed layers
[118]	paper	0.037 mm	N.A.	No	1.4×10^6 S/m	unknown	combined with CNT and silver ink layer
[88]	single-clad liquid crystall polymer	0.3 mm	cured in oven at 180° for 10 mins	No	1.1×10^7 S/m	Dimatix-2831	conductive layer printed on top of dielectric prints
[89]	PET	40 μ m	dried in a vacuum oven and then sintered with a UV lamp	Novel-coated	0.06 Ω /sq	Dimatix DMP-2800	high frequency and millimetre wave application
[90]	leather	0.8 mm	heated at 160° for 6 hours	No	N.A.	Dimatix 2800	extreme long heating process

printed films is close to their corresponding solid metal bulk conductivity, for instance, the silver inks can reach conductivity of 10^6 to 10^7 S/m.

However, most designs are fabricated with Dimatix model, which is an expensive high-end and specialised model built for laboratory and research use. Additionally, due to the printing mechanism limit, these inkjet printing methods can not be applied to massive production due to their low printing speed.

2.4.2 Screen Printing

Screen printing is the most widely used printing method with low-cost and high effectiveness. As shown in Figure 2.29, to screen print, a master template (mesh screen) with desired pattern, a squeegee, and suitable ink are required [25]. The mesh screen normally has transparent patterned area and opaque non-patterned area, which can be produced by chemical mask process. The squeegee is normally a piece of rigid rubber pad with a perfectly straight lining. The ink for screen printing is usually of high viscosity, so that there is no leaking from the mesh before printing and thick-film patterns can be printed without a large number of passes [25, 93, 128].

Before printing, the ink is first filled onto the patterned mesh area and a substrate is placed under the mesh with desired location and alignment [25]. To start, the squeegee moves along the screen, applying pressure to the ink to penetrate through the mesh apertures and deposit on the substrate. Thus, the desired pattern is replicated on the substrate. Then the screen can spring back from the substrate, allowing multiple passes for thicker film [25, 94]. For automatic mass production, screen printers are employed as the one shown in Figure 2.30. The placement of printing ink and movement of the squeegee are controlled automatically.

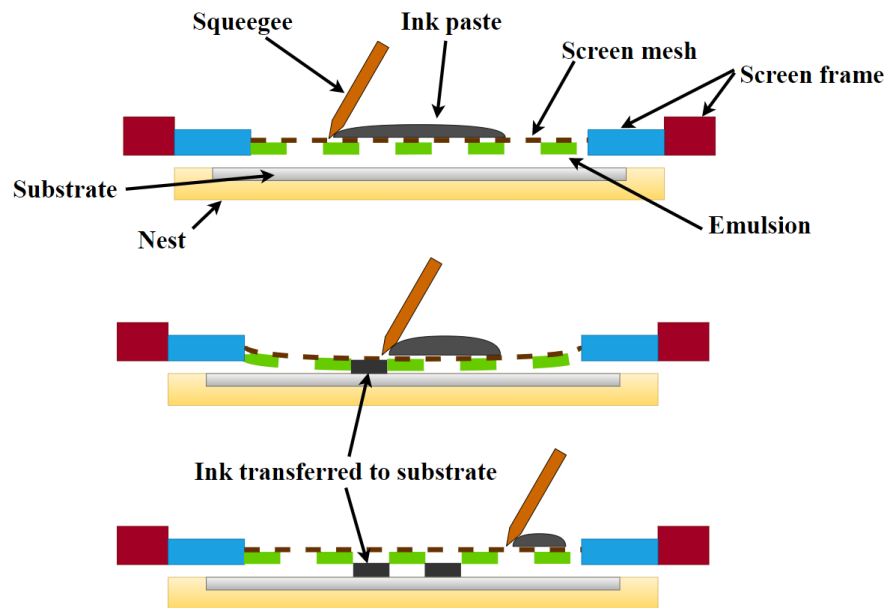
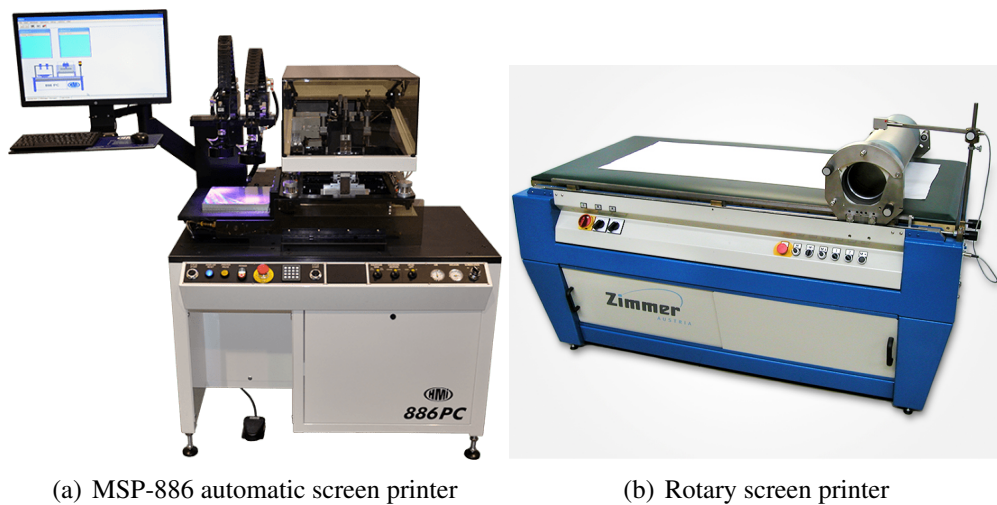


Figure 2.29: Illustration of screen printing progress [25]



(a) MSP-886 automatic screen printer

(b) Rotary screen printer

Figure 2.30: Automatic screen printers [107, 129].

Most screen printers have flat screens and flat substrate holders, like Figure 2.30(a), which feed one sheet of substrate at a time and then move on to next one [129]. To increase productivity, a rotary system can be applied either to the screen or substrate feeder. A precise and accurate control of the screen and substrate positions is required to align them well and to avoid displacement and discontinuity. In Figure 2.30(b), the screen printer applies a rotary screen that integrates both squeegee and printing ink in a

2.4 PRINTING TECHNIQUES

roller to achieve roll-to-roll mode for high-speed passing printing [25, 107].

Screen mask for screen printing normally consists of a frame, a mesh and a stencil on the mesh. The frame can be wooden, metallic, or plastic, strong enough to hold the mesh tight. The mesh is usually fabric, which is made of silk, rubber or even metal fibres [25]. As for the stencil, it is normally produced by optical lithography. Some light-sensitive materials will be deposited on the mesh first and then a desired pattern will be placed on the mesh to block light while the mesh is exposed under ultraviolet (UV) light curing [93, 95]. Thus, the lithographic material on the uncovered mesh will form a sintered layer on the mesh to stop ink penetration and the ones on the covered pattern will not and can be easily removed.

In practice, in order to accurately control the printing resolution and printed film thickness, screen frame selection, mesh and stencil material, mesh density, and ink deposition method need to be selected according to the required criteria. As the development of screen printing technique, the printing resolution has been elevated to a new level, from previously over 100 μm to 10 - 30 μm , by using positive chemically amplified resists as stencil material [25, 95, 128, 129].

As one of the most popular printing techniques, screen printing has the following advantages:

- The conductive ink for screen printing can be prepared with both micro-sized and nano-sized conductive particles. Micro-sized particle ink is relatively easier to obtain and prepare than nano-sized one.
- More options for printing substrates, which can be both flat or curved because the screen can be soft and flexible.
- Due to the high viscosity of the ink, printed film thickness can much more easily reach 10 μm than others.

2.4 PRINTING TECHNIQUES

- High viscosity of the ink enables easier management and control of the printing process.
- Low cost for both printing equipment and materials.

In [106], an RFID tag antenna was screen printed on wood substrate for UHF band (866.6 MHz and 915 MHz) application as shown in Figure 2.31(a). In [130], another RFID antenna was fabricated using screen printing technique for UHF band, but it was printed on FR4 board as shown in Figure 2.31(b). A monopole antenna shown in Figure 2.31(c) was printed in [121] for wideband application between 5 GHz and 13.5 GHz. The antenna was printed on an FR4 board for low-weight. Scarpello et al. presented a screen printed patch antenna as shown in Figure 2.31(d) for wearable and washable applications in [93]. The antenna was fabricated on a textile substrate with a thermoplastic polyurethane (TPU) coating for ink deposition and durability. Similarly, another antenna design for wearable application was reported in [94]. As shown in Figure 2.31(e), the antenna was screen printed on textile substrate to simulate human wearable device. Last, in [95], a screen printed antenna with CPW and defect ground structure (DGS) was presented, which can be seen in Figure 2.31(f).

Detailed information and parameters regarding the aforementioned designs with screen printing technique are listed in Table 2.3 for the sake of comparison.

As can be seen from Table 2.3, screen printing technique can be applied to numerous of substrates to fabricate antennas, from wood, paper to PET film and board. The printing resolution of less than 1 mm can be attained, which is suitable for microwave designs but might be challenging for millimetrewave designs because the physical size of millimetrewave antennas is in the order of millimetre according to the wavelength of the millimetrewave. On average, due to the high viscosity of screen printing ink, one pass of printing process is enough to achieve sufficient thickness. Thus, the screen

2.4 PRINTING TECHNIQUES

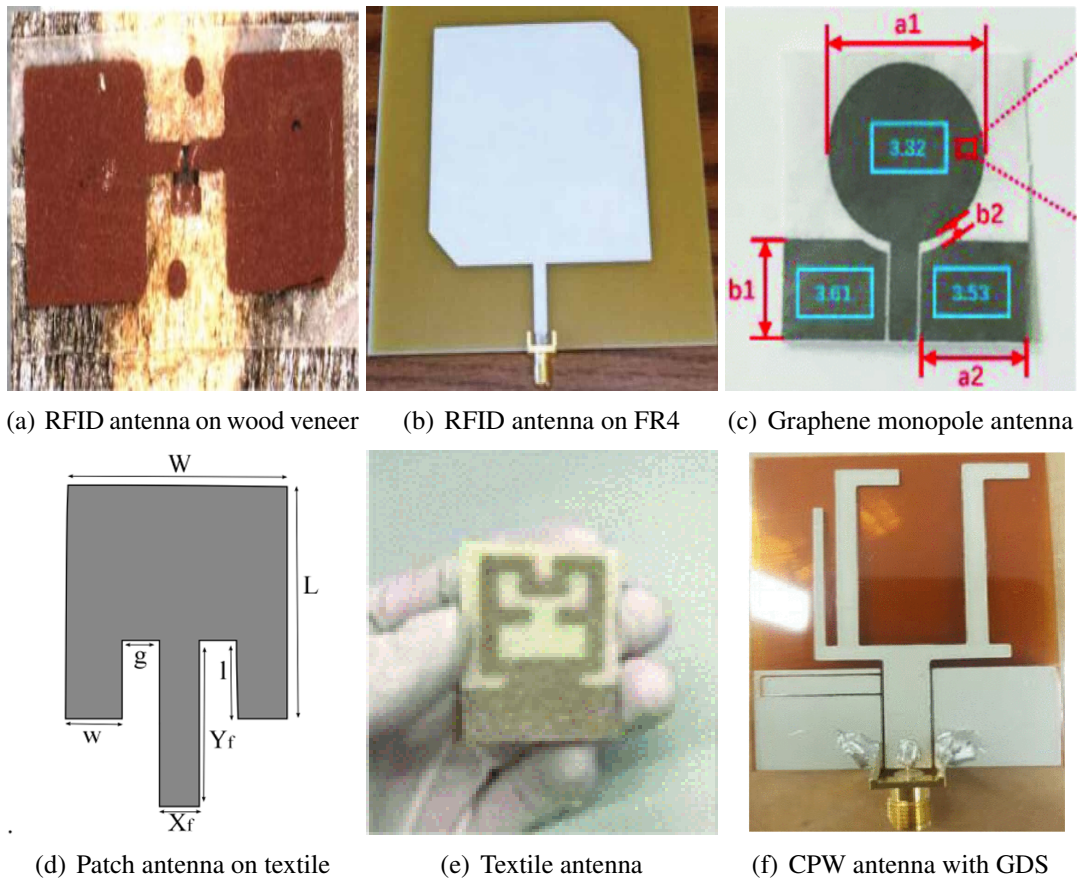


Figure 2.31: Antennas fabricated with screen printing technique [93–95, 106, 121, 130] Copyright © 2015-2021 IEEE.

printing process requires no coating on the substrate; however, extra coating could be used for performance enhancement [93]. Both conventionally basic screen stencils and modern commercial printer can achieve good printing products.

Next, depending on different types of ink selected, the printed film conductivity varies in different cases. Low conductivity will result in high resistance for the current flow and degrade antenna radiation efficiency and overall antenna efficiency.

Another consequence of the high viscosity of the ink is that most of the screen printed antennas need sintering at high temperature above 100°C in post-processing, and the duration varies from 15 minutes to 60 minutes [95]. For certain types of ink, the photonic sintering is also possible [106].

Table 2.3: Comparison between Screen Printed Antennas

Ref.	Substrate	Resolution	Sintering	Coating	Conductivity	Printer	Extra Comments
[106]	wood veneer	2 mm	photonic sintering (3000 V, 4000 μ s, single pulse)	No	overall 2.2Ω	brush printing via stencil	ultra efficient and fast sintering
[130]	A4 paper	0.4 mm	N.A.	No	4.1×10^4 S/m	commercial screen printer with Agile F130 Manual Mill	fine resolution
[121]	FR4 board	N.A.	N.A.	No	2.63×10^6 S/m	Ekra X1 semi-automatic screen printer	N.A.
[93]	cotton polyester	6.25 mm	cured in oven at 120° for 15 mins	TPU	$0.1 \Omega/\text{sq}$	Johannes Zimmer Klagenfurt-type Mini MDF 482	washable
[94]	textile	0.7 mm	cured in oven at 100° for 15 mins	No	N.A.	traditional screen printing stencil	N.A.
[95]	flexible Kapton	0.5 mm	first heated at 120° for 5 mins and then in vacuum oven at 150° for 60 mins	No	1.7×10^7 S/m	laser cut mask as print screen	double sintering process

2.4.3 Gravure Printing

Gravure printing is another common type of direct replicate printing technique, which is also known as intaglio printing technique, where the replicate patterns are engraved in the plate, in form of a matrix of dented dots. Then inks are loaded in the dented dots and excessive amount is scraped off the plate with a doctor blade. After that, the printing plate with ink is transferred to a roller based printing system with substrates feeding. As shown in Figure 2.32, gravure printing system generally consists of a gravure roller, an ink supply, a doctor blade and an impression roller. The replication printing process happens when inks in the gravure roller are pressed by the impression roller in contact.

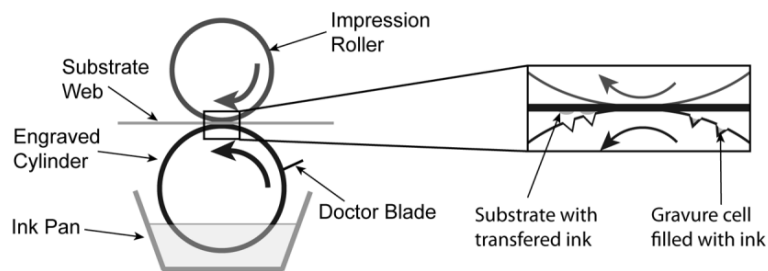


Figure 2.32: Illustration of gravure printing [131] Copyright © 2011 IEEE.

Gravure printing has two modes of substrate feeding philosophies, namely web-fed and sheet-fed, respectively. The web-fed gravure printer employs a roll-to-roll system, which allows substrate to be fed continuously to the rollers as demonstrated in Figure 2.32. For this reason, it can achieve high-speed feeding and printing and it is widely used in industry for mass production with both high quality and speed. Conversely, sheet-fed feeding mechanism is suitable for small batch printing, such as laboratory research application. Generally, a flat gravure plate is applied and one printing sheet is fed at a time.

A gravure plate or roller typically has a delicate structure, which is normally a steel base and a copper plate on top. First, printing pattern is pixelised into a matrix of dots

2.4 PRINTING TECHNIQUES

(generally diamond-shaped), which is the single printing unit to contain ink. The dots then are engraved into the copper plate to form gravure cells, with walls around each of them to keep them separated. Figure 2.33 illustrated the micro-structure of a gravure plate with diamond-shaped cells under microscopy. A protection electroplated layer is normally applied on top of the copper to avoid abrasion from the doctor blade. By tuning the cell shape and depth, it is possible to control both loaded ink volume and printing quality precisely.



Figure 2.33: Gravure cell under microscopy [25].

Given the above, gravure printing has the following advantages. Firstly, due to the ink loading mechanism, inks with low viscosity and high purity dispersion can be used. Secondly, roll-to-roll process enables high-speed printing possible. Thirdly, it is possible to control ink volume and printing quality by choosing proper gravure cell size, shape and depth. Last but not least, gravure printing rollers are durable and can last long without pattern deterioration.

The disadvantages of gravure printing predominantly lie in the gravure plates or rollers, which has high cost to fabricate. This is not suitable for small batch production. In addition, the rigid gravure plate or roller makes it difficult to print on hard substrates, only limited to some flexible substrate materials. At the same time, the gravure cell size

also constrains the printing resolution. Another issue is the challenge of coordinating between ink droplet surface tension and substrate surface adhesiveness, so that the ink droplets can joint each other to form a homogeneous film after being transferred from the disconnected cells onto the substrate. Proper ink formula and surfactants may be considered to overcome this issue.

2.4.4 Flexographic Printing

Similar to gravure printing technique aforementioned, another type of direct replicate printing method is flexographic printing. Instead of using rigid plate or roller, flexographic printing employs an elastic printing plate or roller with a positively mirrored 3D relief pattern in the elastic rubber or polymer layer. Additionally, flexographic printing transfers ink in an additional roller called anilox roller rather than directly with the printing plate roller. The detailed illustration of the printing mechanism is shown in Figure 2.34.

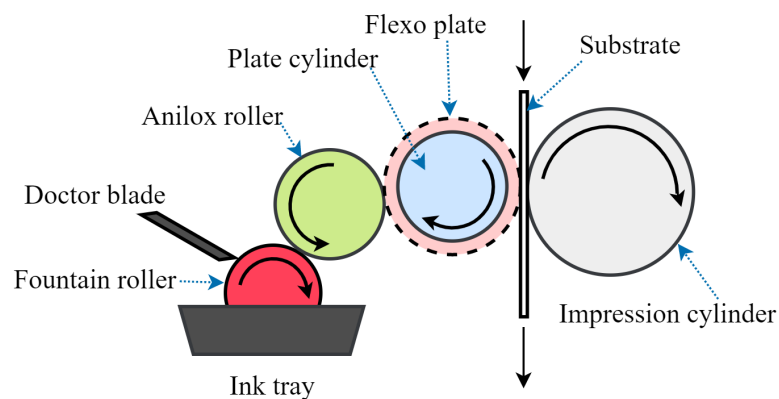


Figure 2.34: Illustration of flexographic printing mechanism [132, 133] (reproduced) Copyright © 2013 IEEE.

A typical flexographic printing system consists of an ink supply (ink tray), an fountain roller, anilox roller with a doctor blade, a plate roller (cylinder) with flexo plate, and an impression cylinder. During printing, the anilox roller picks up ink from the

2.4 PRINTING TECHNIQUES

fountain roller in the ink tray. The anilox roller has similar engraved cell structure on its entire surface like a gravure roller. The doctor blade can remove excessive ink from the anilox roller. After that, the ink is further transferred onto the flexo printing plate from the engraved cells in anilox roller. This process can be done evenly as the uniformly distributed unit cells with ink in anilox roller. The final transfer of the ink then happens between the flexo plate and impression cylinder, between which the substrate is sandwiched by contact force. Then the substrate will be subsequently carried away for drying or curing and other post processing.

The flexographic plate cylinder has a flexible rubber or photopolymer layer with 3D relief image on it. Based on different material chosen, the image layer can be crafted with molded rubber, laser engraved rubber or soluble photopolymer with UV light exposure. Since the ink are transferred and mounted on top of the relief surface, the amount is limited, thus the printed layer is generally thinner than that produced by other printing methods.

The nature of the printing philosophy and the application determine the fundamental requirements of the ink used. Flexographic printing generally have four major types of inks: solvent-based ink, water-based ink, electron beam curing ink, and ultraviolet curing ink, all of which have a viscosity range of 50-200 cP.

Given the above, the advantages of flexographic printing can be concluded as: firstly, printing plate is low cost, durable, resilient and easy to fabricate; secondly, due to the elastic printing plate, it has wide printing range, lower impression pressure; thirdly, thin printed layer with smooth surface; last but not least, ink viscosity is low and ink formulation is easy to prepare.

Disadvantages also exist for flexographic printing technology, including a short life cycle of a printing plate due rubber and polymer degradation, distortion of elastic plate

2.4 PRINTING TECHNIQUES

due to impression, complex printer structure for maintenance.

Gravure and flexographic printing have similar printing mechanism driven by cylinders (or rollers) and templates formed by engraved cells. They both have the features of low-cost, rapid printing process, durable printing rollers, and ease of mass production. However, they are also limited to ink viscosity, flexibility of substrates, and complexity to modify templates. Therefore, thus far, they are basically used for RFID fabrication at relatively low frequency bands.

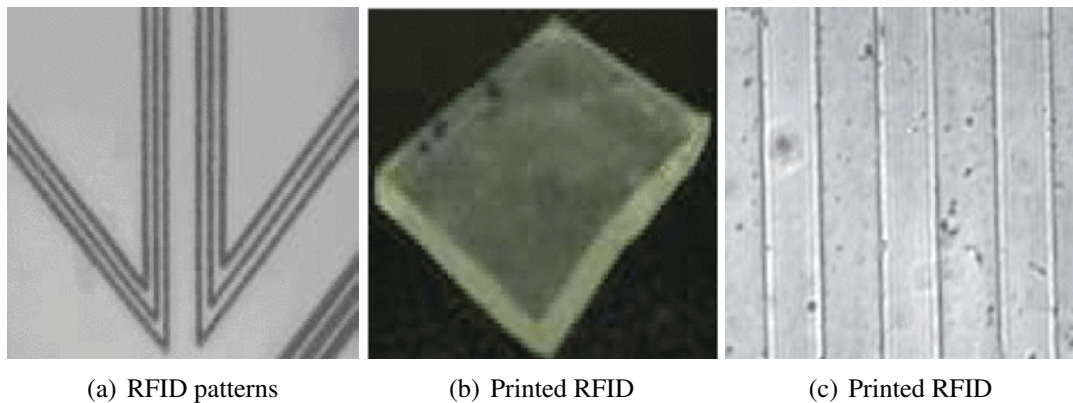


Figure 2.35: Flexographic printed RFID for biomedical applications [132] *Copyright © 2013 IEEE.*

In [132], an RFID antenna transponder with multiple solid lines was printed via flexographic printing technique for biomedical application. The flexographic printer was modified to achieve desired size and results and the parameters were set up and tuned precisely as well. Microcontact printing with polydimethylsiloxane (PDMS) was applied for printing small sized RFIDs, through which the ink can be transferred onto substrate and form self-assembled mono-layer patterns via conformal contact. This combined technique is widely used in surface chemistry and cell biology. The printed lines have a width of $25 \mu\text{m}$.

However, the printed results are very sensitive to the parametric settings, such as applied roller speed, PDMS stamp, applied forces on the ink, etc. Several failure prints

2.4 PRINTING TECHNIQUES

demonstrated the major impacts from inaccurate parameters setup, such as misprinting, cut off patterns, PDMS and deformation. To sum up, flexographic printing methods with the aid of microcontact and PDMS can attain very fine resolution, but they are limited and sensitive to parametric setup.

Table 2.4: Results of printed lines for RFID antennas

Printing Method	Flexographic	Screen Printing	Inkjet Printing
Track thickness (μm)	6	8	0.5
Resistivity (Ω/sq)	80	110	50
Conductivity (S/m)	1.8×10^6	1.3×10^6	40×10^6
Reading distance (m)	5.65	5.38	5.84

In [134], a study of printed line width limit was conducted for RFID antennas by flexographic printing, screen printing, and inkjet printing, respectively. An RFID antenna with 2-mm wide line were printed with those three methods and compared in terms of resistivity and reading distance. The ones printed with flexographic printing and screen printing have similar results; while the inkjet printed one has slightly better result than those printed by the other two methods. The detailed results are listed in Table 2.4. Flexographic and screen printing have close performance in terms of printed thickness, resistivity/conductivity and even the reading distance of the RFID antenna. Inkjet printed trace has lots thinner thickness due to the low viscosity of the ink, but conductivity is relatively higher.

For gravure printing, [135–137] reported printed RFID antenna and tags for different applications and circumstances. A meandered RFID antenna was fabricated by gravure printing in [135] on a PET substrate as shown in Figure 2.36. The printing speed was set as 5 m/min. After printing, the antenna was sintered at 150°C for 2 minutes and then measured in room temperature. The printed trace achieved surface resistance of 7.31 Ω/sq and thickness of 446 nm. However, due to the PVP adhesive substance on the surface of the silver prints, the printed antenna could not resonate at the designed

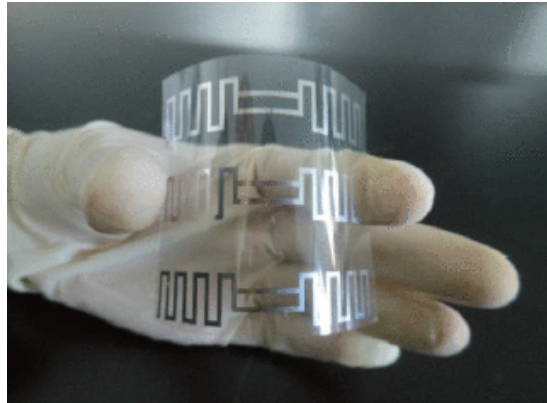


Figure 2.36: Gravure printed RFID antenna [135] *Copyright © 2013 IEEE.*

frequency. The antenna went through two different post-processing procedures: one is freezing process at -40°C for 6 hours; and the other one is drying at room temperature for 30 days. After those post-processing, the resistance of the frozen antenna dropped 9%, whereas that of the dried ones remained the same. This suggests that the ultra thin printing thickness cannot guarantee the conductors to have sufficient conductivity for the antenna to function. Moreover, proper processing methods are needed to improve the printed conductivity.

The RFID proposed in [136] was printed with graphene oxide ink and the single layer of the printed film is $4\ \mu\text{m}$ thick. The RFID was supposed to function at 30.71 MHz, but the measured complex impedance at that frequency is 668 k Ω , which is surprisingly high. This will significantly influence the functionality of the RFID tag and its reading distance. Possible methods to increase the operating frequency include modifying the ink preparation procedure to improve the ink conductivity or adjusting the printing process such as multiple layer print.

In [138], a WLAN dual-band monopole antenna was presented and printed by both flexographic and screen printing techniques. As shown in Figure 2.37, two types of the monopole antenna were designed, one was two cascaded annular rings, and the other one was two disks. Both were printed on a paper substrate. The thickness of

2.4 PRINTING TECHNIQUES

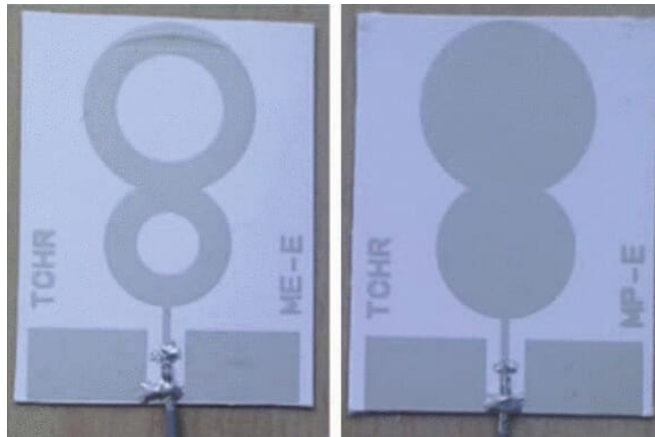


Figure 2.37: Monopole antenna printed by flexographic printing [138] *Copyright © 2016 IEEE.*

printed films by flexographic and screen printing were $2 \mu\text{m}$ and $7 \mu\text{m}$, respectively. The corresponding conductivity were $7.5 \times 10^5 \text{ S/m}$ and $1.71 \times 10^6 \text{ S/m}$, respectively.

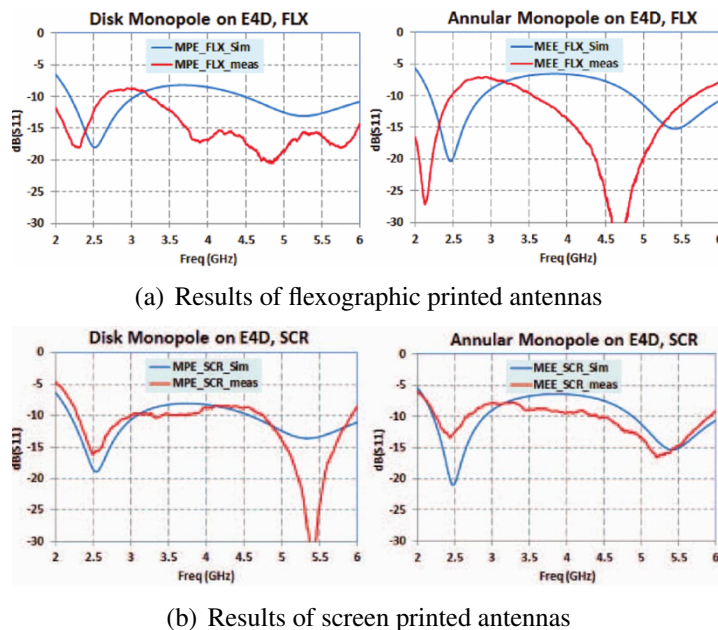


Figure 2.38: Results of monopole antenna by flexographic printing and screen printing [138] *Copyright © 2016 IEEE.*

From Figure 2.38, the screen printed antenna achieved better agreement in measurement and simulation results than the flexographic printed ones. This observation also applies

to the printed thickness and conductivity results. The performance deviation between these two printing techniques may be a consequence of the conductor thickness and surface roughness, which vary from different printing methods.

In summary, this section attempts to provide insights into choosing a proper printing method for antenna design. Flexographic printing and gravure printing are not suitable due to their poor performance and complexity of making printing template roller, which might be even challenging if the antenna design is for higher frequency, such as 5G cellular communication or millimetre wave application, since the antenna size will be smaller too. For inkjet printing and screen printing, both can yield acceptable accuracy and performance. Screen printing has more flexibility in terms of equipment availability, ease of maintenance, and relatively low cost.

2.5 Antennas and Metamaterials

Metamaterial is subset of functional materials, engineered to possess properties that are not found in natural materials [139–141], as shown in Figure 2.39. The word "*meta*" comes from Greek word *meta*, which means "beyond". Metamaterials normally are typically engineered and arranged to exhibit desired features, and consist of a multitude of particularly selected individual elements. With different combinations of selected elements, metamaterials can be used to manipulate different targets, such as sound, microwave, and light. EM metamaterials generally consist of metal and non-metal material elements to affect EM wave radiation, which is one of the most common types of metamaterials [139, 140].

With the arrangement of metal and non-metal materials in periodic patterns, of which the unit cell size is normally smaller than the wavelength of targeted EM waves, metamaterials can influence the EM waves with their newly engineered properties.

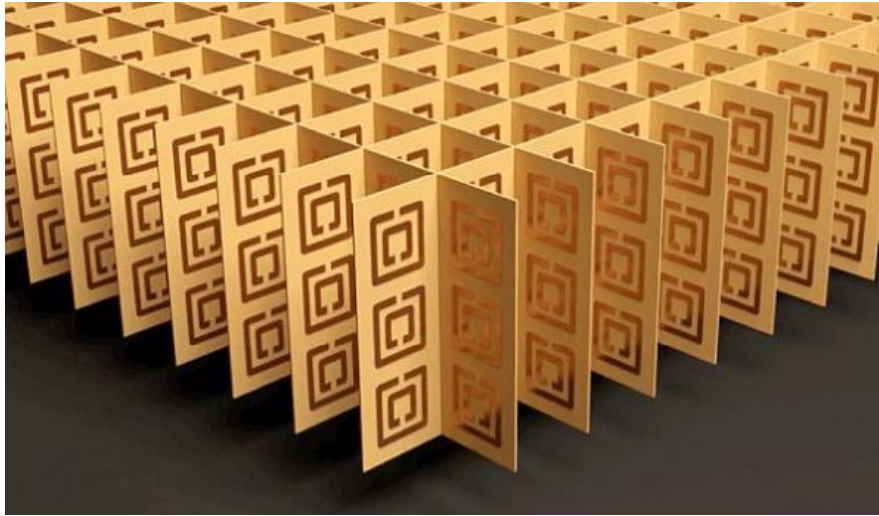


Figure 2.39: Metamaterials [139].

By precise controlling of the parameters of the metamaterial in shape, geometry, size, orientation and periodicity, the EM waves can be easily manipulated in the following formats: blocking, absorbing, enhancing, bending or twisting [141–143].

Due to the various possibilities to manipulate EM waves, EM metamaterials have been applied in microwave and millimetre wave applications, such split-ring resonators (SRR), frequency selective surface (FSS). Another important application of EM metamaterials is metamaterial antennas. They can be utilised to improve antenna performance, enhance antenna radiated power, achieve smaller antenna size, higher directivity and configurable frequency [144–147].

2.5.1 Metamaterials

Normally, the properties of a material is determined by both an electric permittivity (ϵ) and a magnetic permeability (μ). Given the reference material free space (or air) that has the permittivity of ϵ_0 and permeability of μ_0 , the relative permittivity and permeability of a material can be defined as $\epsilon_r = \epsilon/\epsilon_0$ and $\mu_r = \mu/\mu_0$, respectively. Then, the refractive index, can also be defined as $n = \sqrt{\epsilon_r\mu_r}$. Most of the natural materials

have a positive relative permittivity and relative permeability and larger than the ones of free space. Introducing metamaterials enables the entire span of all types of materials with all possible properties [139, 140]. Figure 2.41 illustrates all the combinations of possible material properties in terms of ϵ and μ . There are totally four quadrants in the diagram, which represent right-handed materials (RHM), electric plasma, left-handed materials (LHM), and magnetic plasma, respectively [139, 140, 142, 143].

- First quadrant: RHM, where $\epsilon > 0$ and $\mu > 0$, and waves propagate forward. According to Maxwell's equations, the direction of the wave vector \mathbf{k} has the same direction with the cross product of the electric field \mathbf{E} and the magnetic field \mathbf{H} [139].
- Second quadrant: Electric plasma, of which $\epsilon < 0$ and $\mu > 0$ and evanescent waves are supported [139].
- Third quadrant, where $\epsilon < 0$ and $\mu < 0$, is also well known as LHM and supports backwards propagating waves. Correspondingly, the wave vector \mathbf{k} has opposite direction with the one of the cross product of the electric field \mathbf{E} and the magnetic field \mathbf{H} [139].
- Fourth quadrant, where $\epsilon > 0$ and $\mu < 0$ and waves go evanescent through here [139].

It has to be clarified that the use of handedness to name a certain type of metamaterial. The terminology "left-handed" and "right-handed" have their rationale from the relative positions of the vector triplet (\mathbf{E} , \mathbf{H} , \mathbf{k}) of a linearly polarized wave that propagates in the media. These vectors are electric field, magnetic field, and wave vector, respectively [140]. For an LHM, these vectors form a left-handedness when both the dielectric permittivity and magnetic permeability are negative, which is the region of $\mu < 0$ and $\epsilon < 0$ in Figure 2.41.

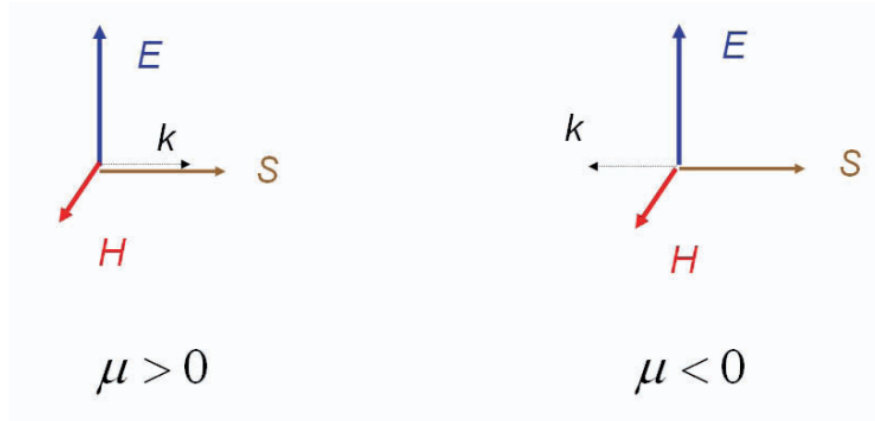


Figure 2.40: Right-handed and left-handed triplet vectors.

Through time-harmonic convention $\exp(j\omega t)$, Maxwell curl equations read for plane-wave functional dependence $\exp(-j\mathbf{k} \cdot \mathbf{r})$ in homogeneous and isotropic background in terms of μ and ε [140]:

$$\mathbf{k} \times \mathbf{E} = \omega \mathbf{B} = \omega \mu \mathbf{H}, \quad (2.57)$$

$$\mathbf{H} \times \mathbf{k} = \omega \mathbf{D} = \omega \varepsilon \mathbf{E}. \quad (2.58)$$

As shown in Figure 2.40, a right-handed vector triplet is represented, where the \mathbf{k} is parallel to the time-dependent Poynting vector $\mathbf{S} = \mathbf{E} \times \mathbf{H}$; whereas for an left-handed vector triplet, they are anti-parallel to each other [140].

The term handedness is also used to describe the polarization of electromagnetic wave as mentioned in previous part. Polarization is the term describing the rotation direction of the electric field vector, which has helicity in its elliptical (circular and line are special cases) temporal trace pattern in its transversal plane when observed along the wave propagation direction. The polarization is denoted as right-handed if the observed vector rotates in a clockwise direction, and left-handed if it rotates in a counterclockwise direction [141].

From Figure 2.41, it is obvious that natural materials only take a small cluster of discrete points along the line of $\mu = \mu_0$ and $\varepsilon \geq \varepsilon_0$. Hence, most of the material properties have to be realised by utilising metamaterials, at some point, including some RHM. Therefore, metamaterials is a broad definition, among which LHM is a popular type being studied, as known as other names due to their predictable existence derived from the theories [141]:

- LHM, as the first label for this certain type of metamaterial, can confuse crucial microstructural issues because the term of handedness has been applied to molecular structure all along for over a century [140].
- Backward-wave (BW) materials, denotes the direction of a plane wave propagation. However, every wave propagates forward, let alone in the context of non-planar waves. So it could be problematic too [140].
- Double negative materials (DNG), indicating the real parts of both permittivity and permeability are negative [140].
- Negative refractive index materials (NIM), referring to the fact that refractive index of the material being negative [140].
- Negative phase velocity (NPV), suggesting that the phase velocity of the wave propagating in the material is negatively directed. This term is rather unambiguous and not incongruous with other physical concepts [140].

Generally speaking, metamaterial is an extremely broad concept, which includes not just LHM. Taking a close look at the ε - μ domain, several particular material properties indicated by points and lines can be found [141]. For instance, the intersection point of $\mu = -\mu_0$ and $\varepsilon = -\varepsilon_0$ stands for some anti-air material in the LHM region, which can be used to make a perfect lens; The point $\mu = 0$ and $\varepsilon = 0$ represents nullity, which

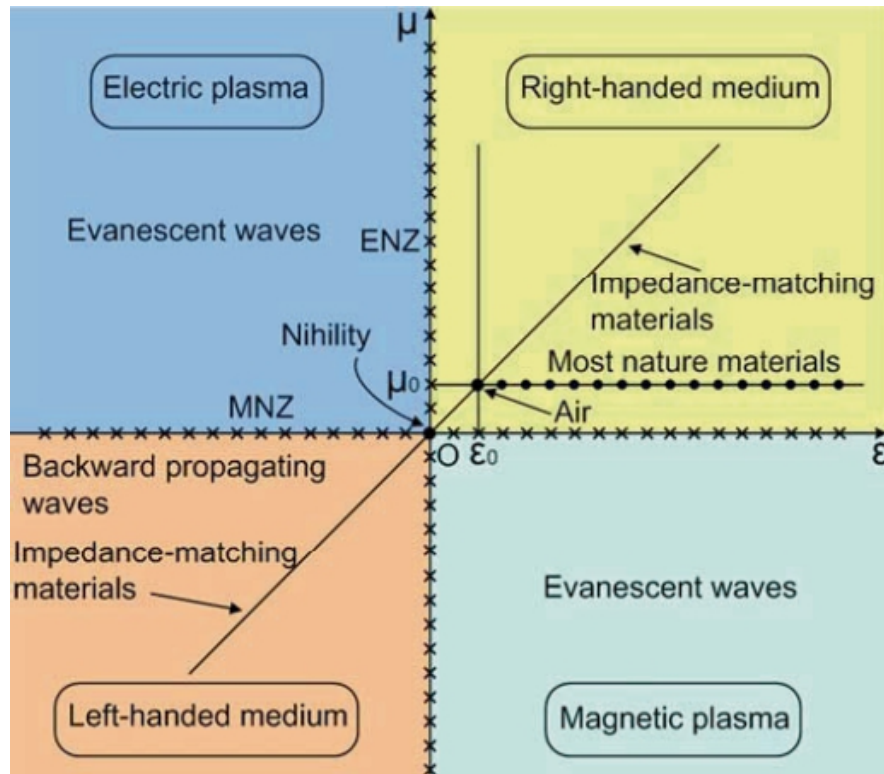


Figure 2.41: Entire span of possible material properties in ε - μ domain [139, 140].

is ideal for tunneling; When it comes to the line of $\mu = \varepsilon$ in RHM and LHM region, it stands for impedance-matching materials that results no reflection with air due to perfect impedance matching; materials in the vicinity of line $\mu = 0$ and $\varepsilon = 0$ have special properties as well and are called μ -near zero (MNZ) material and ε -near zero (ENZ) material, respectively [139, 140].

In reality, there are far more features than those indicated in Figure 2.41. By designing metamaterials in various methods and arrangement, they can demonstrate miscellaneous features and functions. Typically, metamaterials can be either highly anisotropic or weakly anisotropic based on practical requirements. With proper design and arrangement, it is possible to manipulate electromagnetic waves at will with metamaterials [139].

To design a certain type of metamaterial, the currently most common approach is

to apply computational electromagnetics (CEM), where full-wave electromagnetic simulations can be conducted. Generally, there are two major types of CEM techniques, namely finite element method (FEM) and the finite integration technique (FIT) [140]. The corresponding commercial softwares are ANSYS HFSS and CST Microwave Studio, respectively. A general design algorithm and corresponding steps will be provided in Chapter 5.

2.5.2 Metamaterial Functions

Due to the fascinating and beyond-nature features, metamaterials have been applied to a wide range of applications or potential applications. First, metamaterials can be applied to boost antenna designs. When metamaterials are combined with antenna design, it is one of the most popular classes of antenna, i.e., metamaterial antennas. Performance improvement has been proved from various metamaterial antenna designs [142, 143, 148]. It is also found that metamaterials can enhance an antenna's radiated power, [149, 150], which can reduce the input power for the transmitter antenna. For example, by surrounding an antenna with a shell of DNG material, the antenna will act inductively rather than capacitively [151]. Metamaterials can also enable antennas to attain negative permeability so that small antenna size, high directivity and tunable frequency can be achieved [143, 149].

Second, a superlens, which is a device that can achieve ultra-high resolution beyond the diffraction limit due to its negative refraction properties, is another attractive application for metamaterials. As mentioned previously, LHM has double negative coefficients ($\mu < 0$ and $\varepsilon < 0$) to yield negative phase velocity (one characteristic of a LHM medium). Conventional optical lenses have their inherent diffraction limit, which restrains the application. However, the super-resolution feature of superlens is suitable for medical sensing, optical sensing, and nondestructive detections [141].

Third, metamaterials are also a great potential candidate for a practical cloaking device. So far, only some successful experimental demonstrations of cloaks in the microwave domain. However, it brings the possibility for near future, given the rapid development speed of metamaterials [139, 140, 152].

By making use of the loss components caused by material permittivity and permeability, metamaterials can absorb a significant amount of electromagnetic radiation, i.e., they are functioning as electromagnetic absorbers. This feature can be in great use in photodetection and solar photovoltaic applications.

2.5.3 Metasurfaces

Albeit metamaterials have fascinating and attractive functionalities and features, it typically requires a complex 3D structure with particular unit cells, which usually consists of not only one layer. Therefore, it tends to cause extensive losses and makes it much more challenging in both design and fabrication, especially when it comes to micrometer or nanometer order. Additionally, in electromagnetic wave regime, complex metallic components are inevitable in the material structure design, which requires further more rigorous computations and more sophisticated fabrication and assemble techniques [152, 153].

As far as the aforementioned complexity is concerned, metasurfaces have been introduced and rapidly developed to overcome the hindrances that 3D metamaterials have been confronted with. Generally, an electromagnetic metasurface refers to a 2D counterpart of metamaterials with sub-wavelength thickness, i.e., a flat and thin film structure with particular particles or unit cells [152].

Through employing a periodic array of scattering elements with sub-wavelength level dimensions, metasurfaces can attain negligible thickness compared with the target

2.5 ANTENNAS AND METAMATERIALS

operation wavelength, therefore, they can function as an interface where an abrupt change in both electromagnetic wave phase and amplitude can be manipulated [153, 154].

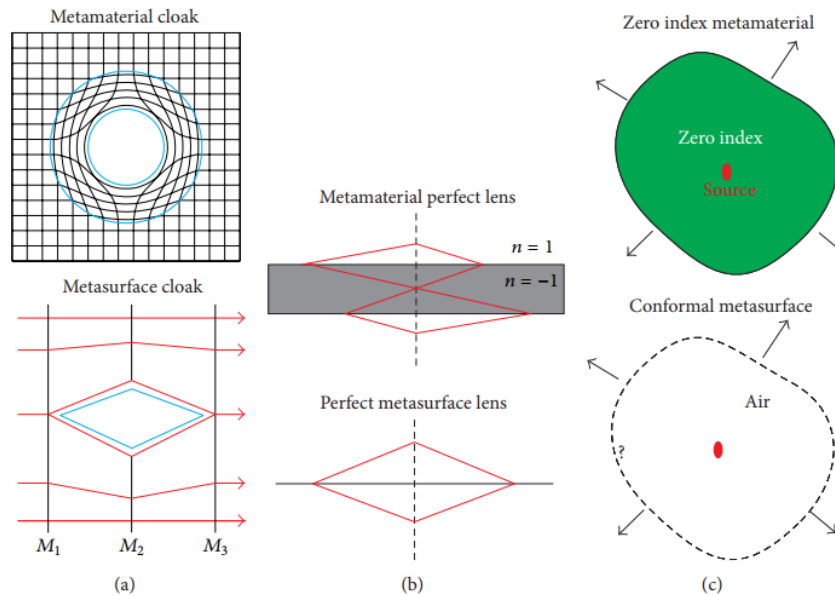


Figure 2.42: Comparison of metasurfaces with metamaterials: (a) Cloaking. (b) Superlens. (c) Conformal metasurface [153] Copyright © 2015 Xiangang Luo et al..

If looking at the essence of both metamaterials and metasurface, it both can be correlated with Maxwell's Equations, which are formulated by James Clark Maxwell in 1863. These equations establish and describe the fundamental features of electromagnetic waves [152]. It is well known that theoretically all electromagnetic problems should be solved once the constitutive parameters (i.e., μ and ε), initial and boundary conditions are given. In fact, the essence of metamaterials is the design procedure of constitutive parameters beyond natural occurrence. Conversely, composing metasurfaces is more like a procedure of modifying the boundary condition to interfere electromagnetic wave propagation, because they have negligible thickness, which theoretically vanishes [153].

As explained above, even if the theoretical mechanisms are different, both metamaterials and metasurface are able to manipulate electromagnetic fields. Actually, metasurfaces

can be regarded as an analogy of metamaterials with reduced dimension [153]. Furthermore, as shown in Figure 2.42, metasurfaces demonstrate advantages over metamaterials in many conditions and applications, for instance, invisible cloaking, superlens, and radar cross-section (RCS) etc. With the great advantage of their 2D structure, metasurfaces are also applied in electromagnetic absorbers, polarization converters, spectrum filters and bio-imaging devices [152].

2.6 Chapter Summary

This chapter revisited antenna theories and characteristics, as well as potential antenna types, especially microstrip patch antennas. Moreover, antenna fabrication methods and conductive inks were discussed, which can be used for flexible antenna designs. In the last section, metamaterials and metasurface are discussed for potential planar antenna enhancement techniques.

Chapter 3

Silver Ink-Printed Flexible Wideband Dipole Array Antenna

After the careful literature review in conductive inks and printing techniques in Chapter 2, this chapter presents a dipole array antenna for wideband 5G applications, which is designed with a flexible structure and fabricated with silver particle based conductive ink and screen printing technique. Simulation and measurement results are given and discussed as well as the evaluation under conformal circumstance.

3.1 Background

Printed electronics have drawn great attention from both industry and academia in recent years [101]. Conductive ink printed devices and systems have been widely used for near-field communication (NFC), RFID, and health monitoring devices. Among several types of conductive inks such as carbon nanotube ink [155], silver particle ink [105] and graphene ink [111], the silver particle ink has become the most commonly commercialised conductive ink due to its salient features of high conductivity, low cost and ease of fabrication [105]. There exist several techniques to print electronics, such

3.1 BACKGROUND

as screen printing, flexography, gravure, and inkjet printing[91] [128].

Patch antennas have become widely used due to their low cost, low profile and easy production. Antennas with dipole element are fabricated with traditional PCB in [156–158]. In [156], a T-shaped dipole antenna was proposed for dual-band and triple-band operation, with a realized gain of 2.69 dBi, 1.65 dBi and 2.76 dBi at 2.5 GHz, 4.6 GHz, 4.6 GHz and 5.6 GHz, respectively. An ultra-wideband antenna array based on planar dipole elements was reported in [157], operating from 1.3 GHz to 3.3 GHz. In [158], an log-periodic dipole array (LPDA) antenna was proposed with a substrate integrated waveguide (SIW) feeding structure and a 7.3-12.5 dBi gain over 40-50 GHz. Ink-printed antennas were reported in [91, 92, 130]. The proximity fed patch array in [91] and the Yagi-Uda antennas in [92] were fabricated with inkjet printing and operating at 24 GHz for mmWave application. However, both of these designs employed multiple printing processes for different structures (radiating patch, feed and substrate) of the antennas. This will increase the cost and difficulty of printing fabrication. In [130], UHF RFID reader antennas using screen printing were presented. These antennas were printed on rigid FR4 substrates, which are not suitable for flexible circumstance, like wearable application for wireless body area networks (WBANs).

WBANs have become popular recently as the development of 5G technology and IoT [159–161]. A WBAN is a network that connects a number of independent and smart nodes that are integrated in the clothes, on the body, on or implanted under the skin of a person. Through a WBAN, the data collected from the person can be transferred for further analysis or monitoring purposes. A WBAN can offer promising applications from remote health monitoring, healthcare, sports guidance to many other areas [162, 163]. The smart nodes in a WBAN must be flexible to conform human body, low energy consumption, and have long operation range, and be resistant to environmental interference. As an essential part of the wireless network, a flexible

antenna plays an important role. Aforementioned ink-printed flexible antennas could be a solution to this.

After reviewing the existing printed antenna designs, we propose a flexible and low-profile antenna for WBAN applications. A dipole array antenna was selected because that it has ultra wide bandwidth and low-profile feature. It is also suitable for planar design using the ink-printing technique for fabrication. It covers a wide frequency band within upper 5G band from 23 GHz to 30 GHz. Moreover, this antenna has a low-profile structure with two conductive layers and one flexible dielectric textile substrate layer. Silver particle based conductive ink and screen printing technique are applied for fabrication.

3.2 Dipole Array Antenna Design

In this section, the proposed flexible dipole array antenna is presented. The antenna is designed on a flexible polyester fabric and fed by a standard $50\text{-}\Omega$ microstrip line with a microstrip-to-coplanar stripline (CPS) balun (unbalance-to-balance). The antenna has three directors for radiation enhancement. The antenna operates in the frequency range from 23 GHz to 30 GHz, which includes 24 GHz - 24.5 GHz in ISM band, 26.5 GHz -29.5 GHz in local multipoint distribution service (LMDS) band, and 24.25 GHz - 27.5 GHz in K-band. Additionally, 24.5 GHz and 28 GHz are included in the 5G mmWave frequency bands (FR2). The applications include but not limit to wearable electronics, medical sensing devices, and data collection devices. The proposed design explored screen printed antenna on flexible fabric substrate, which will also contribute to the development printed electronics.

The proposed antenna structure and its dimensions are shown in Figure 3.1. The design consists of three layers: top antenna layer (grey), middle substrate layer (cyan) and

3.2 DIPOLE ARRAY ANTENNA DESIGN

bottom ground layer (orange). On the top layer, it includes a microstrip-line feed, a microstrip-to-CPS balun to convert from unbalanced to balanced input signal, the main body of the antenna and three equally spaced directors. The middle substrate layer is a flexible dielectric polyester fabric.

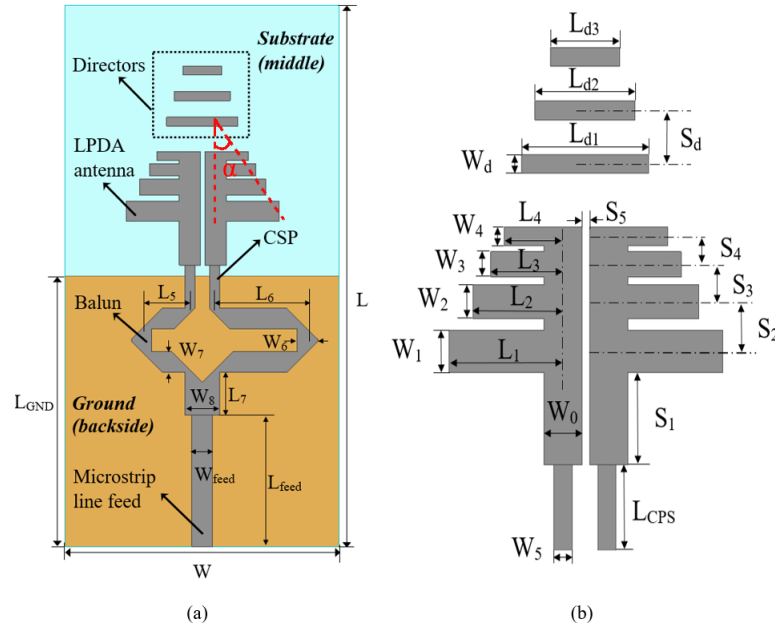


Figure 3.1: (a) Proposed antenna design and (b) its dimensional parameters.

The design parameters of the antenna can be determined as follows: firstly, a scale factor $\tau = 0.75$ and spacing factor $\sigma = 0.112$ are chosen based on the angle $\alpha = 30^\circ$ (as shown in Figure 3.1 (a)) to fulfil the relationship described in (3.1) [164]. Secondly, the length of the first dipole is calculated as $L_1=2.450$ mm, which is equal to a quarter of the effective wavelength of the lowest resonant frequency $f_{min}=24.5$ GHz. Finally, all the other dimension parameters can be calculated by applying the formulae below [158, 164, 165]:

$$\tan \alpha = \frac{1 - \tau}{4\sigma}, \quad (3.1)$$

3.2 DIPOLE ARRAY ANTENNA DESIGN

$$S_{n+1} = 4\sigma L_n, \quad (3.2)$$

$$\frac{L_{n+1}}{L_n} = \frac{W_{n+1}}{W_n} = \tau. \quad (3.3)$$

where $n = 1, 2, 3, 4$ is the number of dipole elements.

The antenna is fed by a microstrip line via a coaxial adaptor, which is an unbalanced source. However, the proposed dipole antenna is a balanced device. Therefore, it requires an unbalance-to-balance conversion from the feed to the antenna [166, 167]. As shown in Figure 3.1, a wide-band microstrip-to-CPS balun is designed, where the length of the right arm is a quarter of the effective wavelength, i.e. $\lambda_{eff}/4$, longer than the left arm. The detailed dimensional parameters of the antenna design are listed in Table 3.1.

Table 3.1: Dimensional Parameters of Proposed Antenna (Unit: mm)

Para.	Value	Para.	Value	Para.	Value
L	25	W_3	0.557	L_{d3}	1.798
W	12.7	W_4	0.418	W_d	0.418
L_{GND}	15	W_4	0.495	S_d	1.178
L_1	2.450	S_1	0.5	L_{CPS}	2
L_2	1.837	S_2	1.098	L_5	2
L_3	1.378	S_3	0.823	L_6	4.064
L_4	1.033	S_4	0.617	L_7	2
W_0	0.990	S_5	0.2	W_6	0.94
W_1	0.940	L_{d1}	3.298	W_7	0.94
W_2	0.742	L_{d2}	2.598	W_8	1.88
L_{feed}	6.06	W_{feed}	0.94	-	-

3.3 Enhancement with Yagi-Uda Directors

In order to increase the directivity of the antenna, a director is required to guide the radiated electromagnetic waves to the forward direction. A director design based on Yagi-Uda design is chosen for this case since the planar dipole array structure of the proposed antenna. Yagi-Uda directors can be used both for 3D design and 2D planar design.

According to the investigation of Yagi-Uda antenna directors [61], the lengths of the directors range between $0.4-0.5\lambda$, whereas the spacing between adjacent directors varies from $0.1-0.5\lambda$. Several simulations are conducted to finalise the parameters for the directors. First, the director width W_d is set the same as the forth dipole, i.e. $W_d = W_4$. Then, parametric study are conducted through simulation to determine the following two parameters, which are the director length coefficient d_l and the director space coefficient d_s .

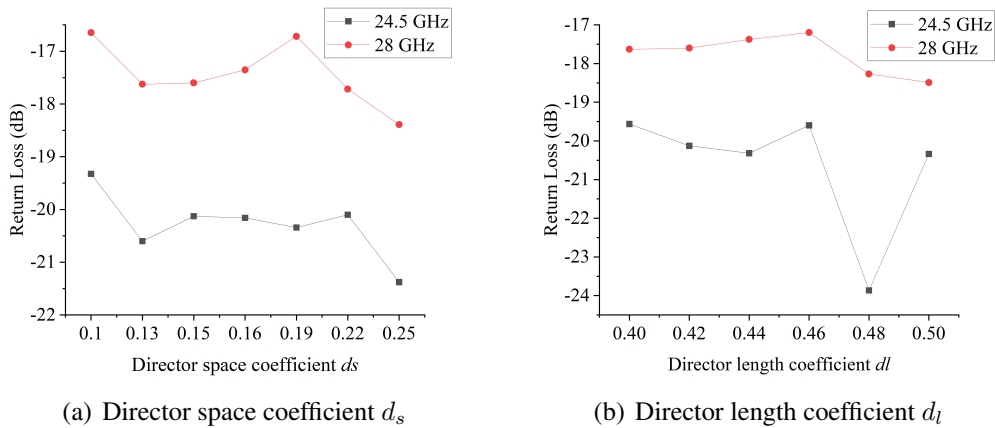


Figure 3.2: Parametric study for directors.

As shown in Figure 3.2, it presents the influences of one parameter has on the antenna return loss at frequencies of interest (24.5 GHz and 28 GHz) while the other one is set as the nominal value. In Figure 3.2(a), according to the limit of the substrate size, the

3.3 ENHANCEMENT WITH YAGI-UDA DIRECTORS

director space coefficient d_s is restrained to $0.1-0.25\lambda$ only. Generally, at 24.5 GHz, the antenna has lower return loss value than that at 28 GHz. When d_s varies from 0.13 to 0.22λ , the impact on antenna return loss or resonant frequency is negligible. The value of 0.15λ is chosen based on the overall antenna size.

Figure 3.2(b) shows the effect of the director length coefficient d_l . We can see that the overall return loss at 24.5 GHz is lower than that at 28 GHz. There is also a relatively sharp drop in the curve of 24.5 GHz when d_l is 0.48 . It suggests a slightly better resonant frequency due to the coefficient value. However, all the other return loss values are also in the acceptable range, below -20 dB. Additionally, as the value of d_l changes from 0.40 to 0.46λ , negligible influence can be observed. Given that all the return loss value fulfil the requirement of this proposed wide band antenna at frequencies of interest, a value of 0.42λ is chosen for director length coefficient.

Altogether, these above parametric study about directors determine the finalised director dimensions: the first director was set as 0.42λ in length and same width with the last dipole. Moreover, the other two directors have slightly decreased length based on the design principle, same width and equal spacing 0.15λ . The enhancement performance of the directors are summarised in terms of antenna directivity, maximum gain, and overall gain.

First, both Figure 3.3 and Figure 3.4 present the total directivity of the antenna in the plane of $\phi = 0^\circ$. In Figure 3.3, the green region indicates the front end of the antenna, i.e. $\theta = 180^\circ$ to 360° and the forward direction is at $\theta = 270^\circ$, of which the vicinity is the main forward propagation direction of the radiating EM waves. The yellow region represents the 75° angle region ($\theta = 225^\circ$ to 300°), where the directivity has been improved by adding the directors. This area takes up to 42% of the entire front end region.

3.3 ENHANCEMENT WITH YAGI-UDA DIRECTORS

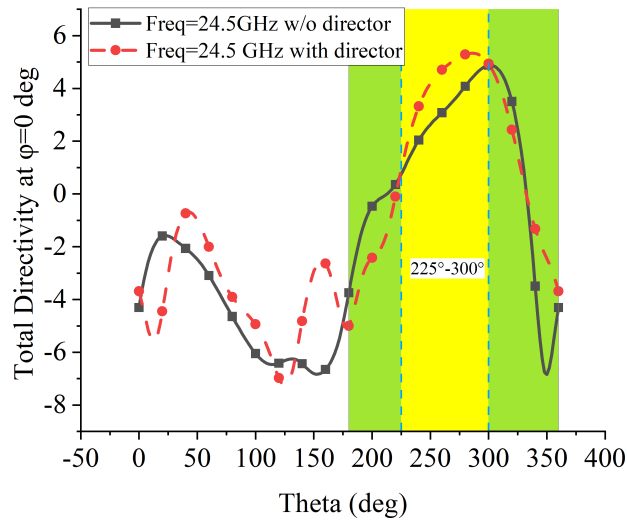


Figure 3.3: Effects of directors on total directivity D_0 at $\phi = 0^\circ$ at 24.5 GHz.

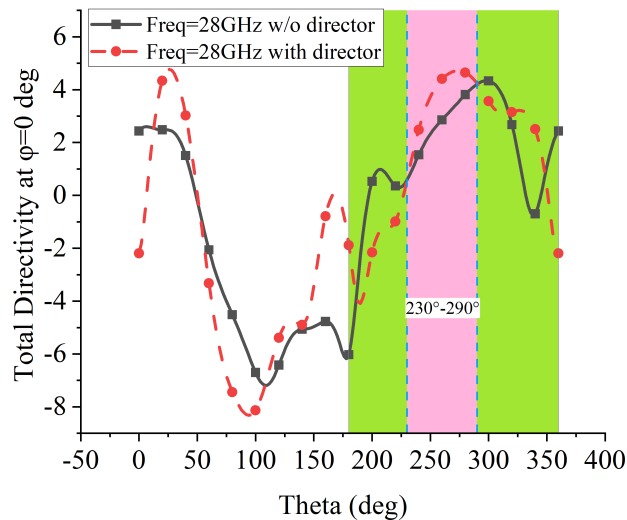


Figure 3.4: Effects of directors on total directivity D_0 at $\phi = 0^\circ$ at 28 GHz.

Similarly, in Figure 3.4, in the front end region, there is an area of 60° ($\theta = 230^\circ$ to 290°), where the directivity of the antenna has been improved by the directors. This is approximately 33.3% of the entire forward front end region. To sum up, these above results affirm that adding those directors has enhanced the directivity of the antenna at its forwarding direction.

3.3 ENHANCEMENT WITH YAGI-UDA DIRECTORS

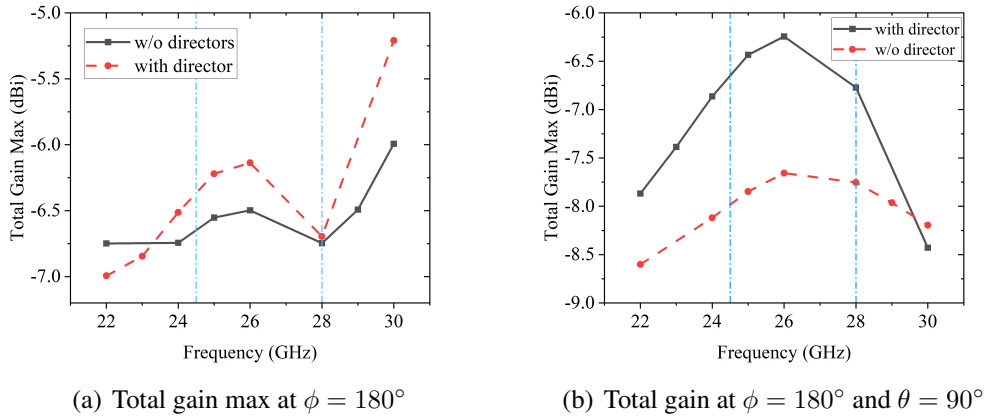


Figure 3.5: Effects of directors on antenna gain.

Figure 3.5(a) presents the maximum of the total gain G_{0max} on the plane of $\phi = 180^\circ$. It is obvious that from 23.5 GHz to 30 GHz, the overall gain with directors is higher than that without directors. At 24.5 GHz, G_{0max} increases about 0.5 dBi, whereas at 28 GHz, the increase is not that significant. On the other hand, Figure 3.5(b) demonstrates the gain $G_{0forward}$ at the forward direction ($\phi = 180^\circ$ and $\theta = 90^\circ$). Similarly, a positive improvement of $G_{0forward}$ can be found from 22 GHz to 29.5 GHz, and the improvement at 24.5 GHz and 28 GHz are significant, which is 1.25 dBi and 1 dBi, respectively. The above results also echo with the ones of directivity, which has shown the gain enhancement by adding the directors.

Altogether, these aforementioned results suggest that there are positive enhancements for the proposed antenna design by adding the Yagi-Uda based directors. In summary, the directivity at the desired direction, and antenna gain at the desired plane and direction are improved by the directors. In the next section, printing method and the corresponding conductive ink are elaborated.

3.4 Flexible Polyester Fabric Substrate

In order to achieve flexible structure and compatibility with potential wearable applications, a polyester fabric is selected as the substrate material and fabricated in our laboratory. To achieve a suitable substrate thickness, 8 layers of polyester fabric are assembled by a thin TPU film, which is thermally sensitive and turns adhesive when exposed to more than 120°. The combined and layered polyester substrate is 0.35 mm thick. The dielectric constant of the entire substrate is characterised using the double microstrip line methods proposed in [168]. Two microstrip lines with different lengths are fabricated with the substrate material and their S-parameters are measured over 1 to 30 GHz. Then the measured results are compared with calculated theoretical ones based on a matching algorithm via Matlab. The overall characterised dielectric constant ϵ_r of the substrate is 2.2 for simulation and design purposes.

3.5 Metalon HPS-021LV Silver Nanoparticle Ink

Table 3.2: Physical Properties of HPS-021LV Silver Ink.

Physical Properties	Values
Viscosity	>1000 cP (Brookfield spindle LV#4, 30 rpm)
Specific Gravity	3.1
Flash Point	Non-flammable
Particle Size	D50 2.0 micron, D90 4.0 micron
Ag Content	75 wt%
Sheet Resistance	0.011 Ω /sq
Resistivity	$1.69 \times 10^{-5} \Omega \cdot \text{cm}$
Conductivity	$5.92 \times 10^6 \text{ S/m}$

To screen print the proposed antenna on the polyester substrate, a commercial silver nanoparticle conductive ink from Metalon HPS-021LV is selected. This is an electrically conductive silver ink designed to produce conductive traces on low-temperature to high-temperature substrates such as paper, PET, glass, polyimide, and silicon. It is also

3.5 METALON HPS-021LV SILVER NANOPARTICLE INK

specially formulated for screen printing.

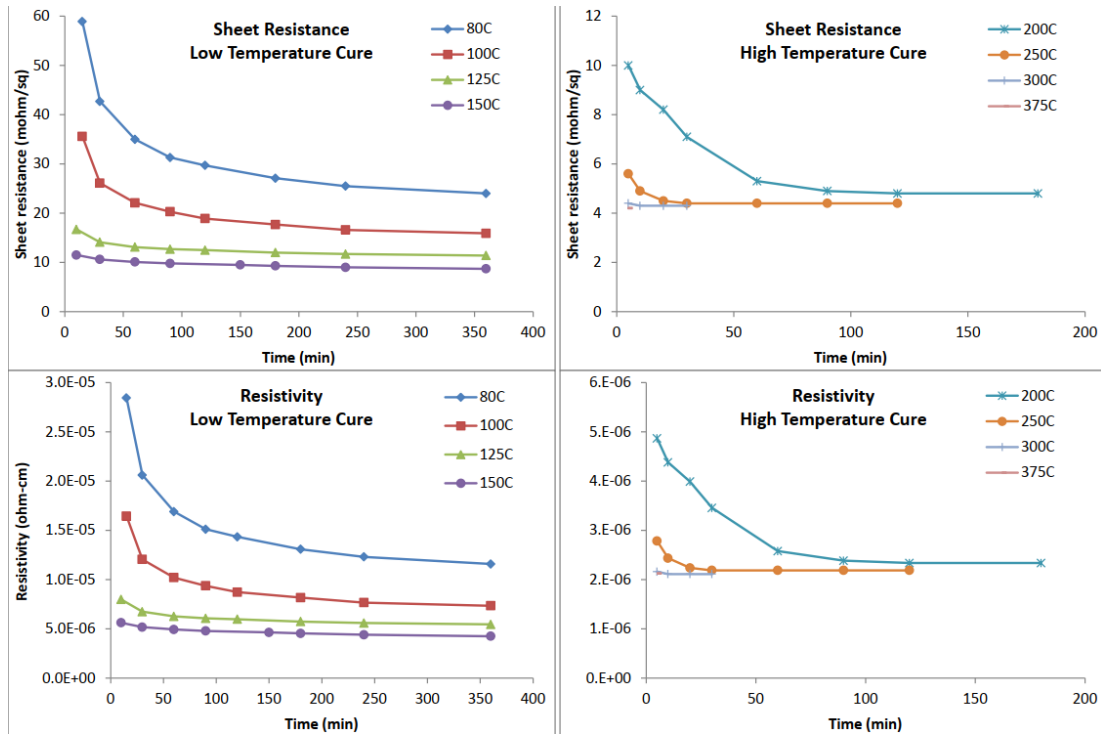


Figure 3.6: Curing temperature and duration for HPS-021LV silver ink [169].

The physical properties of the HPS-021LV silver ink are listed in Table 3.2 [170]. It shows that the ink has high viscosity of 1000 cP (whereas that of water at 25°C is only 0.890 cP), so that it is easy for the ink to attach onto the substrate and solidify after curing. The size of the conductive particles is 2 and 4 microns to form a smooth and uniform solution. The weight percentage of the silver particles is up to 75% to guarantee the conductivity of the ink.

The relationship between post curing temperature and the ink resistivity are described in the data sheet as shown in Figure 3.6. Two temperature ranges, i.e., low temperature range at 80-150°C and high temperature range at 200-375°C, are compared in terms of sheet resistance and (volume) resistivity, respectively. From the two figures in the top, it can be seen that the higher the temperature at which it is cured, the lower the

sheet resistance can be achieved. The sheet resistance of the printed ink decreases much faster in the high temperature range to a lowest value of about $4\text{ m}\Omega/\text{sq}$ over 25 minutes; while it is a much slower progress in the low temperature range to reach the lowest sheet resistance value of $10\text{ m}\Omega/\text{sq}$ over 150 minutes. On the other hand, the same situation happens to resistivity as indicated in the two figures in the bottom. The resistivity of the printed ink reaches its lowest value of $5\times 10^6\Omega/\text{cm}$ in the low temperature range, and $2\times 10^6\Omega/\text{cm}$ in the high temperature range. To conclude the above information, the silver ink needs to be cured at high temperature (above 200°C over around 50 minutes to achieve best sheet resistance and volume resistivity.

3.6 Antenna Fabrication

Although each printing technique has its respective advantages, screen printing has become the most widely used industrial printing technique [25, 107, 128, 129]. Screen printing is basically a replication process. The desired patterns or images are replicated from a master template to a substrate surface. By using the printing ink formulated with micro-sized solid materials, screen printing can easily achieve a thickness up to tens of microns with a single printing pass. Hence, the cost of screen printing is lower than the ones using nano-sized particle ink and the printing process does not need multiple passes [25]. Given the major advantage of screen printing mentioned previously, the proposed antenna design is chosen to be screen printed in Auckland University of Technology Printing Lab.

According to the procedure of screen printing as illustrated in Figure 3.7, the first step is to customise a screen stencil with the desired pattern. An ultra-fine silk screen is used for making the stencil and a photosensitive film is applied on the silk screen first. Then the antenna pattern is extracted and printed out with black and white colour on

3.6 ANTENNA FABRICATION

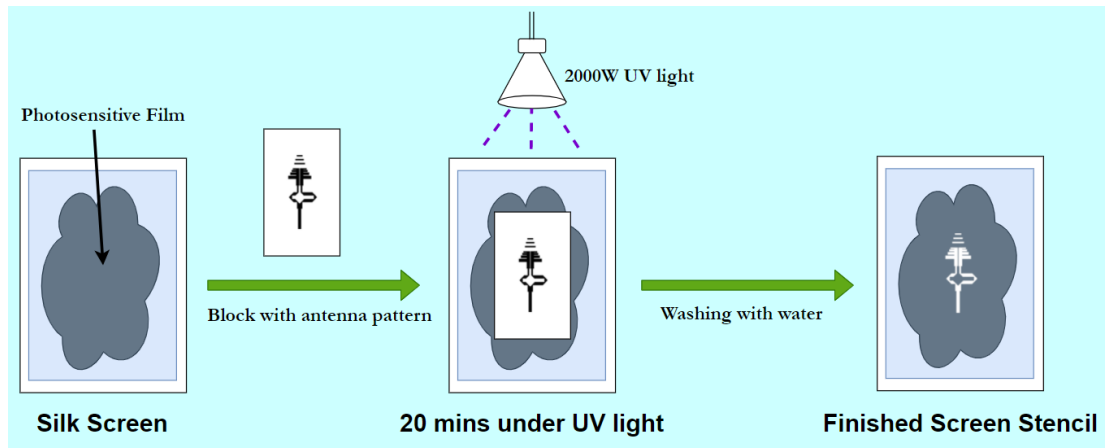


Figure 3.7: Process of making a silk screen stencil.

an A4 paper. After that, the silk screen is placed under a 2000-watt UV light for 20 minutes with the printed black antenna pattern on top. The UV light will cause the photosensitive emulsion to harden and coat to the film, while the part blocked by the black antenna pattern will remain soft and dissolve in water. After UV exposure, the silk stencil is washed with water to removed the soft emulsion, leaving the antenna pattern in the screen.

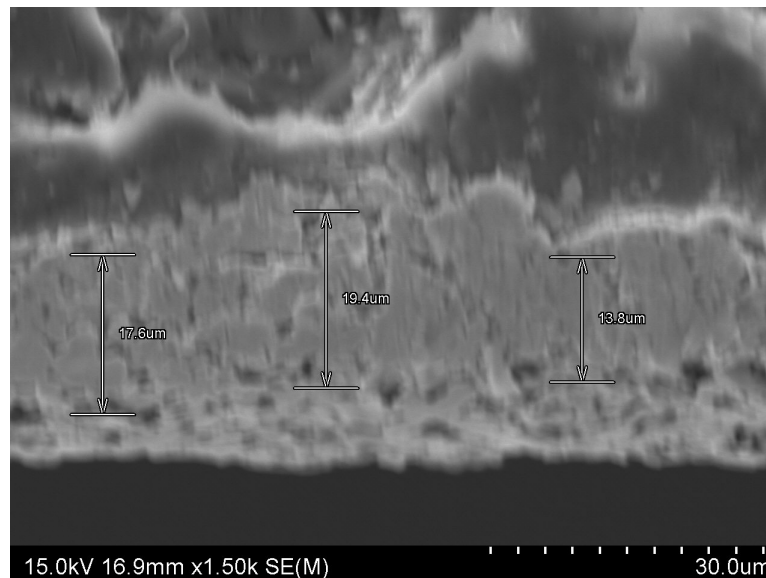


Figure 3.8: Cross-section image of silver ink print trace under SEM.

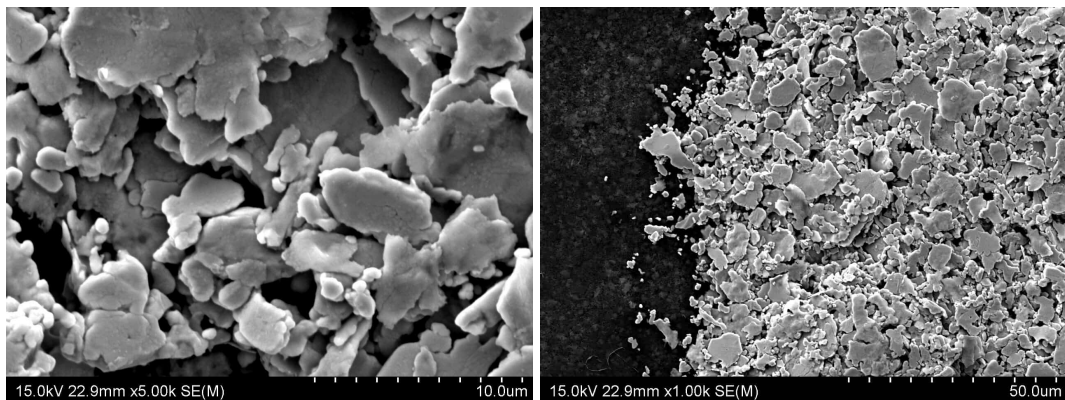
Second step is replicating the antenna pattern on to substrate. The Metalon HPS-021LV

3.6 ANTENNA FABRICATION

conductive ink is applied on the stencil first and then pushed through the stencil onto the substrate with a squeegee. This process is repeated 3 times to guarantee the thickness of printed films. Due to the high viscosity of the silver ink, more than 3 times printing may cause unwanted stickiness and stencil blocking issues.

After printing, the antenna was dried under the heating plate for 5 minutes for initial drying. Then the antenna is sintered in the WEISS WKL34 chamber oven at 180° for 30 minutes to achieve the optimal conductivity without damaging the substrate by over heating.

The printed sample is inspected under the SEM in Auckland University of Technology SEM lab. Both cross-section area and surface of the printed trace are analysed. As shown in Figure 3.8, the image has 1500 times magnification within a working distance of 16.9 mm and under 15 kV voltage. It can be seen that the thickness at three sampling points on the cross-section area are $17.6 \mu\text{m}$, $19.4 \mu\text{m}$, and $13.8 \mu\text{m}$, respectively. This lead to an average thickness of $16.93 \mu\text{m}$.



(a) SEM image of ink surface

(b) SEM image of ink trace edge

Figure 3.9: Printed ink trace surface under SEM.

On the other hand, the images of the ink trace surface are shown in Figure 3.9, visualising the sintered silver particle clusters. Figure 3.9(a) gives an 5000 times magnified view

3.7 MEASUREMENT RESULTS AND DISCUSSION

of the ink surface, where the ink flake clusters all have random size, roughly ranging from $10\ \mu\text{m}$ to $100\ \mu\text{m}$. On the edge of the printed trace, Figure 3.9(b) shows an image of 1000 times magnification. It can be seen that within approximately $80\ \mu\text{m}$, the roughness of the edge is visible and clear.

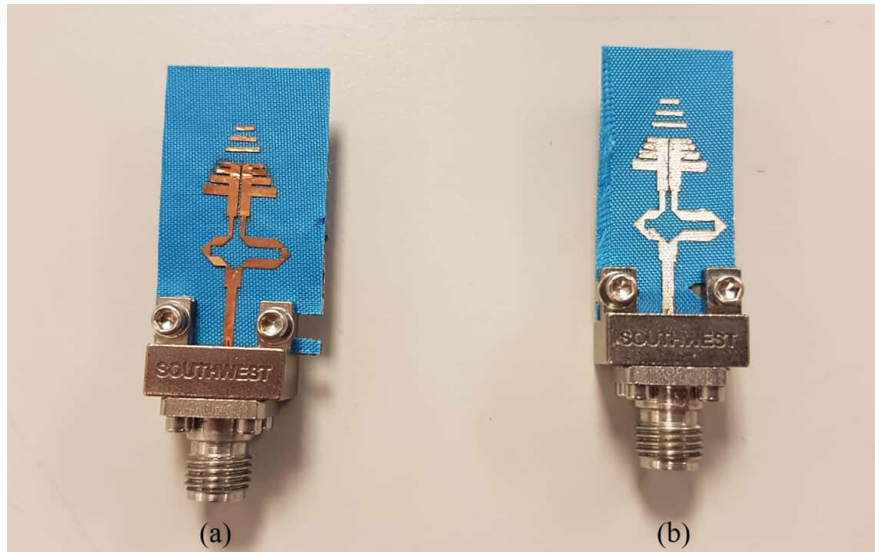


Figure 3.10: Copper laser-cut antenna (a) and silver-ink printed antenna (b).

The fabricated antenna is shown in Figure 3.10 (b), and for comparison, another antenna of the same design is fabricated but its conductive parts are made of copper foil using laser cutting with $50\ \mu\text{m}$ accuracy as shown in Figure 3.10 (a). The copper foil has thickness of $35.56\ \mu\text{m}$ and conductivity of $5.8 \times 10^7\ \text{S/m}$.

3.7 Measurement Results and Discussion

Both the silver ink antenna and the copper foil reference antenna are fabricated, and measured with far field scanning in an anechoic chamber as shown in Figure 3.11. A reference horn antenna is applied as well for antenna gain measurement as shown in Figure 3.12.

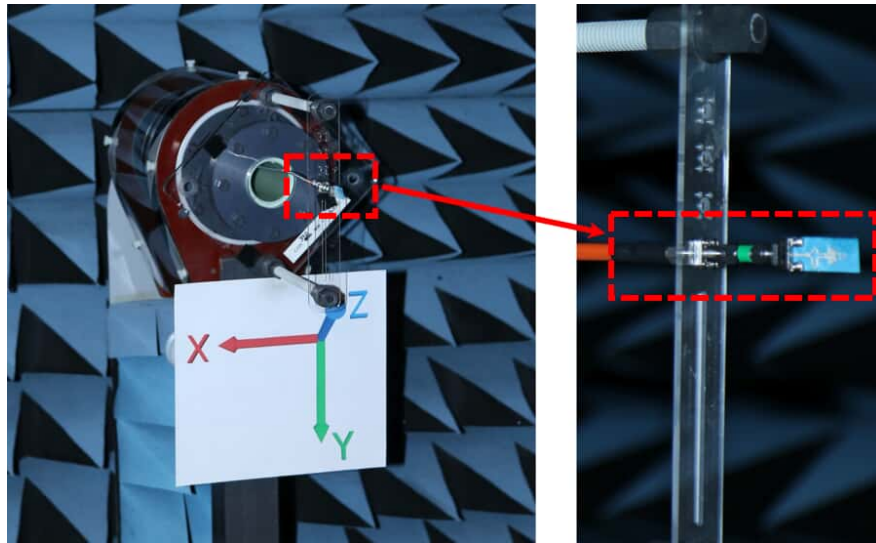


Figure 3.11: The measurement of antenna under test in anechoic chamber.

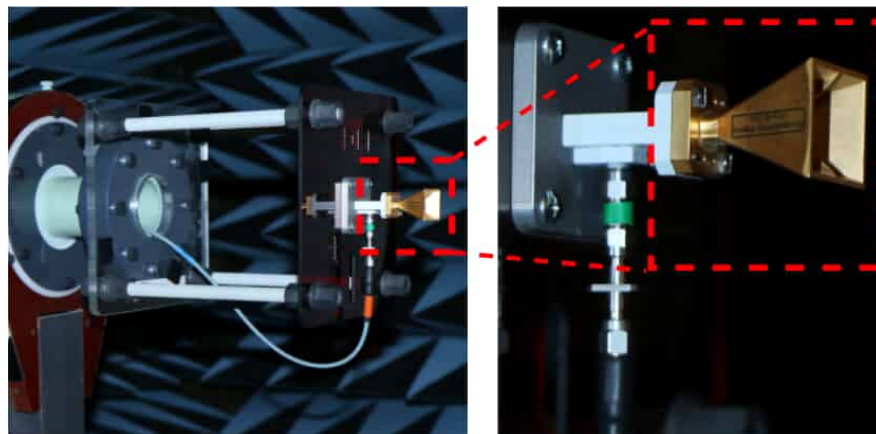


Figure 3.12: Reference horn antenna in the anechoic chamber.

As shown in Figure 3.13, the simulated gains of both antennas are similar, which are above 8 dBi from 23 GHz to 28.5 GHz. However, the copper laser-cutting antenna has roughly 4 dB higher measured gain than the silver-ink printed one, which has a maximum value of 5.5 dB at starting frequency 23 GHz and gracefully decreases over the considered frequency range. The efficiency curves follow the trends of the gain curves, with both efficiency dropping after 28 GHz.

Generally, both antennas have overall 80% efficiency, whilst the copper laser-cutting antenna has 5% higher efficiency than the silver-ink printed antenna. For the return

3.7 MEASUREMENT RESULTS AND DISCUSSION

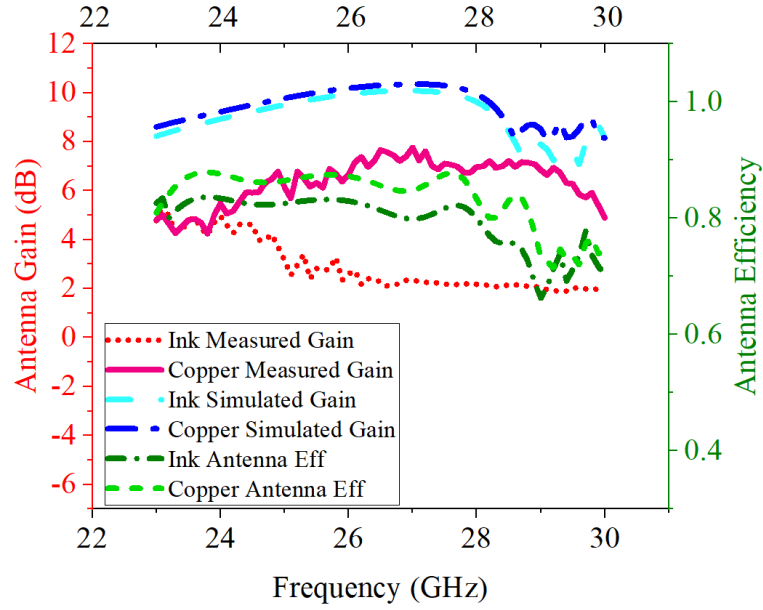


Figure 3.13: The forward gains and efficiency of silver-ink printed and copper laser-cutting antennas.

loss in Figure 3.14, the $|S_{11}| < -10$ dB range of both antennas almost covers the whole desired frequency band of interest, including 24.5 GHz and 28 GHz. The percentage bandwidth (%BW) of the ink-printed antenna is 26.4%, which is defined as a normalised measure of how much frequency variation a system or component can handle and can be calculated by:

$$BW\% = \frac{f_H - f_L}{(f_H + f_L)/2} = 2 * (f_H - f_L) / (f_H + f_L) \quad (3.4)$$

where f_H and f_L are the highest and lowest operating frequencies of the antenna, respectively.

It was noticed that the measured results did not exactly match the simulation results. We considered the following three factors during investigation. First, it is caused by the imperfect fabrication process, i.e. the air gap between the ink (or copper foil) and the the substrate fabric. The dielectric constant of the air, $\epsilon_0 = 1$, is different from that of the substrate, $\epsilon_r = 2.2$. Thus, the propagation of waves travelling in the air and

3.7 MEASUREMENT RESULTS AND DISCUSSION

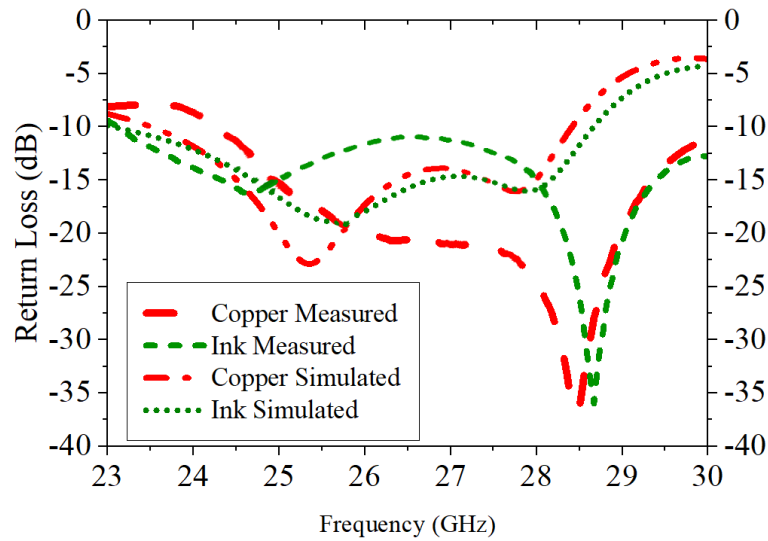


Figure 3.14: The return loss of silver-ink printed and copper laser-cut antennas.

the substrate would be different. Therefore, the equivalent substrate and its effective dielectric constant ϵ_{reff} need to be considered (illustrated in Figure 3.15), which is defined as the dielectric constant of the uniform dielectric material so that the EM waves has identical characteristics travelling in that material. The effective dielectric constant ϵ_{reff} has values in the range of $\epsilon_0 = 1 < \epsilon_{reff} < \epsilon_r = 2.2$ [61].

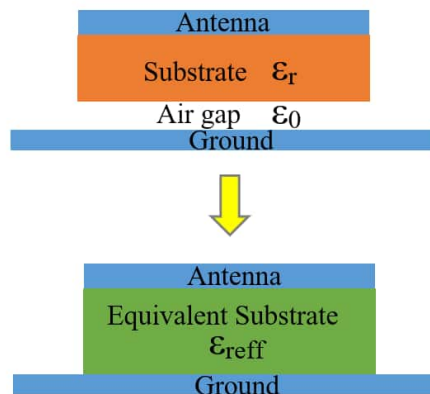


Figure 3.15: Illustration of air gap analysis.

This will explain the influence on the performance of the antenna when there is gap between the printing layer and substrate. Accordingly, we have added a simulation

3.7 MEASUREMENT RESULTS AND DISCUSSION

scenario with air gap between printing layer and substrate to prove the above explanation, where the return loss has significant change as the gap thickness varies from 0.005 mm to 0.025 mm with a step of 0.005 mm (Figure 3.16). For brevity, only the results of the ink antenna are presented. It can be observed that the return loss has noticeable change with different simulated air gap sizes. However, within this hypothetical range, the return loss stays below -10 dB, while the resonant frequencies have shifted. The measurement result stays in the -10 dB region with similar frequency shifting.

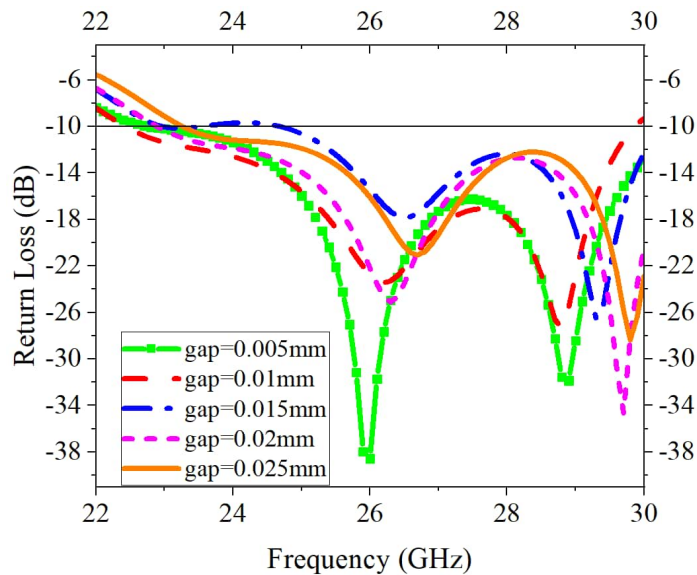


Figure 3.16: Effect of air gap size on return loss.

Secondly, the measurement error in the thickness of the substrate has also been investigated. Flexible polyester fabric has been chosen for the substrate in this design, which was prepared in our lab and of which the thickness was measured with a micrometer screw gauge. Due to the curvature and softness of the material, there would be measurement error of the substrate thickness. Therefore, this error will have a non-negligible influence on an antenna's characteristics and performance [61].

We have conducted another simulation scenario to support our explanations, where the antenna return loss was evaluated at different substrate thickness values, i.e., 0.30 mm,

3.7 MEASUREMENT RESULTS AND DISCUSSION

0.32 mm, 0.34 mm, 0.36 mm, 0.38 mm, and 0.40 mm (Figure 3.17). The return loss was evaluated for these cases, which showed fluctuation in the antenna characteristics and performance. In Figure 3.17, significant variations in return loss can be observed with even minor substrate thickness changes. For the cases of 0.38 mm and 0.40 mm, the resonant frequency of the antenna is beyond the selected range. The measured result lies in an acceptable range regarding resonant frequency and return loss. Thoroughly, the substrate thickness has much more significant effect on the antenna performance than the air gap.

Thirdly, the micro-structure of the silver and non-conductive particles in the ink may cause the lower electrical conductivity. Hence the current flow undergoes resistive loss during conduction across the antenna. Then it contributes to the total radiation loss and gain degradation during the transmission.

The radiation patterns of the silver-ink printed and copper laser-cutting antennas at 24.5 GHz and 28 GHz are illustrated in Figure 3.18 and Figure 3.19 respectively, including both E-plane and H-plane patterns. For the silver-ink printed antenna, the results agreed

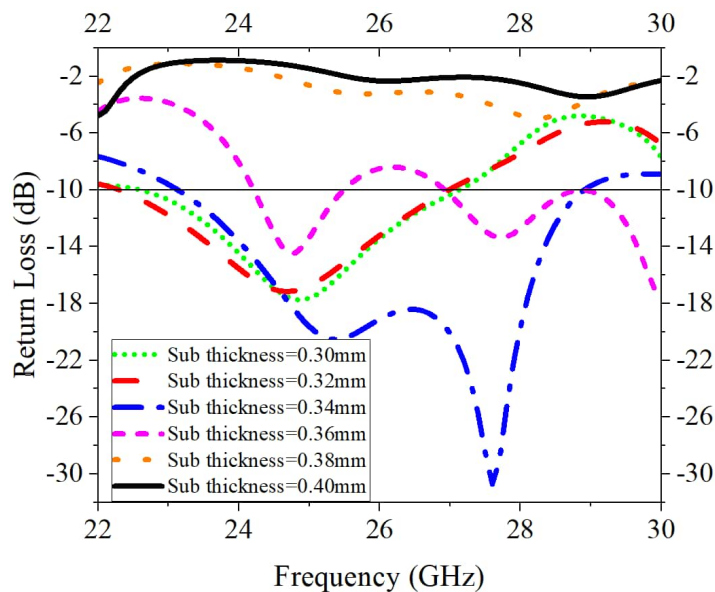


Figure 3.17: Effect of substrate thickness on return loss.

3.7 MEASUREMENT RESULTS AND DISCUSSION

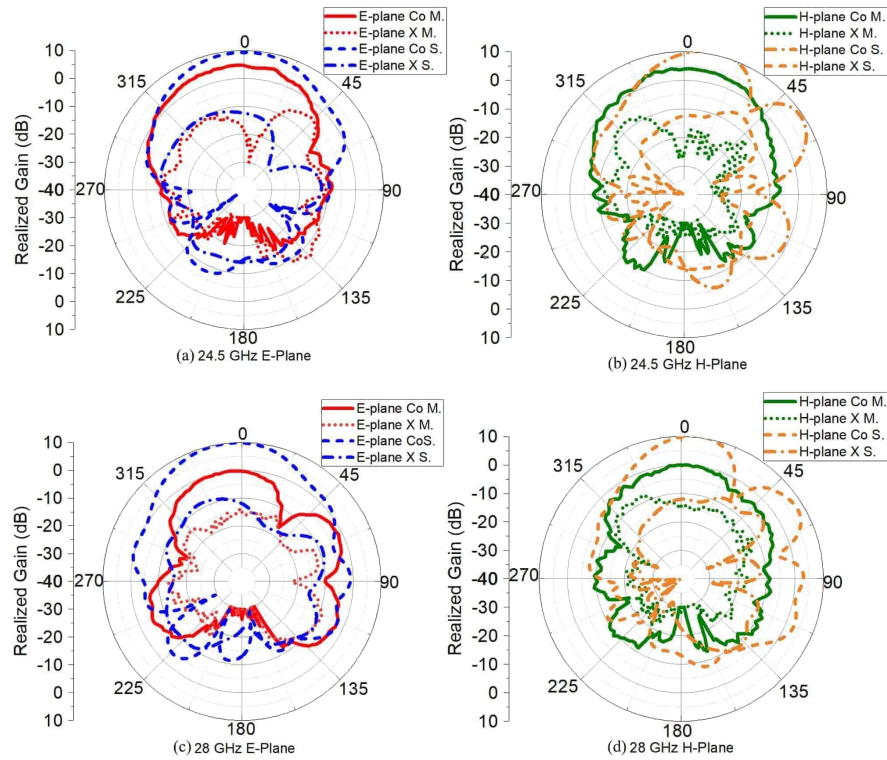


Figure 3.18: Radiation patterns of silver-ink printed antenna: (a) 24.5 GHz E-plane, (b) 24.5 GHz H-plane, (c) 28 GHz E-plane and (d) 28 GHz H-plane (Co: Co-polarization; X: Cross-polarization; M: Measured; S: Simulated).

well with the simulations at 24.5 GHz and resulted in good symmetry and directivity for both E-plane and H-plane. However, for 28 GHz, there are minor discrepancies in the simulated and measured results. This could have incurred due to the housing of the SubMiniature version A (SMA) connector, which has been connected and tightened with screws instead of soldering. The connector itself also extends outside ground boundary and adds additional impedance to the system. Additionally, the cross-polarization radiation patterns in both figures are unexpectedly high, which might be caused by the error of substrate thickness measurement, or the errors in the design of balun. To suppress the cross-polarization, it can be achieved by adding a defected ground structure and redesigning the balun [171, 172].

3.7 MEASUREMENT RESULTS AND DISCUSSION

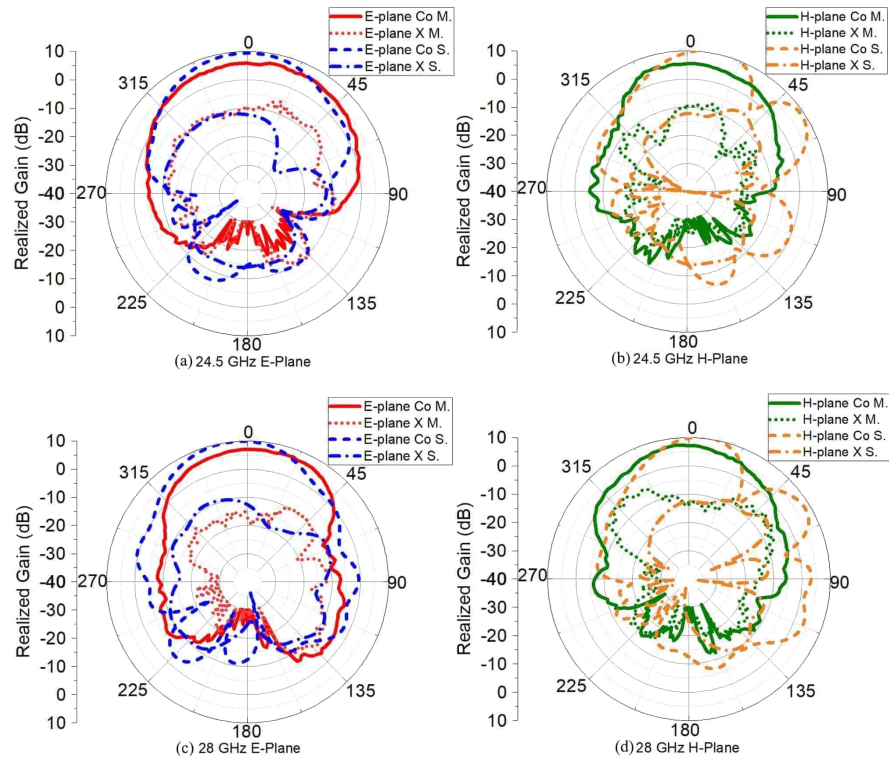


Figure 3.19: Radiation patterns of of copper laser-cutting antenna: (a) 24.5 GHz E-plane, (b) 24.5 GHz H-plane, (c) 28 GHz E-plane and (d) 28 GHz H-plane (Co: Co-polarization; X: Cross-polarization; M: Measured; S: Simulated).

Moreover, the curvature and deformation of the flexible antenna substrate during measurement could also have caused the mismatch of radiation patterns between simulation and measurement. Furthermore, the effects from the air gap and error in substrate thickness measurement also cannot be ignored. It can also be observed that the side lobes are becoming larger, which indicates a decreased directivity of the antenna. The cross-polarization level at both frequencies are not ideally low due to the structure and material property. However, this proposed antenna is designed for wearable electronic devices, where the EM waves propagate from the antenna towards space (away from the wearer). This antenna has a relatively large electrical size (the ratio of the largest length to the wavelength of the EM wave at operating frequency) of 3.02, i.e., the antenna size compared to the wavelength, which means larger numbers of E-field lines radiating from the antenna body, summing up to be viewed as the local maximums, i.e., the

3.8 CONFORMAL TESTS

lobes. However, the antenna is designed to cover a proper large enough area while it's radiating along the main direction. Hence, the side lobes give better coverage and have negligible impact for this application.

Table 3.3: Comparison of Designs in the Literature

Ref.	Fabrication	Size (mm ²)	Elec. Size	Gain (dBi)	RL (dB)	%BW
[91]	Inkjet Printing	18.6×12	2.13	4	12	12.24%
[92]	Inkjet Printing	27.5×13	3.82	6.2	15	19.35%
[130]	Screen Printing	120×120	0.76	0.5	15	4.9%
[111]	Screen Printing	92×25	0.49	-6	20	5%
[158]	PCB	10×19	4.22	9.8	25	31.1%
[156]	PCB	50×18	0.77	2.5	15	11.2%
[157]	PCB	56×48	0.69	N.A.	8	87%
AUT	Screen Printing	25×12.7	3.02	4.2	18	26.4%

The comparison of the proposed antenna with similar antennas reported in the literature was listed in Table 3.3, including fabrication technology, physical size, electrical length, antenna gain and percentage bandwidth. Our proposed antenna has relatively high antenna gain (4.2 dBi) and wider bandwidth (26.4%), which is close to that of the conventional PCB antenna. This shows the outstanding overall performance and potential of the proposed antenna.

3.8 Conformal Tests

To evaluate the antenna performance under conformal circumstances, several conformal bending tests are simulated in HFSS. The ink-printed dipole array antenna is wrapped around a non-model cylinder (non-model means the cylinder is ignored by HFSS and not included in the simulation calculation, it is just for shaping purposes) so that the

3.8 CONFORMAL TESTS

entire antenna bends along the curvature as shown in Figure 3.20. The radius of the cylinder is set as a variable whose value is 20 mm, 50 mm, and 80 mm to represent the level of bending.

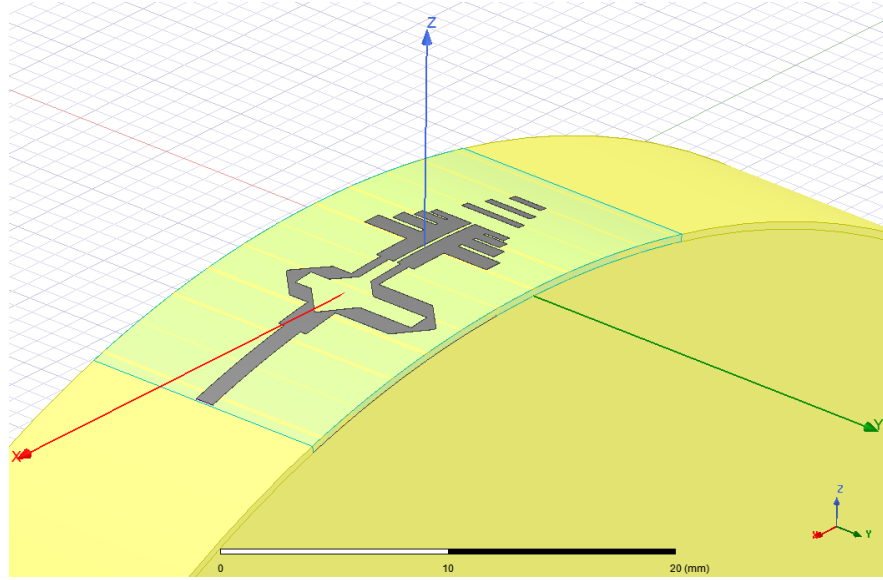


Figure 3.20: Conformal bending tests for the dipole array antenna in HFSS.

As illustrated in Figure 3.21, at different value of radius, the bending angle α of the antenna surface can be approximated as

$$\alpha = \frac{1}{2} \frac{L/2}{2\pi r} 360 \text{ (deg)}. \quad (3.5)$$

Therefore, the bending angles for the three scenarios are 17.91° , 7.17° , 4.48° , respectively. Since the cylinder is set as a non-model, it has no effect on the simulation. Preliminary effects can be observed from the bending, which is the return loss, as illustrated in Figure 3.22. It is obvious that with a bending radius of 20 mm, the $|S_{11}| < -10$ dB area reduced from 22.5-28.5 GHz to 22.5-27.2 GHz, i.e., from 6 GHz to 4.7 GHz bandwidth, or 21.7% decrease in bandwidth. However, an interesting aspect of the graph is that there was a significant resonant frequency at 23.3 GHz roughly, where $|S_{11}|$ is below -30 dB. It might be caused by the sharp bending, where the radiating

3.8 CONFORMAL TESTS

plate formed a curved shell that has parasite capacitance in it. On the other hand, for the case of radius of 50 mm and 80 mm, the bandwidth change is negligible.

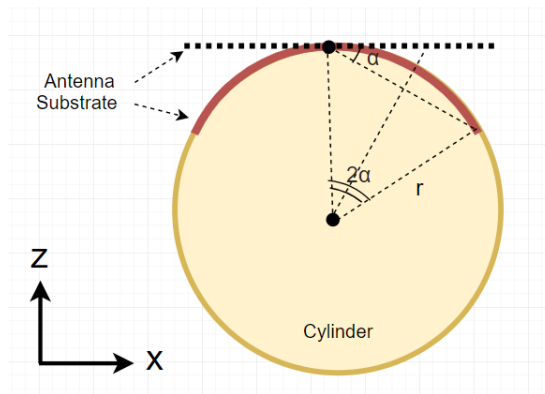


Figure 3.21: Approximation of bending angle.

Figure 3.23(a) illustrates the peak gain of the antenna for these conformal circumstances. It can be seen that over the frequency range from 22 GHz to 26 GHz, the antenna peak gain of these three cases are nearly congruous. However, from 26 GHz to 28 GHz, divergence happens, where the curve of bending radius 80 mm starts declining while the other two keep going up. At 29 GHz, all the three curves reach their minimum point. At one of our frequency of interest, 28 GHz, even though the antenna peak gain is the lowest but still in acceptable range (about 5.2 dB) when bending along the 80 mm radius cylinder.

The antenna radiation efficiency is demonstrated in Figure 3.23(b), which shows agreement over the frequency range for all the three cases. This means that the bending surface has negligible influence on antenna radiation efficiency. From the Chapter 2, we already know that antenna radiation efficiency e_{cd} includes both conduction efficiency e_c and dielectric efficiency e_d . Since both the conductivity and dielectric constant are intrinsic properties of the conductor (ink) and fabric substrate, respectively, the two relevant efficiencies are not affected.

3.8 CONFORMAL TESTS

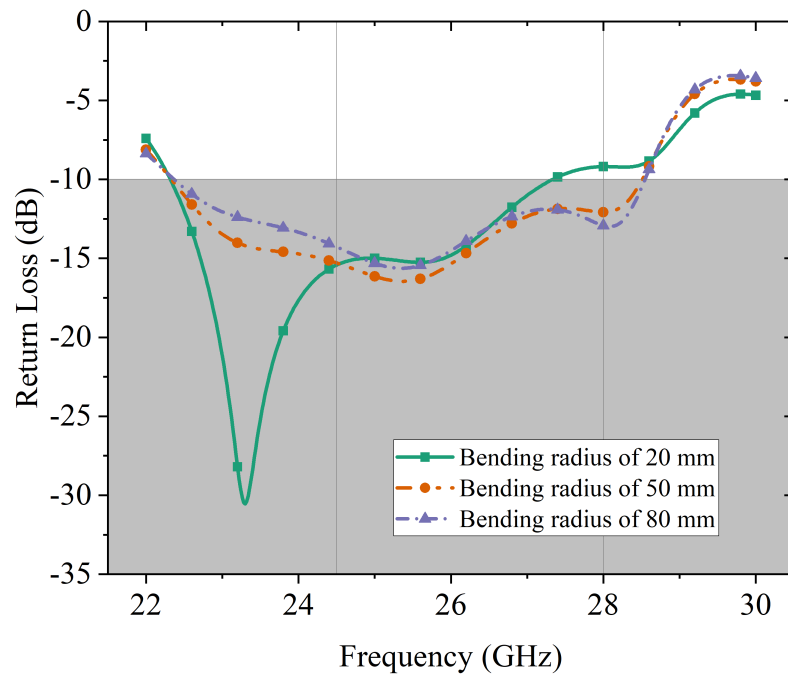


Figure 3.22: Antenna return loss for bending tests.

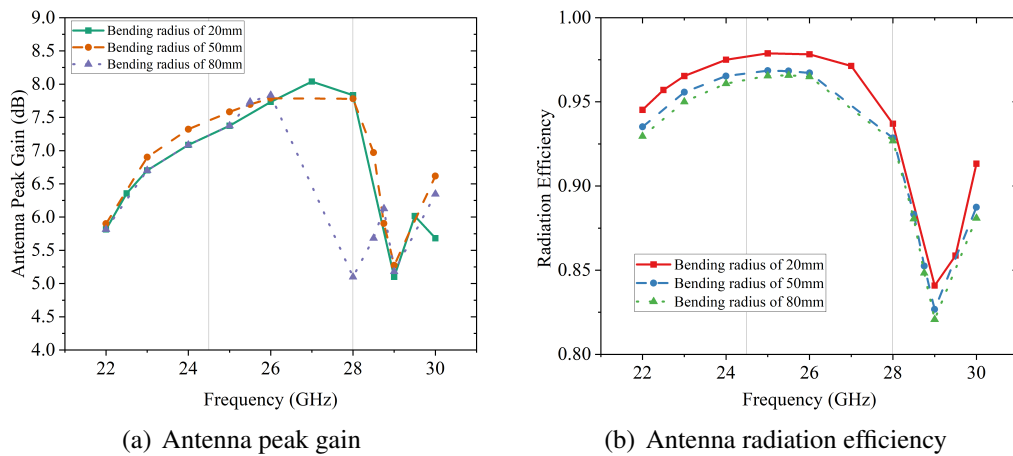


Figure 3.23: Antenna performance for bending tests.

Figure 3.24 compares the principle planes (E-plane and H-plane) of the antenna at two frequencies of interest (24.5 GHz and 28 GHz) for all the three scenarios. From the radiation patterns in Figure 3.24, one can conclude that the radiation patterns for both E-plane and H-plane have no significant deviations between each scenarios. Additionally, the radiation patterns suggest that the antenna is not particularly directional, which is a

3.8 CONFORMAL TESTS

feature of patch antenna. Moreover, the directivity of the antenna remains unchanged during bending tests.

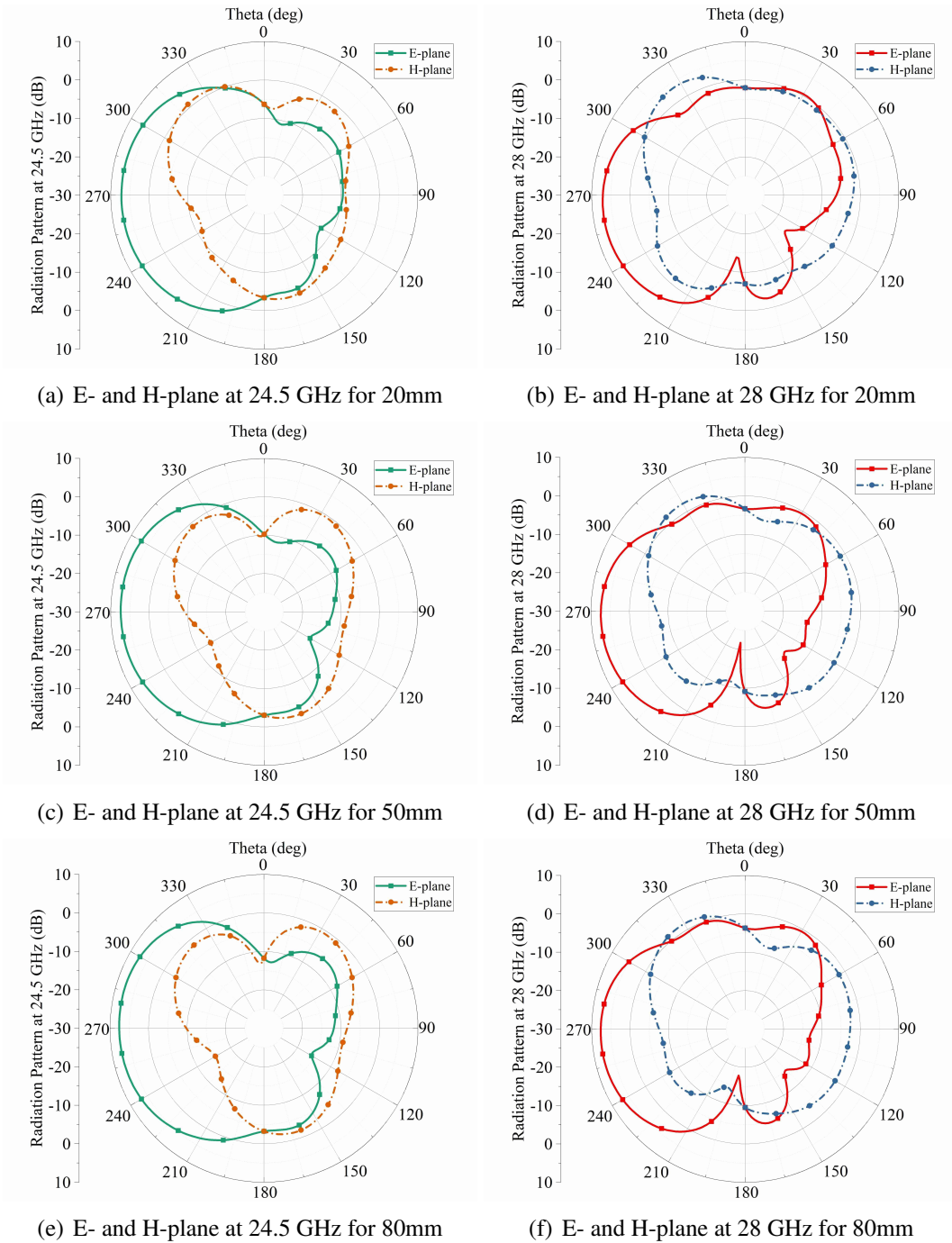


Figure 3.24: E-plane and H-plane for bending tests.

3.8 CONFORMAL TESTS

Table 3.4: Antenna Parameters for Bending Tests

	$r = 20\text{mm}$		$r = 50\text{mm}$		$r = 80\text{mm}$	
f (GHz)	24.5	28	24.5	28	24.5	28
D_{max} (dB)	5.41	6.48	5.76	6.46	6.00	6.74
G_{max} (dB)	5.28	6.07	5.57	6.00	5.78	6.25
P_{rad} (W)	0.95	0.82	0.94	0.87	0.93	0.88
$E_{max} _{\phi}$ (V)	0.00	0.21	-0.03	0.17	-0.03	0.17
$E_{max} _{\theta}$ (V)	4.68	4.57	4.85	4.54	4.92	4.57
E_{max} (V)	17.55	17.90	18.01	18.37	18.26	18.86
U_{max} (W/sr)	0.41	0.42	0.43	0.45	0.44	0.47
e_{cd}	0.98	0.94	0.97	0.93	0.96	0.93

As can be seen from Table 3.4, the main characteristics of the antenna are summarised for all bending tests. It includes maximum directivity D_{max} , maximum antenna gain G_{max} , power radiated P_{rad} (total incident power is set as 1 W), maximum θ component of electric field $E_{max}|_{\theta}$, maximum ϕ component of electric field $E_{max}|_{\phi}$, the maximum of the total electric field E_{max} , maximum radiation intensity U_{max} , and radiation efficiency e_{cd} . The optimal results are highlighted in green, while the minimum values are coloured red instead.

It is clear that as the bending angle increases, these critical parameters also decrease. Half of the optimal parameters appear in the case of minimum bending angle, that is, a bending radius of 80 mm. This means that bending surfaces have relatively noticeable influences on the key antenna parameters and performance. Interestingly, at the largest bending angle and 24.5 GHz, the antenna still has the maximum radiated power and radiation efficiency. The possible reason for this might be that the bending curvature of the conductor patch and ground plane forms a curved open loop, which is equivalent to a passive inductance or capacitance and has an impact on the impedance of the antenna so that the conduction efficiency is altered. This might be the same reason for the frequency shift in earlier observations too.

3.9 Chapter Summary

This chapter presented a dipole array antenna for wideband 5G applications, which is screen-printed on a flexible textile substrate with silver particle-based conductive inks. Despite the minor disagreement between measurement and simulation results caused by fabrication process and other potential reasons, the proposed antenna demonstrates promising performance with an ultra-wide bandwidth and high gain. Furthermore, the simulation of the conformal tests suggests that the proposed antenna has a strong resilience to the bending effect when the bending angle is less than 17.91° . As the bending angle increases further, the performance of the antenna will predictably deteriorate. Apart from the simulation, measurements for the bending tests are planned for the future work. The prototype fabricated can be worn by a person and measured in the anechoic chamber.

Chapter 4

A Flexible Slot Antenna for Conformal and Wearable Applications

As was discussed in Chapter 3, in order to achieve applications for conformal applications, it is important for the antenna to have a planar structure, like the microstrip patch antenna, the dipole array antenna, and the slot antennas.

In this chapter, slot antennas are explored for conformal situation and further potential wearable applications for human body. Two planar slot antenna designs on a flexible structure are presented, which are a single band microstrip slot antenna with parallel slits loading and a triband multiple-slot microstrip patch antenna. Both slot antennas are proposed and evaluated, and their potentials for conformal structure and wearable applications are also verified by HFSS simulations.

4.1 Slot Antennas

Slot antennas generally refers to those antennas with slots in the main body [173]. A slot antenna normally consists of a metal surface, a flat or curvature plate, which has one or more slots cut out [174, 175]. The metal plate is driven by a time-varying current

to excite electromagnetic waves radiation from the slots, which operates similarly in the way that a dipole antenna does. The radiation pattern of a slot antenna is determined by the shape and the size of the slot at different frequencies [24, 176, 177]. In the UHF and microwave frequency range, a waveguide can be used as radio waves carrier. Thus, waveguide with slots on it, often referred to as slotted waveguide antenna, is also a common antenna type. With the development of printing technology and compact electronic devices, slot antennas in planar structure are attracting increasing amount of attention.

4.1.1 Common Slot Antenna Designs

As the dominant part of a microstrip slot antenna, the slot can be adjusted and tuned to manipulate the antenna characteristics and performance for miscellaneous applications. Since many antenna designs are based on 3D structure, like a cavity, a horn shape, a spiral shape, and a waveguide, cutting slots on a cavity or waveguide structure is one common method to produce a slot antenna, like the slotted spherical antenna presented in [178]. The antenna was 3D-printed on a air-filled high-quality-factor spherical resonator with slots cut on the shell. The antenna has two operating frequency bands, 9.88-10.68 GHz, and 13.05-15.05 GHz, respectively. The antenna is fed by a rectangular waveguide at the bottom of the sphere. This spherical slotted antenna applied 3D printing technique for easy fabrication and the antenna achieved good performance with <-20 dB return loss and >6 dBi gain.

In [179], a circularly polarized SIW slot antenna was reported using a high-order dual-mode cavity. As shown in Figure 4.2, the antenna has three layers connected by via holes and shorting pins, yielding a two-mode cavity. The slots on the top layer were etched to guide current flow so that a circular polarization can be obtained. The antenna achieved good return loss of -17 dB and 500 MHz bandwidth at 12.3 GHz. The axial

4.1 SLOT ANTENNAS

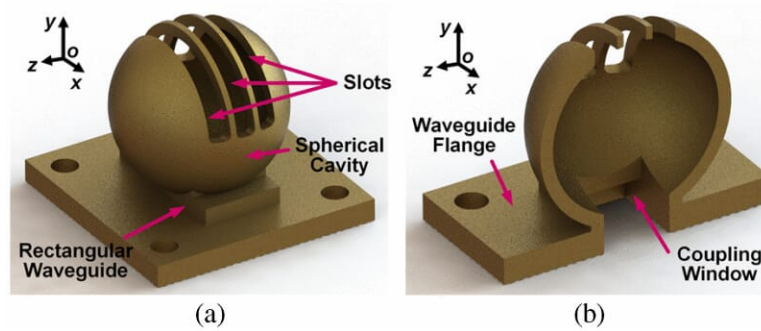


Figure 4.1: Structure of the slotted spherical antenna (a) entire view, (b) half-profile view [178] Copyright © 2020 IEEE.

ratio was below 3 at 12.3 GHz for circular polarization.

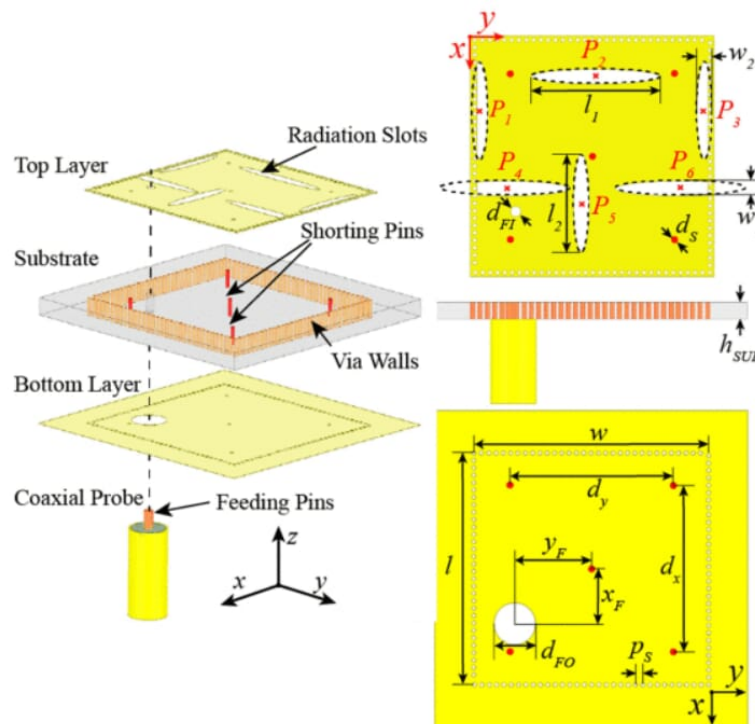


Figure 4.2: Illustration of the SIW slot antenna [179] Copyright © 2020 IEEE.

Similarly, two cavity-backed slot antennas were presented in [180] and [181], respectively, which applied printed gap waveguide technique for a compact design. Apart from the main slot in the middle layer, another 2×2 radiating slot array were etched on the top layer in [180] as shown in Figure 4.3. The antenna bandwidth increased from 110

4.1 SLOT ANTENNAS

MHz to 400 MHz at 15.6 GHz and side lobe level was reduced to -12.34 dB and -13.84 dB for H-plane and E-plane, respectively. The measured gain was 12 dBi.

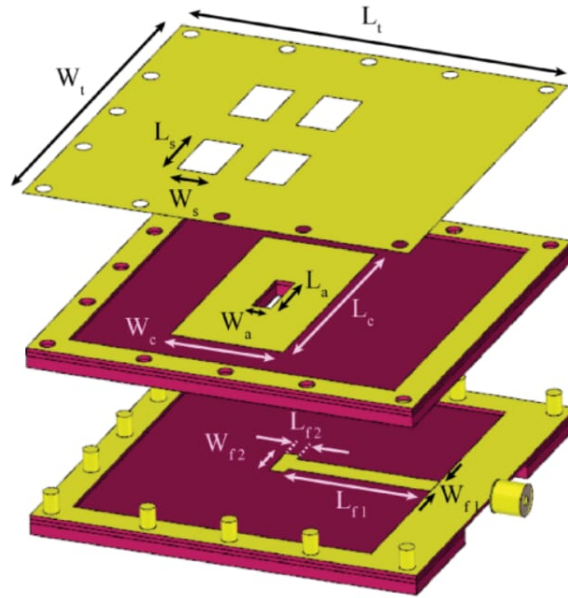


Figure 4.3: Band-gap slot antenna with 2×2 slot array [180] Copyright © 2020 IEEE.

For the design in [181], two centrosymmetrical spiral slots were etched on the top layer as radiating slots. With the printed gap waveguide structure, the antenna operates at millimetre wave range from 34.45 GHz to 40.21 GHz with a 23.42% 3 dB axial ratio. The antenna also has a 3 dB gain bandwidth of 23.69% from 33.97 GHz to 43.1 GHz and 20.33% from 34.25 GHz to 42 GHz.

However, the bulky 3D structure in [178] is difficult to be integrated with other structures with limited space; the multi-layer cavities and rigid substrate and conductors in [179–181] make it impractical to be fit on flexible surfaces, let alone its possible printing fabrication and application in wearable devices. To adapt for compact applications, a planar structure with either microstrip line feed or CPW feed is an efficient approach for slot antenna designs, which was presented in [182, 183] and [177, 184], respectively. The two CPW-fed antennas presented in [177, 184] both attained dual bands in the

4.1 SLOT ANTENNAS

frequency range of 2-5 GHz, while the two microstrip line fed antennas in [182, 183] were designed as wideband antennas, by combining the slots in ground and radiating patch structures. In addition, open slot technique was applied in both CPW-fed antenna designs to achieve larger bandwidth.

Despite of the advantage of the aforementioned planar structures, they are still restrained by the material flexibility of the rigid printed circuit boards, making it hard to be applied for conformal and wearable applications. In [90, 185], the researchers proposed slot antenna designs for on-body applications.

In [185], a 15×40 mm² slot antenna fabricated on FR4 substrate was proposed for wearable wireless local area network (WLAN) application. The antenna was simulated in an idealised human body tissue model and demonstrated good performance. However, the antenna is based on ordinary PCB material and not flexible, which may not be suitable for extended applications.

A dual-band bow-tie slot antenna employed printing technique and flexible leather shoes for mine-detecting application in [90]. Conformal bending tests were conducted based on the shoe shape and the deviations before and after bending was given. However, further testing was not discussed, such as effect of human body tissue and the amount of radiation energy that will be absorbed by human body and shoes.

In summary, there are various designs of slot antennas for miscellaneous applications, and several techniques can be used to enhance their performance. To achieve flexible structure and wearable application, a planar slot antenna with compact conformal materials is necessary. This motivates us to study a microstrip slot antenna, which is derived from microstrip line. In the next section, microstrip slot antennas are revisited, followed by our proposed antenna design for flexible wearable application.

4.1.2 Microstrip Slot Antennas

A microstrip slot antenna is a slot antenna excited by a strip line [24]. Microstrip slot antennas have numerous promising features, such as planar feeding structure, wide operating band, high isolation, etc. Microstrip slot antennas have a significant advantage of being able to produce bidirectional and unidirectional radiation patterns with large bandwidth [174, 176, 177, 185–188], which is of our interest to study it in this chapter.

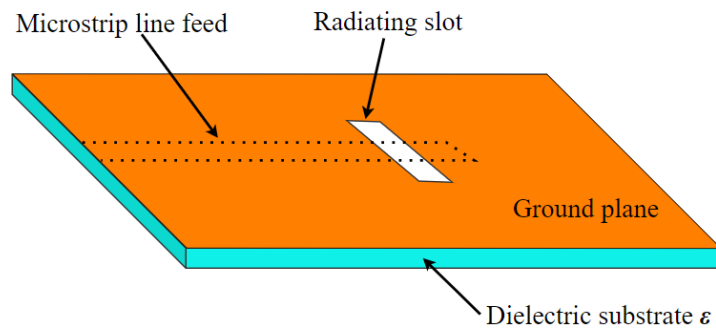


Figure 4.4: Basic structure of a microstrip slot antenna.

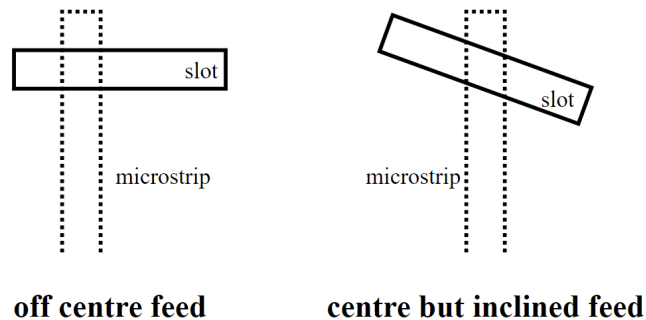
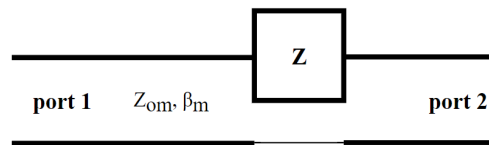


Figure 4.5: Feeding techniques to reduce antenna input impedances.

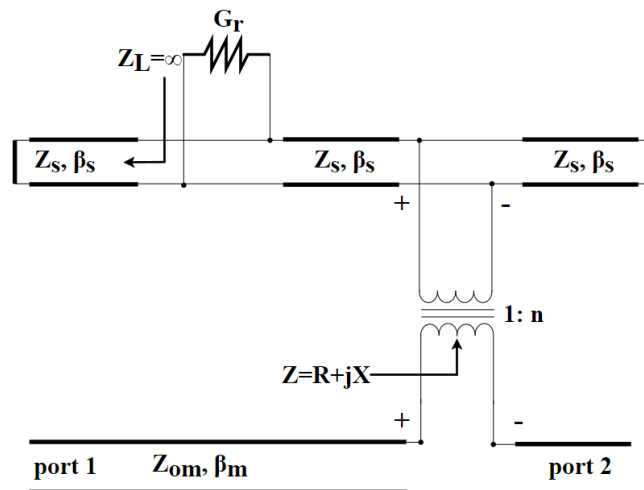
Since microstrip slot antennas evolve from slot antennas and microstrip line, their low profile feature makes them applicable in scenarios where there is limited antenna installation space and complex integration with other systems. Moreover, the planar structure yields great potentials for flexible structure, printed electronics and wearable applications.

4.1 SLOT ANTENNAS

As shown in Figure 4.4, a microstrip slot antenna comprises a slot cut in the ground plane of the microstrip line. Normally, the slot is perpendicular to the strip of the microstrip line. Two common feeding techniques to reduce the antenna input impedance are illustrated in Figure 4.5, namely off-centre feed and inclined feed (centred), respectively [24].



(a) Equivalent circuit of microstrip slot antenna.



(b) Equivalent network model for microstrip slot antenna.

Figure 4.6: Equivalent circuit and network model of microstrip slot antenna [24].

The microstrip slot antenna can be viewed as a microstrip line discontinuity and represented by an equivalent circuit [24, 175, 189] as illustrated in Figure 4.6. The slot antenna can be modelled as a series load impedance Z in the microstrip line as shown in Figure 4.6(a). For further analysis, the equivalent network model in Figure 4.6(b) presents the details. It consists of an ideal transformer, a radiation conductance, and a slot line with short circuits at two terminals. The slot is equivalent to two parallel

connected sections of slot line, which has characteristic impedance Z_S and phase constant β_S . The radiation conductance G_r accounts for the radiation power from the slot. Additionally, the ideal transformer represents the coupling between the slot and the microstrip line.

Based on the aforementioned critical features and analytical methods, a slot antenna with parallel slits loading and a slot microstrip patch antenna are proposed for flexible surface and wearable applications in Section 4.2 of this thesis.

4.2 Slot Antenna Design for Conformal Applications

To fully achieve compact and flexible planar structure for the potential conformal and wearable applications, a microstrip slot antenna and a microstrip patch slot antenna are proposed in the following section. The first design is a microstrip slot antenna with parallel slits loading at 5.8 GHz, which has flexible structure and can be applied for Wireless Local Area Network (WLAN) and industrial and medical application from IMS bands; the second one is a microstrip patch based triband slot antenna operating at 5.8 GHz, 6.2 GHz and 8.4 GHz, respectively, which can be applied for WLAN, C band and X band satellite navigation and communication. Both antennas are proposed with flexible PCB for fabrication.

4.2.1 A Slot Antenna with Parallel Slits Loading

4.2.1.1 Background

With the rapid deployment of 5G cellular networks, wireless applications like IoT [9] and Intelligent Transportation System (ITS) [190, 191] become popular. The demand for conformal surface circumstances and wearable devices is also increasing phenomenally.

4.2 SLOT ANTENNA DESIGN FOR CONFORMAL APPLICATIONS

For these applications, slot patch antennas are desired due to their simplicity for integration with planar structures and their good tolerance for manufacturing discrepancies [192–194].

A common antenna design techniques is to add extra slits in order to enhance slot antennas' performance. Different methods were studied to apply slit structure to slot antennas. In [192], L-shaped slits were added to a hexagonal slot antenna to achieve triple operating frequency bands, i.e., 3.4 GHz, 3.8 GHz, and 4.2 GHz. However, the performance at the first band (3.4 GHz) was not as good as the other two bands due to the complexity of the antenna structure. Meandering, straight, and loop slits were applied in [193–195], for resonant frequency reduction, up to 41.54%, shifting from 2 GHz to 1.21 GHz, but the proposed slit structures were complex and did not have high manufacturing tolerance.

In [196], V-shaped slits were applied to a pentagonal mono-pole patch antenna for gain enhancement and impedance matching, though the frequency range of the antenna was very sensitive to the slit parameters, making performance tuning quite difficult. A parallel slit microstrip line model was investigated and applied to a tripolarized antenna design in [197], which effectively improved on current distribution along the strip line and mutual coupling suppression. However, the tripolarized antenna takes a relatively large space, making it not suitable for application in limited space and with flexible surfaces.

Through a careful review of the literature, we noticed that there are few works focussing on slot antennas on conformal surface and wearable applications. Hence, we propose a flexible slot antenna design. On the basis of the traditional slot antenna structure, a paralleled slit loading is added to the slot antenna for performance enhancement. Additionally, the proposed fabrication method is flexible PCB, which is suitable for conformal circumstances. The antenna operates at 5.8 GHz, which can potentially be

used for flexible integration surface and wearable devices for WLAN and IMS band applications. The antenna has a microstrip line feed and paralleled slit structure in the slotted ground plane. A prototype was fabricated for initial measurements and conformal mounting surface and integration with human body wearable application have been scrutinised via HFSS simulation.

4.2.1.2 Antenna Design and Parametric Study

The proposed slot antenna operates at 5.8 GHz, which adopts a parallel slit-loading on the edges of the ground plane. The antenna consists of three layers, i.e., slotted ground plane, dielectric layer, and tapered microstrip line feed. Based on the designing principle of slot antenna, a half-wavelength slot is opened at the center of the ground plane. The slot size is determined by the guided wavelength λ_g , which is related to the effective dielectric constant of the substrate ϵ_{reff} , as shown in (4.1) and (4.2) [24, 61]

$$\lambda_g = \frac{\lambda}{\sqrt{\epsilon_{reff}}}, \quad (4.1)$$

$$\epsilon_{reff} = \frac{\epsilon_r + 1}{2} + \frac{\epsilon_r - 1}{2} \left[1 + 12 \frac{h}{w} \right]^{-1/2}, \quad (4.2)$$

where h and w are the thickness and width of the substrate, respectively, while ϵ_r is the dielectric constant of the substrate. In this design, a thin and flexible Rogers RT5880 dielectric layer (dielectric constant $\epsilon_r = 2.2$, thickness $h = 0.787$ mm) is applied. The antenna is fed by an off-center tapered 50- Ω microstrip line feed on the other side through coupling through the main slot.

A parallel slit structure is applied along the main slot to improve performance. Parametric sweeps about the slit width W_{slit} and length L_{slit} is conducted to finalise the slit dimension. In Figure 4.7(a) and 4.7(b), it can be seen that the slit length L_{slit} has

4.2 SLOT ANTENNA DESIGN FOR CONFORMAL APPLICATIONS

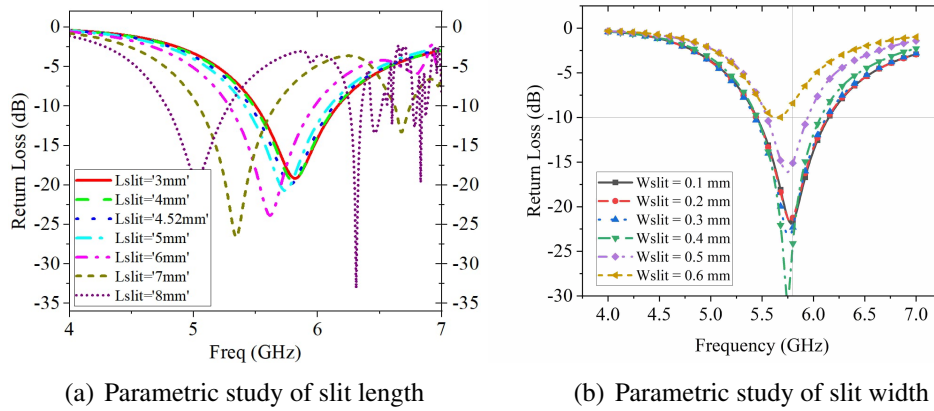


Figure 4.7: Parametric study of the size of the slit.

more influence on the antenna resonant frequency shift whereas the slit width W_{slit} only affects the return loss value.

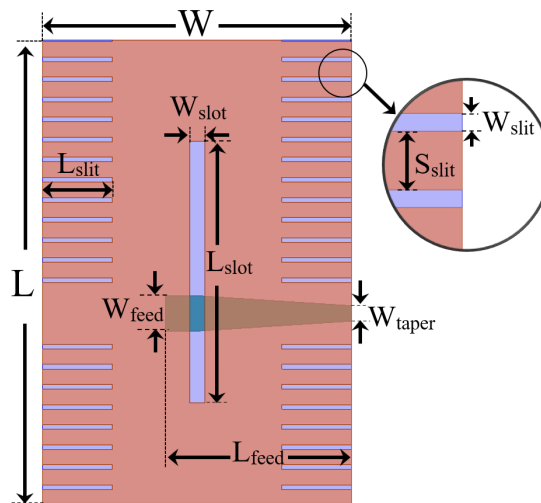


Figure 4.8: Slit slot antenna layout and dimensions.

After optimisation, the slit is finalised with values of $L_{slit} = 4.52$ mm and $W_{slit} = 0.3$ mm. Therefore, the antenna dimension can be determined as indicated in Figure 4.8. The values of the dimensional parameters are: $L = 30$ mm, $W = 20$ mm, $L_{slot} = 16.943$ mm, $W_{slot} = 0.999$ mm, $L_{feed} = 12.07$ mm, $W_{feed} = 2.294$ mm, $W_{taper} = 1$ mm, $L_{slit} = 4.52$ mm, $W_{slit} = 0.3$ mm, $S_{slit} = 1$ mm.

4.2.1.3 Experimental Measurements

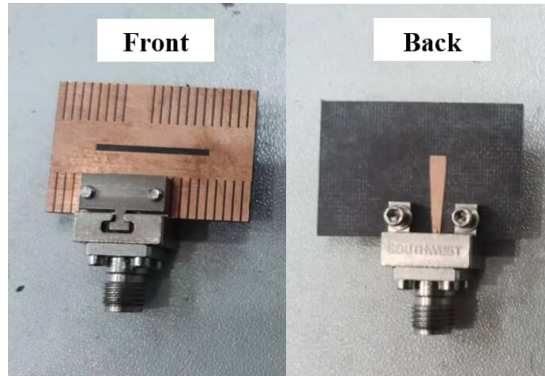


Figure 4.9: Front and back side of fabricated antenna.

Antenna prototypes were fabricated on Rogers RT5880 flexible PCB for initial measurements in an anechoic chamber. In Figure 4.10(a), the return loss of the antenna is shown between 4 GHz and 7 GHz, which indicates the resonant frequency of 5.8 GHz. Additionally, the measured -10 dB bandwidth of the proposed antenna is 450 MHz. The gain of the antenna around its operating frequency is illustrated in Figure 4.10(b), which ranges from 5.75 GHz to 5.85 GHz. Both simulation and measurement show that the antenna has an approximate overall efficiency of 80%.

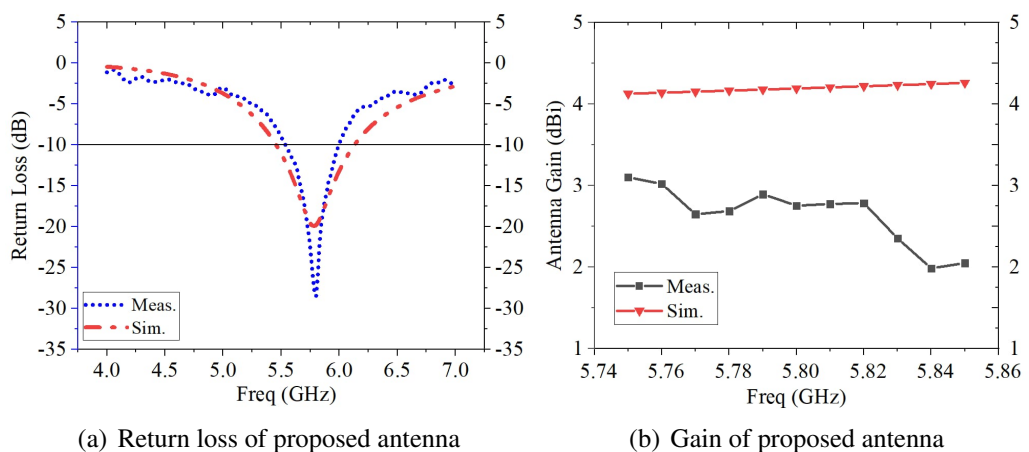


Figure 4.10: Simulated and measured results of the antenna.

The antenna gain has a decreasing trend over the frequency range, with a value of 2.75

dB_i at 5.8 GHz. The reason that measured gain is slightly lower than the simulation could be the power dissipation happened at the connector. E-plane and H-plane radiation patterns of the antenna are presented in Figure 4.11(a) and Figure 4.11(b), respectively, where the measured results match the simulated ones. The X-polarization radiation patterns of both E-plane and H-plane are below -30 dB. The discrepancy between the measured and simulated radiation patterns might be caused by the screw hole on the antenna for the RF connector, which has an equivalent parasite capacitance to the antenna. This needs further verification through simulations. The symmetry in the Co-polarization polarization patterns also validates the symmetrical structure of the antenna.

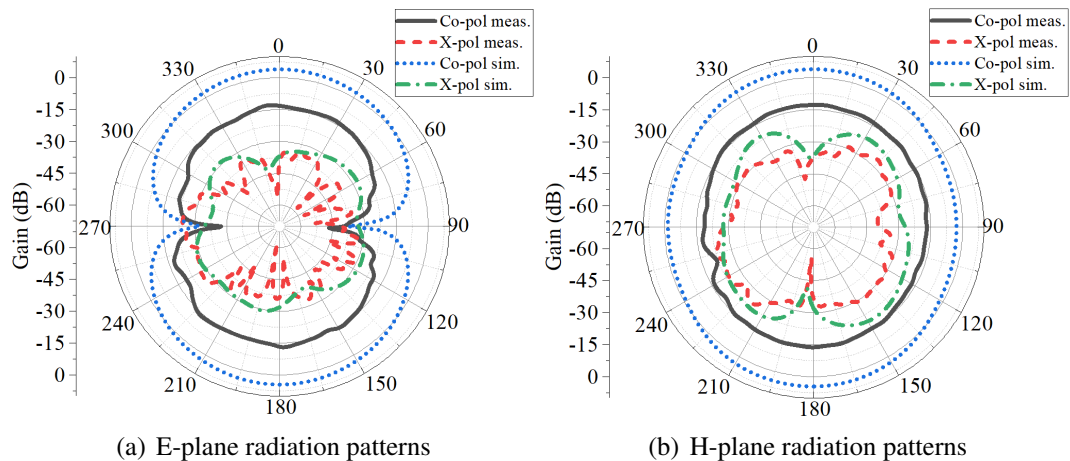


Figure 4.11: Principle planes radiation patterns at 5.8 GHz.

4.2.1.4 Conformal Application Test

In order to apply this antenna design for conformal circumstances, a series of conformal bending tests are conducted via HFSS simulation. The entire antenna structure is wrapped around a cylinder, which is placed right below the antenna and has an varying radius from 20 to 100 mm to denote the level of bending. The corresponding bending angles are 21.5° , 10.7° , 7.1° , 5.3° , and 4.3° , respectively. Note that the cylinder is set

4.2 SLOT ANTENNA DESIGN FOR CONFORMAL APPLICATIONS

as a non-model in HFSS so that it would not be included for simulation and have no effects on the results. The bending model is illustrated in Figure 4.12.

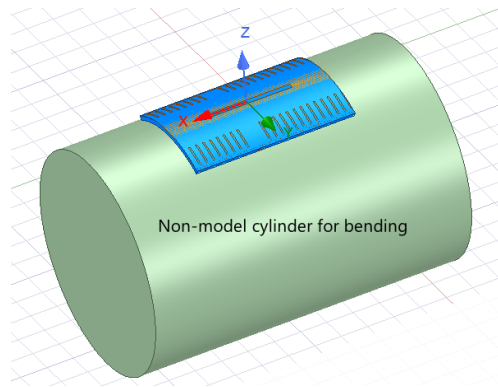


Figure 4.12: Antenna wrapped onto a cylinder for conformal surface test.

Figure 4.13(a) presents the results obtained from the preliminary effects on resonant frequency from curvature surface. It can be noted that the antenna resonant frequency fluctuates slightly near the original 5.8 GHz, although with noticeable return loss value change. However, a significant resonant frequency shift is only observed when cylinder radius is 60 mm.

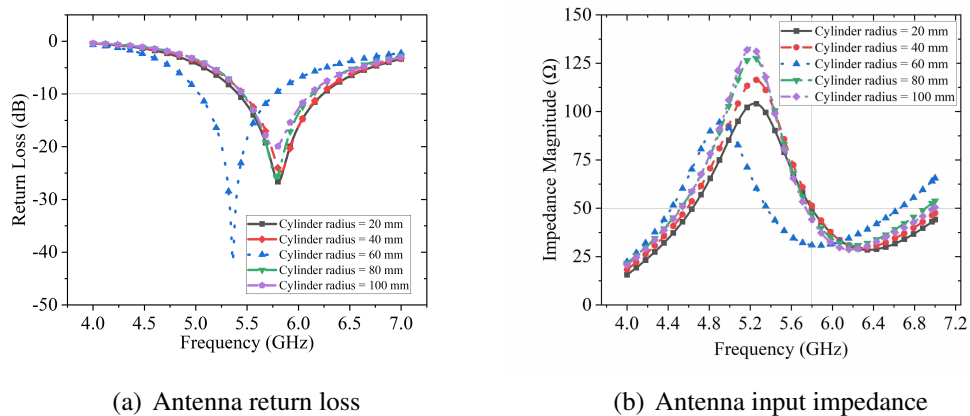


Figure 4.13: Antenna return loss and input impedance with different bending tests.

The aforementioned frequency shift agrees with the antenna impedance mismatch illustrated in Figure 4.13(b), where the antenna input impedance at 5.8 GHz has fallen

4.2 SLOT ANTENNA DESIGN FOR CONFORMAL APPLICATIONS

to 30Ω for cylinder radius equals to 60 mm, while for the rest cases, it remains approximately 50Ω . This might be caused by the parasite capacitance formed by the bending conductive surfaces at 60 mm radius. Its return loss at resonant frequency of 5.36 GHz is -41.88 dB and this might be caused by resonance enhancement from the symmetrically bending part of the antenna long sides.

Figure 4.14(a) and 4.14(b) show the corresponding principle E-plane and H-plane radiation patterns at different level of bending. An overall shrinking of the radiation patterns can be observed in both E-plane and H-plane patterns, which indicates that the radiation performance is decreasing as the bending level increases, i.e., the cylinder radius decreases.

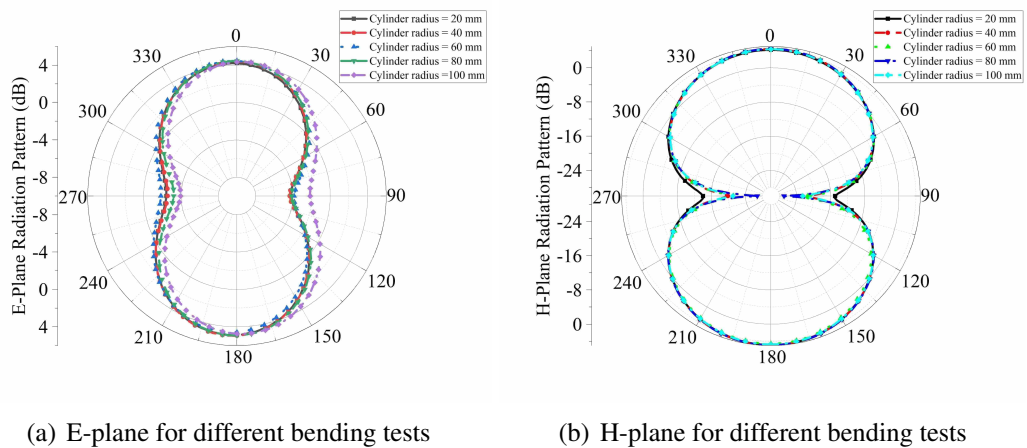


Figure 4.14: Radiation patterns for different bending tests.

In Figure 4.15, we can see that the antenna peak gains exhibit slight deviation over the frequency bands from 4 GHz to 7 GHz. Noteworthy, the peak gain curve of cylinder radius = 60 mm is relatively flat from 5 GHz, and it has a lower magnitude at the high frequency band near 6-7 GHz. This corresponds to the frequency shift in previous result of return loss in Figure 4.13(a). The other curves almost have the same trends with minor deviations in overall values. When the cylinder radius are 40 mm and 80 mm,

the antenna has largest overall peak gains.

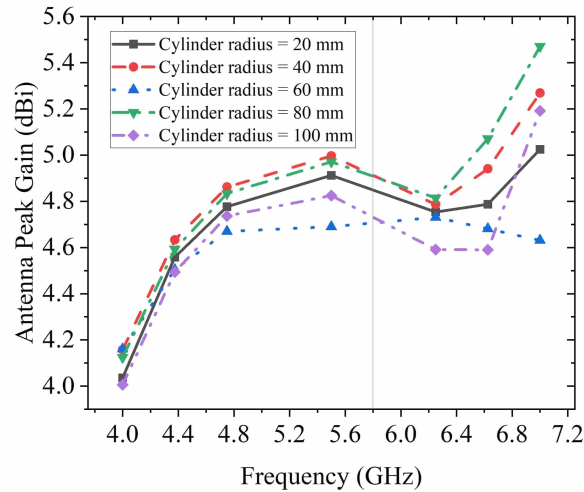


Figure 4.15: Antenna Peak Gain for different bending tests

Antenna front to back ratios have been illustrated in Figure 4.16. For most of the cases, the front to back ratio is around 1 dB, i.e., the front and back lobe power radiation are at the same level. What stands out in the diagram is the case of cylinder radius of 80 mm, where it reaches 2.8 dB at 6.9 GHz, which means the front lobe is lots larger than the back one.

The simulation results from bending tests are rather promising and encouraging for conformal applications. It can be clearly seen that bending surfaces have noticeable influences on the antenna characteristics and radiation performances, and more complicated curved surfaces need to be scrutinised. Nevertheless, the deviations and disagreements are in acceptable range and does not affect the antenna's functionality at desired frequency bands, surprisingly some of them are even improved.

Despite of the findings above, there is abundant room for further progress in scrutinising potential conformal applications on human body for wearable circumstances. Hence, in the next section, the condition is applied with the cylinder radius set as 80 mm and

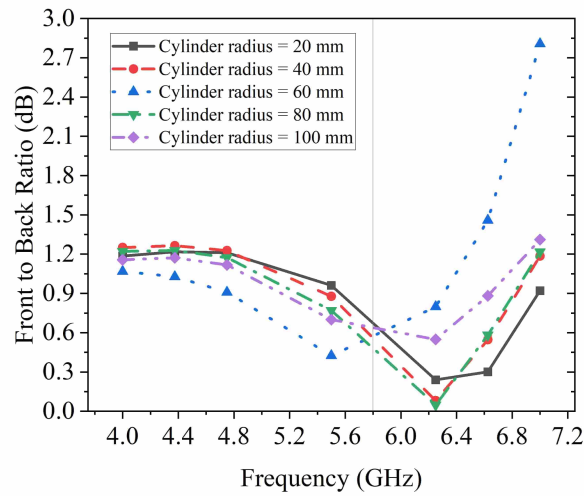


Figure 4.16: Antenna front to back ratio for different bending tests

further exploration will be conducted through a new antenna system integrated with human body parts. Simulations results and analysis are provided for different scenarios to cover potential practical applications.

4.2.1.5 Simulation for Wearable Applications

As the rapid development of IoT and wearable devices, antennas for wearable applications have drawn great attentions. To investigate how the proposed antenna can interact with human body for wearable applications, several simulations are conducted, where a male human left hand model placed under the proposed antenna at various contact distances. Then the antenna performance is evaluated and discussed in this section. Due to the limitation of measurements and humanity and ethic considerations, experiments upon real human body are considered as future work. The male human left hand model is pre-built in HFSS with default parameters, which are average data derived from empirical database. Additionally, the mesh size is also adjusted according to the wavelength of the operating frequency to optimise the simulation time. Hence, the results only represent reference and deviations are expected from practical results

due to alteration in different individuals.

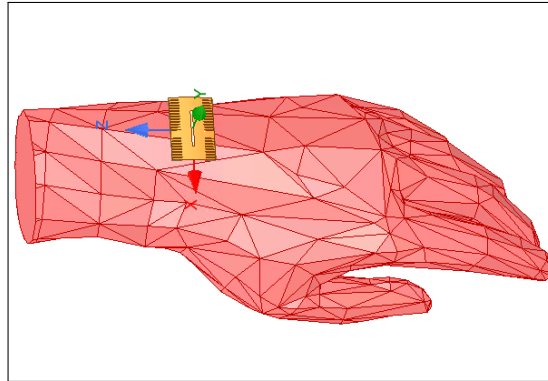


Figure 4.17: Simulation with human left hand model in HFSS.

As shown in Figure 4.17, the proposed antenna is rotated 90° clockwise and placed upon the middle of the hand model, with a distance variable set to be tuned for later. After that, the whole system (antenna and hand model) are included in an air box (radiation box) and simulated. Scenarios with different contact distances from 5 mm to 30 mm with a step size of 5mm are applied corresponding to the practical applications.

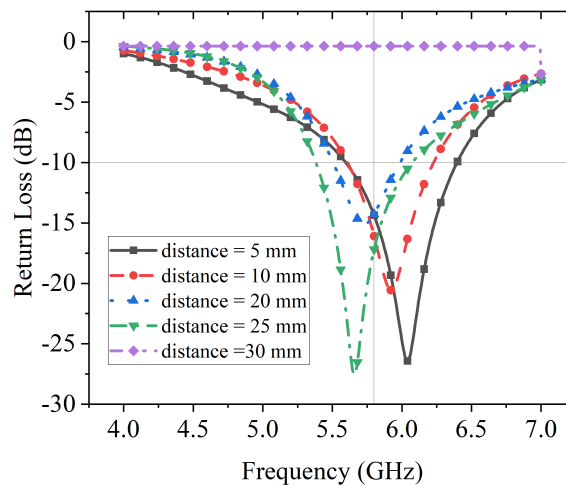


Figure 4.18: Antenna return loss with human body model.

Due to the dielectric property of human body, the electromagnetic wave passing through

it will be altered in phase and polarization as well as attenuation in magnitude. Consequently, the overall radiation on the back side of the antenna will be significantly affected while the front side has less influences.

As can be seen from Figure 4.18, taking the case of cylinder radius equals to 60 mm for instance, the antenna resonant frequency has a minor of shift from 6 GHz to 5.5 GHz. However, the desired frequency 5.8 GHz is included in the area of $|S_{11}| < -10$ dB, which validates the functionality of the antenna under the human body influence. Interestingly, the antenna bandwidth has remained approximately 500 MHz, which gives a radio frontend more flexibility to capture the electromagnetic waves. However, for the case of 30 mm distance, the antenna resonates out of the targeted frequency range, that is why the return loss curve is flat and close to 0 dB.

Further results from Figure 4.19 and 4.20 elaborate the radiation variation of the antenna, in which the back lobes of the radiation patterns shrink significantly, especially for the H-plane radiation patterns in Figure 4.20. Please note that both radiation patterns are rotated 90° clockwise according to the antenna rotation in HFSS.

In the E-plane radiation pattern diagram, it can be seen that the lobe size grows as the distance between antenna and hand model increases, which indicates the attenuation caused by human hand model is decreasing as the distance goes up. Based on practical circumstances for wearable devices, the distance should be restricted within 30 mm. When the distance reaches 30 mm, the maximum magnitude of the E-plane pattern gains a value of 5 dB approximately.

On the other hand, in the H-plane radiation pattern diagram, the main lobe sizes of all the scenarios are almost the same. In contrast, the back lobe size differs noticeably between each scenario. Similar to the trend in E-plane pattern lobes, the sizes of these H-plane back lobes also increase with the distance. Therefore, there is a big gap between

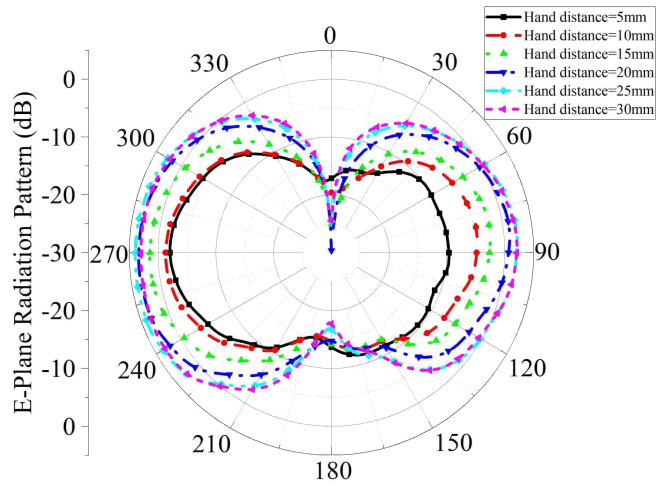


Figure 4.19: E-plane radiation patterns with different distances from human body model.

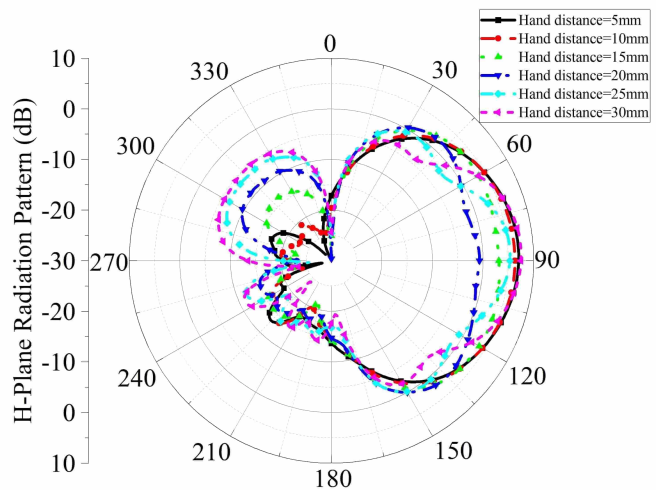


Figure 4.20: H-plane radiation patterns with different distances from human body model.

front and back lobe peak gains, which reach up to 26 dB for hand distance of 5 mm in the H-plane radiation pattern.

This shows in agreement with the aforementioned effects from human hand model. Correspondingly, the front to back ratio has also changed greatly. This can be observed from Figure 4.21 that for the distance of 5 mm and 10 mm, the front to back ratio

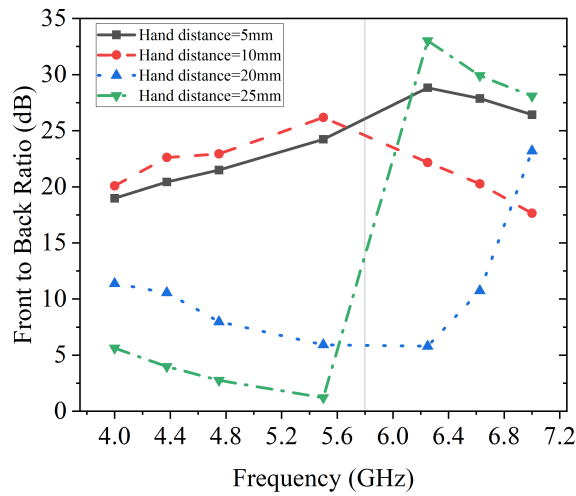


Figure 4.21: Antenna front to back ratio with human hand model.

is above 20 dB, which is remarkably higher than that without hand model. On the contrary, in the cases of 20 mm and 25 mm, there are steep rise at 5.6 GHz and 6.5 GHz respectively. However, the overall front to back ratios are higher than 1 dB, which suggests the front lobe size is larger than that of back lobes. At 5.8 GHz, the minimum value is approximately 7.5 dB when the distance is 20 mm from the hand model.

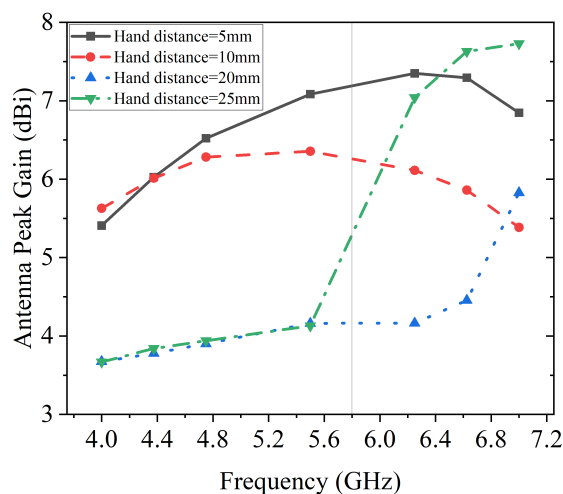


Figure 4.22: Antenna peak gain with human hand model.

4.2 SLOT ANTENNA DESIGN FOR CONFORMAL APPLICATIONS

Correspondingly, the antenna peak gains shown in Figure 4.22 have very similar trends with the front to back ratio in Figure 4.21. When the distance is 5 mm and 10 mm, respectively, the overall peak gain is above 5 dB and the curves have local maximums near 5.8 GHz. Conversely, in the cases where distance is 20 mm and 25 mm, steep rises can be observed at 6.6 GHz and 5.4 GHz respectively. Before the rise, the average peak gain is around 4 dB, and after rising point, both curves reach 6 dB and 8 dB, respectively.

Furthermore, another metric to evaluate the antenna for human body wearable application is the specific absorption rate (SAR), which is defined as the rate that electromagnetic energy is imparted to unit mass of biological body. An average SAR report is given below, including the average SAR 2D plot on the XoY and YoZ cross-section planes of the human hand model, and the average SAR value along a straight line across the hand model.

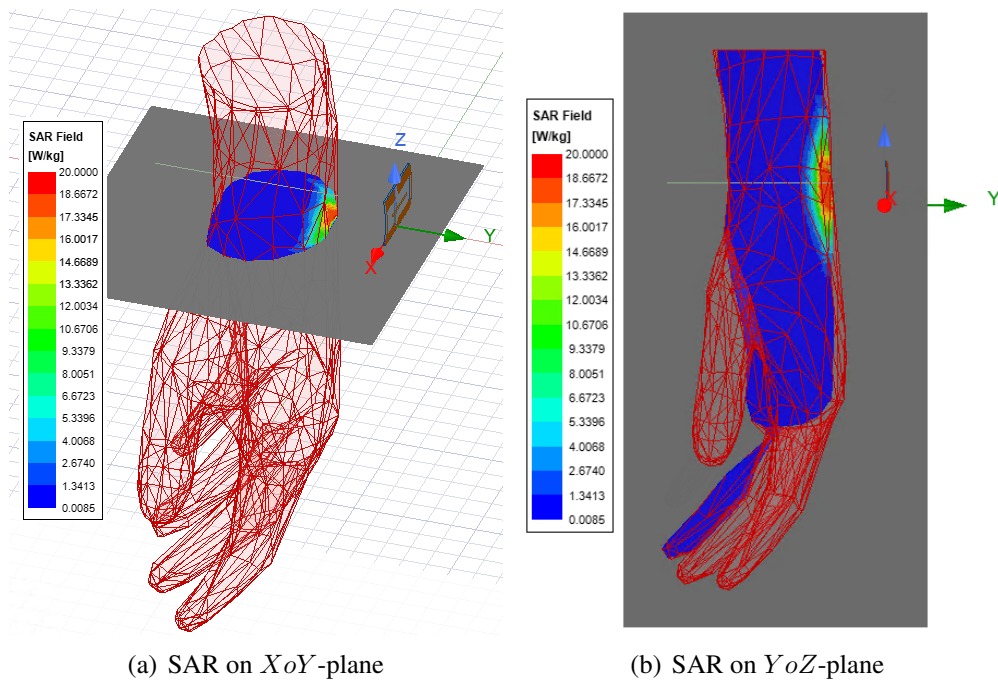


Figure 4.23: SAR plot on 2D cross-section planes for 20 mm distance.

4.2 SLOT ANTENNA DESIGN FOR CONFORMAL APPLICATIONS

As shown in Fig. 4.23, it can be clearly seen that the SAR value on the superficial region of the hand model is beyond the SAR limit value, while the blue region is within the limit. As indicated in Fig. 4.24, five cases are simulated as the distance between the antenna and the hand model, d_{ant} , varies from 5 mm to 30 mm. According to the standard of the Council of the European Union, the SAR limit over 1 gram of actual tissue is 2 W/kg. The highlighted blue area represent the region within the limit, and the intersections indicate the safe distance, under which the SAR is within the safe allowance for each scenario. For instance, when the antenna is placed 5 mm away from the hand model, the region 15.53 mm under the surface is within the SAR limit. Detailed data is listed in Table 4.1, from which one can observe that as the antenna is moving further away from the hand model, the safe region is approaching the surface as well, yielding the optimal case when the antenna is 30 mm away from the hand model.

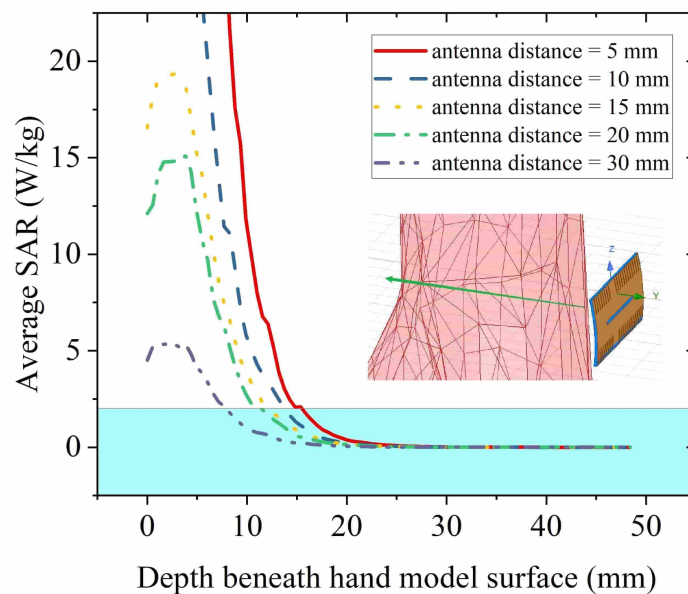


Figure 4.24: Average SAR along the line across hand model

In summary, despite of deviations from different testing scenarios, positive results are found from the simulation of conformal antenna integrated with human hand model

Table 4.1: Safe distance under skin for different scenarios

d_{ant} (mm)	Safe distance under skin (mm)
5	15.53
10	13.80
15	12.06
20	11.31
30	7.92

in terms of antenna characteristics, radiation performances. This can be regarded as a solid evidence for the proposed antenna to be employed for conformal situations or wearable application for human body. To develop a full picture of practical wearable application, additional studies and simulations are needed, in which a human body model with more parts than just one hand can be used for better accuracy. Moreover, methods to further reduce the SAR along the superficial region of human body are required. Furthermore, measurements with real human body can be undertaken so that the results can be precise.

4.2.2 Triband Slot Patch Antenna for Conformal and Wearable Applications

Microstrip patch antennas have been a popular research topic in both industry and academia ever since its first appearance. With great features such as compact size, low-cost fabrication and light weight, microstrip patch antennas have become widely applied in PCB designs [198]. Nowadays, a new printing technology with conductive-particle based ink has brought significant revolution in printed electronics [199]. Clearly layered structure enables microstrip patch antenna to be ink-printed. In [200], the author proposed an inkjet printed antenna for global positioning system (GPS) application with double frequency band at 1.575 GHz and 2.4 GHz. The printed antenna achieved promising performance, but the adopted substrate material is 3D printed and rigid, not

suitable for flexible surface application.

To fully utilise the advantages of microstrip patch antennas and printing technology for conformal surface and wearable applications, we propose a flexible microstrip patch antenna with tunable slots, which grants the antenna three operating frequency bands above 5 GHz. It is also noticed that in the literature, few works studied their antennas on conformal surfaces and wearable applications. Therefore, further simulation when the antenna is applied on curvature surfaces and human body are conducted and discussed.

4.2.2.1 Patch Antenna Design

A triband slot microstrip patch antenna is proposed with conductive ink-printing for conformal applications. The antenna has three operating bands, namely 5.8 GHz, 6.2 GHz and 8.4 GHz, respectively. The substrate material chosen for this design is flexible PET film, which has potential for conformal applications. The triband slot antenna is based on microstrip patch structure, consisting of radiating patch on the top and ground plane at the bottom, isolated by a PET dielectric layer in the middle. The patch dimensions are determined via equation (4.3) to (4.5) with respect to the lowest frequency of 5.8 GHz [61].

$$\varepsilon_{eff} = \frac{\varepsilon_r + 1}{2} + \frac{\varepsilon_r - 1}{2} \left[1 + 12 \frac{H}{W} \right]^{-1/2} \quad (4.3)$$

$$L_{eff} = L + 2\Delta L \quad (4.4)$$

$$\frac{\Delta L}{h} = 0.412 \frac{(\varepsilon_{reff} + 0.3) \left[\frac{W}{h} + 0.264 \right]}{(\varepsilon_{reff} - 0.258) \left[\frac{W}{h} + 0.8 \right]} \quad (4.5)$$

4.2 SLOT ANTENNA DESIGN FOR CONFORMAL APPLICATIONS

where W and L are patch width and length, h is substrate thickness and ϵ_r is the dielectric constant of the substrate material. The antenna is fed by a $50\text{-}\Omega$ microstrip line.

4.2.2.2 Parametric Study for Multiband Slots

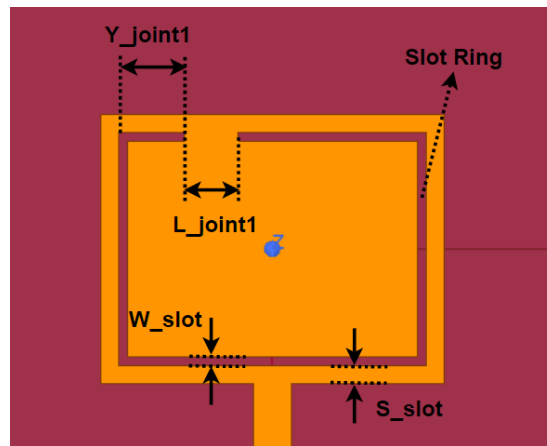


Figure 4.25: Adding first joint part on the top of ring slot.

Adding slots to the patch will significantly affect the current flow on the patch, hence altering and even adding more resonant frequencies [61, 182, 184, 185, 201–204]. The theoretical mechanism of a slot on a patch is similar to that of the equivalent dipole antenna, where the slot is regarded as the reciprocal dipole. Based on the above fundamental concept, a parametric study of the slots on the patch has been done via simulation.

Firstly, a ring slot is etched on the patch as shown in Figure 4.25. The width of the slot ring W_{slot} is set as 0.504 mm based on the aforementioned dipole theory and the space between the ring and the patch edge S_{slot} is set as 1.02 mm.

Secondly, to achieve multiple bands, jointing parts are needed to separate the slot ring into different parts. Two major parametric simulation are conducted to achieve this step by step. Taking the top left corner of the ring slot as reference point, the distance

4.2 SLOT ANTENNA DESIGN FOR CONFORMAL APPLICATIONS

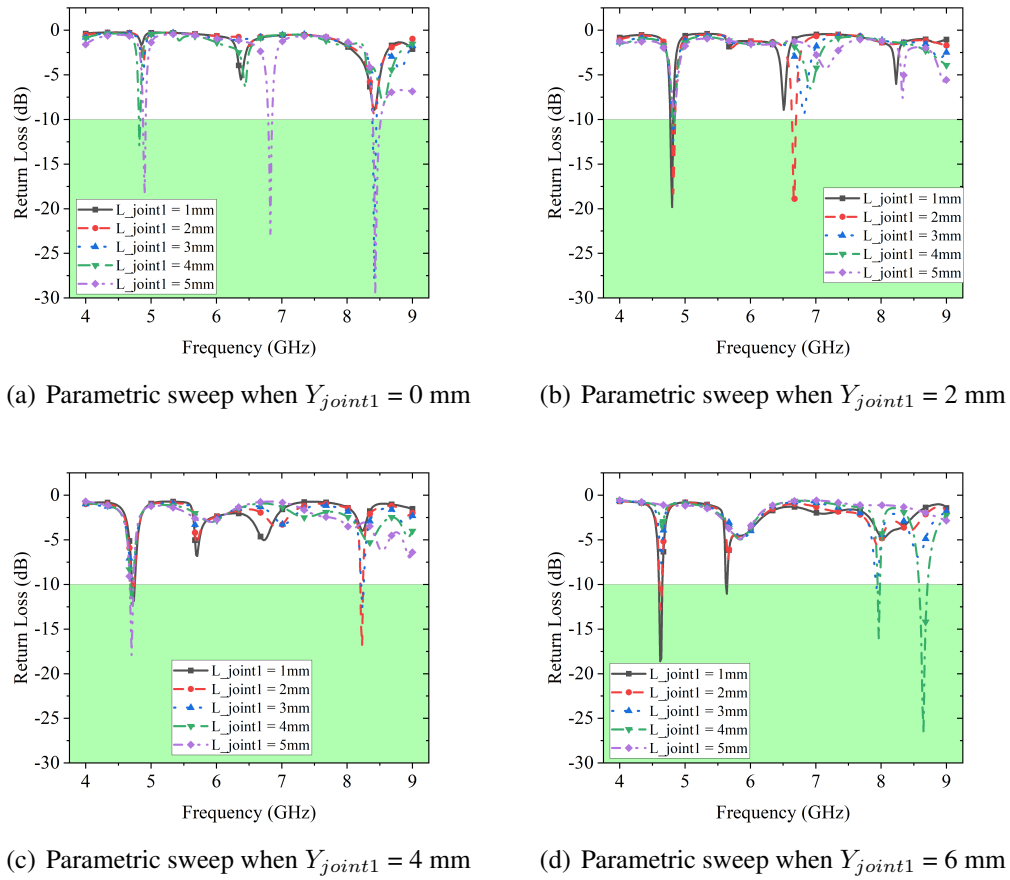


Figure 4.26: Parametric study of joint1 length L_{joint1}

between joint1 and the reference point Y_{joint1} and the length of joint1 L_{joint1} are studied in the simulation, where parametric sweeps are conducted in the range of 0-10 mm, and 0-5 mm, respectively.

The corresponding resonant frequency response and return loss is given in Figure 4.26 and 4.27. Making the position of joint1 fixed by setting Y_{joint1} as 0 mm, 2 mm, 4 mm, and 6 mm, respectively, parametric sweeps are conducted with different values of L_{joint1} . It is obvious that there is a resonant frequency band near 5 GHz for all the four cases in Figure 4.26. Another frequency band near 6 GHz appears stable in the second sweep as shown in Figure 4.26(b), whereas the third frequency band near 8 GHz is flickering and ambiguous across the four sweeps. In Figure 4.26(a), only one

4.2 SLOT ANTENNA DESIGN FOR CONFORMAL APPLICATIONS

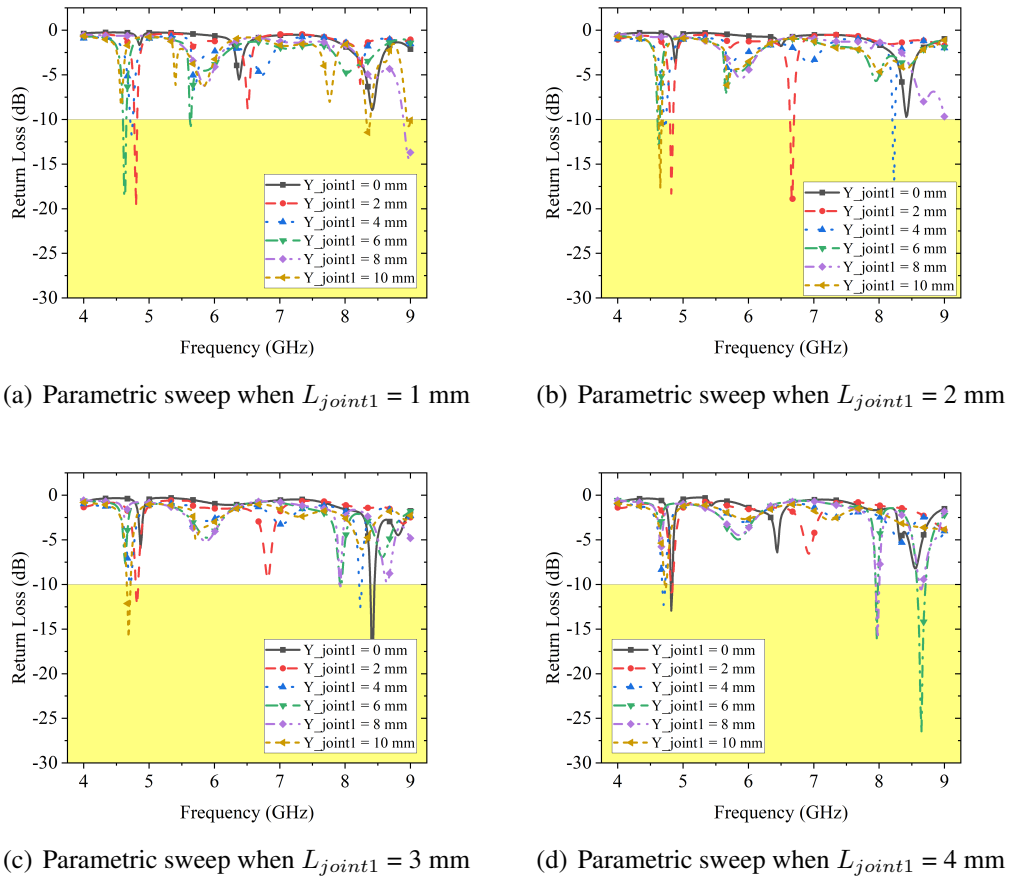
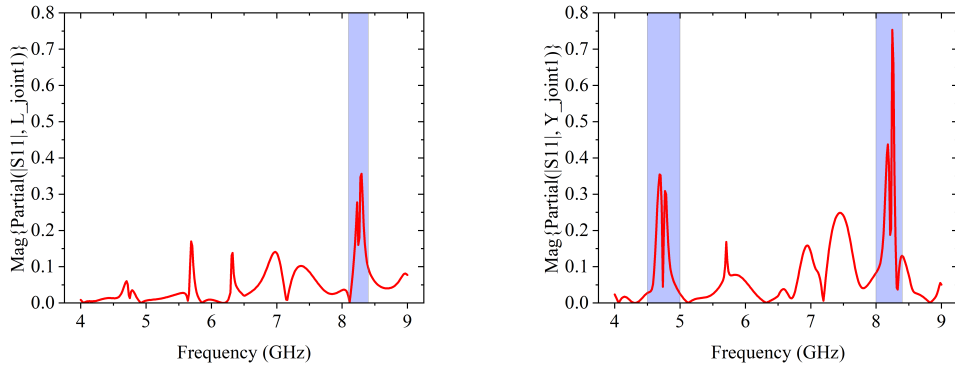


Figure 4.27: Parametric study of joint1 position Y_{joint1}

case shows completely three frequency bands at $L_{joint1} = 5$ mm and $Y_{joint1} = 0$ mm. To summarise the impact of joint1 length L_{joint1} , it has more influence on the 8 GHz frequency band.

The parametric sweeps of joint1 position along y -axis are shown in Figure 4.27, by setting the joint length L_{joint1} as 1 mm, 2 mm, 3 mm, and 4 mm, respectively. The near 5 GHz band is relatively stable in each sweep scenario. On top of that, a band near 8 GHz also shows in most of the sweep cases, but not stable enough, and only a few cases fulfil the -10 dB standard. Additionally, the resonance of the 6 GHz band is not strong enough.

The above results regarding L_{joint1} and Y_{joint1} can also be validated in the parametric



(a) Magnitude of the partial derivative of S_{11} over L_{joint1} .
 (b) Magnitude of the partial derivative of S_{11} over Y_{joint1} .

Figure 4.28: Parameter sensitivity of Y_{joint1} and L_{joint1} .

sensitivity report in Figure 4.28, which presents the magnitude of the partial derivative of $|S_{11}|$ with respect to these two parameters, respectively. As indicated in the highlight areas, in Figure 4.28(a), the magnitude of reflection coefficient $|S_{11}|$ is very sensitive to L_{joint1} at the frequency band of 8.1-8.4 GHz; in Figure 4.28(b), $|S_{11}|$ reacts to Y_{joint1} much more at the band of 4.5-5 GHz and 8-8.4 GHz. This agrees with the above parametric sweeps of those two parameters and one can conclude that adding joint1 yields a frequency band at near 8 GHz, which may affect the 6 GHz band as well.

Altogether, these above results suggest that adding joint1 gives a second frequency band at near 8 GHz, which is sensitive to the y -axis location Y_{joint1} and length L_{joint1} of the joint. These two parameters will be fine tuned later together with those of joint2.

Thirdly, a second joint is added on the right of the ring slot as shown in Figure 4.29. Taking the bottom right corner of the ring slot as reference point, the distance between joint2 and the reference point X_{joint2} and the length of joint2 L_{joint2} are also swept in HFSS simulation in the range of 0-3 mm and 0-8 mm, respectively.

Figure 4.30 presents the influence on the antenna's resonant frequencies from L_{joint2} . The results of four parametric sweeps are presented in the diagram while X_{joint2} is set

4.2 SLOT ANTENNA DESIGN FOR CONFORMAL APPLICATIONS

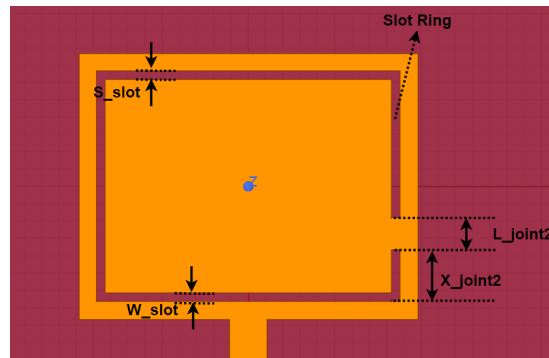


Figure 4.29: Adding second joint part at the bottom right of ring slot.

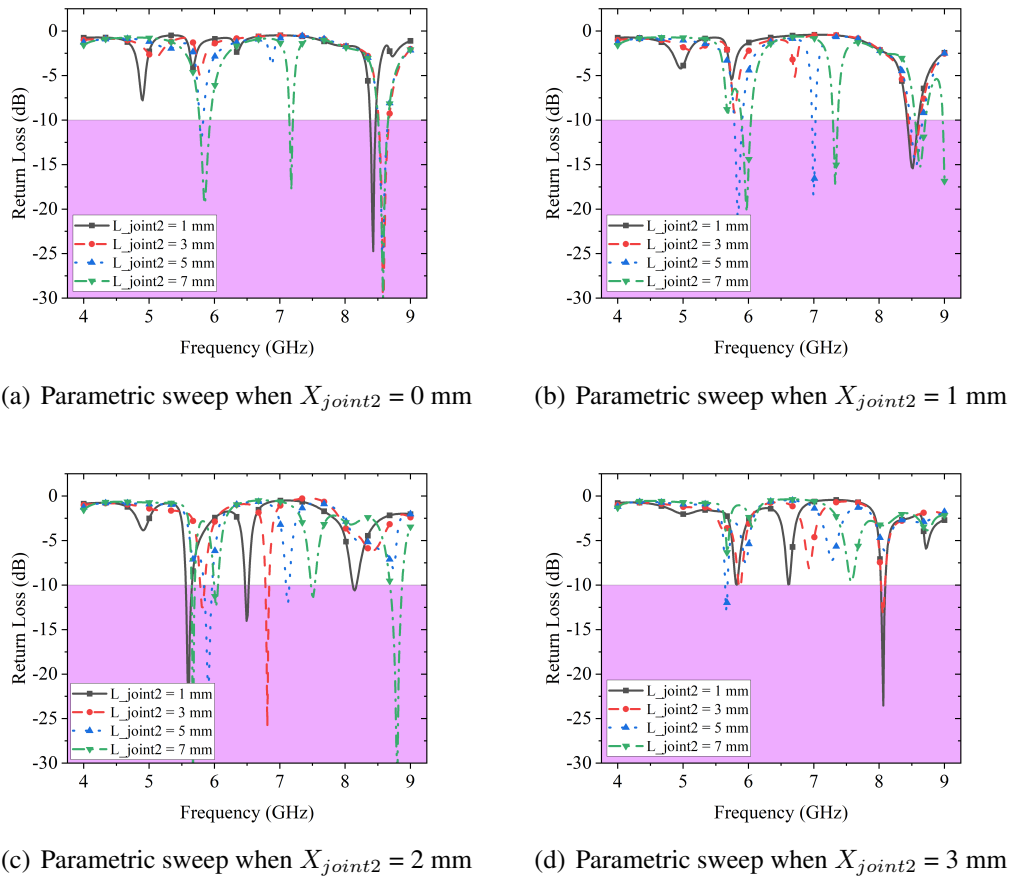


Figure 4.30: Parametric study of joint2 length L_{joint2}

fixed as 0 mm, 1 mm, 2 mm, and 3 mm, respectively. The first three scenarios in Figure 4.30(a) to 4.30(c), three resonant frequencies can be found at near 6 GHz, 7 GHz, and 8 GHz, respectively. However, the the one near 7 GHz is flickering and not quite sensitive.

4.2 SLOT ANTENNA DESIGN FOR CONFORMAL APPLICATIONS

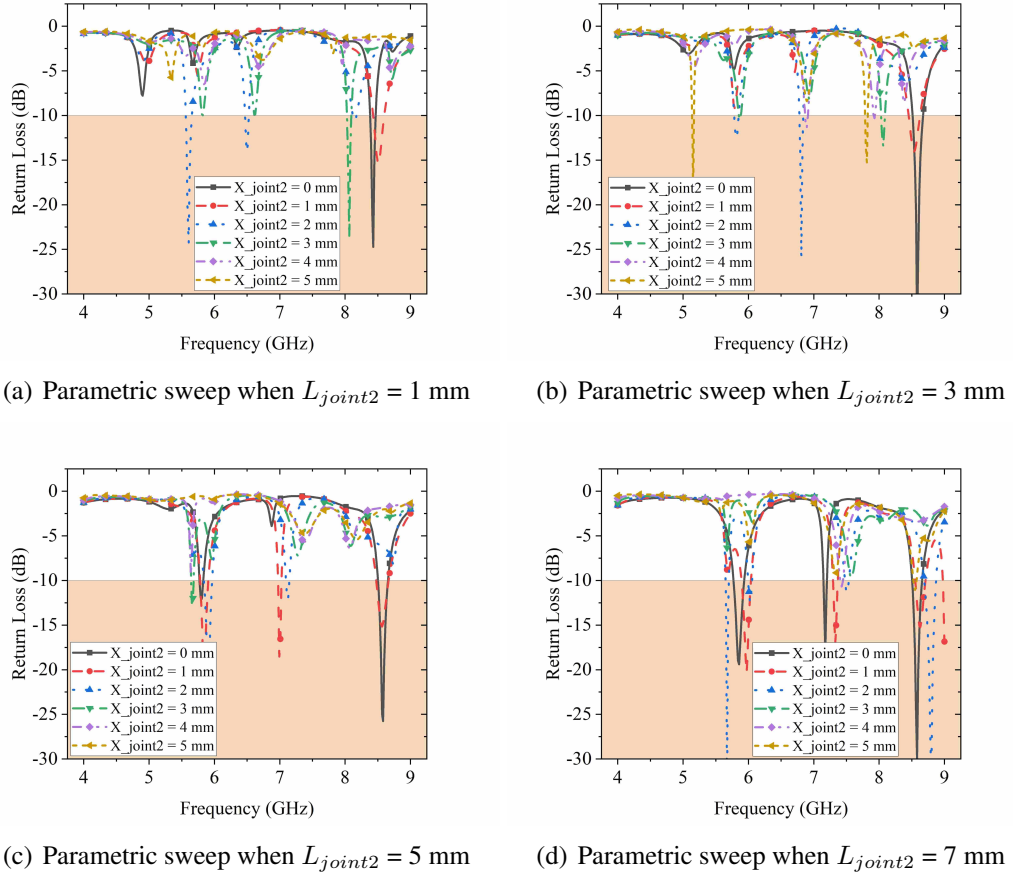
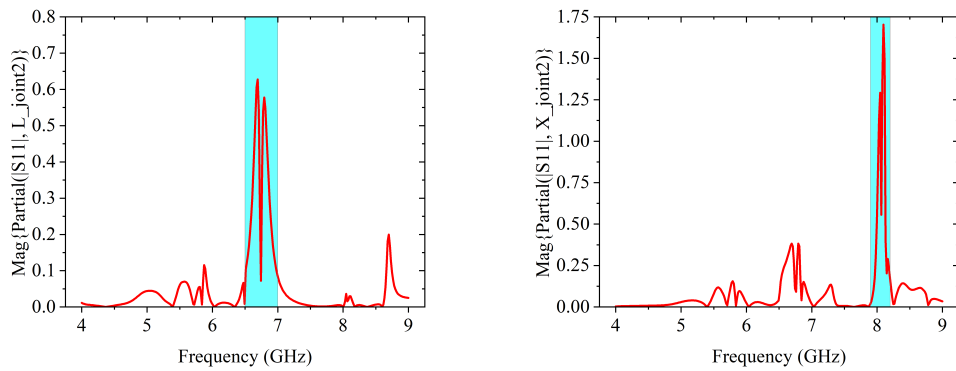


Figure 4.31: Parametric study of joint2 position X_{joint2}

Additionally, the near 8 GHz band in Figure 4.30 and the near 6 GHz band in Figure 4.30(c) are relatively stable. For the scenario in Figure 4.30(b), the frequency band at near 8 GHz is relatively stable while no resonant frequency can be found apart from that. These observations suggest that there is a link between L_{joint2} and a resonant frequency band near 7 GHz.

On the other hand, in Figure 4.31, the joint2 length L_{joint2} is set fixed as 1 mm, 3 mm, 5 mm, and 7 mm, respectively for the parametric sweep of X_{joint2} . In the four scenarios, one can observe three resonant frequency bands approximately at near 6 GHz, 7 GHz, and 8 GHz, especially in Figure 4.31(c) and 4.31(d), the three bands are distinguishable, while those in the other two cases are not steady and not matching the -10 dB criteria,

4.2 SLOT ANTENNA DESIGN FOR CONFORMAL APPLICATIONS



(a) Magnitude of the partial derivative of S_{11} over $L_{\text{joint}2}$.
 (b) Magnitude of the partial derivative of S_{11} over $X_{\text{joint}2}$.

Figure 4.32: Parameter sensitivity of $X_{\text{joint}2}$ and $L_{\text{joint}2}$.

especially the near 7 GHz band, which is floating between 6-7 GHz. It shows that $X_{\text{joint}2}$ is another important determinant of the middle band near 6-7 GHz.

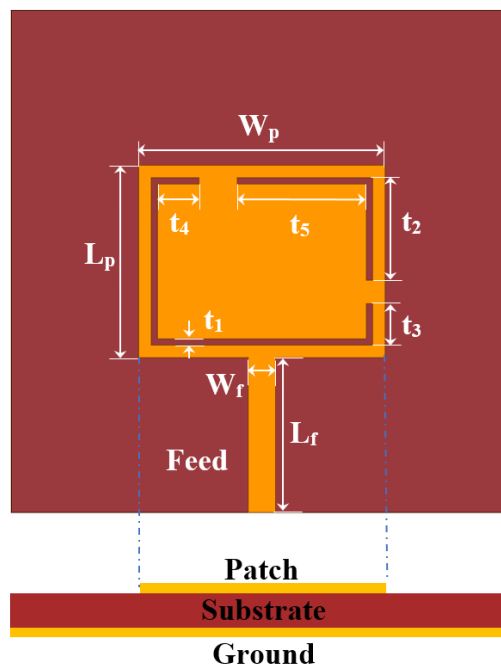


Figure 4.33: Triband slot antenna structure layout.

From Figure 4.32, one can observe the parametric sensitivity of those two parameters of joint2. In Figure 4.32(a), it shows that the magnitude of the reflection coefficient $|S_{11}|$

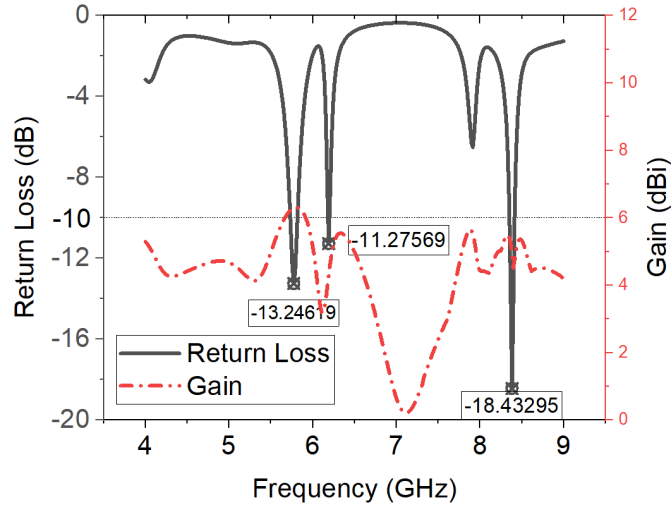


Figure 4.34: Return loss and gain of proposed antenna

is very sensitive to L_{joint2} at frequency band of 6.5-7 GHz as shown in the highlight area; In Figure 4.32(b), the impact from X_{joint2} on $|S_{11}|$ at near 6 GHz is at about the same level of that from L_{joint2} . These above observations are in agreement with the previous parametric sweeps. However, the impact at 7.9-8.2 GHz band is surprisingly much higher, which may suggest that tuning X_{joint2} will not only affect the 6-7 GHz band, but also the near 8 GHz band.

By optimising the parameters of the two joints, the antenna dimensions are finalised as: $L_p = 15.37$ mm, $W_p = 19.64$ mm, $L_f = 12.32$ mm, $W_f = 2.15$ mm, $t_1 = 0.504$ mm, $t_2 = 8.192$ mm, $t_3 = 3.282$ mm, $t_4 = 3.808$ mm, $t_5 = 10.74$ mm. The overview of the finalised antenna is shown in Figure 4.33 and it operates at three resonant frequency bands at 5.8 GHz, 6.2 GHz, and 8.4 GHz, respectively.

4.2.2.3 Results and Discussion

The proposed antenna is evaluated in ANSYS HFSS and the results are presented in this section. The return loss and antenna gain illustrated in Figure 4.34 show that the antenna operates at three frequency bands ($|S_{11}| < -10$ dB), i.e. 5.8 GHz, 6.2 GHz and 8.4 GHz,

respectively; bandwidth values are 91 MHz, 10 MHz and 65 MHz, respectively; the corresponding antenna gain at these operating frequencies are 6.23 dBi, 4.62 dBi and 5.43 dBi, respectively.

In addition, patch surface current distribution at 90° phase and the radiation patterns of E-plane and H-plane at these operating frequencies are also illustrated in Figure 4.35(a) to 4.35(f), respectively. From the patch surface current distribution, it can be seen that the current with maximum magnitude are predominantly scattered around the slots, where the resonance is happening correspondingly. At frequency of 6.2 GHz, there is a relatively large area in the center of the patch with low current distribution, suggesting the poor resonance and narrow frequency bandwidth indicated in Figure 4.34. As for the radiation patterns, due to the asymmetry of the slots along feed line direction, the E-plane ($\phi = 0^\circ$) patterns are symmetrical but not the H-plane ($\phi = 90^\circ$) patterns.

4.2.2.4 Conformal Application Test

In order to evaluate the performance of the antenna under flexible surface circumstance, a set of conformal simulations are conducted, where the entire antenna is wrapped onto a cylinder along y -axis as shown in Figure 4.36. To simulate different level of surface bending, the radius of the cylinder is set as a variable with value of 20 mm, 50 mm, and 100 mm, respectively. The corresponding bending angles can be approximated as 18° , 7.2° , 4.5° , respectively. The cylinder is set as a non-model object, which has no effects on Maxwell's equations calculation or simulation results.

Frequency response of the antenna and return loss are illustrated in Figure 4.37 for the three bending tests. There is clear resonant frequency at 5.8 GHz and 6.2 GHz and the return loss values are below -15 dB. However, the resonance at 8.4 GHz is weak when the bending cylinder radius is 20 mm, which means most of the energy is reflected by the antenna. The antenna appears to be affected significantly by large angle bending.

4.2 SLOT ANTENNA DESIGN FOR CONFORMAL APPLICATIONS

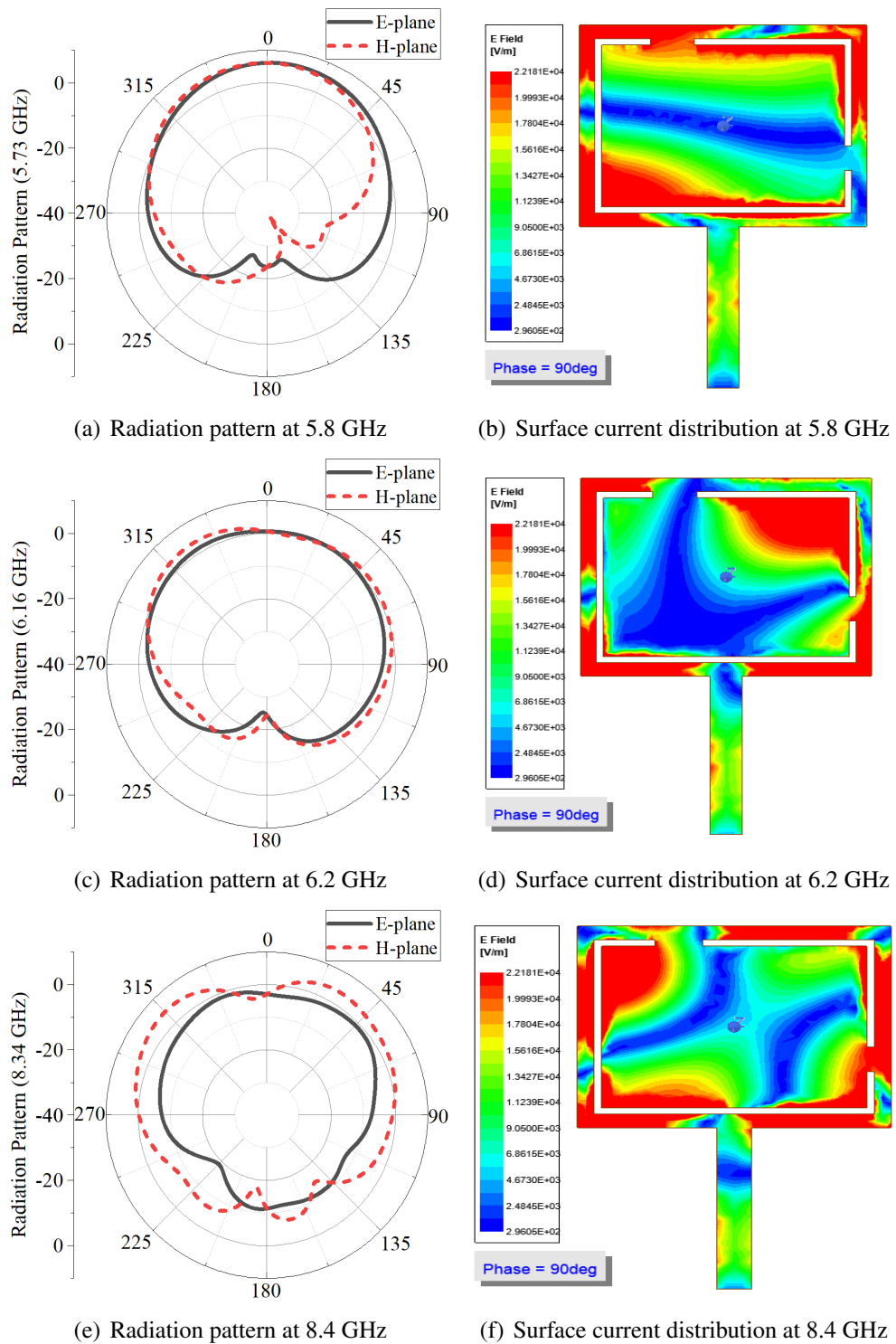


Figure 4.35: Antenna performance at three bands

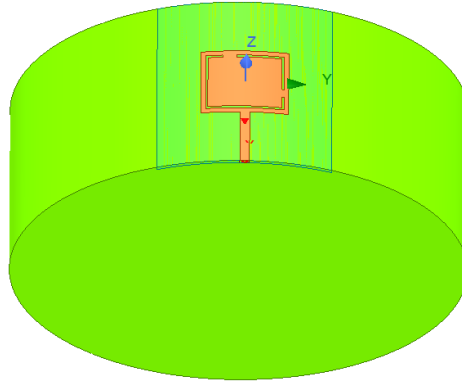


Figure 4.36: Conformal test with antenna wrapped onto a cylinder

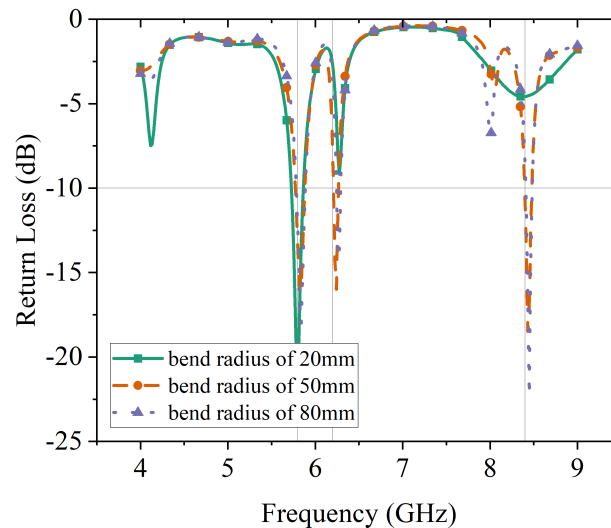


Figure 4.37: Antenna return loss for bending tests

When the bending angle is 18° (or cylinder radius is 20 mm), the 3D polar plots of E-field of the antenna at three frequency bands are illustrated in Figure 4.38(a) to 4.38(c). It can be seen that the radiation pattern at 5.8 GHz still has a major lobe concentrating and pointing in the $+z$ -axis direction, whereas the one for both 6.2 GHz splits into one major lobe pointing to $-y$ -axis direction and a minor side lobe pointing to $+y$ -axis direction. As for the plot of 8.4 GHz in Figure 4.38(c), the lobe splits into two approximately equal sized major lobes, pointing at $-y$ -axis and $+y$ -axis, respectively. This may affect the transmission or reception direction set-up in practical applications.

4.2 SLOT ANTENNA DESIGN FOR CONFORMAL APPLICATIONS

The above results suggest that the directivity and antenna gain at 6.2 GHz and 8.4 GHz are altered by the bending effects. It is probably because that bending force folds the antenna into two parts around x -axis, therefore, the radiated field also tends to diverge along the bending.

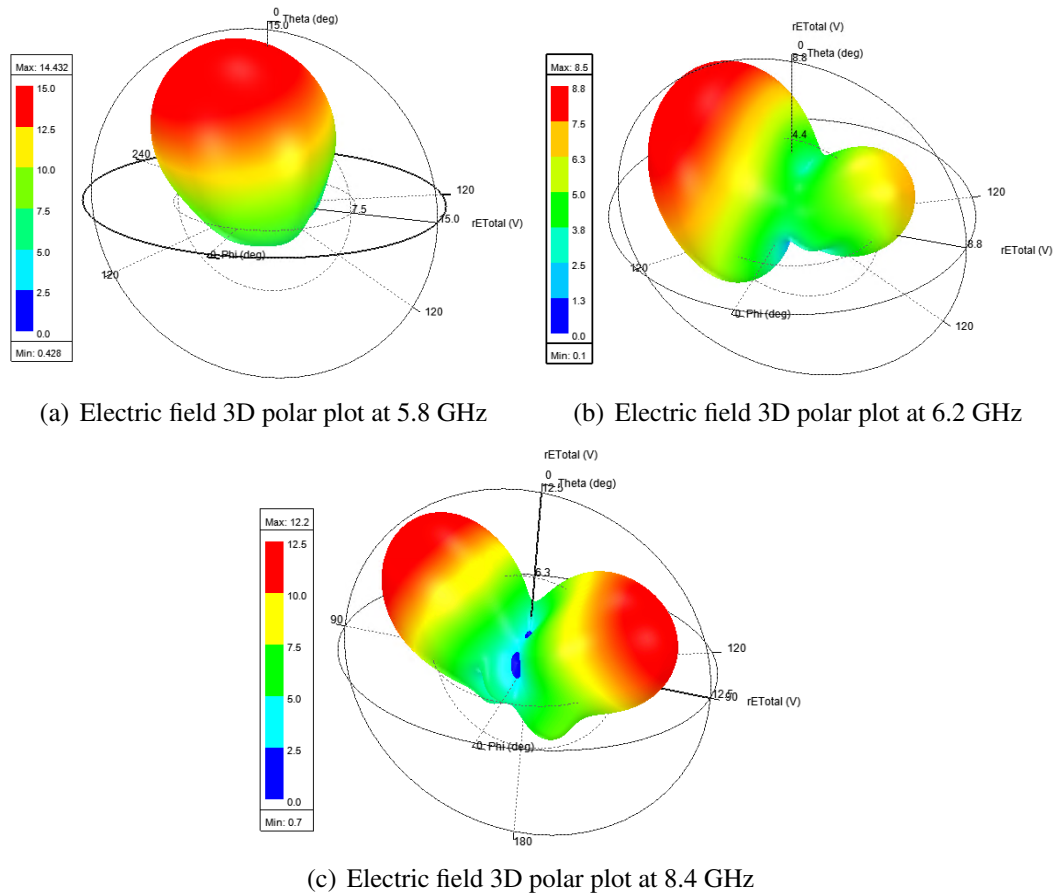


Figure 4.38: Electric field 3D polar plot for cylinder radius of 20 mm.

Moreover, the maximum E-field strength for each frequency band is 14.4 V/m, 8.6 V/m, and 12.2 V/m, respectively, which indicates the radiation intensity of each case. It is obvious that at 5.8 GHz, the antenna radiates the strongest electromagnetic field, followed by 8.4 GHz and then 6.2 GHz. This matches the corresponding return loss at each resonant frequency mentioned earlier.

As for the case of cylinder radius 50 mm and bending angle 7.2° , the 3D polar plots of

4.2 SLOT ANTENNA DESIGN FOR CONFORMAL APPLICATIONS

E-field are demonstrated in Figure 4.39(a) to 4.39(c). The general patterns of E-field 3D polar plot at 5.8 GHz and 8.4 GHz remain similar to those of previous case where cylinder radius is 20 mm. A significant pattern change happens at 6.2 GHz, where most of the E-field concentrates above the radiating patch, pointing along $+z$ -axis, but it also shows a tendency to split into two lobes. The maximum E-field strength are measured as 15.2 V/m, 10.6 V/m, and 14.6 V/m, respectively. At 6.2 GHz band, the antenna radiates relatively weaker electromagnetic fields.

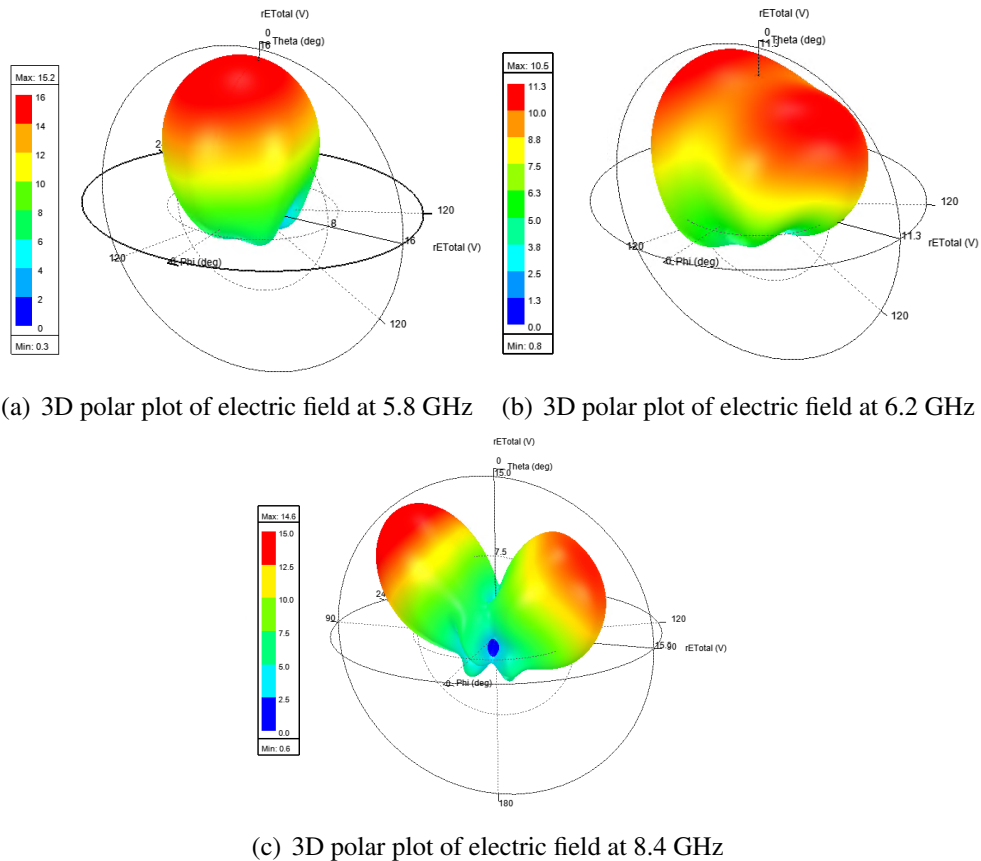


Figure 4.39: Electric field 3D polar plot for cylinder radius of 50 mm.

When it comes to the case of 80 mm cylinder radius, there are not significant pattern changes in the E-field 3D plots at 5.8 GHz and 8.4 GHz compared with the case of 50 mm cylinder radius. Interestingly, Figure 4.40(b) reveals a gradual deviation of the E-field strength pattern, which is the tendency of main lobe splitting into two is

4.2 SLOT ANTENNA DESIGN FOR CONFORMAL APPLICATIONS

getting higher. It is approaching the similar shape of that at 8.4 GHz. Overall, the maximum E-field strength is 15.2 V/m, 8.4 V/m, and 13.9 V/m, respectively. The radiation performance at 5.8 GHz and 8.4 GHz is still stronger than that at 6.2 GHz.

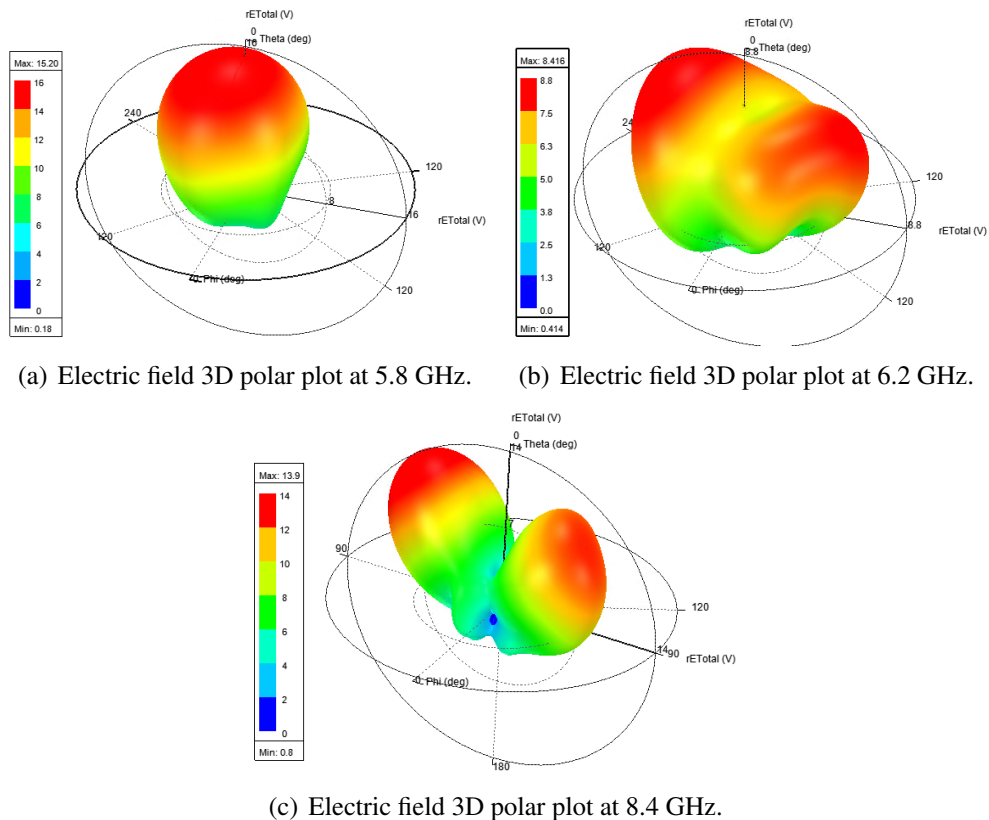
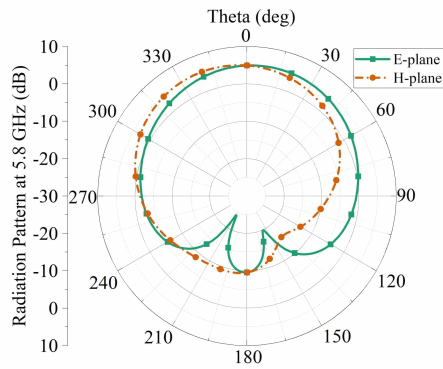


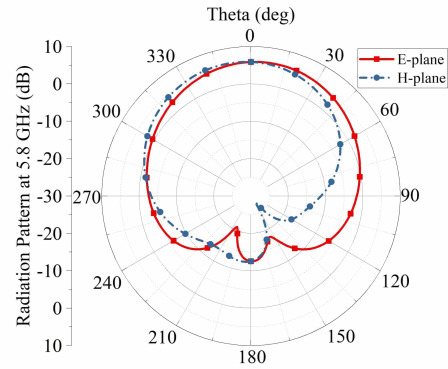
Figure 4.40: Electric field 3D polar plot for cylinder radius of 80 mm.

Taking a further look at the principle E-plane and H-plane radiation patterns in Figure 4.40, one can conclude that only minor changes can be found in the radiation patterns at 5.8 GHz. For the case of 6.2 GHz, the overall pattern of E-plane increases whereas that of H-plane shrinks as the cylinder radius increase, which suggests the E-field radiation has noticeable improvement. Also, the size of back lobe of the E-plane drops to a lower level. As for the frequency band of 8.4 GHz, the E-plane radiation patterns changed significantly when the bending angle is large for the cylinder radius of 20 mm. At the same time, the directivity is obvious for the 8.4 GHz band. The H-plane patterns have

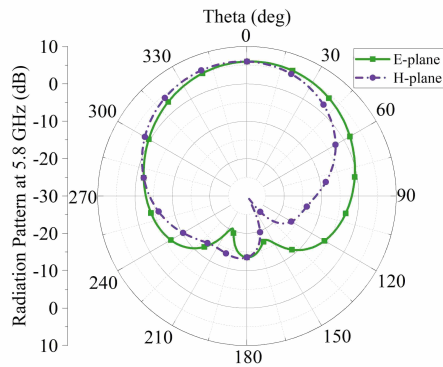
4.2 SLOT ANTENNA DESIGN FOR CONFORMAL APPLICATIONS



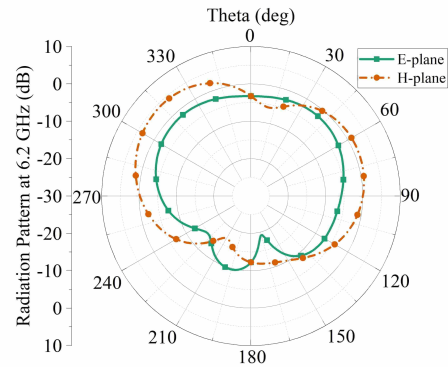
(a) E- and H-plane at 5.8 GHz for 20mm



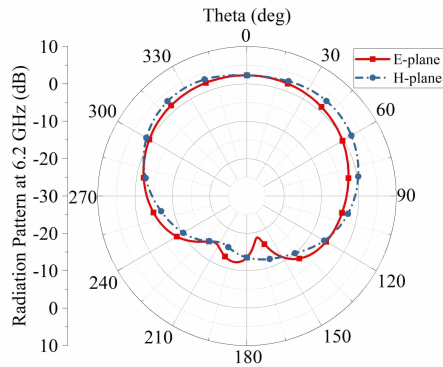
(b) E- and H-plane at 5.8 GHz for 50mm



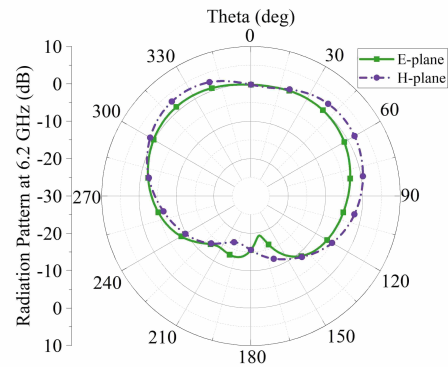
(c) E- and H-plane at 5.8 GHz for 80mm



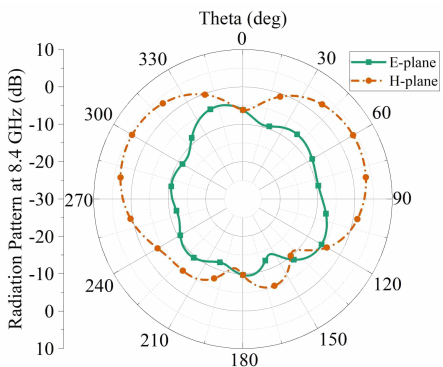
(d) E- and H-plane at 6.2 GHz for 20mm



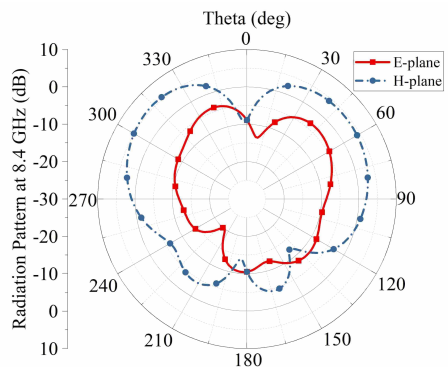
(e) E- and H-plane at 6.2 GHz for 50mm



(f) E- and H-plane at 6.2 GHz for 80mm

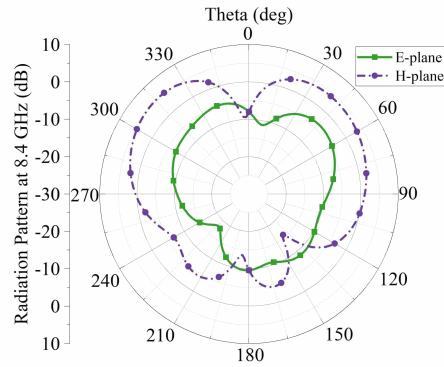


(g) E- and H-plane at 8.4 GHz for 20mm



(h) E- and H-plane at 8.4 GHz for 50mm

4.2 SLOT ANTENNA DESIGN FOR CONFORMAL APPLICATIONS



(i) E- and H-plane at 8.4 GHz for 80mm

Figure 4.40: E-plane and H-plane for conformal tests

two predominantly major lobes and two small back lobes as well.

As further observation, surface current distribution on the radiating patch is presented for the bending case of cylinder radius of 50 mm. Figure 4.41, 4.42, and 4.43 represent the cases for three frequency bands at 5.8 GHz, 6.2 GHz, and 8.4 GHz, respectively.

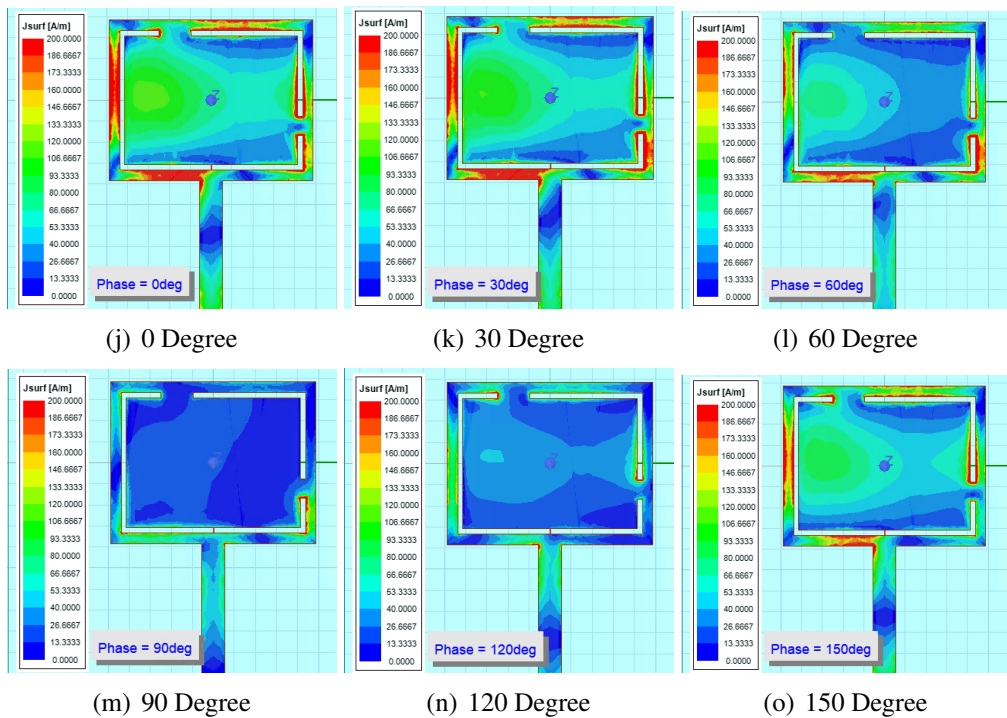


Figure 4.41: Surface current distribution at 5.8 GHz for cylinder radius of 50 mm

4.2 SLOT ANTENNA DESIGN FOR CONFORMAL APPLICATIONS

Different phases of the power source are listed in each sub-figure, i.e., 0° , 30° , 60° , 90° , 120° , and 150° , respectively.

At 5.8 GHz, when the phase is 90° and 120° , the overall current distribution is low and below 26 A/m. For other phases, the surface current concentrates around the edge of the patch and vicinity of the slot, up to above 200 A/m. At 6.2 GHz, the current distribution at different phases is similar to that of 5.8 GHz, but with higher overall concentration and coverage.

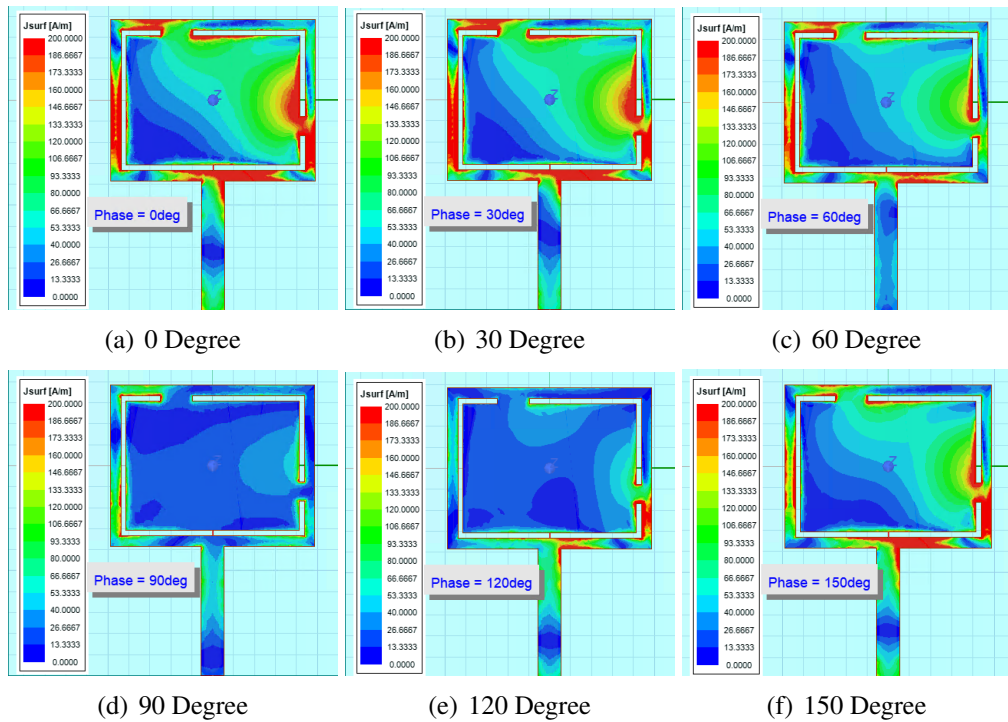


Figure 4.42: Surface current distribution at 6.2 GHz for cylinder radius of 50 mm

Deviations can be found in Figure 4.43 regarding the surface current distribution at 8.4 GHz. The current level at 60° and 90° is lower than that of other phases, whereas the current level at 0° , 30° , and 150° is much intenser and higher than that in the other two frequency bands.

Overall, these results about surface current distribution suggest that under the effect of

4.2 SLOT ANTENNA DESIGN FOR CONFORMAL APPLICATIONS

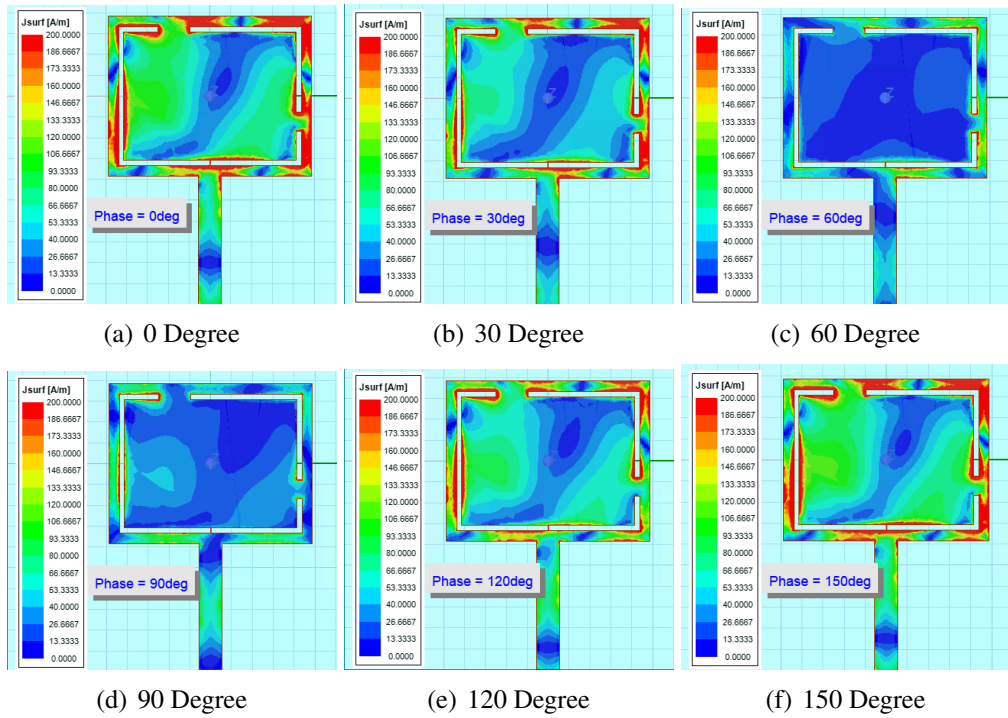


Figure 4.43: Surface current distribution at 8.4 GHz for cylinder radius of 50 mm

both frequency and bending effect, the current flow inside the radiating patch varies and the low current area contributes to the conduction loss of the antenna. The high level of time-varying current on the patch at 8.4 GHz also corresponds to the relatively high level induced magnetic field shown in the radiation patterns in Figure 4.40.

Figure 4.44 suggest that the peak gain of the antenna across the frequency sweep range from 4 GHz to 9 GHz. Basically, the results from the three bending tests have a similar trend, apart from that the overall peak gain values of the case of 20 mm cylinder radius is slightly lower than the other two cases, especially at the frequencies of interest.

Figure 4.45 presents the antenna radiation efficiency for the three bending tests. Taking both conduction loss and dielectric loss into account, antenna radiation efficiency indicates the portion of input energy that is transmitted by the antenna. From Figure 4.45, it is clear that the antenna has high radiation efficiency above 80% at two frequencies of interest, i.e., 5.8 GHz and 6.2 GHz. At the vicinity of 8 GHz, the radiation efficiency is

4.2 SLOT ANTENNA DESIGN FOR CONFORMAL APPLICATIONS

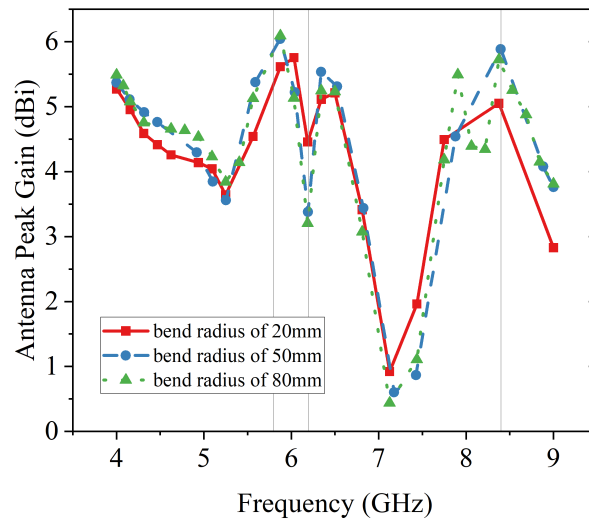


Figure 4.44: Antenna peak gain for bending tests

between 70% and 80%, and the cases of 50 mm and 80 mm cylinder radius are relatively unstable.

Table 4.2 summarises the main characteristics of the antenna for the conformal bending tests. Three frequencies of interest are individually evaluated as well. These parameters

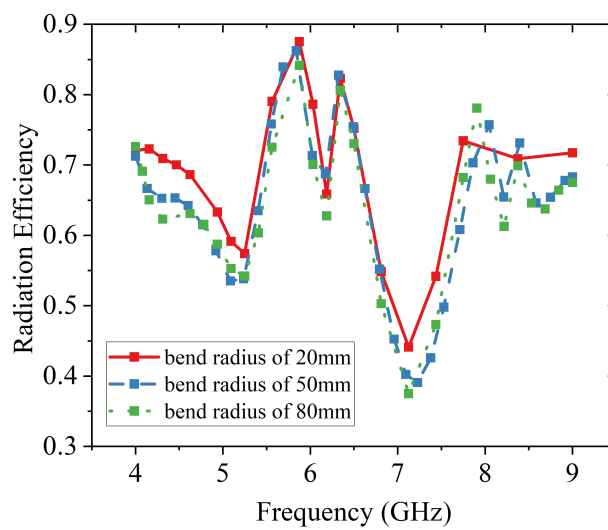


Figure 4.45: Antenna radiation efficiency for bending tests

4.2 SLOT ANTENNA DESIGN FOR CONFORMAL APPLICATIONS

include maximum directivity D_{max} , maximum antenna gain G_{max} , radiated power P_{rad} (total input power is set as 1 W), maximum θ component of E-field $E_{max|\theta}$, maximum of total electric field E_{max} , maximum radiation intensity U_{max} , and radiation efficiency e_{cd} . The optimal results among the tests are highlighted in green. Conversely, the minimum values are in red.

Table 4.2: Antenna Parameters for Conformal Tests

	$r = 20\text{mm}$			$r = 50\text{mm}$			$r = 80\text{mm}$		
f (GHz)	5.8	6.2	8.4	5.8	6.2	8.4	5.8	6.2	8.4
D_{max} (dB)	3.96	3.89	4.60	4.67	2.98	5.30	4.81	3.21	5.39
G_{max} (dB)	3.50	2.62	3.27	4.04	2.21	3.87	4.09	2.10	3.78
P_{rad} (W)	0.88	0.31	0.54	0.83	0.62	0.67	0.80	0.37	0.60
$E_{max \phi}$ (V)	-1.12	1.40	1.26	2.30	-1.85	1.36	2.30	1.22	-1.82
$E_{max \theta}$ (V)	0.35	5.48	5.24	6.07	0.52	5.48	6.11	5.66	0.80
E_{max} (V)	14.43	8.52	12.20	15.20	10.52	14.55	15.20	8.42	13.92
U_{max} (W/sr)	0.28	0.10	0.20	0.31	0.15	0.28	0.31	0.09	0.26
e_{cd}	0.88	0.67	0.71	0.87	0.74	0.73	0.85	0.66	0.70

Predictably, the scattering of the data highlighted in green in Table 4.2 shows a noticeable trend to reflect the effect of bending. As the bending cylinder radius increases (i.e., bending angle decreases), the number of optimal results increases as well. However, something unexpected is that at 6.2 GHz and bending radius of 80 mm, it also possesses the largest number of minimum results highlighted in red, even though some of the values are very close to each other.

To sum up, all the results of the conformal bending tests suggest that bending surfaces have general negative effects on the antenna performance, and it is proportional to the bending angle. Therefore, large bending angle or strong surface deformation should be avoided in practical applications. Despite of those adverse impacts, the antenna still holds acceptable performance under conformal situations. Furthermore, some results like the antenna parameters at 6.2 GHz for cylinder radius of 80 mm in Table 4.2 also suggest the association between conformal effects and antenna performance is not

strictly fixed and predictable. Practical measurements and tests are required for further verification.

4.2.2.5 Simulation for Wearable Applications

In the previous section, assessment of the antenna under conformal circumstances with bending curvature is conducted and the antenna demonstrates acceptable resistance and promising performance. One common application for conformal circumstance is wearable devices for human body, which requires further evaluation according to various criteria. In this section, the antenna is measured together with part of human body model to simulate its performance as a wearable device with a close distance with human body tissue. Limited by model mesh complexity and computation time, a male human left hand model from ANSYS HFSS library is used for simulation. Note that the model applies an approximate average density 1 g/cm^3 .

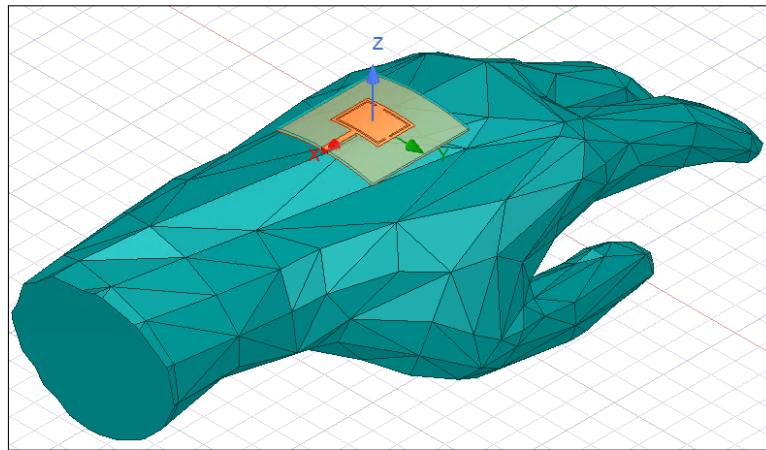


Figure 4.46: Triband antenna with hand model in HFSS.

As demonstrated in Figure 4.46, the hand model is placed under the antenna, which is set bending along the 80 mm cylinder from previous conformal test. The curvature of the entire antenna has close match with the hand model. The distance between the antenna and the hand model is set as a variable d_{ant} with values of 0 mm, 10 mm, 20

4.2 SLOT ANTENNA DESIGN FOR CONFORMAL APPLICATIONS

mm, 30 mm, and 40 mm.

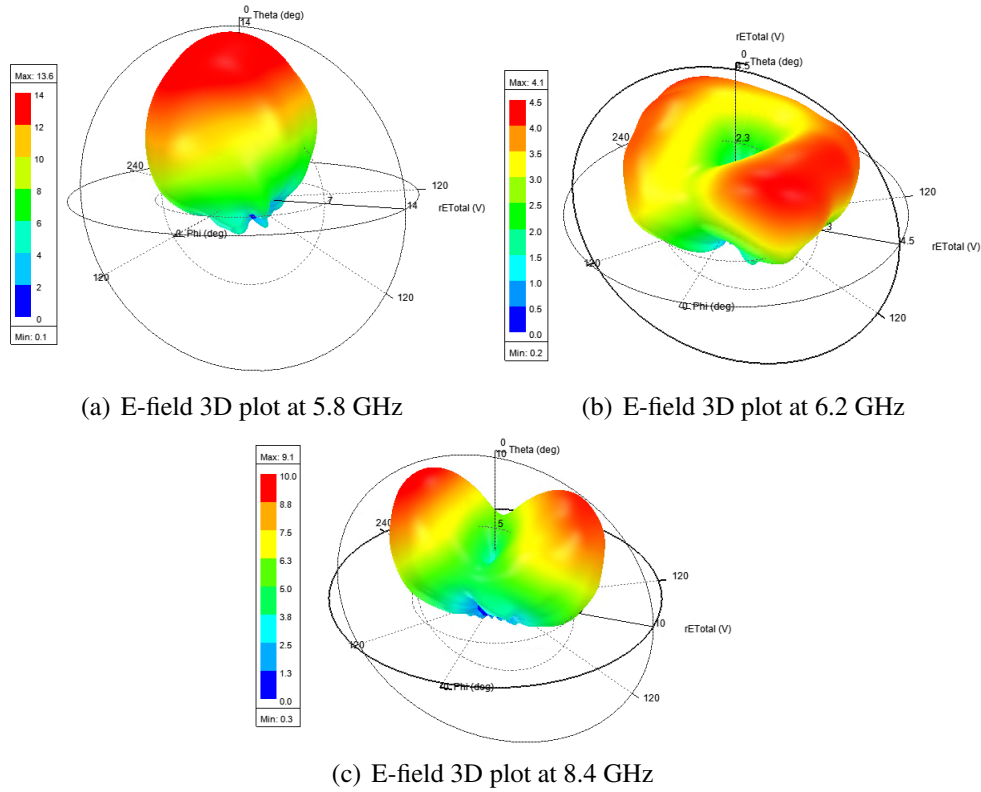
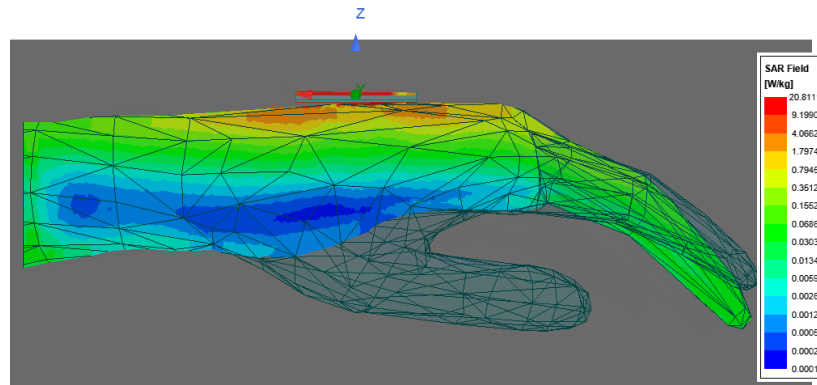


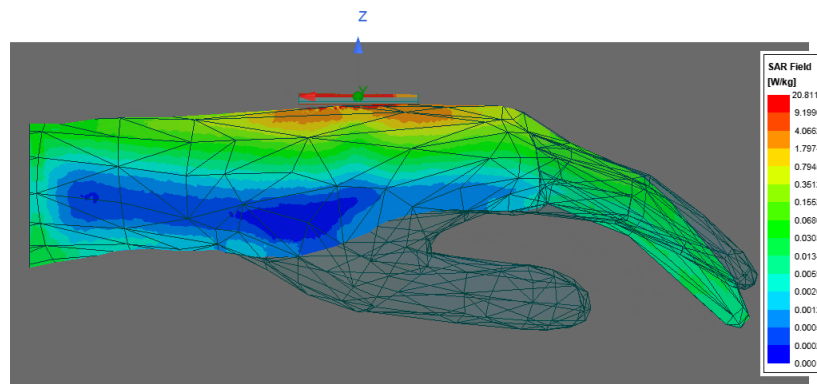
Figure 4.47: E-field 3D plot for $d_{ant} = 0$ mm

Figure 4.47 illustrates the 3D plots of E-field strength at three frequencies of interest. It can be seen that the general pattern shapes remain similar to those in conformal bending tests. The maximum E-field strength is largest at 5.8 GHz, i.e., 13.6 V/m, followed by 8.1 V/m at 8.4 GHz and 4.1 V/m at 6.2 GHz. Additionally, the patterns also suggest that most of the radiation energy concentrates above the XoY -plane, which indicates a less absorption if the antenna is attached above human body.

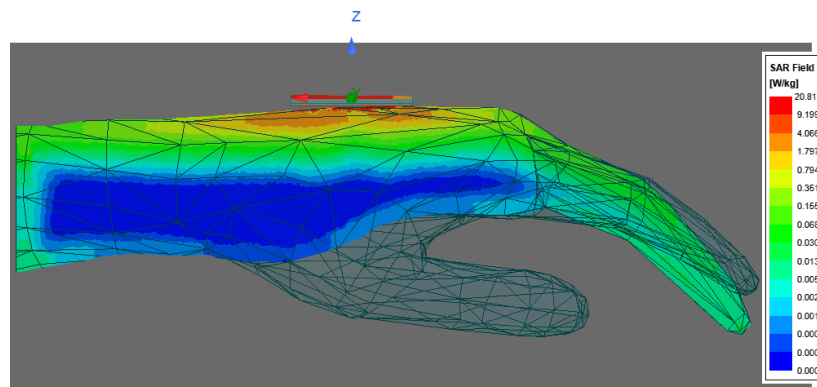
The 2D SAR plots on the cross-section planes of the hand model are illustrated in Figure 4.48 for XoZ -plane and Figure 4.49 for YoZ -plane. Note that average SAR calculation is applied, computed by averaging over a volume that surrounds each mesh point in the hand model. Also, to be harmless to human body, an SAR limit is set as 1.6 W/kg in the U.S.A. and 2 W/kg in the E.U., respectively.



(a) Average SAR on XoZ -plane at 5.8 GHz



(b) Average SAR on XoZ -plane at 6.2 GHz



(c) Average SAR on XoZ -plane at 8.4 GHz

Figure 4.48: SAR plot on XoZ -plane when $d_{ant} = 0$ mm

In Figure 4.48, one can observe clearly that the SARs in most of the cross-section area in the three cases is below 2 W/kg, which means it is safe for human body tissue. The orange area (1.79-4.06 W/kg) and yellow (0.36-1.79 W/kg) in each diagram are nearly the same size, while the size of the blue region (below 0.0012 W/kg) differs in the three

4.2 SLOT ANTENNA DESIGN FOR CONFORMAL APPLICATIONS

cases. At 8.4 GHz, the plot has the largest blue region, followed by the case at 6.2 GHz and then 5.8 GHz.

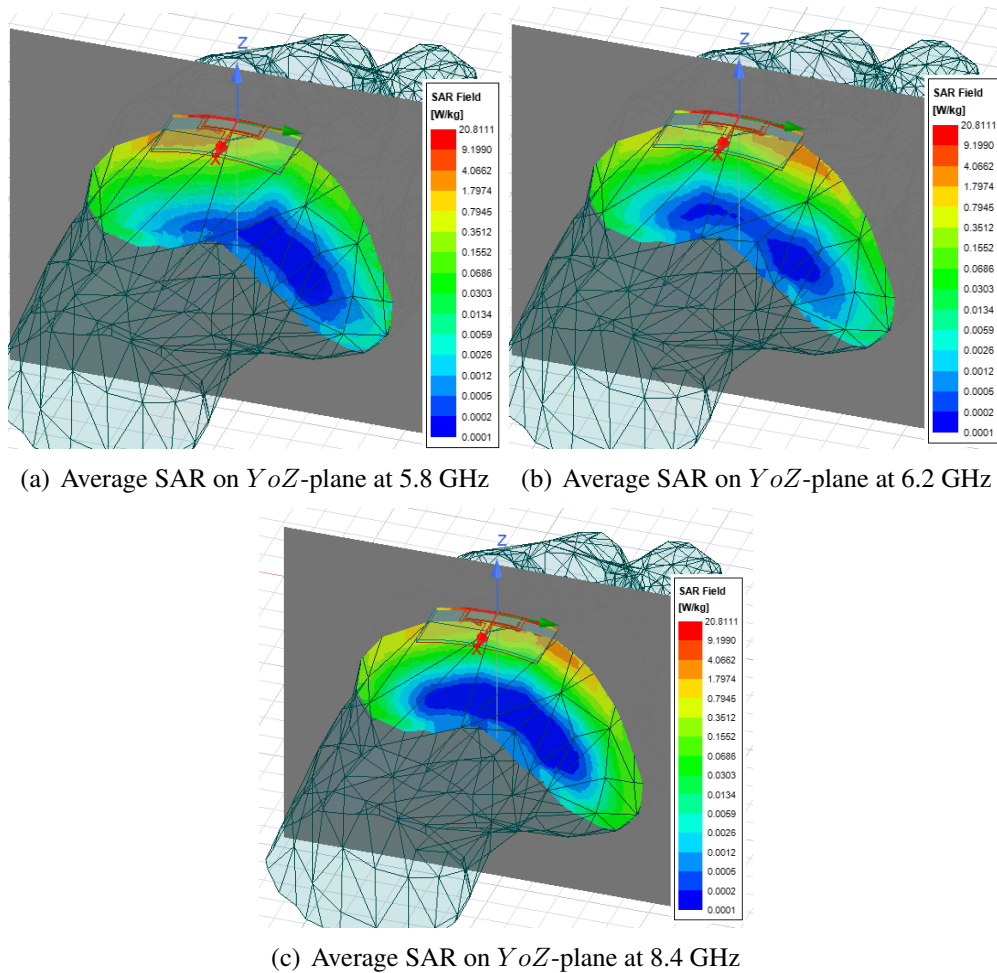
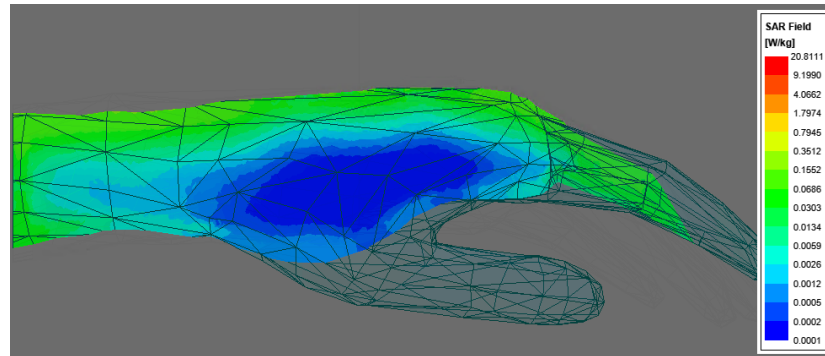
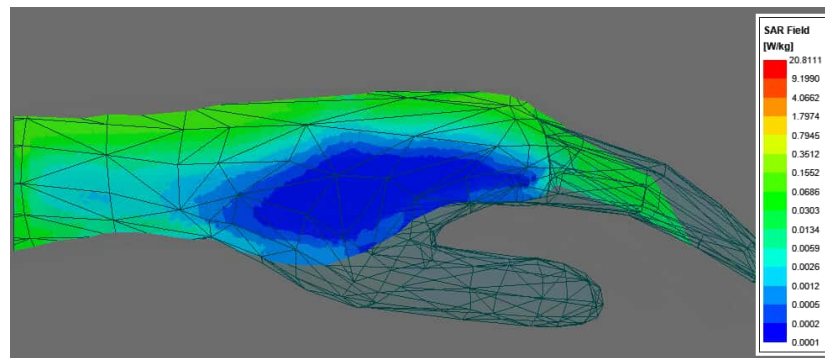


Figure 4.49: SAR plot on $Y-o-Z$ -plane when $d_{ant} = 0$ mm

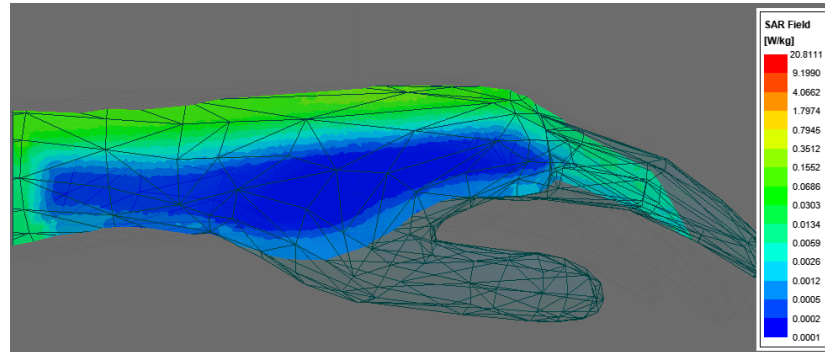
As for the $Y-o-Z$ -plane SAR plots in Figure 4.49, similarly, most of the cross-section area is under the safe limit level. Some noticeable deviation is that the high SAR regions (red and orange regions) are located differently. For instance, at 5.8 GHz, the left part of the hand model has relatively higher SAR, whereas at 6.2 GHz and 8.4 GHz, it is on the right part. On top of that, the size of the blue regions also varies in different cases. For instance, the one at 5.8 GHz is the largest and located in the bottom right region.



(a) Average SAR on XoZ -plane at 5.8 GHz



(b) Average SAR on XoZ -plane at 6.2 GHz



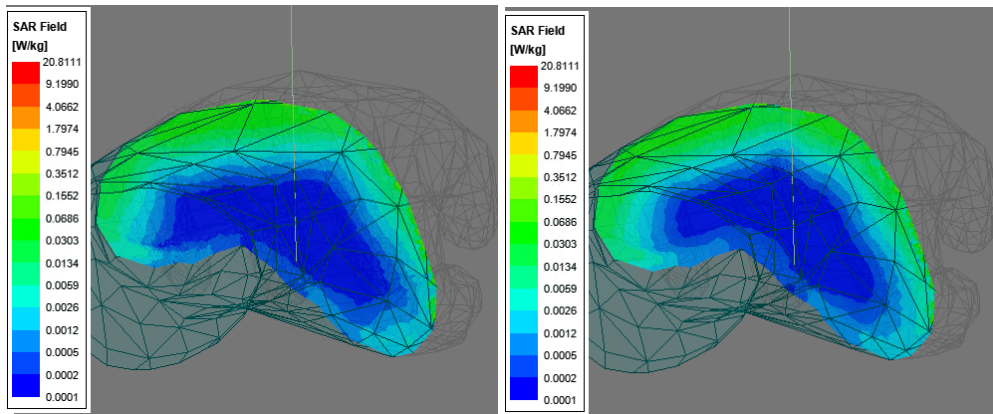
(c) Average SAR on XoZ -plane at 8.4 GHz

Figure 4.50: SAR plot on XoZ -plane when $d_{ant} = 40$ mm

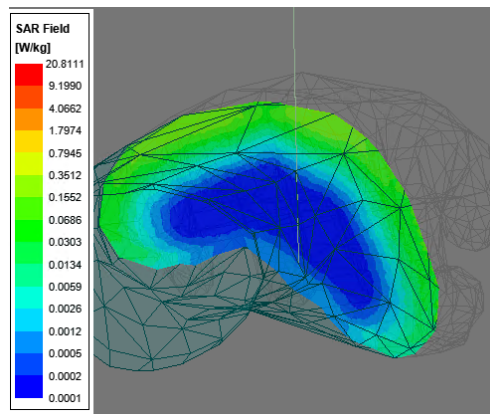
Combining the SAR results on two cross-sections, one can conclude that the overall SAR level inside human hand model is within the limit, except a small area on the surface close to the antenna, indicated by the red regions. These above cases represent the situation when the antenna is in close contact with human body, i.e. $d_{ant} = 0$ mm. In practical application, a gap may exist between the antenna and human body,

4.2 SLOT ANTENNA DESIGN FOR CONFORMAL APPLICATIONS

therefore, other cases where $d_{ant} = 10$ mm, 20 mm, 30 mm, and 40 mm, are also simulated. Predictably, as the antenna moves further away from the hand model, the radiation intensity inside the body tissue will decrease. For simplicity of presentation and readability, the 2D SAR plots of the case $d_{ant} = 40$ mm is presented in Figure 4.50 for XoZ -plane and Figure 4.51 for YoZ -plane.



(a) Average SAR on YoZ -plane at 5.8 GHz (b) Average SAR on YoZ -plane at 6.2 GHz



(c) Average SAR on YoZ -plane at 8.4 GHz

Figure 4.51: SAR plot on YoZ -plane when $d_{ant} = 40$ mm

For the XoZ -plane SAR value, it can be clearly seen in Figure 4.50 that all the regions for three frequencies of interest are below 0.16 W/kg, which is only 8% of the SAR limit. Additionally, the blue region (below 0.005 W/kg) also takes up to half of the whole cross-section area for at 5.8 GHz and 6.2 GHz, and more than half at 8.4 GHz.

4.2 SLOT ANTENNA DESIGN FOR CONFORMAL APPLICATIONS

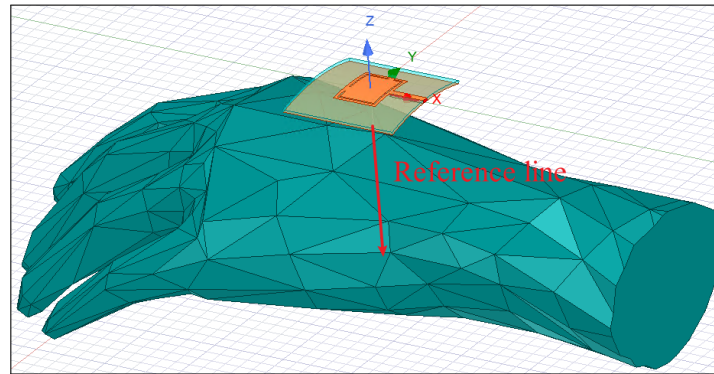


Figure 4.52: Reference line inside hand model to calculate SAR.

Looking at the plots of $Y o Z$ -plane in Figure 4.51, a similar conclusion can be drawn that the SAR value of entire cross-section area is below 0.16 W/kg , which is far below the SAR limit. What is different from previous $X o Z$ -plane plot is that the blue region at 5.8 GHz is larger than that at 6.2 GHz and 8.4 GHz . This corresponds to the fact that the back lobes of radiation pattern at 5.8 GHz is rather small compared with that at 6.2 GHz and 8.4 GHz . Consequently, the radiated energy below the antenna is less as well.

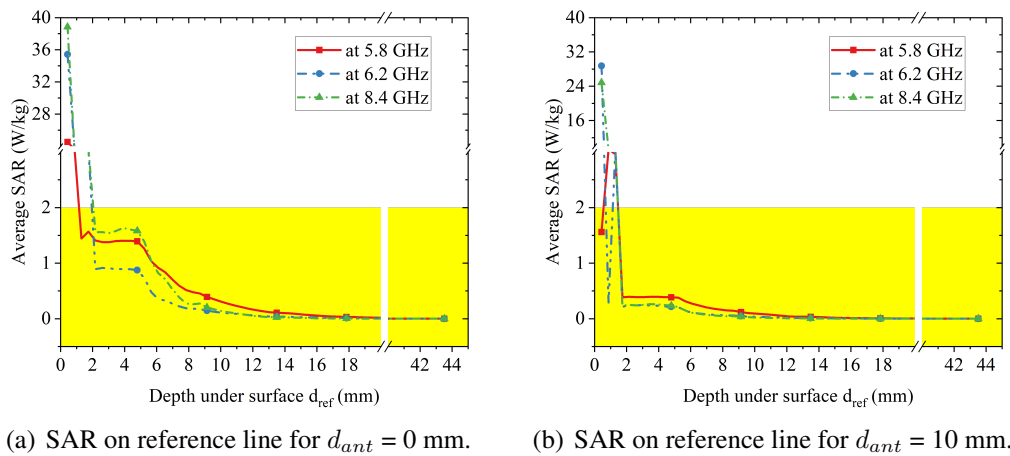
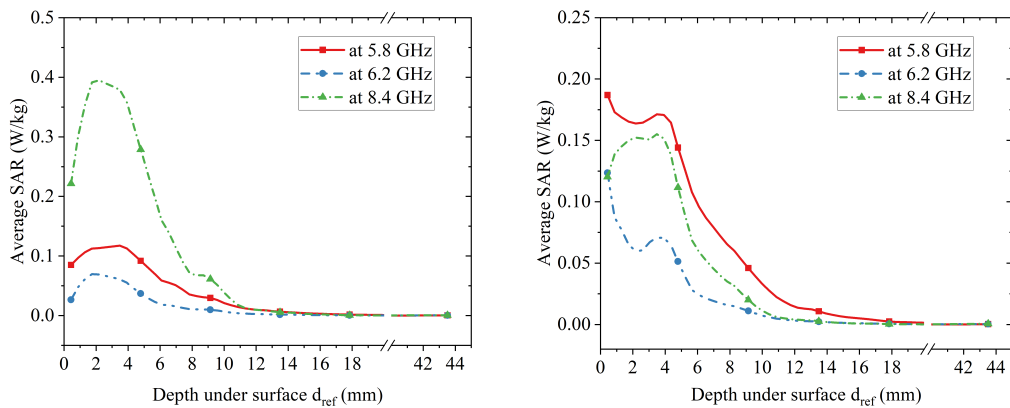


Figure 4.53: Average SAR vs. d_{ref} along the reference line.

To elaborate the SAR results for different d_{ant} , a reference line is created along $-z$ -axis across the hand model as indicated in Figure 4.52. The SAR values are plotted along the line with respect to d_{ref} , the depth from top surface of the hand model along $-z$ -axis.

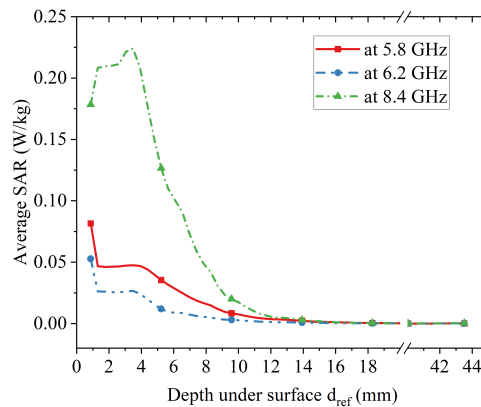
4.2 SLOT ANTENNA DESIGN FOR CONFORMAL APPLICATIONS

As can be seen from Figure 4.53, all the SAR curves approach zero beyond the point $d_{ref} = 15$ mm, before which lie the variations of each case. In Figure 4.53(a), the SAR curves are above 2 W/kg before the point $d_{ref} = 2$ mm and up to 40 W/kg, which means that within 2 mm under the surface, human tissue is absorbing excessive radiated electromagnetic energy, and the amount drops below the threshold for deeper region and reaches zero after the point $d_{ref} = 15$ mm. Similarly, in Figure 4.53(b), the threshold point is also near $d_{ref} = 2$ mm. Moreover, a steep decline of SAR happens at this point.



(a) SAR on reference line for $d_{ant} = 20$ mm.

(b) SAR on reference line for $d_{ant} = 30$ mm.



(c) SAR on reference line for $d_{ant} = 40$ mm.

Figure 4.54: Average SAR vs. d_{ref} along the reference line.

However, the results for the other three cases where d_{ant} is 20 mm, 30 mm, and 40 mm, the SAR value in the entire region is below 2 W/kg. Only difference is the decline tendency before threshold $d_{ref} = 15$ mm. The trends in Figure 4.54(a) and 4.54(c) are

similar, where the overall SAR value of the 8.4 GHz curve is the highest and has a steep decline, followed by the 5.8 GHz one and then the 6.2 GHz one, both of which have a rather smooth decline. Surprisingly, for the case of $d_{ant} = 30$ mm as shown in Figure 4.54(b), the curve of 5.8 GHz is above the one of 8.4 GHz. All the three curves have steep decline.

4.2.3 Remarks

A flexible slot antenna with parallel slit-loading structure is proposed for conformal surfaces and wearable application. The fabricated antenna prototype has achieved 2.75 dBi gain and 450 MHz bandwidth at operating frequency of 5.8 GHz. Despite the discrepancy between simulated and measured antenna gains and radiation patterns, the antenna exhibits acceptable functionality for desired frequency. Further simulation in conformal surfaces and integration with human body model for wearable applications show promising results with acceptable deviations.

A triband slot antenna design operating at 5.8 GHz, 6.2 GHz, and 8.4 GHz is presented. Design theory and parametric study are given for the design procedure. The antenna demonstrates promising performance in simulation and measurements. Since the antenna is proposed with flexible substrate for future conformal situations and potential wearable applications, successive exploration and simulation are conducted. The conformal tests with a cylinder bending surface indicate that the antenna performance undergoes some fluctuation at different level of conformal surfaces, but the overall results are acceptable. Furthermore, the simulations integrated with human body model suggest promising performance for wearable application with certain conditions, such as the distance between the antenna and human body. For the triband slot antenna, there is also a potential to adapt a frequency reconfigurable structure so that each frequency band can be tuned for different applications without interference. This can be achieved

by employing active components like a transistor to switch on and off the slot structure.

Due to the facility restriction and time limit, the proposed slit-slot antenna and triband slot patch antenna are not measured for practical conformal circumstances and wearable application with real human body, only simulated results are provided.

4.3 Chapter Summary

In this chapter, two slot antennas are proposed for conformal surfaces and wearable applications. One is a microstrip slot antenna with parallel slits loading operating at 5.8 GHz, the other one is a triband slotted microstrip patch antenna operating at 5.8 GHz, 6.2 GHz, and 8.4 GHz, respectively. Both antennas demonstrate good performance and promising potentials in the conformal cylinder bending tests and simulation together with human body hand model for wearable applications.

Chapter 5

Metasurface in Antenna Design as Polarization Converter

Chapter 3 and Chapter 4 proposed and discussed different approaches of flexible antenna designs for mobile communication, WLAN, and satellite applications, including ink-printed technique on flexible textile substrate and slot antennas fabricated on flexible PCB. In practical cases, even though planar antennas have many advantages such as low profile and low cost, they are restricted by low gain and narrow return-loss bandwidth (RLBW). In general, the RLBW is associated with both the dielectric substrate thickness t and wavelength of operating frequency in free space λ_0 [23, 205]. When the ratio of t/λ_0 is very small, the planar antenna has a very narrow RLBW as well.

Recently metasurfaces are becoming increasingly popular and applied in many applications integrated with antenna designs [144–147, 206]. Metasurface could be the complementary solution to the mentioned drawbacks of planar patch antennas, such as the narrow RLBW or linear polarization. A metasurface based linear-to-circular (LTC) polarization converter can convert linearly polarized (LP) signal into a circularly polarized (CP) signal with enhanced RLBW, while maintaining the planar structure

and low-profile and low-cost features. In this chapter, a general design algorithm for metamaterial/metamaterial surface is discussed, and then a split ring resonator (SRR) based metamaterial surface LTC converter is proposed at 12.4 GHz for K_u -band satellite communication and navigation applications. The design can be easily tuned for other frequency bands applications as well by manipulating the metamaterial surface parameters. Furthermore, conformal test simulations are provided to evaluate the performance for flexible surfaces and wearable applications.

5.1 Metasurface Design Algorithm

In this section, a metamaterial/metamaterial surface design algorithm from the perspectives of system level, particle level and mask generation is presented. As discussed previously in Chapter 2, metamaterials consist of artificial sub-wavelength unit cells, which are deployed spatially discrete and are regarded as a particle. To design a type of metamaterial with certain functionalities, the principle is to obtain the optimised geometric parameters of the particles so that the metamaterial system with these particles can attain desired homogeneous or inhomogeneous parameters.

As illustrated in Figure 5.1, the design procedure includes three fundamental steps: system level design, particle level design, and mask generation [139].

5.1.1 System Level Design

In the first stage, with desired metamaterial functionalities given, the material parameters determining its spatial distribution can be computed. To be specific, the spatially varying permittivity, permeability, and refractive index will be computed via optical transformation. Both analytical computation and numerical computation can be applied in this stage.

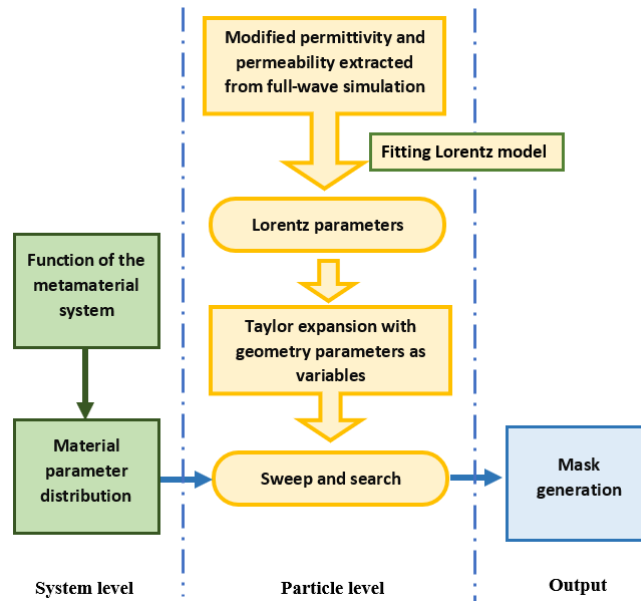


Figure 5.1: Metamaterial design procedure diagram [139, 140].

5.1.2 Particle Level Design

In the particle level design procedure, it aims to generate the geometric parameters of the particles or unit cells, which are optimised through computation. There are totally four sub-steps as explained below.

1. A small group of samples are simulated, where miscellaneous geometric parameters are assigned to the proposed metamaterial particles. Then the simulated particles' constitutive parameters (permittivity and permeability) can be extracted from simulated transmission coefficient T and reflection coefficient R in the local field response. If the metamaterial particles are resonant, these extracted parameters should agree in the form of Drude-Lorentz model.
2. Depending on if the simulated metamaterial particles are resonant or not, those extracted permittivity and permeability curves will be fitted with a Drude-Lorentz model or by Taylor expansion. Drude-Lorentz model is for the resonant particles, whereas Taylor expansion can be applied for the non-resonant particles.

3. This step is to set up a mathematical relation between the Drude-Lorentz model and the metamaterial particles' geometric parameters through another curve fitting process. Theoretically, a mathematical relation between the Drude-Lorentz model (or Taylor expansion) coefficients and particle geometric parameters can be obtained in this step.
4. In order to obtain the optimised material parameters, a sweep will be performed across all the available geometric parameters, based on which, material parameters can be calculated by the mathematical relation from Step three. During the sweeping, some other considerations will be taken into account, such as the limitation in fabrication process and the actual dimensions in practical applications etc.

In particle level design, it targets at determining the geometric dimensions of metamaterial particles so that the overall metamaterial parameters will fit the system level design. Computational electromagnetics based full-wave simulation and Scattering (S)-parameter retrieval methods will be applied to achieve a rapid design procedure within a small and limited number of simulations, despite of the the number of metamaterial particles involved.

5.1.2.1 Drude-Lorentz Model

It is known that metamaterials normally have resonant particles as their unit cell, some common ones are the split ring resonator (SRR), the electric field coupled resonator (ELC), and the complimentary SRR (CSRR). Responses to electromagnetic fields are caused by the resonance. These responses are then governed by dispersive permittivity $\bar{\epsilon}$ for electric fields and dispersive permeability $\bar{\mu}$ for magnetic fields, respectively. Drude-Lorentz model is applied to describe the dispersion and can be extracted from averaging the local fields [139, 140].

5.1 METASURFACE DESIGN ALGORITHM

At the same time, there is also alternative approaches to retrieve the effective constitutive parameters, i.e., the effective permittivity ε_{eff} and the effective permeability μ_{eff} , respectively. The average ($\bar{\varepsilon}$ and $\bar{\mu}$) and effective set (ε_{eff} and μ_{eff}) of constitutive parameters theoretically will not be congruent due to both the non-zero particle size and the homogenisation approximation as they are regarded as homogeneous materials.

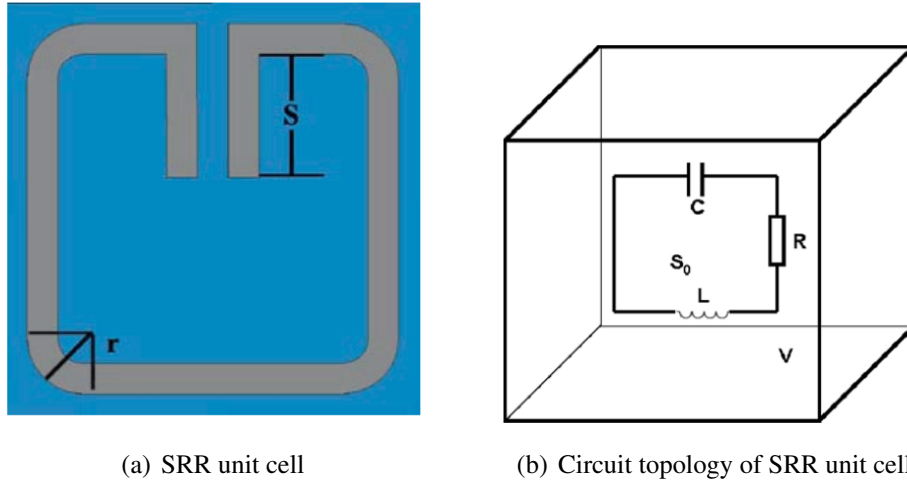


Figure 5.2: SRR unit cell example and its equivalent circuit spatial model [139, 140].

As illustrated in Figure 5.2, for an SRR metamaterial particle, it can be described by an equivalent RLC circuit with unit cell area S_0 and unit cell volume V . When magnetic flux across the area of the SRR unit cell, resonance is excited in the circuit. Analytical solution suggests that the permeability of an SRR unit cell can be given by Drude-Lorentz model with a frequency dispersion as [139, 140]

$$\bar{\mu} = \mu_0 \left(1 + \frac{F f^2}{f^2 - f_0^2 + i\gamma f} \right), \quad (5.1)$$

where F , γ , and f_0 are fitting parameters, representing oscillation factor, damping factor, and resonant frequency, respectively [139, 140].

$$F = \frac{\mu_0 S_0^2 / V}{L + \mu_0 S_0^2 / V}, \quad (5.2)$$

5.1 METASURFACE DESIGN ALGORITHM

$$f_0 = \frac{1}{2\pi\sqrt{(L + \mu_0 S_0^2/V)C}}, \quad (5.3)$$

$$\gamma = \frac{R}{2\pi(L + \mu_0 S_0^2/V)}. \quad (5.4)$$

Meanwhile, the effective permittivity ε_{eff} and permeability μ_{eff} have a relation to refractive index n [139, 140]. Additionally, the refractive index can be expressed in terms of the set of average constitutive parameters $\bar{\varepsilon}$ and $\bar{\mu}$.

$$n = \pm\sqrt{\mu_e \varepsilon_e}, \quad (5.5)$$

$$\sin\left(\frac{nk_0 d}{2}\right) = \pm\frac{\omega d}{2}\sqrt{\bar{\mu}\bar{\varepsilon}}, \quad (5.6)$$

where d is the unit cell dimension along the direction of wave propagation. Equations (5.5) and (5.6) indicate that when d is infinitely small and approaching 0, i.e., the unit cell size is infinitely small, these two equations tend to become equivalent, as well as $\bar{\varepsilon}$, $\bar{\mu}$ and ε_{eff} , μ_{eff} .

On the other hand, the wave impedance η refers to the ratio of electric and magnetic field intensity and can be represented as

$$\eta = \sqrt{\frac{\mu_e}{\varepsilon_e}}, \quad (5.7)$$

and through a complex analysis [207], wave impedance can be related to average permittivity and permeability in terms of pure electric resonance and pure magnetic resonance, represented in equation (5.8) and (5.9), respectively:

$$\eta = \sqrt{\frac{\bar{\mu}}{\bar{\varepsilon}}} \cdot \cos \frac{\theta}{2}, \quad (5.8)$$

$$\eta = \sqrt{\frac{\bar{\mu}}{\bar{\varepsilon}}} \cdot \left(\cos \frac{\theta}{2} \right)^{(-1)}. \quad (5.9)$$

Given transmission and reflection coefficients, R and T , we can obtain refractive index n and wave impedance η from equations (5.10) and (5.11):

$$\cos(nkd) = \frac{1}{2T} (1 - R^2 + T^2), \quad (5.10)$$

$$\eta = \sqrt{\frac{(1 + R)^2 - T^2}{(1 - R)^2 - T^2}}. \quad (5.11)$$

However, assuming the resonance happening in the particles is pure electric or magnetic resonance does not match most of the practical cases, which are far more complicated. For the cases where both electric and magnetic resonance coexist over different frequencies, it is necessary to have a modified method to retrieve the dispersion curves for permittivity and permeability. Hence, another modified set of constitutive parameters, ε_m and μ_m are introduced.

$$\tan \frac{nk_0d}{2} = \pm \frac{\omega d}{2} \sqrt{\mu_m \varepsilon_m}, \quad (5.12)$$

$$\eta = \sqrt{\frac{\mu_m}{\varepsilon_m}}, \quad (5.13)$$

where $\bar{\varepsilon}$ and $\bar{\mu}$ are transformed into ε_m and μ_m with approximation for curve fitting.

The following scenarios apply:

- $\mu_m = \bar{\mu}$, $\varepsilon_m = \bar{\varepsilon} \cdot \frac{1}{\cos^2(\theta/2)}$ for pure electric resonance;

5.1 METASURFACE DESIGN ALGORITHM

- $\mu_m = \bar{\mu} \cdot \frac{1}{\cos^2(\theta/2)}$, $\varepsilon_m = \bar{\varepsilon}$ for pure magnetic resonance;
- $\mu_m = \bar{\mu} \cdot \frac{1}{\cos(\theta/2)}$, $\varepsilon_m = \bar{\varepsilon} \cdot \frac{1}{\cos(\theta/2)}$ for simultaneous electric and magnetic resonances.

Research shows that the modified constitutive parameters ε_m and μ_m have advantages in demonstrating electric and magnetic resonant frequencies unambiguously when multiple resonances coexist concurrently at different frequencies, especially when the metamaterial particle is in complex structure. In conclusion, this set of constitutive parameters can be utilised to accomplish a sophisticated design, in which material parameters are involved, such as refractive index n , wave impedance η , effective permittivity ε_m and permeability μ_m , transmission T and reflection R coefficients.

5.1.2.2 Fitting Drude-Lorentz Model

Thus far, the frequency-dispersive constitutive parameters of the metamaterial particles are obtained as a function of frequency at discrete points, i.e., $\varepsilon_m(f)$ and $\mu_m(f)$, respectively. The next step is to obtain their analytical expressions [139, 140].

Based on the Drude-Lorentzian resonance, we need to fit the curves of $\varepsilon_m(f)$ and $\mu_m(f)$ into the forms indicated in equation (5.14) and (5.15):

$$\mu_m(f) = \mu_0 \left(1 - \frac{F_u f^2}{f^2 - f_{0u}^2 + i\gamma_u f} \right), \quad (5.14)$$

$$\varepsilon_m(f) = \varepsilon_0 \left(1 - \frac{F_e f^2}{f^2 - f_{0e}^2 + i\gamma_e f} \right). \quad (5.15)$$

where μ_0 and ε_0 are the background permeability and permittivity, F_u and F_e are the magnetic and electric resonant intensity, f_{0u} and f_{0e} are the magnetic and electric

5.1 METASURFACE DESIGN ALGORITHM

resonant frequency, γ_u and γ_e are the magnetic and electric damping factor, respectively. These two sets of parameters are called Lorentz parameters.

For μ_m , we need to extract magnetic Lorentz parameters μ_0 , F_u , f_{0u} , γ_u . It can be noticed that at the resonant frequency f_{0u} , the imaginary part of μ_u has its maximum value, therefore, f_{0u} can be determined by where $\mu_m = \max(\text{imag}(\mu_m(f)))$ happens.

Then, in the frequency range $f_{pu} > f_{0u}$, by locating the points of the minimum value of real part of μ_m , i.e., $\mu_m = \min(\text{real}(\mu_m(f)))$, we can obtain

$$1 - \frac{F_u f_{pu}^2}{f_{pu}^2 - f_{0u}^2 + i\gamma_u f_{pu}} = 0 + i\delta, \quad (5.16)$$

where $\delta = \text{imag}(\mu_m(f_{pu}))$, and the damping factor γ_u is around the scale between $f_{pu}/1000$ and $f_{pu}/10$. Therefore, equation (5.16) can be simplified with approximation as

$$1 - \frac{F_u f_{pu}^2}{f_{pu}^2 - f_{0u}^2} = 0, \quad (5.17)$$

Thus, F_u can be expressed as

$$F_u = 1 - \frac{f_{0u}^2}{f_{pu}^2}. \quad (5.18)$$

After determining f_{0u} and F_u in equation (5.14), one needs to decide μ_0 and γ_u . By rearranging the discrete frequency points f and corresponding value of μ_m from simulations into matrix, we can get

$$[f] = \begin{bmatrix} f_1 \\ f_2 \\ \dots \\ f_m \end{bmatrix}, [f^2] = \begin{bmatrix} f_1^2 \\ f_2^2 \\ \dots \\ f_m^2 \end{bmatrix}, [\mu_m] = \begin{bmatrix} \mu_m(f_1) \\ \mu_m(f_2) \\ \dots \\ \mu_m(f_m) \end{bmatrix}, \quad (5.19)$$

where an initial value of μ_0 is assigned, and $f_{1,2,\dots,m}$ are the discrete frequencies. Then equation (5.14) can be rewritten as

$$F_u [f^2] = \left(1 - \frac{[\mu_m]}{\mu_0}\right) (f_{0u}^2 - [f^2] + i\gamma_u [f]). \quad (5.20)$$

This leads to an overdetermined equation to be solved to find γ_u . Note that we can assume $\mu_0 = 1$ for background materials without magnetic polarizability. On the contrary, for the cases where $\mu_0 \neq 1$, iteration substitution can be applied by submitting γ_u back to equation (5.20) for solving the overdetermined equation again to obtain an improved value of μ_0 , until both μ_0 and γ_u converge at stable values. Altogether, we have obtained all the parameters for equation (5.14) and the reconstructed Drude-Lorentz model.

5.1.2.3 Taylor Expansion of Lorentz Parameters

With the Lorentz model reconstructed and Lorentz parameters retrieved, the next step is to establish a link between the geometric parameters of the metamaterial particle and the Lorentz model. In the full-wave simulation, a key geometric parameter s can be set as a variable while other geometric parameters remain fixed values. By doing so, different sets of reflection and transmission coefficients with respect to s can be obtained from the full-wave simulation. Additionally, other aforementioned parameters f_{0u} , F_u , γ_u and μ_0 are also calculated with respect of each value of s . As the value of s increases, a smooth variation of the Lorentz parameters will be observed and each of

5.1 METASURFACE DESIGN ALGORITHM

them can be expand into Taylor series with respect of s [139, 140]:

$$\begin{aligned}
 f_{0u} &= a_0 + a_1s + a_2s^2 + a_3s^3 + \dots, \\
 F_u &= b_0 + b_1s + b_2s^2 + b_3s^3 + \dots, \\
 \gamma_u &= c_0 + c_1s + c_2s^2 + c_3s^3 + \dots, \\
 \mu_0 &= d_0 + d_1s + d_2s^2 + d_3s^3 + \dots
 \end{aligned} \tag{5.21}$$

Generally, by fitting the second- or third-order Taylor expansion is precise enough to get a stable set of parameters. After that, the modified permeability μ_m can be calculated with any given value of s by equation (5.21) and its the related Taylor coefficients.

For the modified electric permittivity ε_m , it can be regarded as non-dispersive and approximated as $\varepsilon_m = \varepsilon_0$ if no electric resonance in the frequency range is observed. And the constant ε_0 can be expressed in Taylor series as

$$\varepsilon_0 = e_0 + e_1s + e_2s^2 + e_3s^3 + \dots \tag{5.22}$$

If there is another geometric parameters r of the metamaterial particle varying, f_{0u} , F_u , γ_u , μ_0 , and ε_0 should be in the form of Taylor series with two variables:

$$\left\{ \begin{array}{l}
 f_{0u} = a_0 + a_1s + a_2r + a_3s^2 + a_4r^2 + a_5sr + a_6s^3 + a_7r^3 + a_8s^2r + a_9sr^2 + \dots, \\
 F_u = b_0 + b_1s + b_2r + b_3s^2 + b_4r^2 + b_5sr + b_6s^3 + b_7r^3 + b_8s^2r + b_9sr^2 + \dots, \\
 \gamma_u = c_0 + c_1s + c_2r + c_3s^2 + c_4r^2 + c_5sr + c_6s^3 + c_7r^3 + c_8s^2r + c_9sr^2 + \dots, \\
 \mu_0 = d_0 + d_1s + d_2r + d_3s^2 + d_4r^2 + d_5sr + d_6s^3 + d_7r^3 + d_8s^2r + d_9sr^2 + \dots, \\
 \varepsilon_0 = e_0 + e_1s + e_2r + e_3s^2 + e_4r^2 + e_5sr + e_6s^3 + e_7r^3 + e_8s^2r + e_9sr^2 + \dots.
 \end{array} \right. \tag{5.23}$$

Likewise, if multiple geometric parameters appear to be variables, the previous procedure can still be applied by using multiple variable Taylor series expansion. For the

simplicity of the article, it is omitted here. Further calculation of effective parameters can be done by

$$\begin{aligned}\varepsilon_e &= n/\eta, \\ \mu_e &= n\eta.\end{aligned}\tag{5.24}$$

5.1.2.4 Sweep and Search

Ultimately, taking the systematic requirements into consideration, the available sets of geometric parameters of the particle are swept and the optimal set is selected to fulfil the appropriate fabrication standard and resolution.

5.1.3 Mask Generation

After dimension parameters determined in previous step, all the miscellaneous metamaterial particles will be incorporated to generate masks for the fabrication.

5.2 Metasurface Waves Analysis

Metasurfaces can be regarded as an analogy of metamaterials in a 2D structure with a negligible thickness. To manipulate electromagnetic waves propagation, metasurfaces modify the boundary condition due to their theoretically vanishing thickness, whereas normal 3D structured metamaterials are regarded as a reconstruction of the medium with desired constitutive parameters. As a result, metasurfaces can be a substitute of 3D structured metamaterials in some applications.

In this section, a theoretical approach to analyse metasurface will be introduced, and some popular applications in electromagnetic waves will be given as well. Due to the vanishing thickness in metasurface compared with 3D structured metamaterials, the analysis of metamaterials is less effective to be applied in metasurfaces. Instead, an

5.2 METASURFACE WAVES ANALYSIS

impedance theory [153?] is discussed here. We assume that the theory is confined in uni-axial metasurfaces.

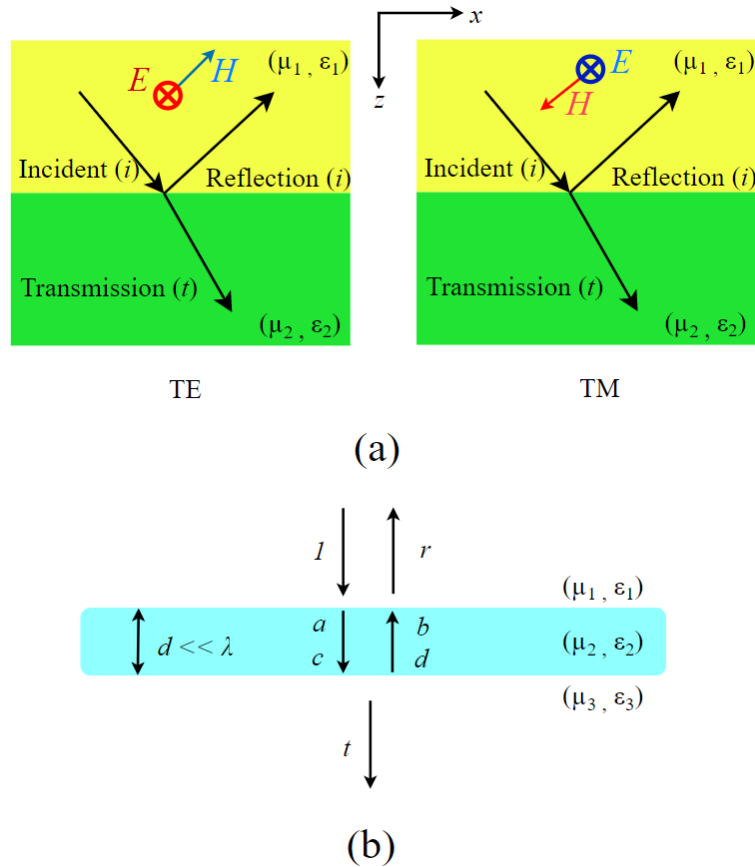


Figure 5.3: Boundary conditions for (a) two adjacent materials and (b) a third thin slab material between two different materials [153] (reproduced) Copyright © 2015 Xiangang Luo et al..

As illustrated in Figure 5.3, first, at the interface between two different dielectric media, the tangent components of the electric field E and magnetic field H have to be continuous to fulfil the electromagnetic boundary condition. Then we can write the boundary conditions for both transverse electric (TE) polarization and the transverse magnetic (TM) polarization as below:

$$\begin{cases} 1 + r = t \\ Y_1(1 - r) = Y_2 t \end{cases} \quad (5.25)$$

5.2 METASURFACE WAVES ANALYSIS

where r and t are the reflection and transmission coefficients, respectively and can be expressed as

$$\begin{cases} r = E_{yr}/E_{yi}, \\ t = E_{yt}/E_{yi} \end{cases} \quad (5.26)$$

for TE polarization, and

$$\begin{cases} r = E_{xr}/E_{xi}, \\ t = E_{xt}/E_{xi} \end{cases} \quad (5.27)$$

for TM polarization. The the admittance Y along the horizontal direction can be determined as

$$Y_i = H_{xi}/E_{yi} \quad (5.28)$$

for the TE polarization, and

$$Y_i = H_{yi}/E_{xi} \quad (5.29)$$

for the TM polarization, where i indicates the medium layer index. Recall and combine Maxwell equations, displayed as equation (5.30) with the boundary conditions, we can get equation (5.31)

$$\begin{cases} \nabla \times E = -\mu\mu_0 \frac{\partial H}{\partial t}, \\ \nabla \times H = \varepsilon\varepsilon_0 \frac{\partial E}{\partial t}, \end{cases} \quad (5.30)$$

$$Y_i = \begin{cases} \frac{k_{zi}}{\mu_i\mu_0\omega} = \frac{\sqrt{\varepsilon_i\mu_i k_0^2 - k_x^2}}{\mu_i\mu_0\omega}, & \text{for TE,} \\ \frac{\varepsilon_i\varepsilon_0\omega}{k_{zi}} = \frac{\varepsilon_i\varepsilon_0\omega}{\sqrt{\varepsilon_i\mu_i k_0^2 - k_x^2}}, & \text{for TM.} \end{cases} \quad (5.31)$$

Note that k_x is the continuous horizontal wave vector in the system for all planar

5.2 METASURFACE WAVES ANALYSIS

multiple layers. If electromagnetic wave propagates from air to another medium and the incidence angle is given as $\theta_i = \arcsin(k_x/k_0)$. By rearranging equation (5.25), the reflection and transmission coefficients r and t can be rewritten as follows:

$$\begin{cases} t = \frac{2Y_1}{Y_1 + Y_2}, \\ r = \frac{Y_1 - Y_2}{Y_1 + Y_2}. \end{cases} \quad (5.32)$$

since the reflection and transmission coefficients r and t are the same for both TE and TM polarization, this approach characterises as concise.

For the case where the metamaterial slab is between two other types of dielectric materials as shown in Figure 5.3, their boundary condition can be expressed as

$$\begin{cases} 1 + r = a + b, \\ Y_1(1 - r) = Y_2(a - b), \\ c + d = t, \\ Y_2(c - d) = Y_3t, \end{cases} \quad (5.33)$$

where 1, 2, and 3 are the layer index from the top to bottom and a , b , c , and d stand for the coefficients for the counter-propagating waves in the metamaterial. The relations between these coefficients are expressed as

$$\begin{cases} a = c \exp(-ik_{z2}h) \\ b = d \exp(ik_{z2}h) \end{cases} \quad (5.34)$$

If the metasurface has vanishing thickness like this case where $|k_z h| \ll 1$, approximation can be made so that

$$\begin{cases} a = c(1 - ik_{z2}h), \\ b = d(1 + ik_{z2}h). \end{cases} \quad (5.35)$$

By rearranging equation (5.35), the following expressions can be obtained

$$\begin{cases} a + b = (c + d) + ik_{z2}h(c - d), \\ a - b = (c - d) - ik_{z2}h(c + d). \end{cases} \quad (5.36)$$

For the discussion in this case, the metamaterial slab permittivity and/or permeability are larger than those of the vicinity. As we know that for a non-magnetic layer, of which $Y_2 \gg Y_3$, i.e., $c - d \ll c + d$. Then equation (5.36) can be approximated as

$$\begin{cases} a + b = (c + d), \\ a - b = \frac{Y_3}{Y_2}t - ik_{z2}ht. \end{cases} \quad (5.37)$$

By substituting equation (5.37) into equation (5.33), it yields

$$\begin{cases} 1 + r = t, \\ Y_1(1 - r) = Y_3t - iY_2k_zht. \end{cases} \quad (5.38)$$

Comparing the above equation with the electric impedance boundary conditions

$$\begin{cases} 1 + r = t, \\ Y_1(1 - r) = Y_3t + Y_e t, \end{cases} \quad (5.39)$$

the electric admittance Y_e of the metamaterial slab can be derived as

$$Y_e = -iY_2k_{z2}h = \begin{cases} -i\frac{\varepsilon_2k_0^2 - k_x^2}{\mu_0\omega}h \approx -i\omega\varepsilon_2\varepsilon_0h, \\ -i\omega\varepsilon_2\varepsilon_0h. \end{cases} \quad (5.40)$$

Alternatively, if the permeability μ is much higher than ε , we have $Y_2 \ll Y_3$, i.e., $c - d \gg c + d$, equation (5.36) can be approximated as

$$\begin{cases} a + b = c + d - ik_{z2}h(c - d), \\ a - b = c - d. \end{cases} \quad (5.41)$$

Similarly, by substituting the above equations into equation (5.33), we will have

$$\begin{cases} 1 + r = t - ik_{z2}h\frac{Y_3}{Y_2}t, \\ Y_1(1 - r) = Y_3t. \end{cases} \quad (5.42)$$

If we compare these equations with the magnetic impedance boundary conditions

$$\begin{cases} 1 + r = t + Z_m Y_3 t, \\ Y_1(1 - r) = Y_3 t, \end{cases} \quad (5.43)$$

it yields the magnetic impedance as follows:

$$Z_m = -i\frac{k_{z2}h}{Y_2} = \begin{cases} -i\omega\mu_2\mu_0h, \\ -i\frac{\varepsilon_2\mu_2k_0^2 - k_x^2}{\varepsilon_2\varepsilon_0\omega}h \approx -i\omega\mu_2\mu_0h. \end{cases} \quad (5.44)$$

Thus far, it is clear that if $k_z h \ll 1$ and the metamaterial permittivity and permeability are greatly larger than 1, all the above assumptions will stand valid even for oblique incidence. Additionally, equations (5.40) and (5.44) are very similar with previous results [208], and they are valid for homogeneous materials. For those metasurfaces with sub-wavelength structures, a similar approach can be applied to obtain their effective impedances [154].

For the cases where no magnetic response in the thin slab, their corresponding reflection and transmission coefficients can be derived from equation (5.39) as:

$$\begin{cases} r = \frac{Y_1 - Y_3 - Y_e}{Y_1 + Y_3 + Y_e}, \\ t = \frac{2Y_1}{Y_1 + Y_3 + Y_e}. \end{cases} \quad (5.45)$$

These equations can be regarded as revised Fresnel equations for metasurfaces, which is an analogy to equation (5.32). There are two general types of metasurface waves:

5.2 METASURFACE WAVES ANALYSIS

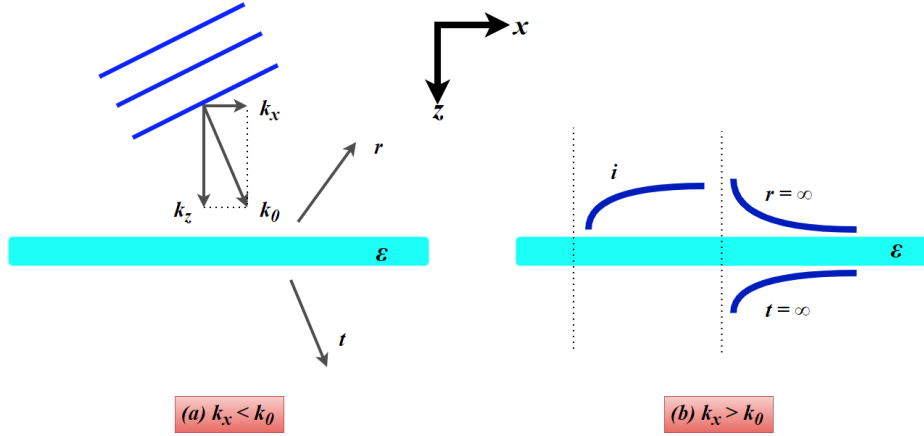


Figure 5.4: Illustration of two types of metasurface waves: (a) $k_x < k_0$, (b) $k_x > k_0$ [153] (reproduced) Copyright © 2015 Xiangang Luo et al..

with the condition $k_x < k_0$ for metasurface wave propagating through the surface and $k_x > k_0$ for the metasurface wave propagating along the surface, respectively.

The first case of $k_x < k_0$, metasurface waves tend to propagate through the surface, and both transmission and reflection will happen at the boundary. Due to the difference between these media, an abrupt change in the phase and amplitude of the reflection and transmission coefficients will be observed and calculated previous analysis and equations (5.32) to (5.45).

On the other hand, for the case where $k_x > k_0$ and metasurface waves propagating along the surface, the surface plasmon mode can be derived through enforcing the reflection and transmission coefficients to be simultaneously infinite. The boundary condition at a single interface with dielectric and metal from equation (5.32) will become $Y_1 + Y_2 = 0$, which leads to a propagation constant for TM polarization:

$$\beta = k_x = k_0 \sqrt{\frac{\varepsilon_1 \varepsilon_2}{\varepsilon_1 + \varepsilon_2}}. \quad (5.46)$$

Because we limited the analysis to the case of nonmagnetic response, there is no solution for TE polarization. The above equation can just be the solution of traditional surface

plasmon polariton (SPP) mode.

For another case illustrated in Figure 5.3, where a metallic layer is embedded in a dielectric media (insulator-metal-insulator, IMI), the guiding wave can be achieved in the same way earlier as $Y_1 + Y_3 + Y_e = 0$. The propagation constant can be obtained through

$$\frac{\varepsilon_1}{\sqrt{\varepsilon_1 k_0^2 - \beta^2}} + \frac{\varepsilon_3}{\sqrt{\varepsilon_3 k_0^2 - \beta^2}} + \frac{Y_e}{\varepsilon_0 \omega} = 0. \quad (5.47)$$

If we assume that $\varepsilon_1 = \varepsilon_3$, the propagation constant will be given as:

$$\beta = k_0 \sqrt{\varepsilon_1 - (2Y_1/Y_e)^2}, \quad (5.48)$$

By substituting $Y_e = -i\omega\varepsilon_2\varepsilon_0h$, it can be rewritten as:

$$\beta = \sqrt{\varepsilon_1 k_0^2 + \left(\frac{2\varepsilon_1}{\varepsilon_2 h}\right)^2}. \quad (5.49)$$

According to the above equation, as the thickness decreases, the wavelength of the coupled SPP tends to vanish. However, this approximation does not hold for the MIM structure. Instead, by solving the Maxwell's equations with boundary conditions, we can get more accurate propagation constants derived from directivity [209]:

$$\tanh\left(\sqrt{\beta^2 - \varepsilon_d k_0^2} h/2\right) = -\frac{\varepsilon_d \sqrt{\beta^2 - \varepsilon_m k_0^2}}{\varepsilon_m \sqrt{\beta^2 - \varepsilon_d k_0^2}}. \quad (5.50)$$

Most metal conductors behave as almost perfect conductors in microwave frequencies, so no SPP could be found on an ideal planar metal surface. Conversely, for a metal surface with punctured sub-wavelength holes, the effective permittivity can be freely tuned to sustain SPP, with following parameters:

5.3 METASURFACE BASED S-SHAPED SPLIT RING RESONATOR FOR LINEAR-TO-CIRCULAR POLARIZATION CONVERSION

$$\begin{cases} \mu_x = \mu_y = \frac{8\alpha^2\mu_h}{\pi^2 p^2}, \\ \varepsilon_x = \varepsilon_y = \frac{\pi^2 p^2 \varepsilon_h}{8a^2} \left(1 - \frac{\pi^2 c^2}{a^2 \omega^2 \varepsilon_h \mu_h} \right). \end{cases} \quad (5.51)$$

And the plasmon frequency is the same as the cutoff frequency:

$$\omega_{pl} = \frac{\pi c}{\sqrt{\varepsilon_h \mu_h}}. \quad (5.52)$$

5.3 Metasurface Based S-Shaped Split Ring Resonator for Linear-to-Circular Polarization Conversion

For an antenna, polarization is one of the most important characteristics because its performance can vary significantly due to the inherent polarization-sensitive property in the materials involved in electromagnetic wave propagation. Therefore, polarization conversion of electromagnetic waves becomes significant for certain practical applications, especially LTC polarization conversion [197, 210]. Conventional polarization manipulation methods are normally achieved via the application of complex structures, such as birefringent crystalline liquid or crystals. These converters normally come in large size and thickness, making it difficult for compact system integration. Additionally, low efficiency is another drawback for the conventional polarization converters [197].

In recent years, metamaterial has become popular, providing new ways for polarization conversion. Metamaterials can be defined as artificially crafted composite materials whose properties are derived from internal microstructure, rather than chemical composition found in natural materials. For example, it typically requires multiple stacks of material layers to realise the fascinating functionalities of metamaterials. This not only brings a lot of challenges in nanofabrication, but also leads to extensive losses. Many metamaterials consist of complex metallic wires and other structures that require

5.3 METASURFACE BASED S-SHAPED SPLIT RING RESONATOR FOR LINEAR-TO-CIRCULAR POLARIZATION CONVERSION

sophisticated fabrication technology and are difficult to assemble [141, 152].

To overcome those obstacles faced by metamaterials, metasurfaces are proposed and they feature thin films composed of individual elements. Metasurface generally refers to a periodic or quasi-periodic planar array of sub-wavelength units [152]. By applying different types of unit cell structure and manipulating its parameters, the metasurface will demonstrate different characteristics in reflecting electromagnetic waves, in terms of frequencies, amplitudes, phases and bandwidths. The thickness of metasurface is also relatively smaller depending on the dielectric material selected [197, 210].

In [211], an LTC converter based on substrate integrated waveguide cavity unit cell for 15 GHz - 15.7 GHz was proposed. However, the feasibility of fabrication is high due to the structure of metallic via holes, which can also increase the fragility of the entire surface, given the number and density of the via holes. In [212], a dual-band circular polarization converter based on anisotropic metamaterial was proposed for 4.5 GHz and 7.9 GHz application, however, it employed a three-layer structure, which increased the difficulty for fabrication.

A three-band metasurface based polarization converter was presented in [213]. The design has a double layer structure with "L" shaped periodic element. Depending on the different incident angle, the converter can convert the TM polarized incident wave into RHCP reflection wave at 12.5 GHz, TE polarized reflection wave at 18 GHz, and LHCP reflection wave at 22.5 GHz, respectively. The result of the proposed design was very sensitive to the incident angle. A significant deviation can be observed when the incident angle had a minor change. In addition, the double FR4 layers added complexity to the structure and overall thickness. Another LTC polarization converter for broadband application was reported in [214], which employed a "%"-shaped unit cell on one side of the dielectric substrate and a metal patch on the other side. The converter has high efficiency and conversion rate at desired frequency. However, the

5.3 METASURFACE BASED S-SHAPED SPLIT RING RESONATOR FOR LINEAR-TO-CIRCULAR POLARIZATION CONVERSION

incident angle dependency was high. Similar to the design in [213], the double metallic layer is another drawback of the design.

Through careful literature, a low-profile single layered metasurface based LTC polarization converter is proposed on a flexible substrate. Both the performance in normal and conformal situations are presented.

5.3.1 Structure Design and Parametric Study

Theoretically, when an incident wave reaches on the surface of polarization converter, it will be reflected with a certain magnitude and phase. For instance, given a downward y -polarized incident wave, the reflected wave E_r can be expressed by [197]:

$$\mathbf{E}_r = E_{xr} \mathbf{e}_x + E_{yr} \mathbf{e}_y = E_x \exp(j\phi_{xy}) \mathbf{e}_x + E_y \exp(j\phi_{yy}) \mathbf{e}_y, \quad (5.53)$$

where E_x and E_y are the x and y components of the electric field, respectively; \mathbf{e}_x and \mathbf{e}_y are the x and y unit direction vector, respectively. From equation (5.53), R_{xy} and R_{yy} are defined by equation (5.54) and (5.55), respectively, to represent the reflection coefficient magnitudes of y -to- x and y -to- y polarization conversion, respectively,

$$R_{xy} = |E_{xr}/E_{yi}|, \quad (5.54)$$

$$R_{yy} = |E_{yr}/E_{yi}|, \quad (5.55)$$

whereas ϕ_{xy} and ϕ_{yy} are their corresponding phases. To achieve an LTC polarization conversion, two conditions have to be fulfilled, which are

$$R_{xy} = R_{yy} \quad (5.56)$$

5.3 METASURFACE BASED S-SHAPED SPLIT RING RESONATOR FOR LINEAR-TO-CIRCULAR POLARIZATION CONVERSION

and

$$\Delta\phi = \phi_{yy} - \phi_{xy} = 2n\pi \pm \pi/2, \quad (5.57)$$

where $\Delta\phi$ is the phase difference between E_{xr} and E_{yr} . When $\Delta\phi$ has a " $-\pi/2$ " component, it indicates a right-hand circular polarization (RHCP), whereas a " $+\pi/2$ " component indicates a left-hand circular polarization.

To further evaluate the polarization conversion, four Stroke parameters, I , Q , U , and V , are introduced, as shown in equation (5.58) to (5.61) [197]:

$$I = |R_{xy}|^2 + |R_{yy}|^2, \quad (5.58)$$

$$Q = |R_{yy}|^2 - |R_{xy}|^2, \quad (5.59)$$

$$U = 2 |R_{xy}| |R_{yy}| \cos \Delta\phi, \quad (5.60)$$

$$V = 2 |R_{xy}| |R_{yy}| \sin \Delta\phi. \quad (5.61)$$

As the parameter to describe the degree to which the polarization has been converted, ellipticity e is defined as

$$e = V/I, \quad (5.62)$$

and it is a perfect LHCP conversion when $e = 1$; while it indicates a perfect RHCP conversion when $e = -1$.

Moreover, two angles α and β are defined by the Stroke parameters as expressed in

5.3 METASURFACE BASED S-SHAPED SPLIT RING RESONATOR FOR LINEAR-TO-CIRCULAR POLARIZATION CONVERSION

equation (5.63) and (5.64):

$$\tan 2\alpha = U/Q, \quad (5.63)$$

$$\sin 2\beta = V/I, \quad (5.64)$$

where α is the polarization azimuth angle while β is the ellipticity angle. Additionally, from the given phase difference $\Delta\phi$, the axial ratio (AR) can be calculated by [215]:

$$\text{AR} = \left(\frac{|R_{yy}|^2 + |R_{xy}|^2 + \sqrt{a}}{|R_{yy}|^2 + |R_{xy}|^2 - \sqrt{a}} \right)^{1/2}, \quad (5.65)$$

where

$$a = |R_{yy}|^4 + |R_{xy}|^4 + 2 |R_{yy}|^2 |R_{xy}|^2 \cos(2\Delta\phi). \quad (5.66)$$

Another two parameters, energy conversion efficiency η and polarization conversion rate (PCR), are given by equation (5.67) and (5.68), respectively:

$$\eta = (|E_{xr}|^2 + |E_{yr}|^2) / |E_{yi}|^2 = |R_{xy}|^2 + |R_{yy}|^2. \quad (5.67)$$

$$\text{PCR} = \frac{|R_{xy}|^2}{|R_{xy}|^2 + |R_{yy}|^2}. \quad (5.68)$$

The proposed LTC polarization converter has a periodic unit cell, which is basically a combination of an anisotropic "S"-shaped outer split ring resonators (SRR) and two "C"-shaped inner SRRs as shown in Figure 5.5(a). The two "C"s are placed inside the openings of the "S" so that the entire structure is centrosymmetrical. The proposed converter is designed on a flexible substrate, Rogers RT/droid 5880, which has a thickness $t = 1.575$ mm and a dielectric constant $\epsilon_r = 2.2$. The periodicity of the unit

5.3 METASURFACE BASED S-SHAPED SPLIT RING RESONATOR FOR LINEAR-TO-CIRCULAR POLARIZATION CONVERSION

cell is $p = 13$ mm.

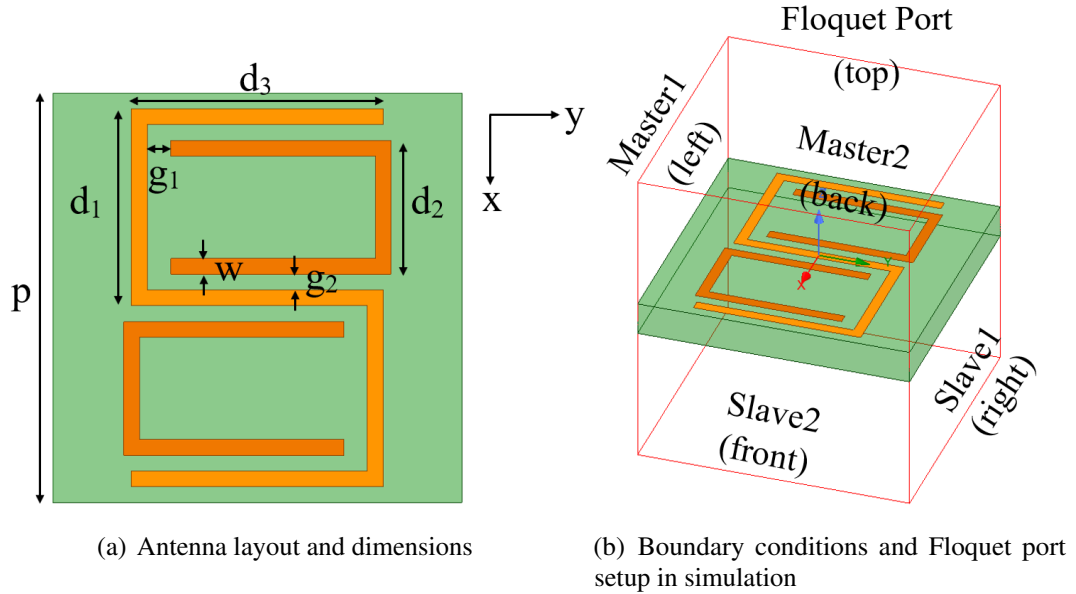


Figure 5.5: Antenna layout and simulation setup.

The design is simulated in HFSS, where the unit cell is placed in an air box as shown in Figure 5.5(b) and the distance between the unit cell and the top/bottom of the air box is set as $\lambda/2$, half wavelength of the frequency of interest. To repeat the periodic structure, master and slave boundary conditions are set up for infinite array approximation. In addition, Floquet port is assigned to the top face of the radiation box, to simulate the incident wave source, as shown in Figure 5.5(b).

For the optimisation of the unit cell dimensions and post-design tuning, several parametric studies are conducted to evaluate the influences caused by g_1 and W_s , namely the gap between "S" and "C" and the conductive trace width, respectively.

A parametric sweep for the gap between "S" and "C", g_1 , is set as values of 0.25 mm, 0.50 mm, 0.75 mm, 1.25 mm, 1.75 mm, and 2.25 mm, respectively. The impact of g_1 on the reflection coefficients of this design is described in Figure 5.6 and 5.7. As can be seen in Figure 5.6(a), the frequency of y -to- y reflection gradually shifts from 12.2 GHz

5.3 METASURFACE BASED S-SHAPED SPLIT RING RESONATOR FOR LINEAR-TO-CIRCULAR POLARIZATION CONVERSION

to 14.8 GHz with the increment of the value of g_1 . In addition, $|R_{yy}|$, the magnitude of the y -to- y conversion reflection coefficient reaches maximum value of about 0.8 when g_1 is 1.75 mm and 2.25 mm, which means 80% of the y -polarized incident wave is reflected remaining the same polarization.

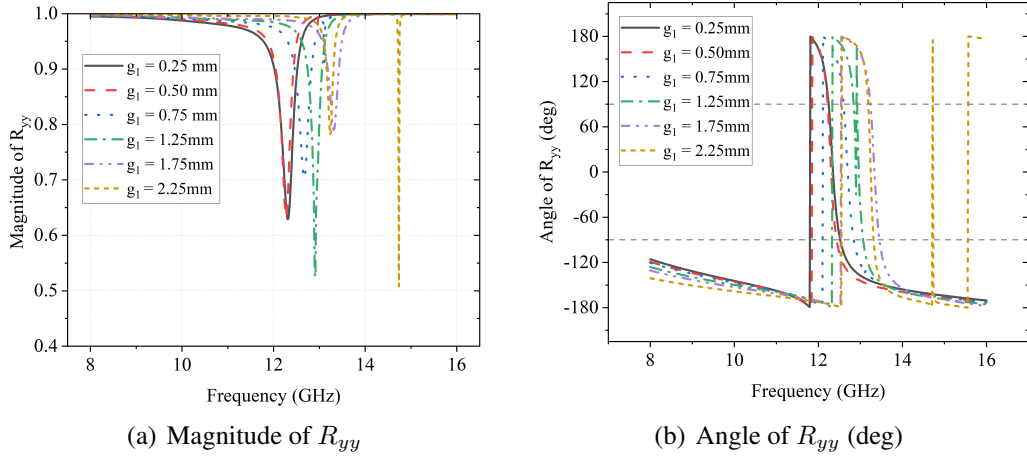


Figure 5.6: Effect of g_1 on R_{yy} .

Correspondingly, there is also phase changes happening along the reflection, which can be seen in Figure 5.6(b). In the scenarios with different g_1 values, an abrupt 360° phase change (from -180° to 180°) can be observed at the same frequencies where the reflection happens.

On the other hand, the magnitude and phase of the reflection coefficient of y -to- x polarization conversion R_{xy} are reflected in Figure 5.7. Figure 5.7(a) presents the phenomenon that the frequency of reflection increase from 12.4 GHz to 13.5 GHz as g_1 varies from 0.25 mm to 2.25 mm, which is similar to that of R_{yy} . The maximum over 70% reflection happens at about 12.4 GHz when g_1 is 0.25 mm and 0.50 mm. As for the phase of y -to- x conversion, ϕ_{xy} , also has an abrupt change from -180° to 180° in each scenario.

Taking the phases of both y -to- y and y -to- x reflection from above results, the phase

5.3 METASURFACE BASED S-SHAPED SPLIT RING RESONATOR FOR LINEAR-TO-CIRCULAR POLARIZATION CONVERSION

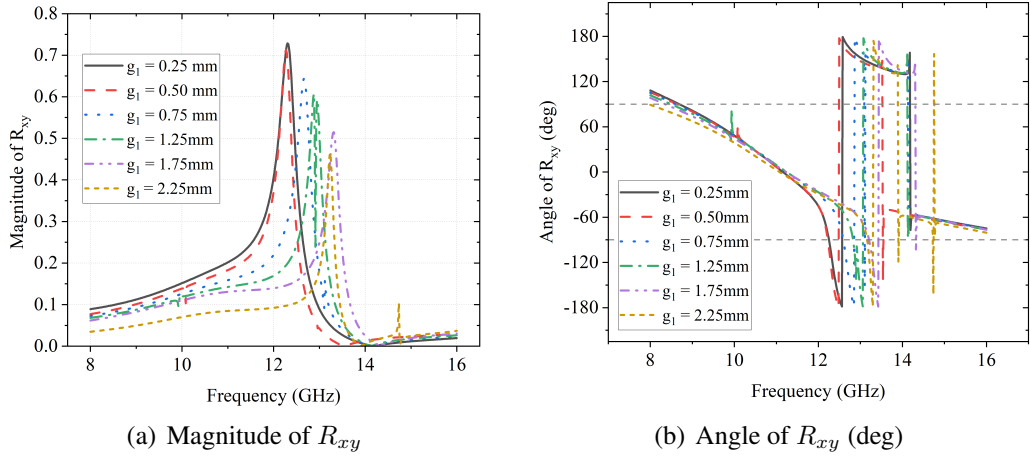


Figure 5.7: Effect of g_1 on R_{xy} .

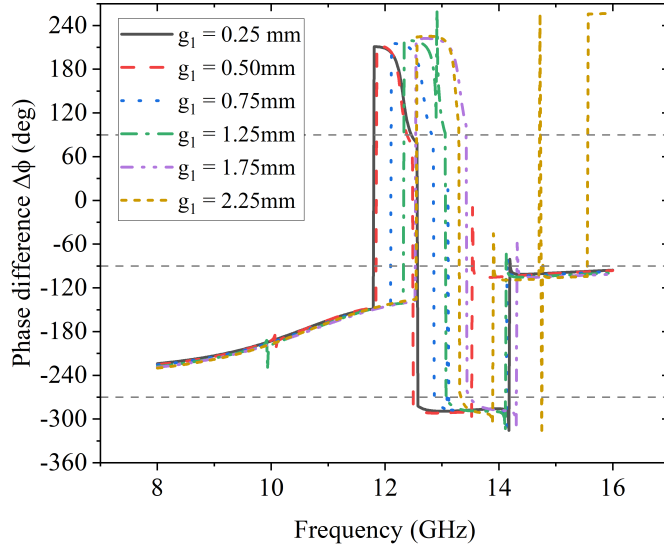


Figure 5.8: Effects of g_1 on phase difference $\Delta\phi$.

difference $\Delta\phi$ can be obtained as shown in Figure 5.8. According to the second condition to achieve LTC conversion in equation (5.57), three grey dash reference lines are plotted in Figure 5.8 to indicate the values of interests when $\Delta\phi = 90^\circ$, -90° and -270° . There are two regions where the $\Delta\phi$ curves coincide with the reference dash lines: one is the region from 12.5 GHz to 14 GHz and $\Delta\phi = -90^\circ$. For different values of g_1 , the spans of the region vary significantly. Approximately, when $g_1 = 0.25$ mm, the curve has largest span from 12.5 GHz to 14 GHz; when $g_1 = 0.75$ mm, the span

5.3 METASURFACE BASED S-SHAPED SPLIT RING RESONATOR FOR LINEAR-TO-CIRCULAR POLARIZATION CONVERSION

is the narrowest near 13 GHz. The other region is from 14.1 GHz to 16 GHz with $\Delta\phi = -270^\circ$, where each curve has roughly the same span.

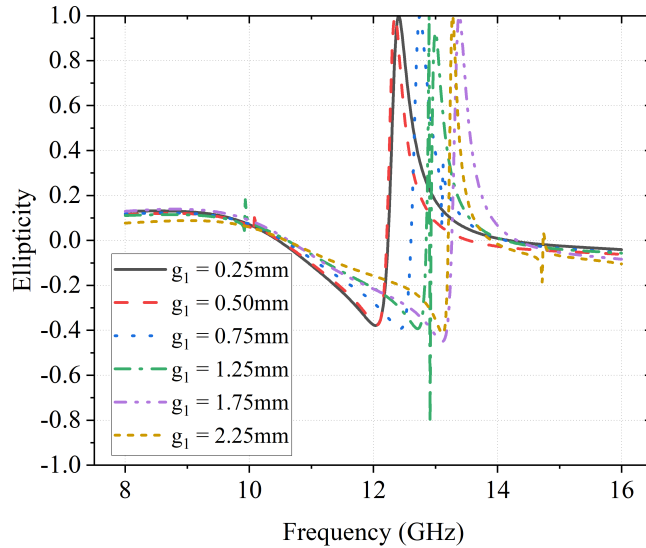


Figure 5.9: Effects of g_1 on ellipticity e .

In Figure 5.9, the ellipticity e derived from the Stroke Parameters is illustrated. It can be observed that e reaches 1 in each case at different frequency, which indicates the converted polarization is LHCP. No RHCP can be found for $e = -1$.

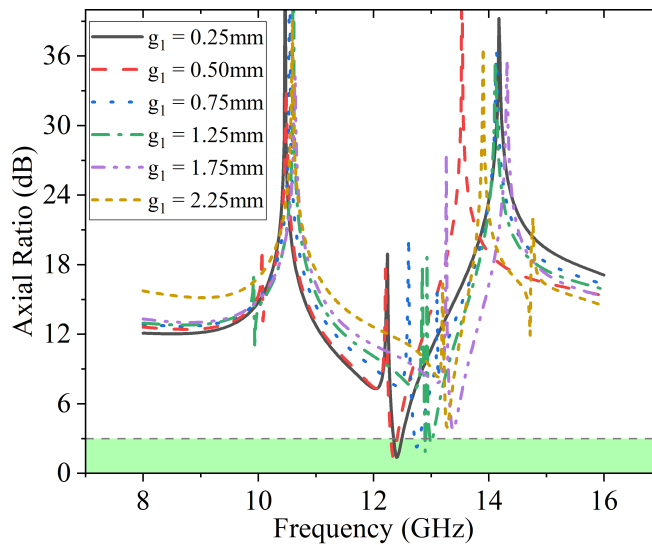


Figure 5.10: Effects of g_1 on axial ratio.

5.3 METASURFACE BASED S-SHAPED SPLIT RING RESONATOR FOR LINEAR-TO-CIRCULAR POLARIZATION CONVERSION

Another criterion to verify a circular polarization is the axial ratio, which is illustrated in Figure 5.10. The highlighted green area indicates the <3 dB region for circular polarization, where only four curves can be found, i.e., $g_1 = 0.25$ mm, $g_1 = 0.50$ mm, $g_1 = 0.75$ mm, and $g_1 = 1.25$ mm.

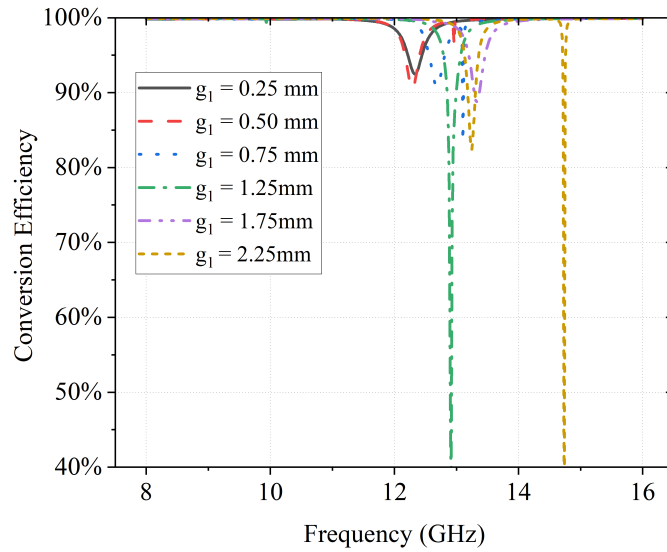


Figure 5.11: Effects of g_1 on conversion efficiency η .

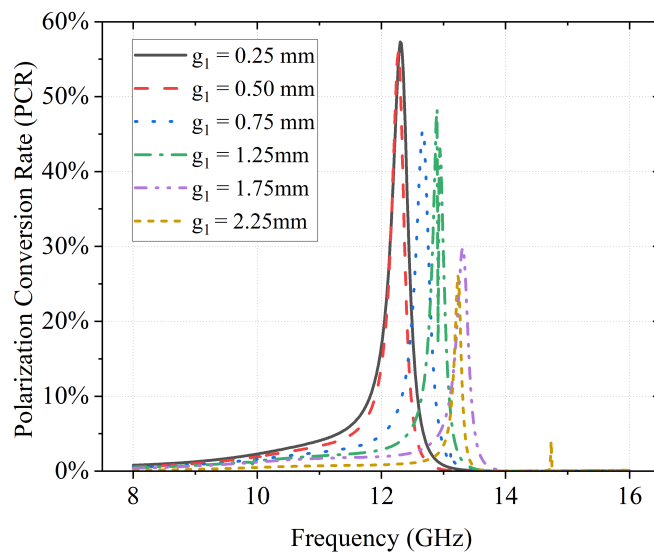


Figure 5.12: Effects of g_1 on polarization conversion rate.

The energy conversion efficiency η and polarization conversion rate are illustrated in

5.3 METASURFACE BASED S-SHAPED SPLIT RING RESONATOR FOR LINEAR-TO-CIRCULAR POLARIZATION CONVERSION

Figure 5.11 and 5.12, respectively. It is clear that the energy conversion efficiency of each case is above 80%, except the case of $g_1 = 1.25$ mm and $g_1 = 2.25$ mm. This might be because that the amount of electromagnetic waves reflected by the unit is very sensitive to the parameter g_1 . On the other hand, the maximum PCRs gradually decrease as g_1 increases. When $g_1 = 0.25$ mm, it has the highest maximum PCR of about 58%.

Next, a parametric sweep of the trace width W_s is simulated, where W_s is set as 0.25 mm, 0.45 mm, 0.50 mm, 0.65 mm, and 0.75 mm. The impacts of W_s on the y -to- y reflection component are illustrated in Figure 5.13. As can be seen in Figure 5.13(a), the magnitude of y -to- y reflection has a minimum at a certain frequency, which shifts from 11.8 GHz to 13 GHz as W_s increases. When W_s is 0.25 mm, $|R_{yy}|$ is 0.6, which means 60% of the y -polarized incident wave is reflected as y -polarized wave. Correspondingly, abrupt 360° changes in phase ϕ_{yy} can be found in Figure 5.13(b) and the frequencies where it happens also have the same shift with the magnitude minimum.

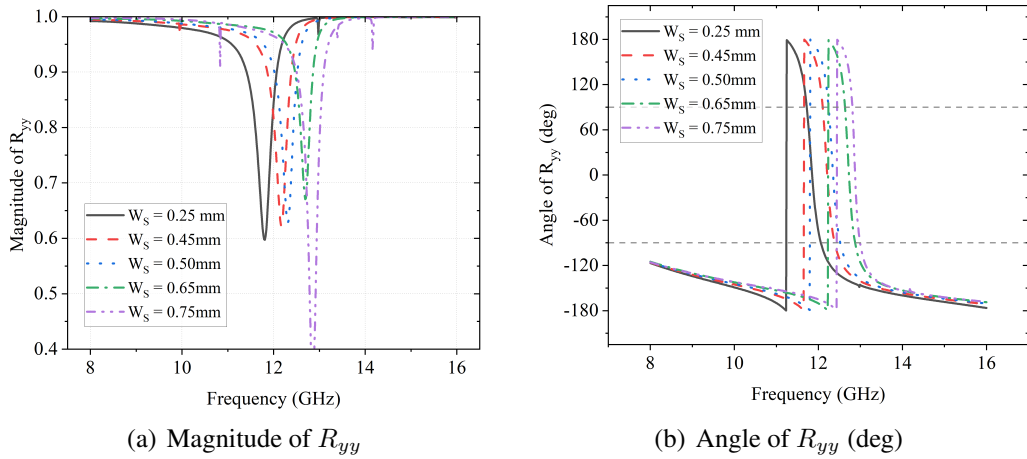


Figure 5.13: Effect of W_s on R_{yy} .

As for the impact of W_s on the y -to- x reflection, it is presented in Figure 5.14. It shows clearly that the peaks of $|R_{xy}|$ shifts from 11.7 GHz to 12.8 GHz as the value of W_s increases in Figure 5.14(a). All the peak values of $|R_{xy}|$ are above 0.65, which means at those frequencies, more than 65% percent of y -polarized waves are reflected

5.3 METASURFACE BASED S-SHAPED SPLIT RING RESONATOR FOR LINEAR-TO-CIRCULAR POLARIZATION CONVERSION

as x -polarized ones. The reflections can also be verified by the 360° change in ϕ_{xy} in Figure 5.14(b). It is also noticeable that the phase reverse happens from 12 GHz to 14 GHz, after which the phase curves continue along their original tendency.

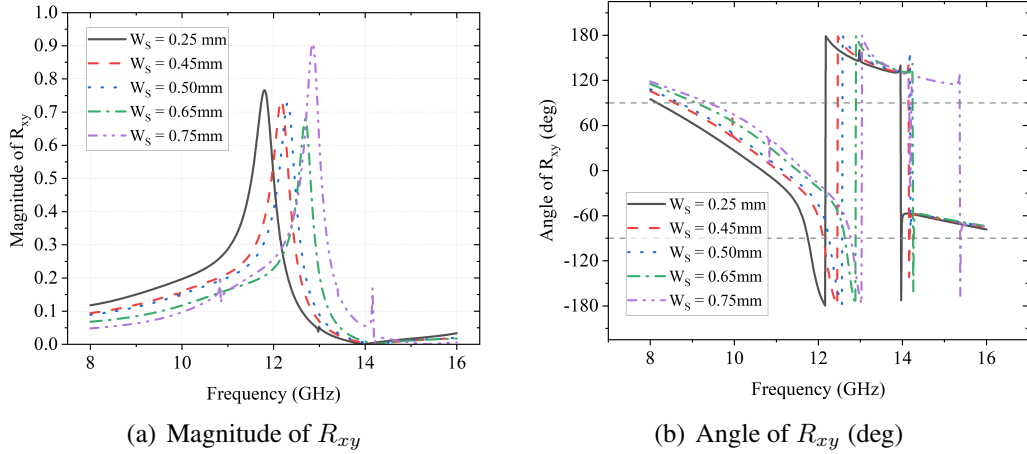


Figure 5.14: Effect of W_s on R_{xy} .

Combining both ϕ_{yy} in Figure 5.13(b) and ϕ_{xy} in Figure 5.14(b), the phase difference $\delta\phi$ is presented in Figure 5.15(a). According to the reference dash lines, two regions where $\Delta\phi$ is -270° and -90° can be found at 12.1-14 GHz and 14-16 GHz respectively. The span of each curve in the first region decreases as W_s increases, whereas each curve have nearly the same span in the latter region. Apart from these regions, there are also two points on each curve where $\Delta\phi = 90^\circ$.

Figure 5.15(b) shows the ellipticity e for the parametric sweep of W_s . One noticeable result is that each scenario has the point where $e = 1$, indicating LHCP. In addition, the ellipticity is approaching -1 at 12.8 GHz when $W_s = 0.75$ mm, which is a tendency that an RHCP can be achieved at some point.

The effect of varying W_s on axial ratio is presented in Figure 5.16 and the highlighted green region suggests the <3 dB part to be qualified as circular polarization. It can be observed that each curve has different portion within the highlighted green region,

5.3 METASURFACE BASED S-SHAPED SPLIT RING RESONATOR FOR LINEAR-TO-CIRCULAR POLARIZATION CONVERSION

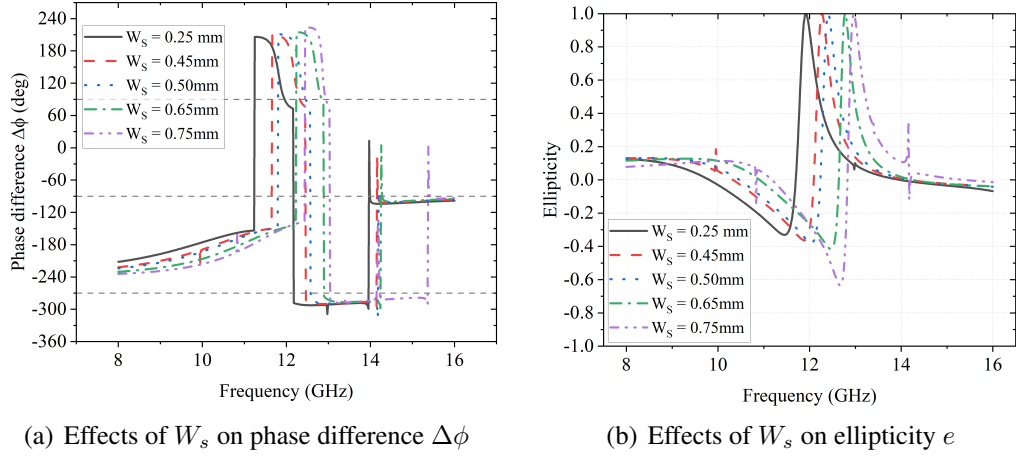


Figure 5.15: Effects of W_s on phase difference $\Delta\phi$ and ellipticity e .

among which it reaches the maximum at 12 GHz when W_s is 0.25 mm.

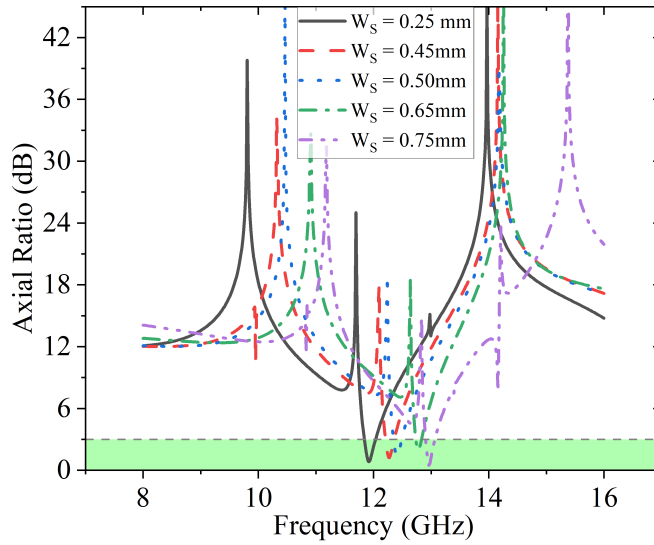


Figure 5.16: Effects of W_s on axial ratio.

The effects of W_s on the energy conversion efficiency η and PCR are illustrated in Figure 5.17(a) and 5.17(b), respectively. It clear that over 90% of energy conversion efficiency are achieved for different W_s values in Figure 5.17(a). On the other hand, the overall PCR is above 50% for each scenario in Figure 5.17(b) and the frequency of the maximum conversion rate shifts from 11.8 GHz to 13 GHz as the value of W_s increases.

5.3 METASURFACE BASED S-SHAPED SPLIT RING RESONATOR FOR LINEAR-TO-CIRCULAR POLARIZATION CONVERSION

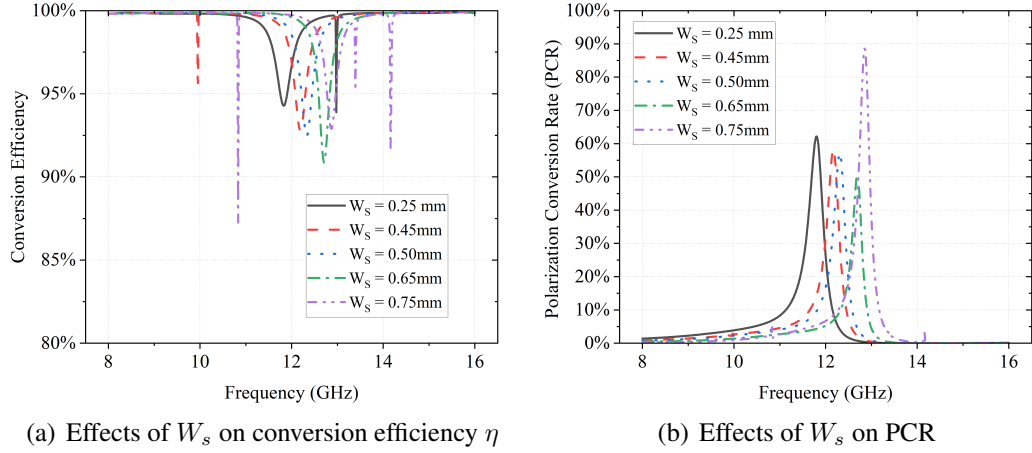


Figure 5.17: Effects of W_s on conversion efficiency η and PCR.

From all the above parametric sweep results of both the gap between the "S" and "C" g_1 and the trace width W_s , significant shifts along frequency can be found in magnitude and phase of the two reflection and conversion components when the parameter value changes. Thus, it is a solid proof that the operating frequency is tunable by adjust the value of those parameters. With the current sweep range, the converter can be tuned between 12 GHz to 14 GHz. In addition, both energy conversion efficiency and polarization conversion rate are relatively high during the sweep simulation.

5.3.2 Simulation Results and Discussion

After the parametric study and optimisation in HFSS, one set of the parameters is chosen so that the proposed design can achieve LTC polarization conversion at 12.4 GHz. The finalised dimensional parameters are listed as: $p = 13$ mm, $d_1 = 5.75$ mm, $d_2 = 4.25$ mm, $d_3 = 8$ mm, $w = 0.5$ mm, $g_1 = 0.75$ mm, $g_2 = 0.5$ mm as shown in Figure 5.5(a).

According to equation (5.56), at 12.4 GHz, the magnitudes of reflection coefficient R_{yy} and R_{xy} need to be equal. As shown in Figure 5.18(a), $|R_{yy}|$ and $|R_{xy}|$ are approximately equal with a value of 0.70 as highlighted in the yellow area. Moreover, a phase difference of $\Delta\phi = -270^\circ$ (or 90°) can be found on the pink curve in Figure

5.3 METASURFACE BASED S-SHAPED SPLIT RING RESONATOR FOR LINEAR-TO-CIRCULAR POLARIZATION CONVERSION

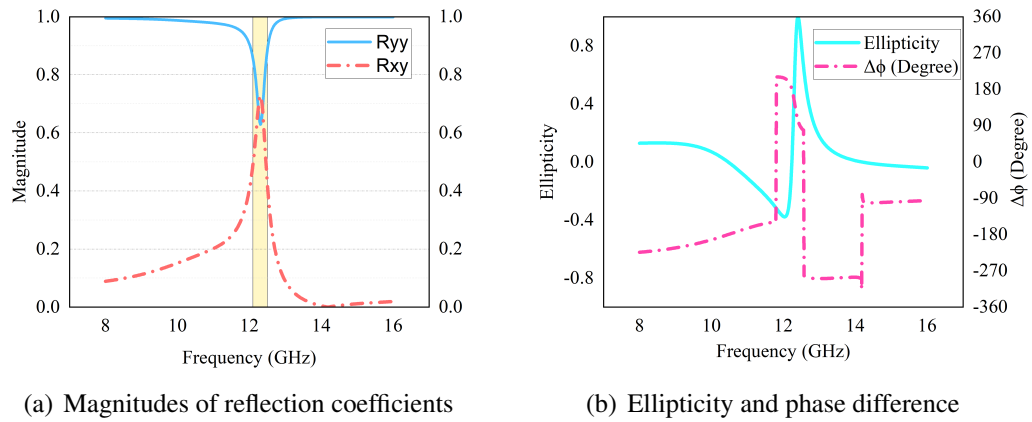


Figure 5.18: Performance of proposed LTC polarization converter.

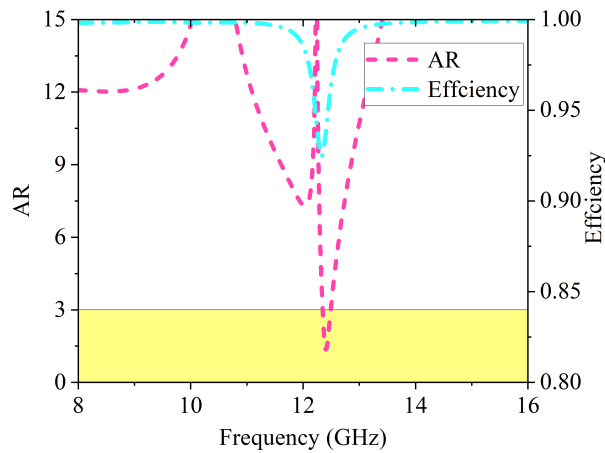


Figure 5.19: Axial ratio and efficiency.

5.18(b), which suggests that the reflected wave is an LHCP wave. This is also verified by the value 1 of ellipticity e at the frequency of interest as shown on the blue curve.

In addition, as illustrated in Figure 5.19, the AR of the proposed design is below 3 dB (highlighted in yellow), which indicates the final electromagnetic wave is qualified as circular polarization. It also suggests that the energy conversion efficiency of this design is about 92% at 12.4 GHz.

To testify the enhancement of the LTC converter, a microstrip patch antenna operating

5.3 METASURFACE BASED S-SHAPED SPLIT RING RESONATOR FOR LINEAR-TO-CIRCULAR POLARIZATION CONVERSION

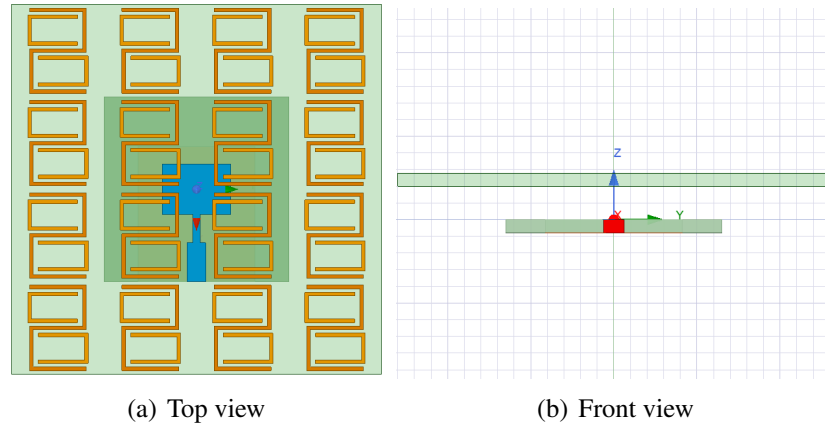


Figure 5.20: Simulation of the patch antenna and proposed LTC converter.

at 12.4 GHz is placed under a finite 4×4 unit cell array as shown in Figure 5.20. The distance between the patch antenna and the LTC converter is a quarter wavelength $\lambda/4 = 4$ mm in the dielectric substrate at 12.4 GHz.

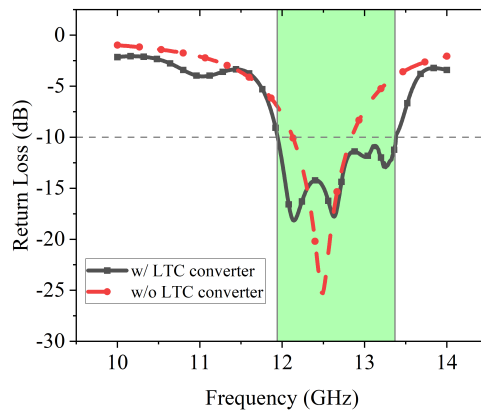


Figure 5.21: Return loss bandwidth of the patch antenna with LTC converter.

As shown in Figure 5.21, it can be seen clearly that the bandwidth of the patch antenna without applying the LTC converter is 0.71 GHz (from 12.13 GHz to 12.84 GHz), whereas the bandwidth with the LTC converter increase to 1.43 GHz as highlighted in green colour (from 11.94 GHz to 13.37 GHz), which is nearly doubled.

5.3.3 Conformal Test with Wavy Curvature Surface

As discussed in Chapter 4 and 5, for antennas applied on conformal surfaces and human body wearable applications, the corresponding polarization converter also need the ability to cope with similar situations. Therefore, a conformal test is conducted in HFSS to evaluate the performance and tolerance of the proposed polarization converter.

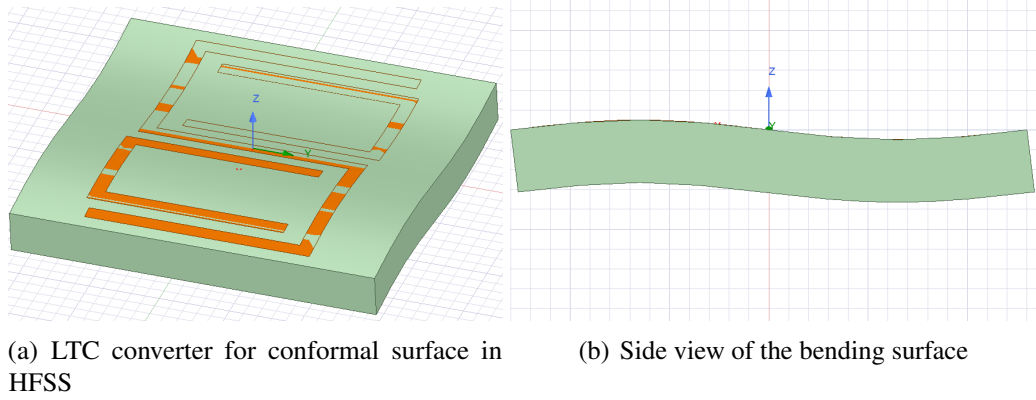


Figure 5.22: Over view of the curvature surface of the proposed LTC converter.

Due to the periodicity of the metasurface, a periodic curved surface is required for conformal test. Therefore, a sinusoidal curve is chosen. In the test, the entire unit cell is bent along a sinusoidal curve on the XoZ -plane as shown in Figure 5.22, where the period of the sine wave equals to the periodicity of the unit cell, i.e. $T = p = 13$ mm. Thus, the curvature of the structure is also repeated with the unit cell. In this case, the amplitude of the sine wave is set as a variable to simulate different levels of bending, namely A_{bend} . The value of A_{bend} is swept from 0 mm to 1 mm with a step size of 0.25 mm.

The magnitude and phase change of y -to- y reflection coefficient R_{yy} are illustrated in Figure 5.23, and those of y -to- x reflection coefficient R_{xy} are presented in Figure 5.24. It can be observed that for both R_{yy} and R_{xy} , their peak magnitudes have minor shifts from 12 GHz to 13 GHz as A_{bend} increases from 0 mm to 1 mm gradually. It suggests

5.3 METASURFACE BASED S-SHAPED SPLIT RING RESONATOR FOR LINEAR-TO-CIRCULAR POLARIZATION CONVERSION

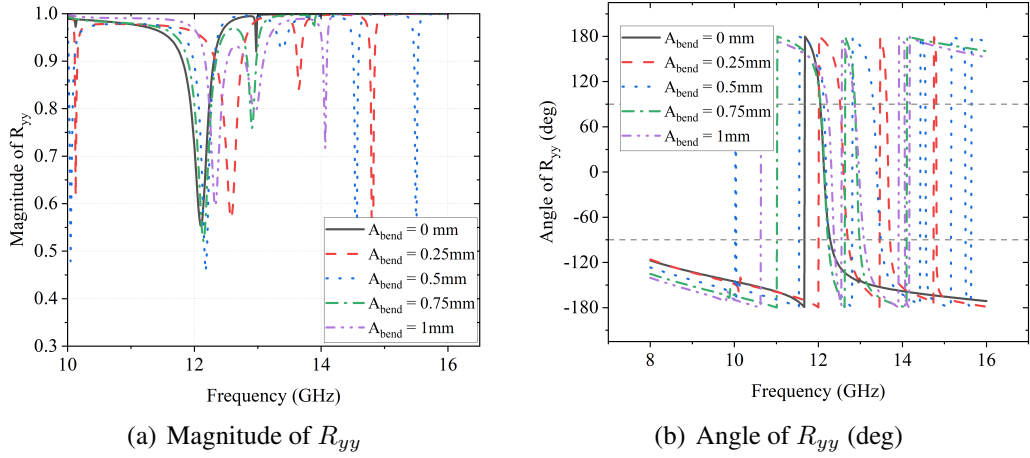


Figure 5.23: Effects of A_{bend} on R_{yy} .

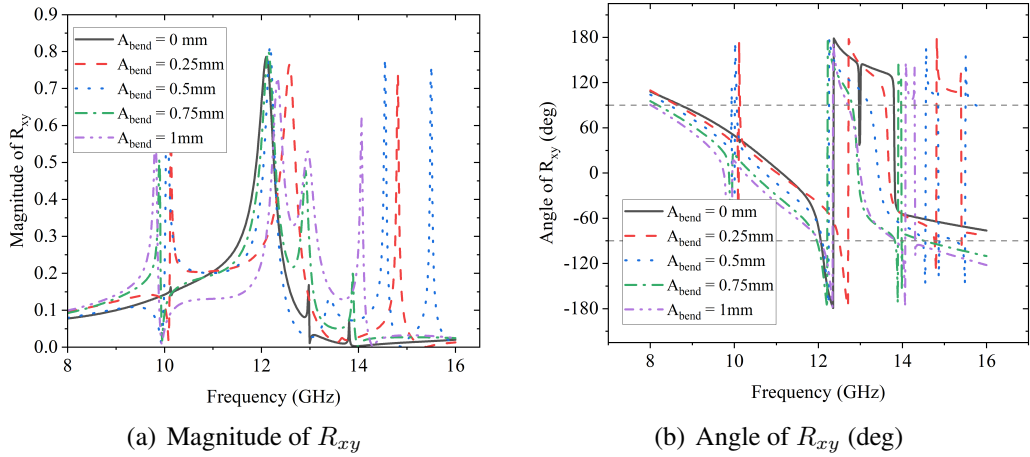


Figure 5.24: Effects of A_{bend} on R_{xy} .

that the frequency where reflection conversion happens has minor deviations due to the conformal surface.

As the second condition to achieve LTC polarization conversion, the phase difference $\Delta\phi$ is important. The impact of the sinusoidal conformal surface on it is presented in Figure 5.25, from which it is noticeable that there are only two points where $\Delta\phi$ is -270° between 12 GHz and 14 GHz for each case except the one without bending ($A_{bend} = 0$ mm).

On the other hand, the results of ellipticity e and axial ratio for the conformal bending

5.3 METASURFACE BASED S-SHAPED SPLIT RING RESONATOR FOR LINEAR-TO-CIRCULAR POLARIZATION CONVERSION

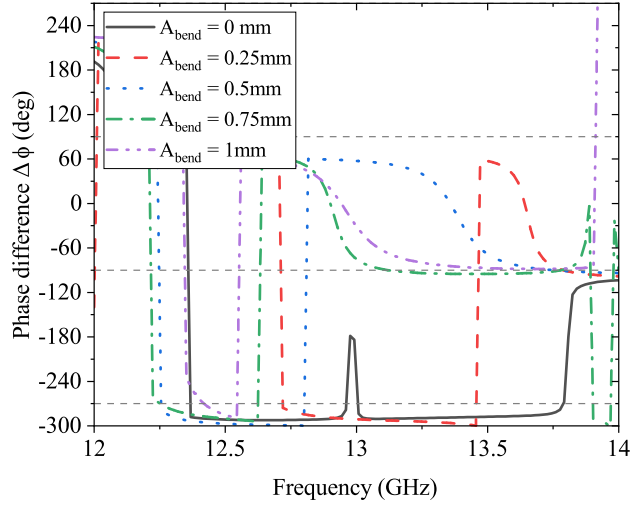
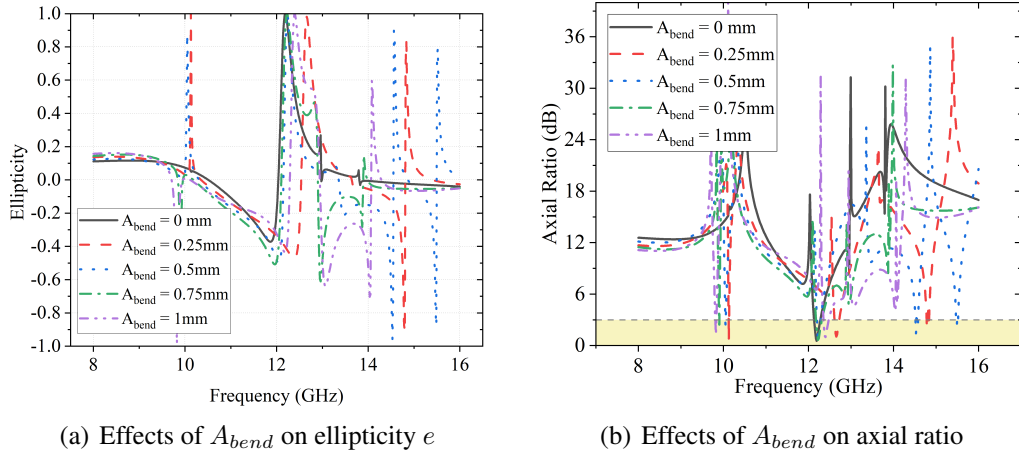


Figure 5.25: Effects of A_{bend} on phase difference $\Delta\phi$.

test are given in Figures 5.26(a) and 5.26(b), respectively. The frequencies where $e = 1$ and $AR < 3$ dB can be found in the figures with minor shifts in agreement to those in Figure 5.23 and 5.24.



(a) Effects of A_{bend} on ellipticity e

(b) Effects of A_{bend} on axial ratio

Figure 5.26: Effects of A_{bend} on ellipticity e and AR.

The overall results of the conformal tests suggest that the proposed LTC polarization converter is subject to operating frequency shift due to the sinusoidal conformal surface. In addition, the phase difference has no perfect range that matches for $\pm 90^\circ$, but only two intersection points. This suggests that the two converted components may not be in

perfect $\pm 90^\circ$ phase difference, which will lead an imperfect circular polarization.

5.3.4 Remarks

To sum up, a low-profile single-layer LTC polarization converter is proposed for 12.4 GHz, which consists of a nested "S"- and "C"- shaped SRR metasurface structure. Simulated results show high polarization conversion rate and energy conversion efficiency. The AR of converted waves at desired frequency is < 3 dB. In addition, a conformal test with a sinusoidal wavy surface is simulated to evaluate the resilience of the design to potential conformal circumstances. The result shows that the design is subject to minor frequency shift due to the curvature surface.

5.4 Chapter Summary

In this chapter, a method is explored to enhance the performance of planar antenna by applying metasurface structure. A metasurface based linear-to-circular polarization converter is proposed to convert a linearly polarized incident wave into a left-handed circularly polarized wave so that the return-loss bandwidth can be broadened. Parametric studies and simulation results are given for the design, which show that at the desired frequency, the converter has a high energy conversion efficiency and polarization conversion rate. Further conformal tests are conducted to test the performance of the design when applied at flexible and curvature surfaces. Result shows that it is subject to minor operating frequency shift. In general, the proposed converter can be applied for LTC polarization or return-loss bandwidth improvement.

Chapter 6

Conclusion and Recommendations for Future Work

6.1 Conclusion

In the era of rapidly developing wireless communication technology such as 5G and IoT, undoubtedly, antennas are a vital part of the wireless systems in our daily lives. As miscellaneous types of wireless communication devices flourish in various areas, antennas are required in different situations.

This thesis explored flexible antenna designs with low-profile and low-cost features, which can be applied in conformal and curvature surfaces, furthermore, in wearable devices on human body. In total, four flexible planar antenna designs were proposed in this thesis: a silver ink based screen-printed wideband dipole array antenna operating from 23 GHz to 30 GHz, a microstrip slot antenna with parallel slits loading operating at 5.8 GHz, a microstrip patch antenna with multiple slots operating at 5.8 GHz, 6.2 GHz, and 8.4 GHz, and a metasurface based S-shaped-SRR LTC polarization converter for performance enhancement for planar patch and slot antennas. All these antennas

6.2 RECOMMENDATIONS FOR FUTURE WORK

were designed on flexible substrates including textile and flexible PCB. Conformal bending tests were simulated in HFSS to evaluate the antennas' performance under flexible and curvature surfaces. It suggests that the designs can basically remain their performance before a threshold bending point, after which non-negligible deterioration might happen. In addition, simulations where the antennas were placed close to human body model were conducted to evaluate the influence on the antennas. The measured SARs suggest that in most part of the involved human body part, the two slot antennas have promising SAR value below the international standard.

The findings in this thesis has shed new light on flexible low-profile planar antenna design for curvature surfaces and added to the rapidly expanding field of WPAN applications. Moreover, the analysis of flexible antennas has made several contributions to the current literature of the performance of planar antennas applied on conformal surfaces and the interactions between flexible antennas and human body. The method to fabricate the proposed antenna has provided practical implications for flexible antenna fabrication.

6.2 Recommendations for Future Work

Due to the limit of time and laboratory equipment and the impact from COVID-19, there are still some imperfection in this thesis. Therefore, the recommendations of the future work will focus on antenna performance enhancement and further experimental investigation, which can be concluded as:

1. To further enhance the gain of the proposed antennas and enlarge operating bandwidth to minimise the limit of the applications. Enhancement techniques should be investigated and applied.
2. To scrutinise and evaluate the performance of the antenna with practical conformal

6.2 RECOMMENDATIONS FOR FUTURE WORK

circumstances and practical wearable application tests on real human body instead of ideal models.

3. To conduct experiments using alternative methods to fabricate flexible antennas to further reduce cost and improve performance while maintaining the low-profile feature.
4. To extend the proposed designs to antenna arrays for potential applications with massive multiple-input multiple-output (MIMO) in 5G technology.

References

- [1] “Wireless,” Oct. 2021, page Version ID: 1050017081. [Online]. Available: <https://en.wikipedia.org/w/index.php?title=Wireless&oldid=1050017081>
- [2] J. W. Klooster, *Icons of Invention: The Makers of the Modern World from Gutenberg to Gates*. Santa Barbara, Calif: Greenwood Press, 2009, oCLC: ocn316098719.
- [3] T. Rappaport, “The wireless revolution,” *IEEE Communications Magazine*, vol. 29, no. 11, pp. 52–71, Nov. 1991.
- [4] J. M. Golio, *RF and microwave passive and active technologies*. Boca Raton: CRC Press, 2008, oCLC: 929288166.
- [5] A. Ghosh, A. Maeder, M. Baker, and D. Chandramouli, “5G evolution: A view on 5G cellular technology beyond 3GPP Release 15,” *IEEE Access*, vol. 7, pp. 127 639–127 651, 2019.
- [6] Y. Yang and K. Hua, “Emerging technologies for 5G-enabled vehicular networks,” *IEEE Access*, vol. 7, pp. 181 117–181 141, 2019.
- [7] L. Chetri and R. Bera, “A comprehensive survey on internet of things (IoT) toward 5G wireless systems,” *IEEE Internet of Things Journal*, vol. 7, no. 1, pp. 16–32, 2020.
- [8] F. Metzger, T. Hoßfeld, A. Bauer, S. Kounev, and P. E. Heegaard, “Modeling of aggregated IoT traffic and its application to an IoT cloud,” *Proceedings of the IEEE*, vol. 107, no. 4, pp. 679–694, 2019.
- [9] D. Plonis, A. Katkevičius, A. Gurskas, V. Urbanavičius, R. Maskeliūnas, and R. Damaševičius, “Prediction of meander delay system parameters for internet-of-things devices using pareto-optimal artificial neural network and multiple linear regression,” *IEEE Access*, vol. 8, pp. 39 525–39 535, 2020.
- [10] W. Liu, E. Park, S. Zhu, and U. Krieger, “Smart and connected e-health R&D platform,” in *2015 17th International Conference on E-health Networking, Application Services (HealthCom)*, 2015, pp. 677–679.

REFERENCES

- [11] H. H. R. Sherazi, W. Asif, and Z. A. Khan, “5G enabled realtime healthcare system for heart patients,” in *2021 IEEE International Smart Cities Conference (ISC2)*, 2021, pp. 1–6.
- [12] A. Spournias, E. Faliagka, C. Antonopoulos, G. Keramidas, and N. Voros, “Social distance monitoring using AI techniques in AAL environments,” in *2021 IEEE International Conference on Smart Internet of Things (SmartIoT)*, 2021, pp. 383–387.
- [13] D. Zhang, J. J. P. C. Rodrigues, Y. Zhai, and T. Sato, “Design and implementation of 5G e-health systems: Technologies, use cases, and future challenges,” *IEEE Communications Magazine*, vol. 59, no. 9, pp. 80–85, 2021.
- [14] M. Sebrechts, S. Borny, T. Wauters, B. Volckaert, and F. De Turck, “Service relationship orchestration: lessons learned from running large scale smart city platforms on kubernetes,” *IEEE Access*, vol. 9, pp. 133 387–133 401, 2021.
- [15] T. Anagnostopoulos, P. Kostakos, A. Zaslavsky, I. Kantzavelou, N. Tsotsolas, I. Salmon, J. Morley, and R. Harle, “Challenges and solutions of surveillance systems in IoT-enabled smart campus: A survey,” *IEEE Access*, vol. 9, pp. 131 926–131 954, 2021.
- [16] R. W. Ahmad, K. Salah, R. Jayaraman, I. Yaqoob, and M. Omar, “Blockchain for waste management in smart cities: A survey,” *IEEE Access*, vol. 9, pp. 131 520–131 541, 2021.
- [17] H. Jo, S. Kang, H. J. Kwon, and J. D. Lee, “In-door location-based smart factory cloud platform supporting device-to-device self-collaboration,” in *2017 IEEE International Conference on Big Data and Smart Computing (BigComp)*, 2017, pp. 348–351.
- [18] S. Bulut, T. G. Giese, M. Wende, and R. Anderl, “The paperless factory: From document driven factories to model driven factories,” in *2020 IEEE International Conference on Teaching, Assessment, and Learning for Engineering (TALE)*, 2020, pp. 725–730.
- [19] C. Chalkiadakis, P. Iordanopoulos, F. Malin, M. Flachi, M. Giannini, E. Mitsakis, and R. Öörni, “An online training tool for better understanding the operation and significance of ITS,” in *2019 6th International Conference on Models and Technologies for Intelligent Transportation Systems (MT-ITS)*, 2019, pp. 1–8.
- [20] F. Zhu, Y. Lv, Y. Chen, X. Wang, G. Xiong, and F.-Y. Wang, “Parallel transportation systems: Toward IoT-enabled smart urban traffic control and management,” *IEEE Transactions on Intelligent Transportation Systems*, vol. 21, no. 10, pp. 4063–4071, 2020.
- [21] B. Ning, T. Tang, Z. Gao, F. Yan, F.-Y. Wang, and D. Zeng, “Intelligent railway systems in China,” *IEEE Intelligent Systems*, vol. 21, no. 5, pp. 80–83, 2006.

REFERENCES

- [22] F. Zhu, Z. Li, S. Chen, and G. Xiong, "Parallel transportation management and control system and its applications in building smart cities," *IEEE Transactions on Intelligent Transportation Systems*, vol. 17, no. 6, pp. 1576–1585, 2016.
- [23] J. D. Kraus and R. J. Marhefka, *Antennas for All Applications*, 3rd ed. New York: McGraw-Hill, 2002.
- [24] R. Garg, Ed., *Microstrip Antenna Design Handbook*. Boston, MA: Artech House, 2001.
- [25] Z. Cui, *Printed Electronics: Materials, Technologies and Applications*. John Wiley Sons, Inc., 2016.
- [26] A. Meredov, K. Klionovski, and A. Shamim, "Screen-printed, flexible, parasitic beam-switching millimeter-wave antenna array for wearable applications," *IEEE Open Journal of Antennas and Propagation*, vol. 1, pp. 2–10, 2020.
- [27] A. S. M. Sayem, R. B. V. B. Simorangkir, K. P. Esselle, R. M. Hashmi, and H. Liu, "A method to develop flexible robust optically transparent unidirectional antennas utilizing pure water, PDMS, and transparent conductive mesh," *IEEE Transactions on Antennas and Propagation*, vol. 68, no. 10, pp. 6943–6952, 2020.
- [28] S. F. Jilani and A. Alomainy, "An inkjet-printed mmw frequency-reconfigurable antenna on a flexible pet substrate for 5G wireless systems," in *Loughborough Antennas Propagation Conference (LAPC 2017)*, Conference Proceedings, pp. 1–3.
- [29] H. Attia, M. L. Abdelghani, and T. A. Denidni, "Wideband and high-gain millimeter-wave antenna based on FSS Fabry-Perot cavity," *IEEE Transactions on Antennas and Propagation*, vol. 65, no. 10, pp. 5589–5594, 2017.
- [30] M. Awais, H. S. Khaliq, and W. T. Khan, "A novel dual-band millimeter-wave antenna for automotive radar and multi-gigabit wireless communications," in *2017 Progress in Electromagnetics Research Symposium - Fall (PIERS - FALL)*, Conference Proceedings, pp. 2802–2807.
- [31] Y. Cao, K. S. Chin, W. Che, W. Yang, and E. S. Li, "A compact 38 GHz multibeam antenna array with multifolded butler matrix for 5G applications," *IEEE Antennas and Wireless Propagation Letters*, vol. 16, pp. 2996–2999, 2017.
- [32] L. Chang, S. He, J. Q. Zhang, and D. Li, "A compact dielectric-loaded log-periodic dipole array (LPDA) antenna," *IEEE Antennas and Wireless Propagation Letters*, vol. 16, pp. 2759–2762, 2017.
- [33] Q. X. Chu, X. R. Li, and M. Ye, "High-gain printed log-periodic dipole array antenna with parasitic cell for 5G communication," *IEEE Transactions on Antennas and Propagation*, vol. 65, no. 12, pp. 6338–6344, 2017.

REFERENCES

- [34] S. Dahal, S. Ahmed, H. King, and M. Faulkner, "Antenna gain in a millimetre-wave multipath environment," in *2018 Australian Microwave Symposium (AMS)*, Conference Proceedings, pp. 93–94.
- [35] H. A. Diawuo and Y.-B. Jung, "Wideband proximity coupled microstrip linear array design for 5G mobile communication," *Microwave and Optical Technology Letters*, vol. 59, no. 12, pp. 2996–3002, 2017.
- [36] T. J. Ellis and G. M. Rebeiz, "Mm-wave tapered slot antennas on micromachined photonic bandgap dielectrics," in *1996 IEEE MTT-S International Microwave Symposium Digest*, vol. 2, Conference Proceedings, pp. 1157–1160 vol.2.
- [37] E. Kim, S. T. Ko, Y. J. Lee, and J. Oh, "Millimeter-wave tiny lens antenna employing U-shaped filter arrays for 5G," *IEEE Antennas and Wireless Propagation Letters*, vol. 17, no. 5, pp. 845–848, 2018.
- [38] B. Lee and Y. Yoon, "Low-profile, low-cost, broadband millimeter-wave antenna array for High-Data-Rate WPAN systems," *IEEE Antennas and Wireless Propagation Letters*, vol. 16, pp. 1957–1960, 2017.
- [39] S. Li, T. Chi, Y. Wang, and H. Wang, "A millimeter-wave dual-feed square loop antenna for 5G communications," *IEEE Transactions on Antennas and Propagation*, vol. 65, no. 12, pp. 6317–6328, 2017.
- [40] Y. Liu, O. Bshara, I. Tekin, and K. R. Dandekar, "A 4 by 10 series 60 GHz microstrip array antenna fed by butler matrix for 5G applications," in *2018 IEEE 19th Wireless and Microwave Technology Conference (WAMICON)*, Conference Proceedings, pp. 1–4.
- [41] K. R. Mahmoud and A. M. Montaser, "Optimised 4 × 4 millimetre-wave antenna array with dgs using hybrid ECFO-NM algorithm for 5G mobile networks," *IET Microwaves, Antennas Propagation*, vol. 11, no. 11, pp. 1516–1523, 2017.
- [42] M. Mantash and T. A. Denidni, "Millimeter-wave beam-steering antenna array for 5G applications," in *2017 IEEE 28th Annual International Symposium on Personal, Indoor, and Mobile Radio Communications (PIMRC)*, Conference Proceedings, pp. 1–3.
- [43] A. Mehdipour, I. D. Rosca, A. R. Sebak, C. W. Trueman, and S. V. Hoa, "Carbon nanotube composites for wideband millimeter-wave antenna applications," *IEEE Transactions on Antennas and Propagation*, vol. 59, no. 10, pp. 3572–3578, 2011.
- [44] A. G. Samoylov, S. A. Samoylov, and T. P. Kurakova, "Modeling of radio channels of millimeter waves range," in *2018 Systems of Signals Generating and Processing in the Field of on Board Communications*, Conference Proceedings, pp. 1–4.

REFERENCES

- [45] H. Sharifi, J. May, K. Shinohara, M. Montes, C. McGuire, and H. Kazemi, "First demonstration of W-band millimeter-wave flexible electronics," in *2013 IEEE MTT-S International Microwave Symposium Digest (MTT)*, Conference Proceedings, pp. 1–4.
- [46] M. T. Hafeez and S. F. Jilani, "Novel millimeter-wave flexible antenna for RF energy harvesting," in *2017 IEEE International Symposium on Antennas and Propagation USNC/URSI National Radio Science Meeting*, Conference Proceedings, pp. 2497–2498.
- [47] M. Wagih, Y. Wei, and S. Beeby, "Flexible 2.4 GHz node for body area networks with a compact high-gain planar antenna," *IEEE Antennas and Wireless Propagation Letters*, vol. 18, no. 1, pp. 49–53, 2019.
- [48] B. Mohamadzade, R. B. V. B. Simorangkir, R. M. Hashmi, and A. Lalbakhsh, "A conformal ultrawideband antenna with monopole-like radiation patterns," *IEEE Transactions on Antennas and Propagation*, vol. 68, no. 8, pp. 6383–6388, 2020.
- [49] J. Zhou, L. Kang, B. Tang, B. Tang, J. Huang, and C. Wang, "Adaptive compensation of flexible skin antenna with embedded fiber bragg grating," *IEEE Transactions on Antennas and Propagation*, vol. 67, no. 7, pp. 4385–4396, 2019.
- [50] Z. Hamouda, J. L. Wojkiewicz, A. A. Pud, L. Kone, S. Bergheul, and T. Lasri, "Magneto-dielectric nanocomposite polymer based dual-band flexible antenna for wearable applications," *IEEE Transactions on Antennas and Propagation*, pp. 1–1, 2018.
- [51] H. Prasad and M. J. Akhtar, "Flexible substrate based CPW-fed antenna for WiMAX application," in *2017 IEEE Applied Electromagnetics Conference (AEMC)*, Conference Proceedings, pp. 1–2.
- [52] S. N. Zabri, N. M. Salleh, M. Abu, and S. Y. Mohamad, "Study of a flexible antenna for intelligent transport system application," in *2017 IEEE Asia Pacific Microwave Conference (APMC)*, Conference Proceedings, pp. 1357–1360.
- [53] E. Li, X. J. Li, B.-C. Seet, and X. Lin, "Ink-printed flexible wideband dipole array antenna for 5G applications," *Physical Communication*, vol. 43, p. 101193, 2020.
- [54] E. Li, X. J. Li, and Q. Zhao, "A design of ink-printable triband slot microstrip patch antenna for 5G applications," in *2020 4th Australian Microwave Symposium (AMS)*, 2020, pp. 1–2.
- [55] E. Li, X. Lin, B.-C. Seet, F. Joseph, and J. Neville, "Low profile and low cost textile smart mat for step pressure sensing and position mapping," in *2019 IEEE International Instrumentation and Measurement Technology Conference (I2MTC)*, 2019, pp. 1–5.

REFERENCES

- [56] E. Li, X. J. Li, B.-C. Seet, and X. Lin, "Flexible ink-printable wideband log-periodic dipole array antenna for 5G applications," in *2018 IEEE Asia-Pacific Conference on Antennas and Propagation (APCAP)*, 2018, pp. 206–207.
- [57] X. Lin, B.-C. Seet, F. Joseph, and E. Li, "Flexible fractal electromagnetic bandgap for millimeter-wave wearable antennas," *IEEE Antennas and Wireless Propagation Letters*, vol. 17, no. 7, pp. 1281–1285, 2018.
- [58] A. Aneja, X. J. Li, and B. E. Li, "Design of continuously tunable low noise amplifier for multiband radio," in *2017 Mediterranean Microwave Symposium (MMS)*, 2017, pp. 1–4.
- [59] B. E. Li, X. Lin, X. J. Li, and A. Aneja, "Design of ink-printed RFID tags for electronic article surveillance systems," in *2017 Mediterranean Microwave Symposium (MMS)*, 2017, pp. 1–4.
- [60] T. S. Rappaport, S. Sun, R. Mayzus, H. Zhao, Y. Azar, K. Wang, G. N. Wong, J. K. Schulz, M. Samimi, and F. Gutierrez, "Millimeter wave mobile communications for 5G cellular: It will work!" *IEEE Access*, vol. 1, pp. 335–349, 2013.
- [61] C. A. Balanis, *Antenna Theory: Analysis and Design*, 3rd ed. Hoboken, NJ: John Wiley, 2005.
- [62] "Modelling and simulation of 5G antenna system." [Online]. Available: <https://www.ansys.com/resource-center/webinar/modeling-and-simulation-of-5g-antenna-system-innovations1>
- [63] H. Friis, "A Note on a Simple Transmission Formula," *Proceedings of the IRE*, vol. 34, no. 5, pp. 254–256, May 1946. [Online]. Available: <http://ieeexplore.ieee.org/document/1697062/>
- [64] "Diamond Engineering Antenna Measurement." [Online]. Available: <https://www.diamondeng.net/resources/microwave-library/>
- [65] B. Kaur, M. Sharma, P. Rawat, D. Mittal, J. Kaur, D. Singh, and E. Sidhu, "Design and performance analysis of high gain microstrip patch antennas employing leather substrates for earth exploration satellite applications," in *2017 International Conference On Smart Technologies For Smart Nation (SmartTech-Con)*, Conference Proceedings, pp. 1399–1404.
- [66] C. R. Salian, B. Santhosh, and S. Vedagarbham, "A review on design and development of low cost 5 GHz microstrip patch array antenna," in *2017 International Conference on Innovative Mechanisms for Industry Applications (ICIMIA)*, Conference Proceedings, pp. 524–527.
- [67] M. U. Khan, M. S. Sharawi, and R. Mittra, "Microstrip patch antenna miniaturisation techniques: A review," *IET Microwaves, Antennas Propagation*, vol. 9, no. 9, pp. 913–922, 2015.

REFERENCES

- [68] R. G. Mishra, R. Mishra, P. Kuchhal, and N. P. Kumari, "Design and analysis of CPW-fed microstrip patch antennas for wide band applications," in *2017 International Conference on Inventive Computing and Informatics (ICICI)*, Conference Proceedings, pp. 651–654.
- [69] A. H. Radhi, R. Nilavalan, H. S. Al-Raweshidy, and N. A. Aziz, "Comparative study on the diversity performance between different microstrip antenna arrays," in *Loughborough Antennas Propagation Conference (LAPC 2017)*, Conference Proceedings, pp. 1–5.
- [70] A. Gupta, J. P. Saini, and D. K. Srivastava, "Analysis of C-shape microstrip line feed patch antenna for bluetooth, WLAN applications," in *2017 International Conference on Multimedia, Signal Processing and Communication Technologies (IMPACT)*, Conference Proceedings, pp. 252–256.
- [71] P. Kumar, "A T shaped microstrip antenna for wireless local area network (WLAN) applications," in *2017 International Conference on Multimedia, Signal Processing and Communication Technologies (IMPACT)*, Conference Proceedings, pp. 147–150.
- [72] Y. P. Zhang, "LTCC-based millimetre-wave microstrip grid array antennas," in *Loughborough Antennas Propagation Conference (LAPC 2017)*, Conference Proceedings, pp. 1–2.
- [73] N. Kaur and S. Malhotra, "A review on significance of design parameters of microstrip patch antennas," in *2016 5th International Conference on Wireless Networks and Embedded Systems (WECON)*, pages = 1-6, DOI = 10.1109/WECON.2016.7993491, type = Conference Proceedings.
- [74] T. Agale and M. M. Khanapurkar, "A review on design approach for performance enhancement techniques of microstrip patch antenna," in *2017 Third International Conference on Advances in Electrical, Electronics, Information, Communication and Bio-Informatics (AEEICB)*, Conference Proceedings, pp. 436–440.
- [75] Y. M. Madany, A. I. Almahallawy, and H. M. Elkamchouchi, "Methodology of band rejection / addition for microstrip antennas design using slot line theory and current distribution analysis," in *2014 Loughborough Antennas and Propagation Conference (LAPC)*, Conference Proceedings, pp. 602–606.
- [76] M. P. Joshi and V. J. Gond, "Microstrip patch antennas for wireless communication: A review," in *2017 International Conference on Trends in Electronics and Informatics (ICEI)*, Conference Proceedings, pp. 96–99.
- [77] J. R. Brianeze, C. H. d. S. Santos, and H. E. Hernandez-Figueroa, "Evolutionary algorithms applied to microstrip antennas design," in *The Second European Conference on Antennas and Propagation, EuCAP 2007*, Conference Proceedings, pp. 1–8.

REFERENCES

- [78] S. Genovesi, F. Costa, and A. Monorchio, "Design of compact wearable antennas by using printed electronics," in *2017 Progress In Electromagnetics Research Symposium - Spring (PIERS)*, Conference Proceedings, pp. 3891–3894.
- [79] J. Mayer, M. Martina, J. Kowalewski, and T. Zwick, "Investigation of bent pcb laminates for conformal antennas at 80 ghz," in *2019 49th European Microwave Conference (EuMC)*, 2019, pp. 940–943.
- [80] A. Enayati, M. Libois, W. De Raedt, and G. A. E. Vandenbosch, "Conformal antenna-in-package solution implemented in a 3d flex-rigid multilayer pcb technology," in *Asia-Pacific Microwave Conference 2011*, 2011, pp. 118–121.
- [81] I. Szini, C. Di Nallo, and A. Faraone, "The enhanced bandwidth folded inverted conformal antenna (eb fica) for mufti-band cellular handsets," in *2007 IEEE Antennas and Propagation Society International Symposium*, 2007, pp. 4697–4700.
- [82] D. L. Goff, Y. Song, G. Riondet, and K. Mouthaan, "Conformal 2.4 ghz antenna with room temperature vulcanized (rtv) silicone rubber substrate," in *2020 14th European Conference on Antennas and Propagation (EuCAP)*, 2020, pp. 1–5.
- [83] O. Pabst, J. Perelaer, E. Beckert, U. S. Schubert, R. Eberhardt, and A. Tünnermann, "All inkjet-printed piezoelectric polymer actuators: Characterization and applications for micropumps in lab-on-a-chip systems," *Organic Electronics*, vol. 14, no. 12, pp. 3423–3429, 2013.
- [84] Y. Ouyang and W. J. Chappell, "High frequency properties of electro-textiles for wearable antenna applications," *IEEE Transactions on Antennas and Propagation*, vol. 56, no. 2, pp. 381–389, 2008.
- [85] K. Kirschenmann, K. W. Whites, and S. M. Woessner, "Inkjet printed microwave frequency multilayer antennas," in *2007 IEEE Antennas and Propagation Society International Symposium*, Conference Proceedings, pp. 924–927.
- [86] A. Chiolerio, V. Camarchia, R. Quaglia, M. Pirola, P. Pandolfi, and C. F. Pirri, "Hybrid Ag-based inks for nanocomposite inkjet printed lines: RF properties," *Journal of Alloys and Compounds*, vol. 615, Supplement 1, pp. S501–S504, 2014.
- [87] J. Jiang, B. Bao, M. Li, J. Sun, C. Zhang, Y. Li, F. Li, X. Yao, and Y. Song, "Fabrication of transparent multilayer circuits by inkjet printing," *Advanced Materials*, vol. 28, no. 7, pp. 1420–1426, 2016.
- [88] B. S. Cook, B. Tehrani, J. R. Cooper, and M. M. Tentzeris, "Multilayer inkjet printing of millimeter-wave proximity-fed patch arrays on flexible substrates," *IEEE Antennas and Wireless Propagation Letters*, vol. 12, pp. 1351–1354, 2013.

REFERENCES

- [89] K. Hettak, T. Ross, R. James, A. Momciu, and J. Wight, “Flexible polyethylene terephthalate-based inkjet printed CPW-fed monopole antenna for 60 GHz ISM applications,” in *2013 European Microwave Conference*, 2013, pp. 1447–1450.
- [90] M. F. Farooqui and A. Shamim, “Dual band inkjet printed bow-tie slot antenna on leather,” in *2013 7th European Conference on Antennas and Propagation (EuCAP)*, 2013, pp. 3287–3290.
- [91] B. S. Cook, B. Tehrani, J. R. Cooper, and M. M. Tentzeris, “Multilayer inkjet printing of millimeter-wave proximity-fed patch arrays on flexible substrates,” *IEEE Antennas and Wireless Propagation Letters*, vol. 12, pp. 1351–1354, 2013.
- [92] B. K. Tehrani, B. S. Cook, and M. M. Tentzeris, “Inkjet printing of multilayer millimeter-wave Yagi-Uda antennas on flexible substrates,” *IEEE Antennas and Wireless Propagation Letters*, vol. 15, pp. 143–146, 2016.
- [93] M. L. Scarpello, I. Kazani, C. Hertleer, H. Rogier, and D. Vande Ginste, “Stability and efficiency of screen-printed wearable and washable antennas,” *IEEE Antennas and Wireless Propagation Letters*, vol. 11, pp. 838–841, 2012.
- [94] H. Yang and X. Liu, “Screen-printed dual-band and dual-circularly polarized textile antenna for wearable applications,” in *2021 15th European Conference on Antennas and Propagation (EuCAP)*, 2021, pp. 1–4.
- [95] H. F. Abutarboush, W. Li, and A. Shamim, “Flexible-screen-printed antenna with enhanced bandwidth by employing defected ground structure,” *IEEE Antennas and Wireless Propagation Letters*, vol. 19, no. 10, pp. 1803–1807, 2020.
- [96] X. Zhou, T. Leng, K. Pan, M. A. Abdalla, and Z. Hu, “Graphene printed flexible and conformal array antenna on paper substrate for 5.8GHz wireless communications,” in *2020 14th European Conference on Antennas and Propagation (EuCAP)*, 2020, pp. 1–4.
- [97] G. S. Khinda, A. Umar, R. J. Cadwell, M. Alhendi, N. C. Stoffel, P. Borgesen, and M. D. Poliks, “Flexible inkjet-printed patch antenna array on mesoporous PET substrate for 5G applications with stable RF performance after mechanical stress cycling,” in *2020 IEEE 70th Electronic Components and Technology Conference (ECTC)*, 2020, pp. 1824–1831.
- [98] Z. Su, M. Vaseem, W. Li, S. Yang, and A. Shamim, “Additively manufactured frequency/radiation pattern reconfigurable antenna based on monolithically printed VO₂ switch,” in *2019 13th European Conference on Antennas and Propagation (EuCAP)*, 2019, pp. 1–4.
- [99] W. T. Li, Y. Q. Hei, P. M. Grubb, X.-W. Shi, and R. T. Chen, “Inkjet printing of wideband stacked microstrip patch array antenna on ultrathin flexible substrates,” *IEEE Transactions on Components, Packaging and Manufacturing Technology*, vol. 8, no. 9, pp. 1695–1701, 2018.

REFERENCES

- [100] J. Kimionis, S. Shahramian, Y. Baeyens, A. Singh, and M. M. Tentzeris, "Pushing inkjet printing to W-Band: An all-printed 90-GHz beamforming array," in *2018 IEEE/MTT-S International Microwave Symposium - IMS*, 2018, pp. 63–66.
- [101] J. S. Chang, A. F. Facchetti, and R. Reuss, "A circuits and systems perspective of organic/printed electronics: Review, challenges, and contemporary and emerging design approaches," *IEEE Journal on Emerging and Selected Topics in Circuits and Systems*, vol. 7, no. 1, pp. 7–26, 2017.
- [102] H. A. Elmobarak, S. K. A. Rahim, M. Himdi, X. Castel, and T. A. Rahman, "Low cost instantly printed silver nano ink flexible dual-band antenna onto paper substrate," in *2017 11th European Conference on Antennas and Propagation (EUCAP)*, 2017, pp. 3061–3063.
- [103] H. Akamatu, H. Inokuchi, and Y. Matsunaga, "Electrical Conductivity of the Perylene–Bromine Complex," *Nature*, vol. 173, no. 4395, pp. 168–169, Jan. 1954.
- [104] G. Horowitz, F. Garnier, A. Yassar, R. Hajlaoui, and F. Kouki, "Field-effect transistor made with a sexithiophene single crystal," *Advanced Materials*, vol. 8, no. 1, pp. 52–54, Jan. 1996.
- [105] S. K. Sarkar, H. Gupta, and D. Gupta, "Flash light sintering of silver nanoink for inkjet-printed thin-film transistor on flexible substrate," *IEEE Transactions on Nanotechnology*, vol. 16, no. 3, pp. 375–382, 2017.
- [106] E. Sipilä, J. Virkki, L. Sydänheimo, and L. Ukkonen, "Experimental study on brush-painted metallic nanoparticle UHF RFID tags on wood substrates," *IEEE Antennas and Wireless Propagation Letters*, vol. 14, pp. 301–304, 2015.
- [107] "ROTARY.SCREEN Printing," Feb. 2016. [Online]. Available: <https://www.zimmer-klagenfurt.com/en/content/rotaryscreen-printing>
- [108] L. Yu, H. You, Q. Zhang, L. Zhang, and J. Fang, "Digestive ripening mechanism investigation in a classical Lee–Meisel method based on *in situ* UV-vis spectra," *CrystrEngComm*, vol. 21, no. 10, pp. 1529–1533, 2019.
- [109] T. Troha, M. Kaspar, V. Hamplova, M. Cigl, J. Havlicek, D. Pociеча, and V. Novotna, "Silver nanoparticles with liquid crystalline ligands based on lactic acid derivatives," *Nanomaterials*, vol. 9, no. 8, 2019.
- [110] P. C. Lee and D. Meisel, "Adsorption and surface-enhanced Raman of dyes on silver and gold sols," *The Journal of Physical Chemistry*, vol. 86, no. 17, pp. 3391–3395, Aug. 1982.
- [111] T. Leng, X. Huang, K. Chang, J. Chen, M. A. Abdalla, and Z. Hu, "Graphene nanoflakes printed flexible meandered-line dipole antenna on paper substrate for

REFERENCES

- low-cost RFID and sensing applications,” *IEEE Antennas and Wireless Propagation Letters*, vol. 15, pp. 1565–1568, 2016.
- [112] L. Pinder, “Michael Palko (August 23, 1923 - October 22, 2004),” *Promotion & Education*, vol. 11, no. 4, pp. 218–218, Dec. 2004.
- [113] R. S. Murphy and R. Torres-Torres, “An overview of RF and microwave engineering research collaboration between latin america and the rest of the world,” in *2016 46th European Microwave Conference (EuMC)*, Conference Proceedings, pp. 843–846.
- [114] D. B. Davidson, “A review of important recent developments in full-wave CEM for RF and microwave engineering [computational electromagnetics],” in *Proceedings. ICCEA 2004. 2004 3rd International Conference on Computational Electromagnetics and Its Applications, 2004.*, Conference Proceedings, pp. PS/1–PS/4.
- [115] B. K. Tehrani, C. Mariotti, B. S. Cook, L. Roselli, and M. M. Tentzeris, “Development, characterization, and processing of thin and thick inkjet-printed dielectric films,” *Organic Electronics*, vol. 29, pp. 135–141, 2016.
- [116] K. Kirschenmann, K. W. Whites, and S. M. Woessner, “Inkjet printed microwave frequency multilayer antennas,” in *2007 IEEE Antennas and Propagation Society International Symposium, 2007*, pp. 924–927.
- [117] S. D. Keller, A. I. Zaghoul, V. Shanov, M. J. Schulz, and D. B. Mast, “Design considerations for a meshed carbon nanotube thread patch antenna,” *IEEE Antennas and Wireless Propagation Letters*, vol. 12, pp. 1192–1195, 2013.
- [118] G. Cheng, Y.-M. Wu, and B. Li, “CNT-based conformal antenna design suitable for inkjet printing,” in *2017 International Applied Computational Electromagnetics Society Symposium (ACES)*, 2017, pp. 1–2.
- [119] L. Yang, R. Zhang, D. Staiculescu, C. P. Wong, and M. M. Tentzeris, “A novel conformal RFID-enabled module utilizing inkjet-printed antennas and carbon nanotubes for gas-detection applications,” *IEEE Antennas and Wireless Propagation Letters*, vol. 8, pp. 653–656, 2009.
- [120] N. Curreli, L. Schirru, L. Gagliani, E. Maniero, G. Montisci, M. Crepaldi, A. Fanti, G. Mazzarella, F. Bonaccorso, V. Pellegrini, and A. Ansaldo, “Graphene-based ultra-wide band printed bow-tie antenna for remote tracking,” in *2019 13th European Conference on Antennas and Propagation (EuCAP)*, 2019, pp. 1–4.
- [121] K. Pan, T. Leng, Y. Jiang, Y. Fang, X. Zhou, M. A. Abdalla, H. Ouslimani, and Z. Hu, “Graphene printed UWB monopole antenna for wireless communication applications,” in *2019 IEEE International Symposium on Antennas and Propagation and USNC-URSI Radio Science Meeting, 2019*, pp. 1739–1740.

REFERENCES

- [122] P. Gregory, *Chemistry and Technology of Printing and Imaging Systems*. London: Blackie Academic & Professional, 1996, oCLC: 669699931. [Online]. Available: <http://site.ebrary.com/id/10647998>
- [123] M. Ikegawa, E. Ishii, N. Harada, and T. Takagishi, "Ink-Particle Flight and Print Simulation for Continuous Inkjet Printer," *The Proceedings of The Computational Mechanics Conference*, vol. 2014.27, no. 0, pp. 163–164, 2014.
- [124] "Nanocenter - INK-JET printer." [Online]. Available: <http://www.nanocenter.si/index.php?page=ink-jet-printer>
- [125] H. Sadeghian, Y. Hojjat, M. Ghodsi, and M. R. Sheykholeslami, "An approach to design and fabrication of a piezo-actuated microdroplet generator," *The International Journal of Advanced Manufacturing Technology*, vol. 70, no. 5-8, pp. 1091–1099, Feb. 2014.
- [126] "JetLabII Ink-jet Printer | NNCI." [Online]. Available: <https://nnci.net/tools/jetlabii-ink-jet-printer>
- [127] R. Valmiro, H. Kitaguti, and S. E. Barbin, "A silk-screen printed RFID tag antenna," in *2015 Asia-Pacific Microwave Conference (APMC)*, vol. 3, Conference Proceedings, pp. 1–3.
- [128] H. Sun, G. Xiao, S. Lang, Z. Zhang, and Y. Tao, "Screen printed HF RFID antennas on polyethylene terephthalate film," *IEEE Journal of Radio Frequency Identification*, vol. 3, no. 2, pp. 91–97, 2019.
- [129] "MSP-886 Automatic Screen Printer | HMI Printers." [Online]. Available: https://www.hmiprinters.com/msp-886-automatic-screen-printer_8_122_26214.html
- [130] G. Xiao, P. Aflaki, S. Lang, Z. Zhang, Y. Tao, C. Py, P. Lu, C. Martin, and S. Change, "Printed UHF RFID reader antennas for potential retail applications," *IEEE Journal of Radio Frequency Identification*, vol. 2, no. 1, pp. 31–37, 2018.
- [131] E. Hrehorova, M. Rebros, A. Pekarovicova, B. Bazuin, A. Ranganathan, S. Garner, G. Merz, J. Tosch, and R. Boudreau, "Gravure printing of conductive inks on glass substrates for applications in printed electronics," *Journal of Display Technology*, vol. 7, no. 6, pp. 318–324, 2011.
- [132] M. Maksud, M. Yusof, and M. Mahadi Abd Jamil, "Optimizing a polydimethylsiloxane (PDMS) into flexographic printing process for RFID biomedical devices and cell cultures," in *The 6th 2013 Biomedical Engineering International Conference*, 2013, pp. 1–4.
- [133] L. B. Keng, W. L. Lai, C. W. A. Lu, and B. Salam, "Processing and characterization of flexographic printed conductive grid," in *2011 IEEE 13th Electronics Packaging Technology Conference*, 2011, pp. 517–520.

REFERENCES

- [134] J. Siden and H.-E. Nilsson, "Line width limitations of flexographic-screen- and inkjet printed RFID antennas," in *2007 IEEE Antennas and Propagation Society International Symposium*, 2007, pp. 1745–1748.
- [135] F. Zhao, L. Mo, W. Li, W. Li, J. Fu, X. Fan, J. Ran, W. Liu, Y. Hou, and L. Li, "Gravure fabrication and stability study of RFID antenna," in *The 8th Annual IEEE International Conference on Nano/Micro Engineered and Molecular Systems*, 2013, pp. 865–868.
- [136] L. Huang, Z.-P. Wang, J.-L. Pu, L. Shen, and J.-K. Zhang, "Graphene pattern by gravure printing for wireless strain sensor," in *2013 Seventh International Conference on Sensing Technology (ICST)*, 2013, pp. 387–389.
- [137] Y. Jung, H. Park, J.-A. Park, J. Noh, Y. Choi, M. Jung, K. Jung, M. Pyo, K. Chen, A. Javey, and G. Cho, "Fully gravure printed wireless cyclic voltammetry tags," in *Proceedings of the 5th Electronics System-integration Technology Conference (ESTC)*, 2014, pp. 1–2.
- [138] D. L. Hine Tong, A. A. Manga, P. Minard, A. Delattre, L. Crowther-Alwyn, and P. Borel, "Comparative study of WLAN dual-band monopole antennas printed and etched on paper and pet substrates," in *2016 46th European Microwave Conference (EuMC)*, 2016, pp. 1243–1246.
- [139] T. J. Cui, D. R. Smith, and R. Liu, Eds., *Metamaterials: Theory, Design, and Applications*. New York: Springer, 2010, oCLC: ocn495597119.
- [140] S. Zouhdi, A. Sihvola, and A. P. Vinogradov, Eds., *Metamaterials and Plasmonics: Fundamentals, Modelling, Applications*. Dordrecht: Springer Netherlands, 2009.
- [141] Y. Luo, K. Qin, H. Ke, B. Xu, S. Xu, and G. Yang, "Active metamaterial antenna with beam scanning manipulation based on a digitally modulated array factor method," *IEEE Transactions on Antennas and Propagation*, vol. 69, no. 2, pp. 1198–1203, 2021.
- [142] K. B. Alici and E. Özbay, "Radiation properties of a split ring resonator and monopole composite," *physica status solidi (b)*, vol. 244, no. 4, pp. 1192–1196, Apr. 2007.
- [143] S. Enoch, G. Tayeb, P. Sabouroux, N. Guérin, and P. Vincent, "A Metamaterial for Directive Emission," *Physical Review Letters*, vol. 89, no. 21, p. 213902, Nov. 2002.
- [144] M. Chen and G. V. Eleftheriades, "Omega-bianisotropic wire-loop huygens' metasurface for wide-angle refraction," in *2019 IEEE International Symposium on Antennas and Propagation and USNC-URSI Radio Science Meeting*, 2019, pp. 1199–1200.

REFERENCES

- [145] R. Zhu, J. Wang, X. Wang, T. Qiu, H. Wang, and Z. Wang, “Adjustable dual-frequency FSS-amplifier metasurface,” in *2019 Photonics Electromagnetics Research Symposium - Fall (PIERS - Fall)*, 2019, pp. 2658–2662.
- [146] C. H. S. Nkimbeng, H. Wang, and I. Park, “Low-profile wideband unidirectional circularly polarized metasurface-based bowtie slot antenna,” *IEEE Access*, vol. 9, pp. 134 743–134 752, 2021.
- [147] D. A. Sehrai, M. Asif, W. A. Shah, J. Khan, I. Ullah, M. Ibrar, S. Jan, M. Alibakhshikenari, F. Falcone, and E. Limiti, “Metasurface-based wideband MIMO antenna for 5G millimeter-wave systems,” *IEEE Access*, vol. 9, pp. 125 348–125 357, 2021.
- [148] O. Siddiqui, Mo Mojahedi, and G. Eleftheriades, “Periodically loaded transmission line with effective negative refractive index and negative group velocity,” *IEEE Transactions on Antennas and Propagation*, vol. 51, no. 10, pp. 2619–2625, Oct. 2003.
- [149] K. B. Alici and E. Özbay, “Radiation properties of a split ring resonator and monopole composite,” *physica status solidi (b)*, vol. 244, no. 4, pp. 1192–1196, Apr. 2007.
- [150] B.-I. Wu, W. Wang, J. Pacheco, X. Chen, T. M. Grzegorzczuk, and J. A. Kong, “A study of using metamaterials as antenna substrate to enhance gain,” *Progress In Electromagnetics Research*, vol. 51, pp. 295–328, 2005.
- [151] R. Ziolkowski and A. Kipple, “Application of double negative materials to increase the power radiated by electrically small antennas,” *IEEE Transactions on Antennas and Propagation*, vol. 51, no. 10, pp. 2626–2640, 2003.
- [152] J. Wang, Y. Li, Z. H. Jiang, T. Shi, M.-C. Tang, Z. Zhou, Z. N. Chen, and C.-W. Qiu, “Metantenna: When metasurface meets antenna again,” *IEEE Transactions on Antennas and Propagation*, vol. 68, no. 3, pp. 1332–1347, 2020.
- [153] X. Luo, M. Pu, X. Ma, and X. Li, “Taming the electromagnetic boundaries via metasurfaces: From theory and fabrication to functional devices,” *International Journal of Antennas and Propagation*, vol. 2015, pp. 1–80, 2015.
- [154] M. Pu, C. Hu, C. Huang, C. Wang, Z. Zhao, Y. Wang, and X. Luo, “Investigation of fano resonance in planar metamaterial with perturbed periodicity,” *Opt. Express*, vol. 21, no. 1, pp. 992–1001, Jan 2013.
- [155] J. B. Andrews, C. Cao, M. A. Brooke, and A. D. Franklin, “Noninvasive material thickness detection by aerosol jet printed sensors enhanced through metallic carbon nanotube ink,” *IEEE Sensors Journal*, vol. 17, no. 14, pp. 4612–4618, 2017.

REFERENCES

- [156] N. Luo, L. Zhang, S. Wong, W. He, and Y. He, "Dual-band and tri-band parasitic dipole antennas for wearable applications," in *2019 IEEE International Conference on Computational Electromagnetics (ICCEM)*, 2019, pp. 1–3.
- [157] B. Li, J. Zhang, Y. Deng, and Z. Zhou, "Design of a low-profile ultra-wideband antenna array based on planar dipole elements," in *2018 IEEE Radar Conference (RadarConf18)*, 2018, pp. 0125–0128.
- [158] Q. Chu, X. Li, and M. Ye, "High-gain printed log-periodic dipole array antenna with parasitic cell for 5G communication," *IEEE Transactions on Antennas and Propagation*, vol. 65, no. 12, pp. 6338–6344, 2017.
- [159] A. Moin, A. Thielens, A. Araujo, A. Sangiovanni-Vincentelli, and J. M. Rabaey, "Adaptive body area networks using kinematics and biosignals," *IEEE Journal of Biomedical and Health Informatics*, vol. 25, no. 3, pp. 623–633, 2021.
- [160] S.-H. Han and S. K. Park, "Performance analysis of wireless body area network in indoor off-body communication," *IEEE Transactions on Consumer Electronics*, vol. 57, no. 2, pp. 335–338, 2011.
- [161] M. T. I. ul Huque, K. S. Munasinghe, and A. Jamalipour, "Body node coordinator placement algorithms for wireless body area networks," *IEEE Internet of Things Journal*, vol. 2, no. 1, pp. 94–102, 2015.
- [162] "Wireless Body Area Networks (WBAN) | WAVES." [Online]. Available: <https://www.waves.intec.ugent.be/research/wireless-body-area-networks>
- [163] C. A. Tavera, J. H. Ortiz, O. I. Khalaf, D. F. Saavedra, and T. H. H. Aldhyani, "Wearable wireless body area networks for medical applications," *Computational and Mathematical Methods in Medicine*, vol. 2021, pp. 1–9, Apr. 2021. [Online]. Available: <https://www.hindawi.com/journals/cmmm/2021/5574376/>
- [164] R. Carrel, "The design of log-periodic dipole antennas," in *1958 IRE International Convention Record*, vol. 9, 1961, pp. 61–75.
- [165] C. Yu, W. Hong, L. Chiu, G. Zhai, C. Yu, W. Qin, and Z. Kuai, "Ultrawideband printed log-periodic dipole antenna with multiple notched bands," *IEEE Transactions on Antennas and Propagation*, vol. 59, no. 3, pp. 725–732, 2011.
- [166] K. P. Ray, V. S. Jadon, and S. Shukla, "Harmonic analysis of antenna factor and transmit antenna factor of dipole antenna with balun," in *2021 IEEE Indian Conference on Antennas and Propagation (InCAP)*, 2021, pp. 506–509.
- [167] E. S. Sakomura, D. B. Ferreira, I. Bianchi, and D. C. Nascimento, "Analysis of archimedean spiral antenna fed by hecken and exponential microstrip baluns," in *2018 IEEE International Symposium on Antennas and Propagation USNC/URSI National Radio Science Meeting*, 2018, pp. 851–852.

REFERENCES

- [168] X. Lin, B. Seet, and F. Joseph, "Fabric antenna with body temperature sensing for BAN applications over 5G wireless systems," in *2015 9th International Conference on Sensing Technology (ICST)*, 2015, pp. 591–595.
- [169] "HPS-021LV Silver Flake." [Online]. Available: <https://www.novacentrix.com/product/hps-021lv-silver-flake/>
- [170] "Matweb - the online materials information resource." [Online]. Available: <https://www.matweb.com/errorUser.aspx?msgid=2&ckck=nocheck>
- [171] R. Dehdasht-Heydari and M. Naser-Moghadasi, "Introduction of a novel technique for the reduction of cross polarization of rectangular microstrip patch antenna with elliptical dgs," *Journal of Electromagnetic Waves and Applications*, vol. 22, no. 8-9, pp. 1214–1222, 2008. [Online]. Available: <https://doi.org/10.1163/156939308784158788>
- [172] J. Acharjee, K. Mandal, and S. K. Mandal, "Reduction of mutual coupling and cross-polarization of a mimo/diversity antenna using a string of h-shaped dgs," *AEU - International Journal of Electronics and Communications*, vol. 97, pp. 110–119, 2018. [Online]. Available: <https://www.sciencedirect.com/science/article/pii/S1434841118306988>
- [173] S. Chaudhuri, R. S. Kshetrimayum, R. K. Sonkar, and M. Mishra, "Dual circularly polarised travelling wave slot antenna array," *Electronics Letters*, vol. 55, no. 20, pp. 1071–1073, Oct. 2019.
- [174] R. Lian, Z. Wang, Y. Yin, J. Wu, and X. Song, "Design of a low-profile dual-polarized stepped slot antenna array for base station," *IEEE Antennas and Wireless Propagation Letters*, vol. 15, pp. 362–365, 2016.
- [175] R. M. van Schelven, D. Cavallo, and A. Neto, "Equivalent circuit models of finite slot antennas," *IEEE Transactions on Antennas and Propagation*, vol. 67, no. 7, pp. 4367–4376, 2019.
- [176] J.-S. Chen, "Studies of CPW-fed equilateral triangular-ring slot antennas and triangular-ring slot coupled patch antennas," *IEEE Transactions on Antennas and Propagation*, vol. 53, no. 7, pp. 2208–2211, 2005.
- [177] G. Li, H. Zhai, T. Li, L. Li, and C. Liang, "CPW-fed S-shaped slot antenna for broadband circular polarization," *IEEE Antennas and Wireless Propagation Letters*, vol. 12, pp. 619–622, 2013.
- [178] Y. Zhu, J. Li, and G.-L. Huang, "A lightweight 3-D printed dual-band high-gain slotted spherical antenna," *IEEE Antennas and Wireless Propagation Letters*, vol. 19, no. 4, pp. 552–556, 2020.

REFERENCES

- [179] T. Liang, Z. Wang, and Y. Dong, "A circularly polarized siw slot antenna based on high-order dual-mode cavity," *IEEE Antennas and Wireless Propagation Letters*, vol. 19, no. 3, pp. 388–392, 2020.
- [180] A. Nikkhah and H. Oraizi, "Efficient 2×2 printed circuit band-gap cavity-backed slot antenna," *IEEE Transactions on Antennas and Propagation*, vol. 68, no. 4, pp. 2550–2556, 2020.
- [181] E. Baghernia, M. M. M. Ali, and A. R. Sebak, " 2×2 slot spiral cavity-backed antenna array fed by printed gap waveguide," *IEEE Access*, vol. 8, pp. 170 609–170 617, 2020.
- [182] W. Liu, Y. Yin, W. Xu, and S. Zuo, "Compact open-slot antenna with bandwidth enhancement," *IEEE Antennas and Wireless Propagation Letters*, vol. 10, pp. 850–853, 2011.
- [183] S. Cheng, P. Hallbjorner, and A. Rydberg, "Printed slot planar inverted cone antenna for ultrawideband applications," *IEEE Antennas and Wireless Propagation Letters*, vol. 7, pp. 18–21, 2008.
- [184] J.-S. Chen, "Studies of CPW-fed equilateral triangular-ring slot antennas and triangular-ring slot coupled patch antennas," *IEEE Transactions on Antennas and Propagation*, vol. 53, no. 7, pp. 2208–2211, 2005.
- [185] K.-L. Wong, H.-J. Chang, C.-Y. Wang, and S.-Y. Wang, "Very-low-profile grounded coplanar waveguide-fed dual-band WLAN slot antenna for on-body antenna application," *IEEE Antennas and Wireless Propagation Letters*, vol. 19, no. 1, pp. 213–217, 2020.
- [186] W. Liu, Y. Yin, W. Xu, and S. Zuo, "Compact open-slot antenna with bandwidth enhancement," *IEEE Antennas and Wireless Propagation Letters*, vol. 10, pp. 850–853, 2011.
- [187] C. Locker, T. Vaupel, and T. Eibert, "Radiation efficient unidirectional low-profile slot antenna elements for X-band application," *IEEE Transactions on Antennas and Propagation*, vol. 53, no. 8, pp. 2765–2768, 2005.
- [188] Y.-Y. Chen, Y.-C. Jiao, G. Zhao, F. Zhang, Z.-L. Liao, and Y. Tian, "Dual-band dual-sense circularly polarized slot antenna with a C-shaped grounded strip," *IEEE Antennas and Wireless Propagation Letters*, vol. 10, pp. 915–918, 2011.
- [189] Y.-S. Wang and S.-J. Chung, "A short open-end slot antenna with equivalent circuit analysis," *IEEE Transactions on Antennas and Propagation*, vol. 58, no. 5, pp. 1771–1775, 2010.
- [190] A. Wegener, H. Hellbruck, C. Wewetzer, and A. Lubke, "Vanet simulation environment with feedback loop and its application to traffic light assistance," in *2008 IEEE Globecom Workshops*, 2008, pp. 1–7.

REFERENCES

- [191] J. Sadovskis, A. Aboltins, and J. Eidaks, "Modulation recognition of unmanned aerial vehicle control signals using software-defined radio," in *2018 IEEE 6th Workshop on Advances in Information, Electronic and Electrical Engineering (AIEEE)*, 2018, pp. 1–5.
- [192] J. G. Baek and K. C. Hwang, "Triple-band unidirectional circularly polarized hexagonal slot antenna with multiple L-shaped slits," *IEEE Transactions on Antennas and Propagation*, vol. 61, no. 9, pp. 4831–4835, 2013.
- [193] B. Ghosh, S. M. Haque, and D. Mitra, "Miniaturization of slot antennas using slit and strip loading," *IEEE Transactions on Antennas and Propagation*, vol. 59, no. 10, pp. 3922–3927, 2011.
- [194] S. M. Haque and K. M. Parvez, "Slot antenna miniaturization using slit, strip, and loop loading techniques," *IEEE Transactions on Antennas and Propagation*, vol. 65, no. 5, pp. 2215–2221, 2017.
- [195] K. M. Parvez, S. Sinha, and S. M. Haque, "Miniaturization of slot antenna using meander slits," in *2018 IEEE 88th Vehicular Technology Conference (VTC-Fall)*, 2018, pp. 1–5.
- [196] N. Rajasekhar, R. R. Reddy, and N. K. Darimireddy, "V-shaped slits and a slot loaded pentagonal boundary patch antennas for wideband applications," in *2017 IEEE International Conference on Antenna Innovations Modern Technologies for Ground, Aircraft and Satellite Applications (iAIM)*, 2017, pp. 1–5.
- [197] L. Liu, C. Liu, Z. Li, X. Yin, and Z. N. Chen, "Slit-slot line and its application to low cross-polarization slot antenna and mutual-coupling suppressed tripolarized mimo antenna," *IEEE Transactions on Antennas and Propagation*, vol. 67, no. 1, pp. 4–15, 2019.
- [198] S.-L. Yang, A. Kishk, and Kai-Fong Lee, "Frequency reconfigurable U-slot microstrip patch antenna," *IEEE Antennas and Wireless Propagation Letters*, vol. 7, pp. 127–129, 2008.
- [199] F. A. Ghaffar, M. Vaseem, and A. Shamim, "A fully printed ferrite nano-particle ink based tunable antenna," in *2016 IEEE International Symposium on Antennas and Propagation (APSURSI)*. Fajardo, PR, USA: IEEE, Jun. 2016, pp. 1059–1060.
- [200] J. Heirons, S. Jun, A. Shastri, B. Sanz-Izquierdo, D. Bird, L. Winchester, L. Evans, and A. McClelland, "Inkjet printed GPS antenna on a 3D printed substrate using low-cost machines," in *2016 Loughborough Antennas & Propagation Conference (LAPC)*. Loughborough, Leicestershire, United Kingdom: IEEE, Nov. 2016, pp. 1–4.

REFERENCES

- [201] Q.-T. Zhang, Y. C. Jiao, Y. Ding, and B. Li, "Design of a planar monopole multiband antenna with U- and L-shaped slots," in *2011 IEEE International Conference on Microwave Technology Computational Electromagnetics*, 2011, pp. 331–333.
- [202] C. Locker, T. Vaupel, and T. Eibert, "Radiation efficient unidirectional low-profile slot antenna elements for X-band application," *IEEE Transactions on Antennas and Propagation*, vol. 53, no. 8, pp. 2765–2768, 2005.
- [203] R. Lian, Z. Wang, Y. Yin, J. Wu, and X. Song, "Design of a low-profile dual-polarized stepped slot antenna array for base station," *IEEE Antennas and Wireless Propagation Letters*, vol. 15, pp. 362–365, 2016.
- [204] T. H. Choi, S. S. Kim, Y. J. Yoon, and H. Kim, "Wide-band slot antenna on metal bezel for covering 28/39 GHz in 5G communication system," in *2019 IEEE International Symposium on Antennas and Propagation and USNC-URSI Radio Science Meeting*, 2019, pp. 29–30.
- [205] H. L. Zhu, S. W. Cheung, K. L. Chung, and T. I. Yuk, "Linear-to-circular polarization conversion using metasurface," *IEEE Transactions on Antennas and Propagation*, vol. 61, no. 9, pp. 4615–4623, 2013.
- [206] S. B. Celik and H. Canbolat, "Wave scattering by a planar junction between anomalously reflecting metasurface and impedance sheets," *IEEE Access*, vol. 9, pp. 135 689–135 696, 2021.
- [207] R. Liu, T. J. Cui, D. Huang, B. Zhao, and D. R. Smith, "Description and explanation of electromagnetic behaviors in artificial metamaterials based on effective medium theory," *Physical Review E*, vol. 76, no. 2, p. 026606, Aug. 2007.
- [208] A. Karlsson, "Approximate boundary conditions for thin structures," *IEEE Transactions on Antennas and Propagation*, vol. 57, no. 1, pp. 144–148, 2009.
- [209] S. A. Maier, *Plasmonics: Fundamentals and Applications*. New York: Springer, 2007.
- [210] Y. Jiang, L. Wang, J. Wang, C. N. Akwuruoha, and W. Cao, "Ultra-wideband high-efficiency reflective linear-to-circular polarization converter based on metasurface at terahertz frequencies," *Optics Express*, vol. 25, no. 22, p. 27616, Oct. 2017.
- [211] Y. Zuo, J. Shi, J. Li, Z. Jin, R. Chen, and Y. Zhang, "A linear to circular polarization converter based on substrate integrated waveguide cavities," in *2019 Cross Strait Quad-Regional Radio Science and Wireless Technology Conference (CSQRWC)*, 2019, pp. 1–3.
- [212] Y. Cheng, J. Fan, H. Luo, and F. Chen, "Dual-band and high-efficiency circular polarization convertor based on anisotropic metamaterial," *IEEE Access*, vol. 8, pp. 7615–7621, 2020.

REFERENCES

- [213] X. Liu, J. Zhang, W. Li, R. Lu, L. Li, Z. Xu, and A. Zhang, “Three-band polarization converter based on reflective metasurface,” *IEEE Antennas and Wireless Propagation Letters*, vol. 16, pp. 924–927, 2017.
- [214] F. Long, S. Yu, N. Kou, C. Zhang, Z. Ding, and Z. Zhang, “Efficient broadband linear polarization conversion metasurface based on $\%$ -shape,” *Microwave and Optical Technology Letters*, vol. 62, no. 1, p. 226–232, 2020.
- [215] B. Lin, L. Lv, J. Guo, Z. Liu, X. Ji, and J. Wu, “An ultra-wideband reflective linear-to-circular polarization converter based on anisotropic metasurface,” *IEEE Access*, vol. 8, pp. 82 732–82 740, 2020.